Title
Spectral Analysis and Tuning of Quantum Confined, Sensing, and Computing Materials

Author
Shin, Ashley Jiwon

Publication Date
2023

Peer reviewed|Thesis/dissertation

UNIVERSITY OF CALIFORNIA

Los Angeles

Spectral Analysis and Tuning of Quantum Confined, Sensing, and Computing Materials

A dissertation submitted in partial satisfaction of the

requirements for the degree Doctor of Philosophy

in Chemistry

by

Ashley Jiwon Shin

2023

ABSTRACT OF THE DISSERTATION

Spectral Analysis and Tuning of

Quantum Confined, Sensing, and Computing Materials

by

Ashley Jiwon Shin

Doctor of Philosophy in Chemistry

University of California, Los Angeles, 2023

Professor Justin R. Caram, Chair

Molecular systems are ideal platforms for future quantum technologies because molecules can be fine-tuned by synthetic chemistry to provide atomic precision, tunability, and reproducibility. Molecules possess electronic and nuclear degrees of freedom that provide a wide range of transition energies across optical, infrared, and microwave frequencies. In this thesis, I present my studies of the physical and electronic structures of lanthanide organometallic complexes and transition metal chalcogenide nanoplatelets. First, I present my investigation into the spectral properties of Yb(III) complexes, which exhibit an ultra-narrow absorption linewidth in solution at room temperature. The ultra-narrow absorption offers unique applications in magnetic sensing. I demonstrate three different magnetometry techniques that we developed, based on magnetic circular dichroism of the narrow absorption feature. Secondly, I discuss the photophysical properties of highly bound and mobile excitons in colloidal nanoplatelets, which

have atomically precise monolayer thicknesses that can be easily tuned for specific absorption and emission properties. I utilize two concepts (the Elliott model and dielectric screening) commonly applied to 2D materials to investigate the absorption of cadmium and mercury chalcogenide nanoplatelets, reporting exciton binding energies for several nanoplatelets for the first time. The investigations highlighted in these chapters emphasize the importance of chemistry in the rational design of quantum technologies. The last chapter depicts the chemical education research conducted in the remote implementation of general and organic chemistry courses during the COVID-19 pandemic, emphasizing the importance of providing structure to online discussion sections to increase student engagement.

The dissertation of Ashley Jiwon Shin is approved.

Anastassia N. Alexandrova

Benjamin J. Schwartz

Wesley C. Campbell

Justin R. Caram, Committee Chair

University of California, Los Angeles

2023

DEDICATION

The achievements highlighted in this dissertation would not have been possible without the support of my family, friends, mentors, and colleagues. First and foremost, I would like to recognize my family to thank them for their enduring support. My dad, Inho Shin, provided emotional, financial, and intellectual support with an unwavering determination to help me through graduate school. My sister, Nicole, and brother-in-law, Tamás, always believed in me and provided advice whenever I needed guidance. I am grateful for the love and support of my amazing partner, Morgan, who always believed in my abilities and supported me under all circumstances. I truly appreciate Morgan for being the rock that I can rely on at hard times.

I would also like to mention my friends, mentors, and colleagues who had meaningful impacts on me during my PhD. I am grateful for my roommate and dear friend, Zerina, who was my biggest cheerleader during our graduate training. I am thankful for the friendships with Patricia, Stephanie, Alex, Austin, and many others at our department. I am fortunate to have worked with incredible collaborators, such as Changling, Barry, and Yongjia, and to have been mentored by amazing scientists, including Profs. Jennifer Casey, Timothy Atallah, Shanna Shaked, Wes Campbell, Anastassia Alexandrova, and Ben Schwartz. I am eternally grateful to my PI, Prof. Justin Caram, who has guided me through my research and growth as a scientist. Justin supported me through all my adventures during graduate school, for which I am so thankful.

TABLE OF CONTENTS

LIST OF FIGURES

LIST OF TABLES

ACKNOWLEDGEMENTS

Chapter 2 is adopted from an unpublished manuscript, "Shin, A. J.; Zhao, C.; Shen, Y.; Dickerson, C. E.; Li, B. Y.; Bim, D.; Atallah, T. L.; Oyala, P. H.; He, Y.; Roshandel, H.; Alson, L. K.; Alexandrova, A. N.; Diaconescu, P. L.; Campbell, W. C.; Caram, J. R. Toward liquid cell quantum sensing: Ytterbium complexes with ultra-narrow absorption. *ChemRxiv.* **2022.** DOI: 10.26434/chemrxiv-2022-vg4jr. [This content is a pre-print]." Experiments and data analysis: AJS, CZ, YS, TLA, PHO, YH, HR, LKA; modeling: CED, DB, BL; writing: AJS, CZ, YS, CED; editing: all authors; advising: ANA, PLD, WCC, JRC.

Chapter 5 is adopted from the published paper, "Shin, A. J.; Hossain, A.; Tenney, S. M.; Tan, X.; Tan, L.; Foley, J. J.; Atallah, T. L.; Caram, J. R. Dielectric Screening Modulates Semiconductor Nanoplatelet Excitons. *J. Phys. Chem. Lett.* **2021**, *12*, 4958-4964." Experiments: AJS, SMT, XT, and LT; modeling: AH and JJF; writing: AJS; editing: all authors; advising: TLA and JRC.

Chapter 6 includes results from "Tenney, S. M.; Vilchez, V.; Sonnleitner, M. L.; Huang, C.; Friedman, H. C.; Shin, A. J.; Atallah, T. L.; Deshmukh, A. P.; Ithurria, S.; Caram, J. R. Mercury Chalcogenide Nanoplatelets—Quantum Dot Hetereostructures as a New Class of Continuously Tunable Bright Shortwave Infrared Emitters. *J. Phys. Chem. Lett*. **2020**, *11*, 3473-3480," "Tenney, S. M.; Tan, L. A.; Sonnleitner, M. L.; Sica, A. V.; Shin, A. J.; Ronquillo, R.; Ahmed, T.; Atallah, T. L.; Caram, J. R. Mesoscale Quantum-Confined Semiconductor Nanoplatelets through Seeded Growth. *Chem. Mater.* **2022**, *34*, 6048-6056," and "Atallah, T. L.; Sica, A. V.; Shin, A. J.; Friedman, H. C.; Caram, J. R. Decay Associated Fourier Spectroscopy: Visible to Shortwave Infrared Time-Resolved Photoluminescence Spectra. *J. Phys. Chem. A*. **2019**, *123*, 6792-6798."

Chapter 7 is adopted from the unpublished manuscript, "Shin, A. J.; Bhagwandin, D. D.; Prado, R.; Ghoshal, K.; Mensah, S. T.; Shaked, S; Casey, J. R. Course elements associated with observed increase in student engagement in remote discussion sections. *J. Chem. Educ*. **2023.** [submitted]." Experiments and data analysis: AJS, DDB, STM, KG; writing: AJS, DDB, JRC; editing: all authors; advising: SS, JRC.

BIOGRAPHICAL SKETCH

Education

2017 **B. A.,** Chemistry (major) and Computer Science (minor)

Washington University in St. Louis

Select Publications

2023 Shin, A. J.; Bhagwandin, D. D.; Prado, R.; Ghoshal, K.; Mensah, S. T.; Shaked, S; Casey, J. R. Course elements associated with observed increase in student engagement in remote discussion sections. **2023.** [In preparation]

2022 Shin, A. J.; Zhao, C.; Shen, Y.; Dickerson, C. E.; Li, B. Y.; Bim, D.; Atallah, T. L.; Oyala, P. H.; Alson, L. K.; Alexandrova, A. N.; Diaconescu, P. L.; Campbell, W. C.; Caram, J. R. Toward liquid cell quantum sensing: Ytterbium complexes with ultra-narrow absorption. *ChemRxiv.* **2022.** DOI: 10.26434/chemrxiv-2022-vg4jr. [This content is a pre-print].

2021 Shin, A. J.; Hossain, A.; Tenney, S. M.; Tan, X.; Tan, L.; Foley, J. J.; Atallah, T. L.; Caram, J. R. Dielectric Screening Modulates Semiconductor Nanoplatelet Excitons. *J. Phys. Chem. Lett.* **2021**, *12*, 4958-4964.

Select Presentations

2023 Mar. "Toward liquid cell quantum sensing: Ytterbium complexes with ultra-narrow absorption," Poster, American Physical Society.

2022 May "Dielectric Screening Modulates Semiconductor Nanoplatelet Excitons," Oral, Materials Research Society.

2022 May "Yb (III) single molecule magnet as a liquid quantum cell for magnetic sensing," Poster, Materials Research Society.

2022 Mar. "Ytterbium (III) complexes with ultra-narrow absorption: steps toward liquid quantum sensing," Oral, American Chemical Society.

2021 Aug. "Dielectric screening modulates semiconductor nanoplatelet excitons," Oral, American Chemical Society

Awards and Honors

2023 Trueblood Dissertation Award

2022 Womanium Hackathon Quantinuum TKET Challenge Winner and Start Up Potential Runner-up

2022 Materials Research Society Best Poster Award

2022 - 23 Charles E. and Sue K. Young Graduate Student Fellowship

2021 - 22 NSF UCLA AIF-Q Quantum Science and Engineering PhD Fellowship

2019 - 23 Early Career Fellowship from the Center for Diverse Leadership in Science

2021 Ralph and Charlene Bauer Award

2020 Center for Quantum Science and Engineering Graduate Fellowship

2020 Michael E. Jung Excellence in Teaching Award

Service

2019 - 23 *Graduate Mentor*, Nanovation Competition

2018 - 23 *Volunteer and Booth Leader,* Exploring Your Universe

2021 - 23 *Co-founder*, Quantum Computing Student Association

2021 - 23 *Graduate Representative for Physical Chemistry*, Graduate Admission Committee

2021 - 22 *Community Activities Committee Chair*, Graduate Student Association

Chapter 1

Introduction to Absorption Spectroscopy

1.1 Historical Overview of Absorption Spectroscopy

In 1672, Newton demonstrated that white light consists of what we now know as the colors of the rainbow, which he demonstrated by separating sun light through closely spaced sheets of glass. He reported his experimental findings in 1704 by publishing the first edition of *Opticks*.[1] In his treatise, Newton details his observations of light diffraction and dispersion, at the end of which he concludes with a set of queries. He asks, "When a ray of light falls upon the surface of any pellucid body, and is there refracted or reflected, may not waves of vibrations, or tremors, be thereby excited in the refracting or reflecting medium? (*Opticks, Qu. 17.*)" Newton alludes to elastic and inelastic energy transfer that occurs when light interacts with matter, for which mathematical proof will not be achieved until the next decade.

The beginning of spectroscopy as an analytical technique was born out of a series of discoveries in the early 1800's. W. Herschel demonstrated that solar radiation extended into the infrared in 1800, which set the precedence for radiometric measurements of light, leading to further investigation into quantitative measurements of atomic spectral lines. In 1802, Wollaston observed dark bands in the emission spectrum of the sun, which later became known as Fraunhofer lines. In 1814, Fraunhofer discovered that the sun's spectrum had a large number of dark lines but was not able to understand the origin of those lines. In 1859, G. Kirchoff discovered that the emitted and absorbed light are the same for all bodies at the same temperature.[2] With this, Kirchoff and R. Bunsen established that the Fraunhofer lines were due to absorption by the gas-phase elements in

the sun and atmosphere. The use of absorption spectroscopy as an analytical tool expanded when Alan Walsh fabricated the first atomic absorption spectrophotometer in 1953.[3] Since then, absorption spectroscopy has been used to identify the spectral fingerprints of various atoms and molecules.

Now, absorption spectroscopy is a standard method for analyzing the elemental contents of a molecular samples in many applications. The absorption spectrum of molecules can be deconstructed into spectral fingerprints of constituent atoms and functional groups that make up the molecular spectra. With recent advancements in synthetic, theoretical, and spectroscopic techniques, the spectra of large, sophisticated molecules can be assigned and even predicted, connecting their atomic arrangements to specific spectral signatures. This process embodies the analytical framework of the investigations presented in this thesis, in which absorption spectroscopy is used to analyze the geometry, energy, and dynamic nature of the large molecules under investigation – often compared to atomic-like models to represent their behavior.

1.2 Physics of Light Absorption by Matter

In general, light-matter interactions can be described as charged particles exchanging energy with an oscillating electromagnetic (EM) field. In classical electromagnetism, light is represented as an oscillating field with its own electric and magnetic fields that are orthogonal to each other. Light can couple to quantum states of matter, depending on resonance requirements of the given interaction. The Hamiltonian for light-matter interaction can therefore be described as:

$$H = H_M + H_L + H_{LM}$$

Where H_M is the time-independent Hamiltonian of the matter (e.g., atoms and molecules), H_L is the time-dependent expression for the EM field of light and H_{LM} is the interaction term between the light and matter.

For a semi-classical solution, H_M is treated quantum mechanically and H_L is treated classically, focusing on the effect that light has on the matter only. For this purpose, H_L can be ignored, which leads to:

$$H \approx H_M + H_{LM}(t)$$

First, $H_{LM}(t)$ can be derived to produce the electric dipole Hamiltonian, starting with the force experienced by a charged particle in an EM field. Then, H_M can be developed, substituting quantum operators for the physical parameters that describe the charged particle. In order to solve for the classical Hamiltonian, the electromagnetic field must be described in terms of a vector potential and afterwards the interaction between the field with charged particles must be added in. The EM field can be derived by solving the Maxwell's equation, which leads to the vector potential expressed in terms of plane waves. From the vector potential, the electric and magnetic fields ($\vec{E}$ and $\vec{B}$) can be expressed as:

$$\vec{E} = -\frac{\partial \vec{A}}{\partial t} = i\omega A_0 \hat{\varepsilon} \left(e^{i(\vec{k}\cdot\vec{r}-\omega t)} + e^{-i(\vec{k}\cdot\vec{r}-\omega t)} \right)$$

$$\vec{B} = \vec{\nabla} \times \vec{A} = i\left(\vec{k} \times \hat{\varepsilon}\right) A_0 \left(e^{i(\vec{k}\cdot\vec{r}-\omega t)} + e^{-i(\vec{k}\cdot\vec{r}-\omega t)} \right)$$

With these relationships, it should be noted that the wave vector, electric field polarization, and magnetic field polarization are all orthogonal. Now, the classical Hamiltonian of a particle in an EM field in the Coulomb gauge is given by:

$$H = \frac{1}{2m}\left(\vec{p} - q\vec{A}\right)^2$$

This expression can be expanded for a collection of charged particles interacting with an EM field. For spectroscopic measurements, we can assume the weak field limit, ignoring any $\left|\vec{A}\right|^2$ dependence, which gives us:

$$H = H_0 + V(t)$$

$$H_0 = \sum_i \left(\frac{\vec{p}_i^2}{2m_i} + V_0\right)$$

$$V(t) = \sum_i \frac{q_i}{2m_i}\left(\overrightarrow{p_i} \cdot \vec{A} + \vec{A} \cdot \overrightarrow{p_i}\right)$$

1.3 Electric Dipole Hamiltonian to Transition Rates

Now, the classical momentum can be substituted by a quantum mechanical expression, $\vec{p} = -i\hbar\vec{\nabla}$, to derive the electric dipole Hamiltonian (EDH). The vector potential remains the same, keeping the wave equation classical and only modulated by interaction strength. Assuming the electric dipole approximation, where the wavelength of the field is much larger than the molecular dimension, the EDH for a collection of charged particles (e.g., molecules) can be expressed as:

$$V(t) = -\left(\sum_i \frac{q_i}{m_i}\left(\hat{\varepsilon} \cdot \overrightarrow{p_i}\right)\right)\frac{E_0}{\omega}\sin\omega t$$

With the Hamiltonian of the system established, we can derive the rates of transitions induced by $V(t)$. For a perturbation by light excitation, $V(t) = V_0 \sin\omega t$, the rate of transitions between sets of initial and final quantum states induced by an electric field is given by:

$$w_{fi} = \sum_{i,f} \frac{\pi}{\hbar^2} |E_0|^2 |\mu_{fi}|^2 \left(\delta(\omega_{fi} - \omega) + \delta(\omega_{fi} + \omega)\right)$$

Where μ_{fi} is the transition dipole matrix element, the scalar part of which equals to $\langle f|\vec{\mu} \cdot \hat{\varepsilon}|i\rangle$ and $\vec{\mu} = \int \vec{r}\rho(\vec{r})d\vec{r}$. The transition dipole element demonstrates that there must be a change in charge distribution (ρ) between $|f\rangle$ and $|i\rangle$ for a radiative transition to occur. This matrix element dictates the symmetry rules between states, which is based on the light field projecting onto the dipole moment. Therefore, the geometry of the molecule, the symmetry of its electronic states, and the orientation of the molecule relative to the light field are all important concepts that will be discussed throughout this thesis.

The key physical properties that can be extracted from spectroscopic measurements are transition frequencies, oscillator strengths, linewidths, and lifetime, which are all related to each other mathematically. The transition rate can be rewritten to accommodate an excited state that decays exponentially by coupling to a continuum, $|n\rangle$. For absorption, the probability of transition to such excited state, $|f\rangle$, can be expressed as:

$$P_f = \frac{E_0^2 |\mu_{fi}|^2}{4\hbar^4} \frac{1}{(\omega_{fi} - \omega)^2 + \vec{w}_{nf}^2/4}$$

The transition probability has a Lorentzian frequency dependence, in which the linewidth is related to the relaxation rate from the excited state to the continuum ($\vec{w}_{nf}$). In other words, the linewidth of absorption depends on the relaxation rate, which is dependent on the system. Therefore, the linewidth, relaxation rate, and lifetime are intrinsic properties of the molecules under investigation that can be extracted from spectroscopic measurements.

1.4 Einstein Treatment of Absorption

In the Einstein treatment, three processes can occur when light interacts with a two-level system (E_1 and E_2). First, absorption occurs when an atom in the ground state is promoted to the excited state by absorbing the resonant photon energy, $\hbar\nu_{21} = E_2 - E_1$. Second, spontaneous emission occurs when an atom in the excited state decays to the ground state by emission of a photon. Third, stimulated emission occurs when an incident photon with energy $\hbar\nu_{21}$ stimulates, without being absorbed, an atom in the excited state to decay by emission of another photon. In 1917, Einstein introduced this model and corresponding A and B coefficients that describe induced absorption, spontaneous emission, and stimulated emission. The Einstein A coefficient is defined in terms of the total rate of spontaneous emission, and B coefficients are defined in terms of transition rates for induced absorption and stimulated emission.

In this Einstein treatment, oscillator strengths (f) can be extracted by comparing emission/absorption rates of an atom to that of a classical oscillator. The oscillator strength of the transition between the upper and lower states is related to A by:

$$f_{12} = \frac{g_2}{g_1}\frac{2\pi\epsilon_0 mc^3 A_{21}}{\omega_{21}^2 e^2}$$

In this expression, the excited state decay rate is proportional to the observed oscillator strength. Since all of the molecules under investigation in this thesis were studied in solution, it should be noted that the refractive index and the speed of light in this equation must accommodate the dielectric of the solution to give the effective values:

$$\epsilon_{eff} = \epsilon_0 {n_r}^2$$

$$c_{eff} = c/n_r$$

In addition, the excited decay rate is inversely proportional to the spectral linewidth. Therefore, the intensity (oscillator strength) and full-width-at-half-maximum (linewidth) observed in spectroscopic measurements are ultimately reflective of the decay rates involved in the observed transitions.

1.5 Absorption of Atoms, Molecules, and Nanoparticles

As the number of atoms increases, the overall system deviates further from the two-level model described above. More excited states, vibrational and rotational coupling, orbital mixing, and spin-orbit coupling are examples of what contributes to the complex nature of molecules and their interactions with light. Although small organic molecules have tens of atoms, inorganic molecules can have upwards of a hundred atoms, like (thiolfan)YbCl(THF) that is presented in chapters 2, 3, and 4. In these chapters, the aim of the study is to investigate the extent to which the molecular transitions in the infrared can be described as "atomic." Driven by applications in quantum information science, the absorption signatures of the Yb^{3+} center are studied in the context of magnetic circular dichroism spectroscopy. Furthermore, nanoparticles consist of hundreds to thousands of atoms, no longer exhibiting properties of molecules but also of bulk, semiconductors. However, in chapter 5, I describe the absorption of excitons that are created on the surface of the semiconductor nanoplatelets as an analogue to that of hydrogen atoms. In the studies presented in this thesis, I extract information from optical measurements, such as linewidth and oscillator strengths. Using various forms of absorption spectroscopy, I investigate the extent to which these larger inorganic molecules and nanoparticles exhibit atomic-like properties.

Chapter 2

Toward Liquid Cell Quantum Sensing:

Ytterbium Complexes with Ultra-narrow Absorption

Adapted with permission from an unpublished manuscript Ashley J. Shin,* Changling Zhao,* Yi Shen,* Claire E. Dickerson,* Barry Li, Daniel Bím, Timothy L. Atallah, Paul H. Oyala, Yongjia He, Hootan Roshandel, Lianne K. Alson, Anastassia N. Alexandrova, Paula L. Diaconescu, Wesley C. Campbell, and Justin R. Caram. Toward liquid cell quantum sensing: Ytterbium complexes with ultra-narrow absorption. **2023**.

2.1 Introduction to Quantum Sensors in Magnetometry

In quantum technology (such as atomic vapor cells used in precision magnetometry), the energetic disorder induced by a fluctuating liquid environment acts in direct opposition to the precise control required for coherence-based sensing. Overcoming fluctuations requires a protected quantum subspace that only weakly interacts with the local environment. Herein, we report a ferrocene-supported ytterbium complex ((thiolfan)YbCl(THF), thiolfan = 1,1′-bis(2,4-di-*tert*-butyl-6-thiomethylenephenoxy)ferrocene) that exhibits an extraordinarily narrow absorption linewidth in solution at room temperature with a full-width at half-maximum of 0.625 ± 0.006 meV. At 77K, spectral hole burning measurement was performed to resolve an even narrower linewidth of 410 ± 20 peV in a disordered glass. A detailed spectroscopic analysis allows us to assign all near infrared (NIR) transitions to atom-centered *f-f* transitions, protected from the solvent environment. A combination of density functional theory and multireference methods match experimental transition energies and oscillator strengths, illustrating the role of spin-orbit coupling

and asymmetric ligand field in enhancing absorption and pointing toward molecular design principles that create well-protected yet observable electronic transitions in lanthanide complexes. Narrow linewidths allow for a demonstration of extremely low-field magnetic circular dichroism at room temperature, employed to sense and image magnetic fields, down to Earth scale. We term this system an 'atom-like molecular sensor' (ALMS) and propose approaches to improve its performance.

Atomic vapor cells (AVCs) are one of the most sensitive and widely deployed methods of detecting electromagnetic fields with applications ranging from astronomy, medicine, geophysical surveys, explosives detection, to remote sensing.[4,5] AVCs are typically derived from K, Cs, or Rb in a sealed container, where laser excitation is used to drive an 'n*s*' to '(n+1)*p*' transition. By monitoring the absorption/fluorescence of these gas-phase alkali atoms, AVC magnetometers have reached extraordinary sub-femtotesla sensitivity in a relatively compact form factor.[6,7] Furthermore, combining microwave excitation and optical pump lasers allows for the preparation of collective quantum states of these systems that can be used for quantum measurement.[6,8,9]

The established limit of AVC sensitivity for magnetic fields is set by the spin-projection noise:

$$\Delta B \approx \frac{1}{g\mu_B}\frac{\hbar}{\sqrt{N\tau T}}$$

Where ΔB is the uncertainty in the measured magnetic field, g is the ground state Landé factor, μ_B is the Bohr magneton, $\hbar$ is the Planck's constant, N is the number of atoms, τ is the coherence time, and T is the measurement duration.[4] In AVCs, a higher N would improve sensitivity, but in practice it is offset by lower τ due to increased collision-based dephasing.[4,7,10–13] A liquid analogue to an AVC, e.g. an atomic-like molecular sensor (ALMS), would utilize atom-like transitions while minimizing drawbacks by accessing much higher number densities (Figure 2.1). If narrow

linewidths can be retained in solution, the number density/pathlength limits of AVCs could be overcome.

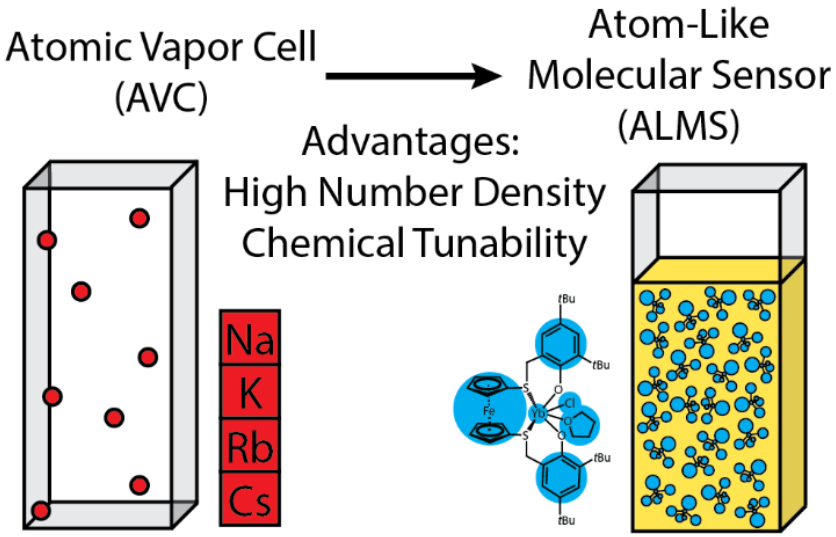

Figure 2.1 Schematic of ALMS as a Liquid Analogue to AVC.

To explore this capability, we chose the *f*-centered transitions in trivalent lanthanide complexes— often referred to as 'atom-like'—as a potential testbed for the applicability of atomic physics technologies in condensed-phase chemistry. We focus on Yb^{3+}, noting that the $4f^{13}$ electron configuration allows for well-protected, electronic transitions between a small manifold of spin-orbit electron configurations. For a Yb^{3+} ion in the gas phase, transitions among spin-orbit states are parity forbidden, interacting only through magnetic dipole. However, the crystal field asymmetry in a Yb^{3+} complex results in coupling between 4*f* and 5*d* orbitals. The 4*f*/5*d* coupling intensifies with further deviation from centrosymmetric point groups, leading to higher oscillator strength. Simultaneously, interactions of the ligands with open 5*d* orbitals lowers their energy, facilitating increased 4*f*/5*d* coupling. The net result is weakly allowed electric dipole transitions among *f*-electron configurations, creating atom-centered transitions with non-negligible oscillator strengths as described by the Judd-Ofelt theory.[14–16] They display near infrared absorption bands,

which retain extremely narrow yet measurable linewidths even in condensed phase environments.[17,18] Solubilization allows for a high number density of these species in a set volume, reaching upwards of 10^{19} molecules per cm^3 (i.e., 10 mM), a value eight orders of magnitude greater than the average density of their AVC counterparts.[19–22]

In this paper, we demonstrate an unprecedented ultranarrow (<1 meV) linewidth achieved in a solution at room-temperature of a molecular lanthanide system—a suggestive first step to liquid-based quantum sensing. Optical and magnetic spectroscopy with detailed electronic structure calculations allow us to assign these spectral features and point to design principles for "near-atomic" localized transitions in the metal center of the molecule and even narrower homogenous linewidths at 77K. We show that a suitably narrow linewidth allows for liquid-based optical measurements of magnetic fields through direct transmission of circularly polarized light, down to the Earth's magnetic field (~0.25 G),[23] paving the way toward a novel liquid-based magnetometry method. Our results represent first steps toward liquid systems which can be analogized to an atomic vapor cell technology.

2.2 Synthesis of Yb(III) Complexes

The Yb^{3+} complex, $[(thiolfan)YbCl]_2$ (thiolfan = 1,1′-bis(2,4-di-*tert*-butyl-6-thiomethylenephenoxy)ferrocene), was synthesized by deprotonating H_2(thiolfan), followed by a reaction with $YbCl_3(THF)_3$ (THF = tetrahydrofuran) at -78 °C. The structure of the monomer with THF coordination, (thiolfan)YbCl(THF), and dimer bridged by two chlorides, $[(thiolfan)YbCl]_2$, were confirmed by single crystal X-ray diffraction measurements (Figures 2.7-2.8). Characterization of the compounds were confirmed by nuclear magnetic resonance (NMR) spectroscopy and elemental analysis (Section 2.8). We note that the spectral measurements in the following sections were performed after dissolving the sample in THF or 2-MeTHF (2-

Methyltetrahydrofuran), in which the compound exists as a monomer. The mononuclear Yb^{3+} compound is expected to coordinate with THF in solution phase, which was confirmed in the solid-state molecular structure (Figure 2.8). The monomer vs. dimer equilibrium is evident in concentration-dependent absorption, diffusion ordered spectroscopy (DOSY), and NMR measurements (Section 2.8).

The magnetic properties were investigated using a superconducting quantum interference device (SQUID) and the Evans method.[24] A magnetic susceptibility value of $\chi_m T = 4.77\ emu \cdot K/mol$ was obtained for the solid sample crushed out of toluene from direct current susceptibility measurements at 290 K after a diamagnetic correction. This is in line with the reported $\chi_m T = 5.14\ emu \cdot K/mol$ for two Yb^{3+} centers ($^2F_{7/2}$, $g_J = 8/7$) (further details in Section 2.8). The paramagnetic properties of the monomer, (thiolfan)YbCl(THF), were evaluated in THF-d_8 revealing $\chi_m T = 2.47\ emu \cdot K/mol$ at room temperature, in line with the reported value for a single Yb^{3+} center ($\chi_m T = 2.57\ emu \cdot K/mol$). This suggests minimal interaction of the Yb^{3+} center(s) in both monomer and dimer forms.

To investigate the relationship between the structural and spectral properties of this class of Yb^{3+} compounds, two derivatives of (thiolfan)YbCl(THF), **1**, were synthesized: (thiolfan*)YbCl(THF), **2**, thiolfan* = 1,1′-bis(2,4-di-*tert*-butyl-6-thiophenol)ferrocene, and (thiolfan)Yb[$N(SiMe_3)_2$], **3**. They were made separately for comparison by modifying the supporting ligand and exchanging the chloride with an amine, respectively. Spectroscopic data presented in this study pertains to Yb samples in THF, unless otherwise noted.

2.3 Electronic Spectroscopy

We measured the broadband electronic absorption spectrum of (thiolfan)YbCl(THF) (Figure 2.2a, b) using a conventional UV-Vis spectrometer (Figure 2.2c, top panels). We observe

several features: a broad ligand absorption band (**I**) in the visible range around 400-600 nm (Figure 2.36), several weakly absorbing transitions (**II** and **III**) from 880-950 nm, and the transition of primary interest: the strongly absorbing, ultranarrow transition (**IV**) at 980 nm. As evident in the small spread of transitions **II-IV**, lanthanide complexes possess strong spin-orbit coupling (~1 eV) and much smaller ligand field splitting (~10-100 meV) than typical transition metal complexes.[25,26] Our primary focus is on the narrow transition denoted **IV**, which shares a similar energy gap as the transition between the $^2F_{7/2}$ and $^2F_{5/2}$ states of the gas phase Yb^{3+} ion (i.e., arising almost entirely from spin-orbit splitting).[27] Conventional UV-Vis spectrometers lack the resolution necessary to quantify sub 1 meV linewidths in the near infrared. Therefore, we utilize a narrowband, continuous-wave Ti:sapphire laser to scan the transmission (Figure 2.2c, bottom panel; Section 2.8 for methods).

The resulting high-resolution spectrum of **IV** fits best to a Lorentzian function with a center energy of 1.2637 eV with a full width at half maximum (FWHM) of 0.625±0.006 meV. Exciting at the ligand absorption band (425 nm), we also recorded the fluorescence spectra using a home-built high-resolution Fourier spectrometer (Figure 2.2d). The emission is collected in an all-reflective off-axis parabolic epifluorescence setup, after which it goes through a Mach-Zender interferometer and towards superconducting nanowire single photon detectors.[28] We note two emission bands, one which overlaps nearly perfectly with **IV** observed in absorption, and another band, **V**, separated by 80 meV. **IV** shows negligible Stokes shift between absorption and emission, consistent with minimal intersystem crossing and vibronic coupling.

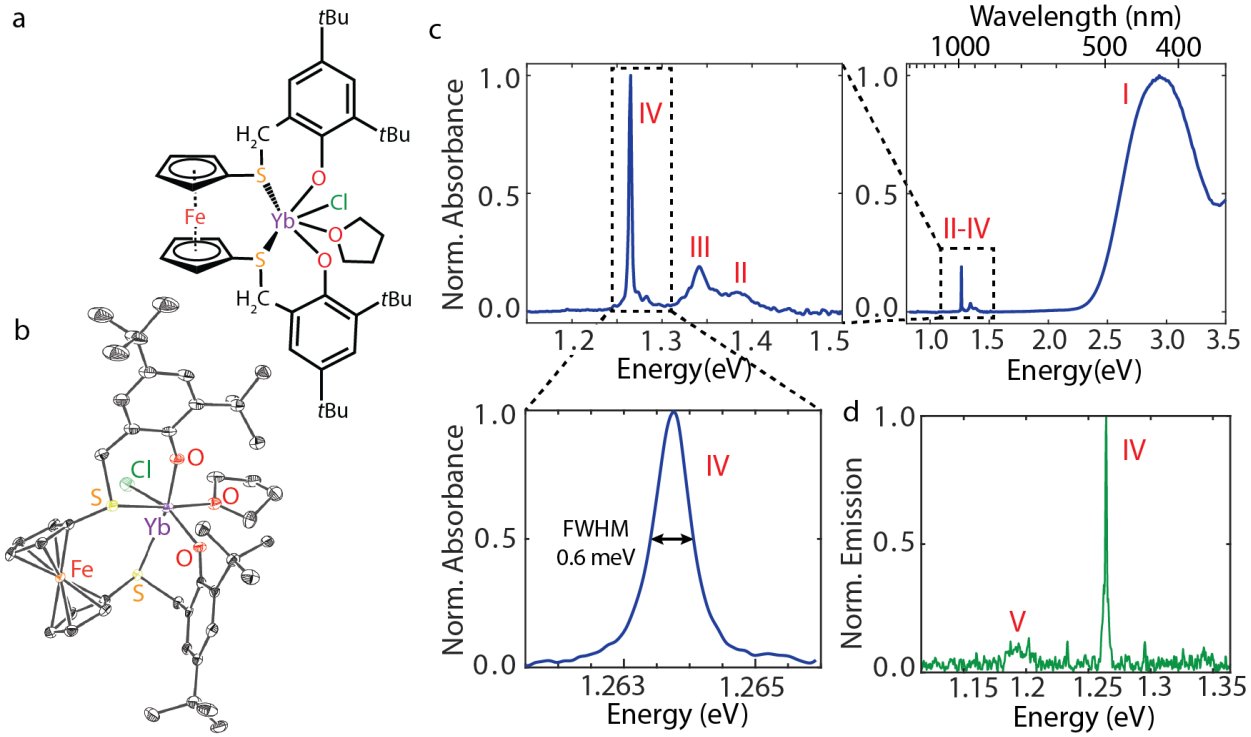

Figure 2.2 Optical Characterization of (thiolfan)YbCl(THF).
(a) Drawing and (b) crystal structure of (thiolfan)YbCl(THF). (c) Wide-field absorption spectrum with zoomed-in absorption spectra around the Yb features, showing a high-resolution absorption scan of the Yb transition with the highest oscillator strength around 980 nm or 1.264 in the bottom left. The absorption spectra were taken with a 3 mM solution in THF at room temperature. (d) Normalized emission spectrum, obtained through Fourier-transform spectroscopy.

To investigate the intrinsic linewidth of transition **IV**, we collected absorption as a function of temperature down to 7 K (Figure 2.3a-b). The feature remains unimodal at cryogenic temperatures, with a slight broadening and blue shift in peak energy as the temperature increases to 300 K (full temperature range shown in Figure 2.38). It should be noted that the sample was frozen in a glass-forming solvent (2-MeTHF), and not crystallized out of solution. Thus, the spectra in Figure 2.3a reflect the optical behavior of the sample in disordered glass at varying temperatures, therefore more closely reflecting its behavior dissolved in solution, as opposed to a solid or crystal. The peak frequency and the FWHM starts to increase near 100 K, corresponding

to the glass transition of the solvent and its concurrent decrease in density.[29] The fact that cryogenic temperatures did not resolve any underlying features suggests that **IV** is dominated by an inhomogeneously broadened set of transitions, brought on by different solvation environments (rather than vibrational coupling). That is, individual chromophores may have slightly different geometries and thus varying transition energies. We hypothesize that the intrinsic linewidth of individual chromophores is most likely narrower than the feature shown in Figure 2.3a. Further discussion on the sources of linewidth broadening can be found in Section 2.8.

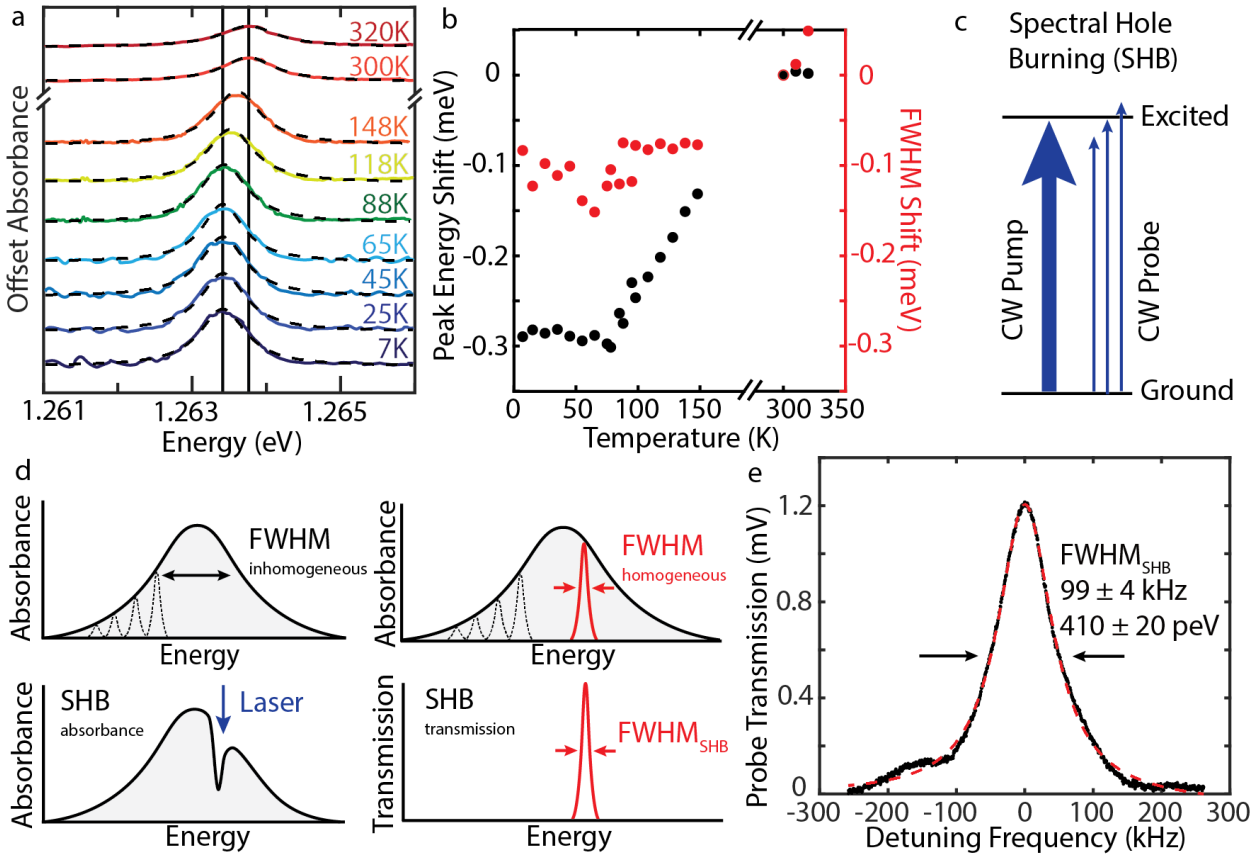

Figure 2.3 Investigating Linewidth Broadening Mechanisms.

a) Temperature-dependent absorption scans of (thiolfan)YbCl(THF). Solid vertical lines are visual guides to emphasize the shift in peak center. b) FWHM and transition energy offsets from corresponding room temperature values. Error bars were too small and are shown in SI fig. S32. c) Energy diagram of the SHB experiment. d) Top panels: diagrams of inhomogeneously and homogeneously broadened linewidth. Bottom panels: diagrams of SHB in absorption and transmission. e) SHB transmission signal of (thiolfan)YbCl(THF) at 77 K.

To resolve the homogeneous linewidth, we performed spectral hole burning (SHB) experiments on (thiolfan)YbCl(THF). A 0.2 mm cuvette with ~30 mM sample in 2-MeTHF is placed in the cryostat and cooled to 77 K. We place a narrow-band, pump laser at the resonant frequency of transition **IV** (305.5 THz) and scan the probe laser around that frequency (SHB setup in Figure 2.39). The CW pump excitation (8 mW) creates a hole in the ground state population, which is detectable by a weaker CW probe beam (0.7 mW), as shown in Figure 2.3c. The homogeneous linewidth can be delineated from the inhomogeneously broadened feature by analyzing the probe transmission as it scans around the pump laser frequency (Figure 2.3d). The probe transmission as a function of the detuning frequency is plotted in Figure 2.3e, demonstrating a narrower feature with a FWHM of 99 KHz or 410 peV, which is more than 6 orders of magnitude narrower than the room-temperature absorption linewidth. Presumably, this 410 peV linewidth is near the limit of the homogeneous linewidth of the transition. The SHB linewidth corresponds to a 1.6 μs lifetime that is very close to the 3.2 μs measured fluorescence lifetime at room temperature (Figure 2.40), which is comparable to lifetimes of other Yb complexes.[30–32] The narrower SHB linewidth indicates that absorption feature at room temperature consists of many transitions. However, we were not able to observe SHB at room temperature, suggesting the liquid environment results in spectral diffusion, frozen out in the glass.

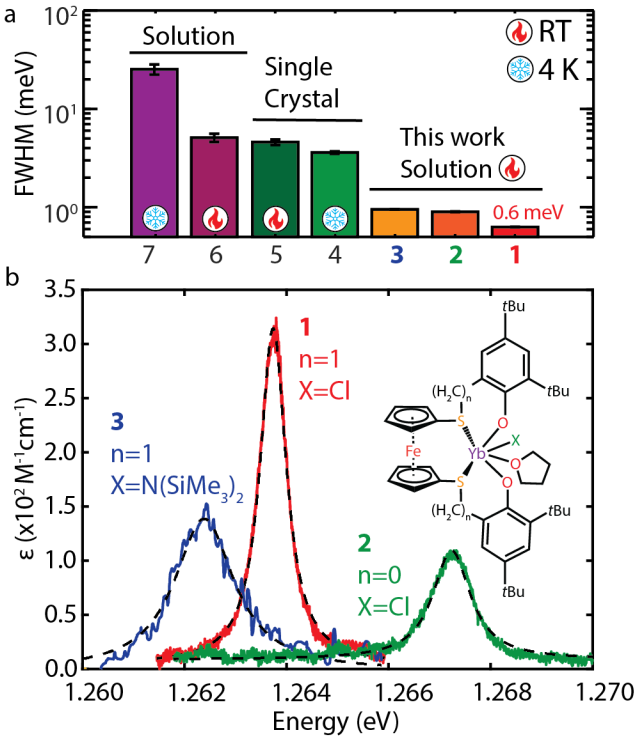

Figure 2.4 Effects of Coordination Environment on Linewidths.

a) Absorption FWHM comparison to other Yb^{3+} complexes.[33–36] b) Drawing of compounds with different ligand designs and their corresponding absorption peaks at 3 mM concentrations. Clarification on the numbered compounds in SI section I-B.

(thiolfan)YbCl(THF) displays a narrower absorption linewidth in solution at room temperature than those of other Yb^{3+} molecules in a variety of media and temperatures. We compare the 0.6 meV linewidth to those of other Yb^{3+} coordination complexes in solution as well as in single crystal, some of which were measured at cryogenic temperatures (Figure 2.4a; expanded linewidth comparison in SI Sec. II-E).[33–36] Our central hypothesis for the correlation between molecular structure and ultra-narrow absorption linewidth is that the rigidity of the ferrocene backbone in the supporting ligand sphere minimizes spectral broadening. For example, Yb(trensal) (where H_3(trensal) is 2,2',2"-tris(salicylideneimino)triethylamine) is a compound with a high degree of magnetic anisotropy and well-defined optical features that shows a linewidth of 4.6 meV (Figure 2.4a #6), roughly an order of magnitude broader than (thiolfan)YbCl(THF).[34]

Contrary to our system, Yb(trensal) shows many absorption features assigned to other spin-orbit transitions and vibrations, and a large apparent Stokes shift, suggesting a more mixed and "molecular" electronic structure in comparison. Even Yb^{3+} doped crystals at 4 K show a larger absorption linewidth of 3.6 meV (Figure 2.4a #7), almost 6 times broader than that of (thiolfan)YbCl(THF), attributed to inhomogeneous crystal environments and phonon coupling.[35,37]

We investigated the relationship between this ultranarrow solution linewidth and molecular geometry by synthesizing two derivatives of (thiolfan)YbCl(THF) with slightly different ligand environments (Figure 2.4b). Variations consists of one fewer carbon connecting the ferrocene and phenoxy moieties (Figure 2.4b: **2**) and of replacing -Cl with $-N(SiMe_3)_2$ (Figure 2.4b: **3**). A high-resolution scan of the transmission of the three derivatives indicates that the linewidth of transition **IV** is preserved, likely because the rigidity of the ferrocene backbone provides protection of the radiative transition **IV** from other sources of line broadening. Compound **3** has a FWHM of 0.947 ± 0.005 meV, while **2** has a FWHM of 0.902 ± 0.007 meV, which are both comparable to the 0.625 meV linewidth of **1**. Although the exact broadening mechanism is unknown, the slight increase in linewidth is mostly likely due to the shorter carbon bridge of **2** changing metal-ligand coupling, and the strong ligand field of the amide group in **3** contributing to the inhomogeneous broadening of the metal transition. The important observation, however, is that all three ytterbium complexes display near record linewidths in solution at room temperature, despite shifts in the primary transition energy that can be attributed to slight deviations in the coordination geometry. Therefore, the original thiolfan ligand preserves the narrowest Yb^{3+} transition linewidth, while minimizing the ligand effects relative to the ground spin-orbit transition (**IV**).

2.4 Electronic Structure Analysis with Multireference Calculations

The isolated Yb^{3+} ion possesses seven degenerate states arising from orbitals of the 4*f* shell with 13 valence electrons. Large electronic spin-orbit coupling separates the 4*f* states into spin-orbit states, creating the optical NIR transition from the 8-state $^2F_{7/2}$ to the 6-state $^2F_{5/2}$ manifolds.[18] In a molecular framework, each spin-orbit manifold is further split due to the ligand-field contributions, giving rise to the individual electronic transitions **II-V** (Figure 2.5a). Magnetic dipole analysis of transition energies and oscillator strengths (Table 2.3) prompted us to assess the degree of molecular/atomic character of electric dipole transitions using multireference electronic structure theory (Section 2.8).[38] Our calculations show that **IV** is primarily composed of states

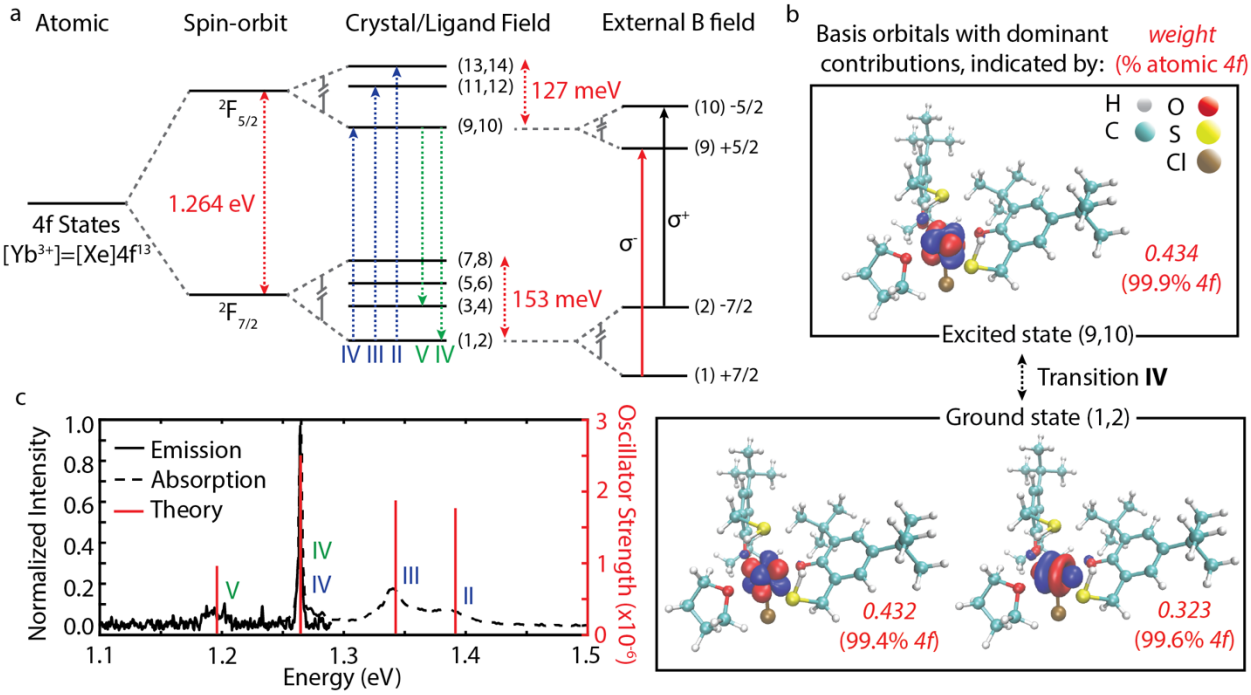

Figure 2.5 Electronic Energy Diagram and Orbitals

a) Electronic structure diagram of (thiolfan)YbCl(THF) showing the incorporation of spin-orbit and ligand field effects on the Yb^{3+} atomic orbitals, calculated with CASSCF/CASPT2/RASSI-SOC level of theory. In a magnetic field, the molecular orbitals are further split to states with primarily spin $\pm\frac{7}{2}$ and $\pm\frac{5}{2}$ characters. b) Visualization of the CASSCF basis orbitals that have dominant contribution(s) to the molecular orbitals involved with transition **IV**, demonstrating "atom-like" properties. c) Comparison between emission/absorption spectra and the calculated transition energies and oscillator strengths.

with ~99% 4*f* character, with the ground and excited states containing mixtures of several 4*f* orbitals. To demonstrate, a visual guide (Figure 2.5b) captures the primary basis orbitals that contribute to the ground and excited state wavefunctions, although we note that these pictures do not reflect the overall multireference nature of the molecular orbitals (full set of complete active space, CAS, orbitals shown in tabs. S3 and S4).

We find that inclusion of the virtual Yb 5*d* orbitals into the '13 electrons in 12 orbitals' active space (i.e., 7 x Yb(4*f*) + 5 x Yb(5*d*)) is critical for obtaining the transition energies and oscillator strengths, in agreement with experiment, and in accordance with the Judd-Ofelt theory (Figure 2.5c).[16,39] Primarily, we attribute the enhanced oscillator strengths to an increased mixing between the 4*f* and 5*d* states, allowing E1 transitions (Table 2.6). The 5*d* virtual orbitals mix with virtual ligand orbitals, lowering them in energy and further enhancing oscillator strength.[40] By incorporating the virtual 5*d* orbitals in the active space, we observe a slight change from the purely 4*f* atomic orbitals to molecular orbitals containing small contributions from the ligands (Table 2.7). Due to lowering the symmetry of 4*f* states, the increased ligand character may also be responsible for an enhancement in the calculated oscillator strengths in transitions **II-IV**. Also, the atom-like characteristic of the molecular orbitals is further confirmed by the agreement among calculated g factors for the ground and excited states ($g_g = 7.89$ and $g_e = 4.26$), the expected g factors of gas-phase Yb^{3+} ($g_g = 8$ and $g_e = 4.28$), and experimentally obtained values ($g_g = 7.486 \pm 0.008$ and $g_e = 3.2 \pm 0.2$; further details in Section 2.8). Altogether, we describe the transitions **II-V** from fig. 4c as dominated by Yb 4*f* orbitals. Since the strength of spin-orbit coupling fundamentally contrasts with the covalency of the metal-ligand bond, we speculate both 4*f*/5*d* and 5*d*/ligand effects must be balanced in the system, and the transition energies and intensities can

thus be influenced by the geometry and the nature of the ligand, as observed for different ligand designs (Figure 2.43).

2.5 Detecting AC and DC Magnetic Fields

We decided to leverage the extraordinarily narrow linewidth of (thiolfan)YbCl(THF) and its open-shell character to detect magnetic fields. We first performed magnetic circular dichroism (MCD) measurements to study spin characteristics. MCD measures the differential absorption of σ^+ and σ^- circularly polarized light induced in a sample under a strong magnetic field that is oriented parallel to the light propagation.[41] Typically, resolving these shifts requires a superconducting magnet, cryogenic temperatures, and lock-in detection.[42] In contrast, we easily measure these shifts using a permanent rare-earth magnet set under the sample at room temperature. With a 0.38 T field, we induce a 23 GHz (0.096 meV) shift in **IV** between right- and left-hand circularly polarized excitations (Figure 2.6a), corresponding to the Zeeman splitting of transition **IV** (Figure 2.5a). We observe a linear correlation between the magnetic field strength and Zeeman splitting by changing the distance between the static magnet and the sample (Figure 2.48). From the linear correlation of the Zeeman splitting with the static magnetic field, we can extract the effective transition magnetic moment as $(2.2 \pm 0.1)\mu_B$. Finally, the subtraction between the σ^+ and σ^- transitions produces the MCD signal, which varies in intensity with the change in magnetic field strength as expected (Figure 2.6b).

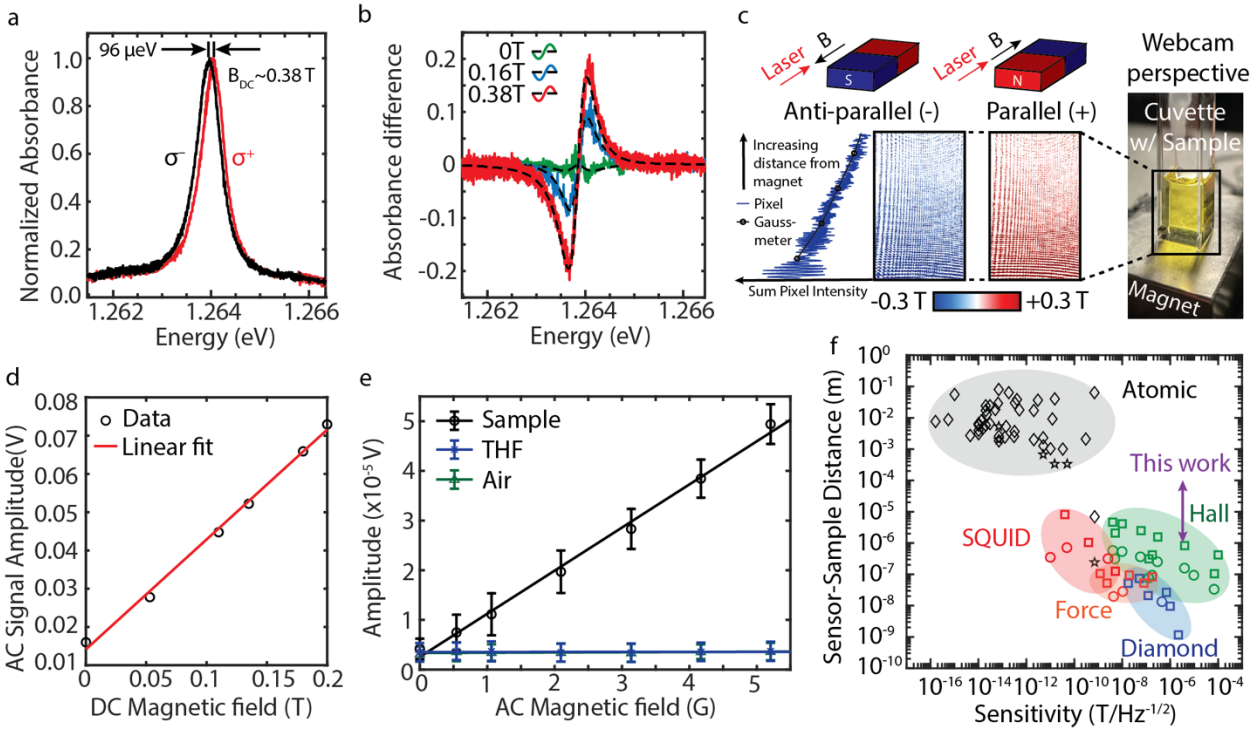

Figure 2.6 Magnetic Circular Dichroism (MCD) Magnetometry.

a) Room temperature Zeeman splitting under a static magnetic field of 0.38 T at around 3 mM concentration. b) Differential absorbance of left and right circularly polarized light under varying DC field strengths. c) Two snapshots of dynamic MCD imaging video demonstrating parallel and anti-parallel orientations of the magnetic field and laser propagation. d) Amplitude of the oscillating transmitted light through the sample under a static magnetic field of 0-0.2 T, measured by a gaussmeter. e) Increase of frequency modulation signal with the amplitude of the applied AC magnetic field in the presence of (thiolfan)YbCl(THF). f) Compilation of sensitivity values of other spin-based magnetometry imaging methods, as it compares to our work, plotted against the "closest" approach of the sensor in proposed device design (fig S49). SQUID: superconducting quantum interference device. Hall: Hall effect magnetometer. Force: magnetic resonance force microscopy. Diamond: nitrogen-vacancy (NV) center in diamond magnetometry. This plot was adapted with permission from Dr. Patrick Appel (University of Basel).

Using this MCD signal, we demonstrate three different schemes for magnetic sensing. First, we imaged a DC magnetic field at room temperature (Figure 2.6c). The transmitted beam

was expanded and imaged with a webcam through the sample in a glass cuvette placed above a static magnet. The pixel intensity was converted to magnetic field strength by calibrating to gaussmeter measurements. Since the circularly polarized transmission varies with the strength of the magnetic field, we can extrapolate to a magnetic field map, both in intensity and relative direction (e.g., parallel or anti-parallel to laser propagation). The sensitivity of this measurement depends on the uncertainty of the g factor and the resolution of the absorption measurement, leading to a sensitivity of 0.05 T (500 G) with this MCD setup (Section 2.8). We include a video of a spinning magnetic altering the transmission as a supplementary video.

Second, we measured a DC magnetic field, using a laser beam with oscillating polarization (experimental setup in Section 2.8). To change the frequency rapidly, we use two acoustic optical modulators, which are driven with different radio frequencies offset by Δf_p. By recombining the two beams, we create a beam that has oscillating polarizations at frequency Δf_p. With the presence of a static magnetic field, the transmitted light intensity will also be modulated at Δf_p, corresponding to the sample's MCD response. At Δf_p = 100 kHz, we can examine how the amplitude of the transmitted light changes with the static magnetic field (Figure 2.6d). We observe the expected linear trend, confirming the capability of this sample to measure static magnetic fields down to a 0.025 T (250 G) difference.

Third, we directly measured an AC magnetic field. We applied a small AC magnetic field (0-5 G at $f_{AC} = 1$ kHz) by adding a Helmholtz coil (Section 2.8) to give rise to two more sidebands at frequency $\Delta f_p \pm f_{AC}$. This signal is measured by a spectrum analyzer, where the sideband peak heights increase with the amplitude of the applied AC magnetic field. The (thiolfan)YbCl(THF) solution shows a monotonically increasing linear trend with the AC magnetic field, whereas the THF solvent and air show no dependence on the magnetic field (Figure 2.6e; signal over time

shown in Figure 2.52). With this method, we can measure AC magnetic fields down to 0.5 G, which is at the scale of the Earth's magnetic field. Even though these measurements are performed with a solution at room temperature, we can achieve a sensitivity of 3.33 μT $Hz^{-\frac{1}{2}}$.

2.6 Comparisons to Other Technologies

There are several important figures of merit in comparing ALMS to other electromagnetic sensing technologies—sensitivity, frequency range, and distance from sample. The most important figure of merit is magnetic field sensitivity, which describes the smallest magnetic field that can be detected within a given measurement time. For (thiolfan)YbCl(THF), the sensitivity is governed by the absorption change upon applying a magnetic field, where the most drastic response comes with the steep slopes in the absorption feature. We estimate that our limit in sensitivity is set by the signal-to-noise difference in transmission, where our best resolution comes from the measurement of a small AC magnetic field with 3.33 μT $Hz^{-\frac{1}{2}}$ sensitivity. We note that quantum sensing technologies operate through modulation of ground-state quantum coherences, prepared through optical and microwave pumping, and readout through changes in absorption, polarization, or fluorescence intensity. Besides AVCs, other spin-based magnetometers include nitrogen vacancies in diamond and color centers in crystal environments, both of which are also enabled by optical state preparation of pure quantum states that enable extraordinary sensitivity.[37, 38] Compact designs of AVCs that are widely used in miniature circuits demonstrate an optimal sensitivity of 50 pT $Hz^{-\frac{1}{2}}$ with the most sensitive atomic optical magnetometer exceeding a 10^{-15} T $Hz^{-\frac{1}{2}}$ sensitivity.[4,7,43] The typical sensitivities of magnetic sensing based on single nitrogen vacancy in diamond range from tens of μT $Hz^{-\frac{1}{2}}$ for DC fields to tens of nT $Hz^{-\frac{1}{2}}$ for AC fields.[44] To be competitive with the sensitivities of these devices a state preparation and readout of spin

superpositions in the electronic ground state are required that have yet to be shown in a liquid or glass environment. Nevertheless, a simple MCD-based magnetometry method with (thiolfan)YbCl(THF) puts us at a comparable sensitivity to other known spin-based magnetometers, such as Hall-effect sensors, as shown in Figure 2.6f.[45,46]

The second figure of merit is the frequency at which these signals can be measured. We measured both DC and higher frequency field modulation up to 1 kHz but have not fully characterized the highest frequency possible to measure. We hypothesize it is likely limited by the excited state lifetime of the system (Figure 2.40), in which case the modulation period must be longer than the lifetime. AVCs tend to have relevant coherence times at the scale of 10^{-3} to 10^{1} seconds, depending on whether they are limited by the spin relaxation time T_1 or coherence time T_2.[47–49] In comparison, our Yb(III)-based ALMS shows much shorter spin relaxation times of T_1 = 518 μs and T_2 = 0.82 μs at 3.6 K and 320 mT field (Figure 2.47). However, it should be noted that spin relaxation is not the major contributor that sets our absorption linewidth at room temperature. The SHB linewidth of 99 kHz corresponds to a lifetime of 1.6 μs, which is nearing the measured T_2 time. We hypothesize that if we achieve narrower linewidths that can be used for MCD magnetometry, then spin dephasing may set the ultimate sensitivity.

The third figure of merit is the distance at which a magnetic field can be measured, namely the sensor-sample distance. Broadly speaking, the sensor-sample distance represents the effective geometry of a given magnetic sensor. In the context of nanoscale imaging, where magnetometers are used to detect single spin fields, it is crucial that the magnetic field sensor can capture the dipole field, which decreases with the cubed distance. Here, systems with high number densities of magnetically sensitive molecules may provide an advantage. For example, (thiolfan)YbCl(THF) can range two magnitudes in concentration while retaining its spectral linewidth (Figure 2.54), and

is able to achieve an optical density of 1 in a thin 0.2 mm path length cuvette. With this advantage of high number density, we estimate a theoretical sensor-sample distance of 1-100 μm can be achieved with further device engineering (Figure 2.55), effectively providing a sensor to sample distance that is considerably shorter than that of current AVC technologies.

This study aims toward a rare-earth alternative to AVC quantum sensors used in biology. A recent publication demonstrates that AVCs are used for magnetoencephalography to detect magnetic fields produced from the flow of electric currents in neurons.[50] The operating principle for AVCs is similar to the one employed for (thiolfan)YbCl(THF) magnetometry, though AVCs utilize state preparation to greatly enhance the change observed due to external fields. While the sensitivity needs to be much improved, the advantage of solubilizing the sensor to overcome the particle density limit is real. Using MCD as a magnetic contrast approach, we determined that the mathematical limit to the sensitivity of an MCD-based method can be approximated as:

$$\Delta OD \approx \frac{g_{eff}}{\Gamma^2}$$

where the sensitivity of the absorption measurement is proportional to the g_{eff} factor of the driven transition and is inversely proportional to the square of the linewidth Γ (see derivation in Section 2.8). This indicates that for transitions with the same oscillator strength, narrowing the linewidth by half will increase the sensitivity by a factor of four, motivating the need for further chemical insight into synthesis and post-synthesis methods that narrow optical transitions. Considering that the linewidth remains the same across two orders of magnitude, (thiolfan)YbCl(THF) poses as a promising candidate for an ALMS prototype that may improve upon existing AVC technology in biomedical applications. If we can achieve a narrower linewidth at room temperature through molecular ligand design in future studies, ALMS can achieve standards of AVCs in their magnetometry applications with the advantage of more than 6 orders or more increase in particle

density. Therefore, future investigations born out of this manuscript may pave the way towards rare earth complex quantum sensors in biology.

2.7 Conclusions

(thiolfan)YbCl(THF) shows an extraordinarily narrow $^2F_{7/2}$ to $^2F_{5/2}$ lanthanide centered optical transition in solution at room temperature. While the design principles for such a narrow transition will require further investigation, crucial orbital mixing between the *d* and *f* orbitals of Yb and further mixing with the ligand orbitals lead to a non-zero oscillator strength for the observed transition. In parallel, the rigidity and low symmetry afforded by the supporting ligand assist in concentrating the minimal oscillator strength to an ultranarrow transition. This suggests that fine tuning the low symmetry structural components may become a primary design consideration in developing new ALMS systems. Further theoretical, synthetic, and spectroscopic work will help elucidate the tradeoffs between ligand rigidity, orbital mixing, covalency, and solvation. In summary, we demonstrate an immediate application of Yb complexes for an MCD-based measurement and imaging of relatively weak magnetic fields. We achieve sufficient sensitivity by leveraging the large number density afforded by direct solvation of the complex. For further work, we hypothesize that investigation of quantum state preparation and readout of (thiolfan)YbCl(THF) will lead to higher sensitivities in analogy to AVCs, paving the way towards lanthanide complexes in precision quantum sensing.

2.8 Supporting Information

Materials and Characterization

All compounds were manipulated and handled under a dry nitrogen atmosphere using standard Schlenk techniques or an MBraun inert-gas glovebox. Solvents were purified using a two-column solid-state purification system by the method of Grubbs and transferred to the glovebox

without exposure to air.[51] 2-Methyltetrahydrofuran (2-MeTHF) was distilled over calcium hydride under nitrogen. All solvents were stored on activated molecular sieves and/or sodium for at least a day prior to use. NMR solvents were obtained from Cambridge Isotope Laboratories, degassed, and stored over activated molecular sieves prior to use.

Nuclear magnetic resonance spectra were recorded on Bruker AV300, Bruker DRX500, and Bruker AV500 spectrometers at 298 K in C_6D_6, THF-d_8 and toluene-d_8 unless otherwise specified. Chemical shifts are reported with respect to solvent residual peaks (C_6D_6 at 7.16 ppm, C_4D_8O at 1.73 ppm, C_7D_8 at 2.08, 6.97, 7.01, and 7.09 ppm). $YbCl_3(THF)_3$ was prepared by stirring $YbCl_3$ in THF. Lithium bis(trimethylsilyl) amide tetrahydrofuran ($LiN(SiMe_3)_2 \cdot THF$) was synthesized according to a published procedure.[52] H_2(thiolfan) (1,1′-bis(2,4-di-*tert*-butyl-6-thiomethylenephenoxy)ferrocene) and H_2(thiolfan*) (thiolfan* = 1,1'-bis(2,4-di-*tert*-butyl-6-thiophenoxy)ferrocene) were synthesized according to the literature.[53,54]

IR spectra were measured on an Agilent Technologies Cary 620 Fourier transform infrared spectrometer (FTIR) fitted with a Cary 600 Series FTIR Microscope using Nujol mulls sandwiched between NaCl optical plates. CHN analyses were performed in house on a CE-440 elemental analyzer manufactured by Exeter Analytical, Inc. Magnetic susceptibility measurements were obtained using a Quantum Design SQUID magnetometer MPMS-XL7 operating between 2 and 300 K for direct-current (DC) applied fields ranging from −7 to +7 T. DC analyses were performed on polycrystalline samples sealed in a polyethylene membrane (prepared in an inert atmosphere) under a field ranging from 0 to 7 T and temperatures between 1.8 and 300 K. In addition, data were collected on different batches to check for consistency. Diamagnetic corrections were applied for the sample holder and the core diamagnetism from the sample (estimated with Pascal constants).[55]

Continuous-Wave (CW) X-band (9.6 GHz) EPR spectra were acquired using a Bruker EMX CW-EPR spectrometer equipped with an ER- 4116DM Dual Mode resonator operating in perpendicular mode. Temperature control was achieved through use of an Oxford Instruments ESR-900 liquid helium flow cryostat and an ITC-503 temperature controller. Pulse EPR data were acquired using a Bruker ELEXSYS E-580 pulse EPR spectrometer operating at X-band with a microwave frequency of 9.36 GHz using a MS-5 split ring resonator, with temperature control achieved through use of an Oxford Instruments CF-935 liquid helium flow cryostat and a Mercury temperature controller. Electron spin-echo (ESE) detected field-swept EPR spectra were collected using a Hahn-echo pulse sequence ($\frac{\pi}{2} - \tau - \pi - \tau - echo$) where τ is a fixed time delay of 300 ns, and $\frac{\pi}{2}$ and π pulse lengths were 40 and 80 ns, respectively.

X-ray quality crystals were obtained from various concentrated solutions placed in a −36 °C freezer in the glovebox. Inside the glovebox, the crystals were coated with oil (STP Oil Treatment) on a microscope slide, which was brought outside the glovebox. The X-ray data collections were carried out on a Bruker SMART 1000 single crystal X-ray diffractometer using Mo or Cu Kα radiation and a SMART APEX CCD detector. The data were reduced by SAINTPLUS, and an empirical absorption correction was applied using the package SADABS.[56,57] The structure was solved and refined using SHELXTL *via* OLEX 2 as a graphical user interface. The structures were then visualized using ORTEP 3.[58–60]

Synthesis of Ytterbium Complexes

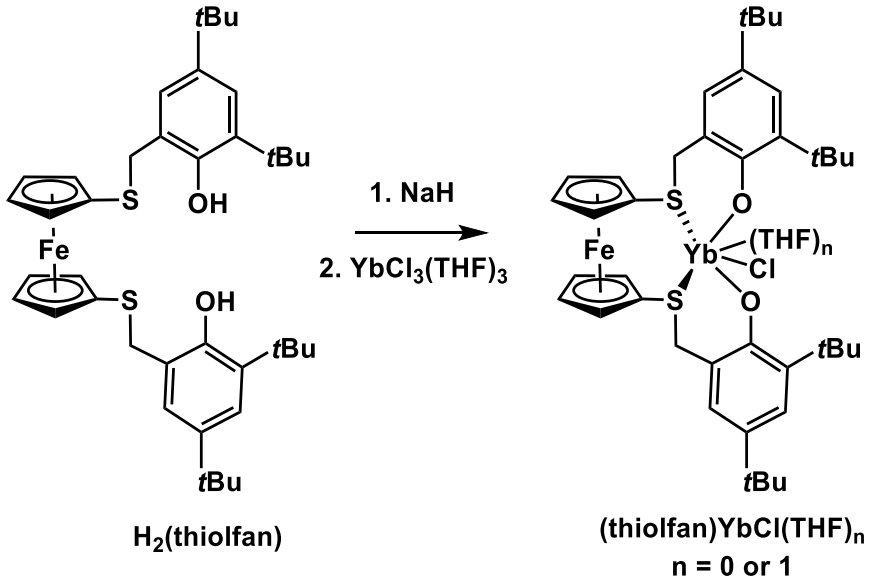

(thiolfan)YbCl(THF). In a nitrogen filled glovebox, 179.5 mg (0.26 mmol, 1 equiv.) of H_2(thiolfan) was dissolved in 3 mL of THF and added dropwise to a stirring slurry of NaH (63.0 mg, 10 equiv., 2.6 mmol) in 2 mL of THF. The mixture was stirred at room temperature for 2 h then filtered through glass fiber twice. The filtrate was cooled to -78 °C and added to the stirring slurry of $YbCl_3(THF)_3$ (128.9 mg, 1 equiv., 0.26 mmol). The reaction was stirred at -78 °C for 15 min then slowly brought to room temperature and stirred for another 2 h. The volatiles were removed under a reduced pressure and the residue was extracted with toluene and filtered through glass fiber twice. The filtrate was concentrated and layered with hexanes, then stored at -36 °C. Yellow crystals were obtained in moderate yield (114.0 mg, 49%). X-ray quality single crystals of $[(thiolfan)YbCl]_2$ were grown from a solution of toluene layered with *n*-pentane at -36 °C. X-ray quality single crystals of (thiolfan)YbCl(THF) were grown from a solution of THF layered with hexanes in a 2 mL glass autosampler vial at -36 °C. Due to the paramagnetic nature of the ytterbium complex, peaks are not assigned in the ^{1}H NMR spectrum. However, a peak at -8.66 ppm and a shoulder at -10.6 ppm were observed in C_6D_6 (Figure 2.9). Elemental analysis for

$[C_{40}H_{52}FeClO_2S_2Yb]_2$, calculated: C, 53.78%, H, 5.87%, N, 0.00%; found: C, 54.59%, H, 5.87%, N, 0.00%.

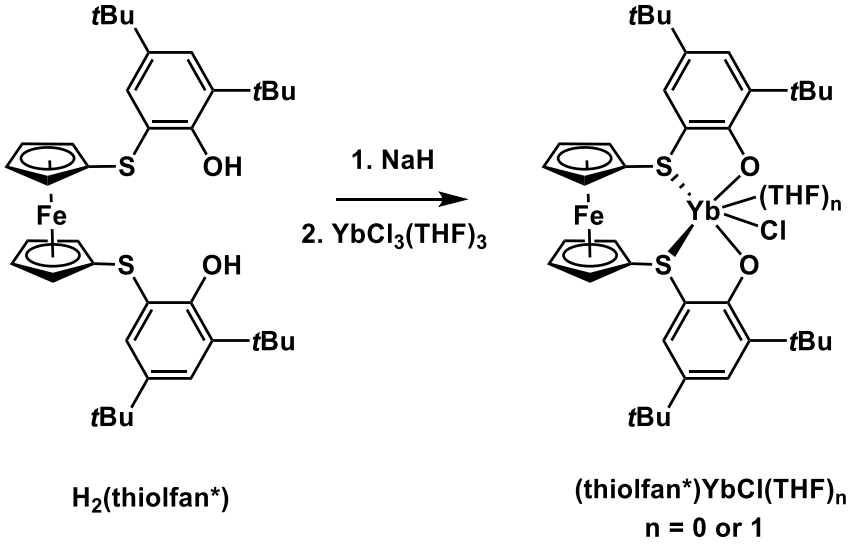

(thiolfan*)YbCl(THF). In a nitrogen filled glovebox, 108.7 mg (0.16 mmol, 1 equiv.) of H_2(thiolfan*) was dissolved in 3 mL of THF and added dropwise to a stirring slurry of NaH (40.0 mg, 10 equiv., 1.6 mmol) in 2 mL of THF. The mixture was stirred at room temperature for 2 h then filtered through glass fiber twice. The filtrate was cooled to -78 °C and added to a stirring slurry of $YbCl_3(THF)_3$ (81.3 mg, 1 equiv., 0.16 mmol). The reaction was stirred at -78 °C for 15 min then slowly brought to room temperature and stirred for another 2 h. The volatiles were removed under a reduced pressure and the residue was extracted with toluene and filtered through glass fiber twice. The filtrate was concentrated and layered with hexanes, then stored at -36 °C. Yellow crystals were obtained in moderate yield (58.0 mg, 41%). Due to the paramagnetic nature of the ytterbium complex, peaks are not assigned in the ^{1}H NMR spectrum (Figure 2.10). Unfortunately, no crystals suitable for X-ray diffraction analysis were obtained. Elemental analysis for $C_{38}H_{48}FeClO_2S_2Yb$, calculated: C, 52.75%, H, 5.57%, N, 0.00%; found: C, 52.74%, H, 6.04%, N, 0.00%.

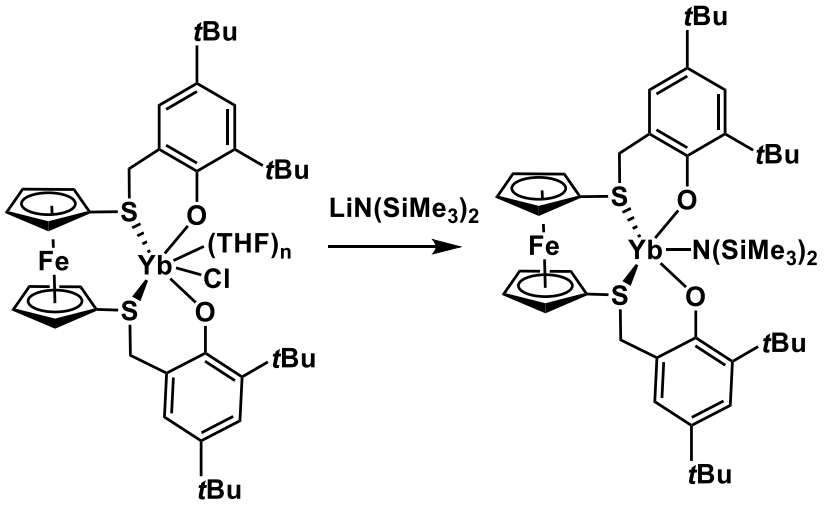

(thiolfan)YbCl(THF)$_n$

n = 0 or 1

(thiolfan)Yb[N(SiMe$_3$)$_2$]

(thiolfan)Yb[N(SiMe$_3$)$_2$]. In a nitrogen filled glovebox, 202.8 mg (0.23 mmol, 1 equiv.) of (thiolfan)YbCl was dissolved in 5 mL of toluene and added dropwise to a stirring solution of lithium bis(trimethylsilyl)amide·THF (54.4 mg, 1 equiv., 0.23 mmol) in 2 mL of toluene. The mixture was stirred at room temperature for 2 h then filtered through glass fiber. The volatiles were removed under a reduced pressure. The solid was re-dissolved in hexanes then stored at -36 °C. The solution was decanted to collect the semi-crystalline product and solids precipitated at the bottom of the vial, which was collected on top of a frit (77.9 mg, 34%). Due to the paramagnetic nature of the ytterbium complex, peaks are not assigned in the ^{1}H NMR spectrum (Figure 2.11). Unfortunately, no crystals suitable for X-ray crystallography analysis were obtained. Elemental analysis for $C_{46}H_{70}FeNO_2S_2Si_2Yb$, calculated: C, 54.26%, H, 6.93%, N, 1.38%; found: C, 54.43%, H, 7.10%, N, 0.86%.

The compound numbers shown in Figure 2.4b in the manuscript are clarified below, with exact molecular formula. While there are slight variations of these compounds discussed in the characterization section below, these numbers refer to the structures we assign the absorption features to, which are shown below.

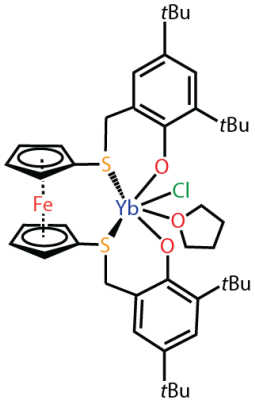

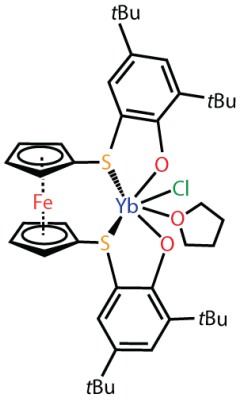

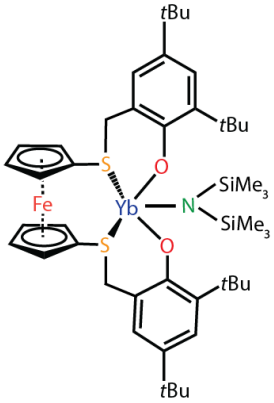

1 (thiolfan)YbCl(THF) **2** (thiolfan*)YbCl(THF) **3** (thiolfan)YbN(SiMe$_3$)$_2$

Solid-state Molecular Structure of [(thiolfan)YbCl]$_2$

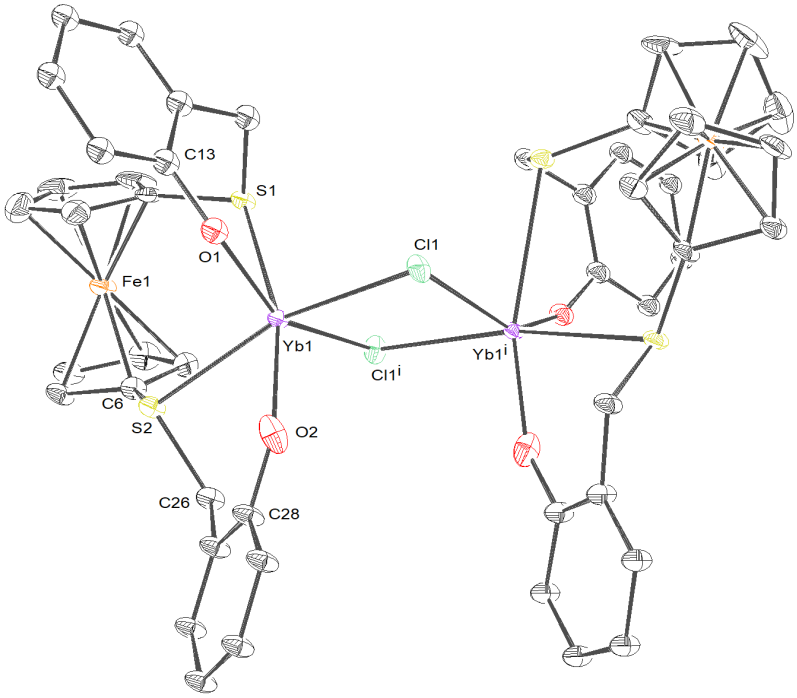

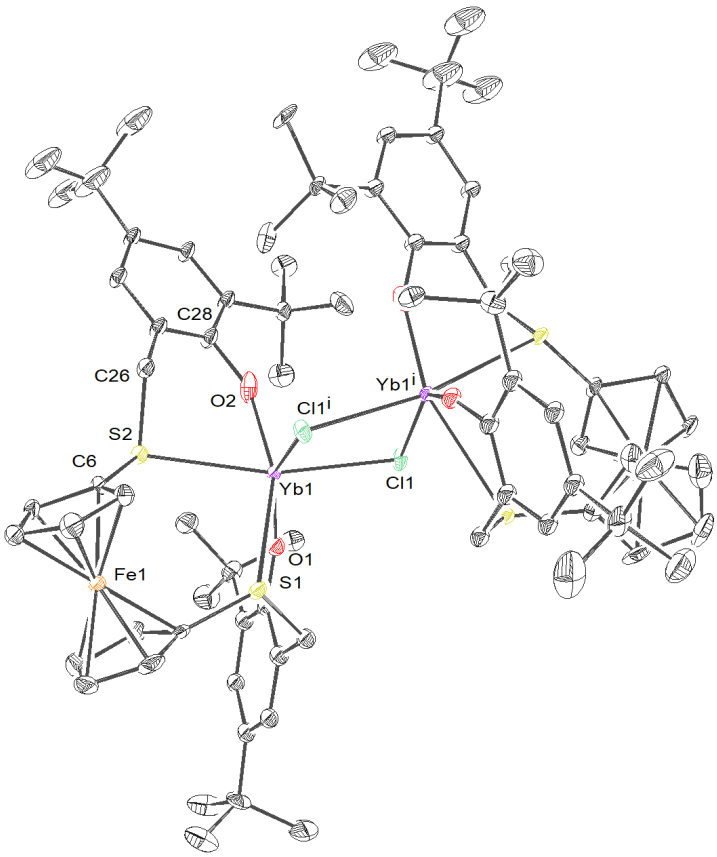

Selected distances (Å) and angles (°) of $[(thiolfan)YbCl]_2$				
Distances	Yb-Cl_1	2.654(2)	Yb-S_2	2.828(2)
	Yb-O_1	2.041(6)	Yb-Cl^i	2.659(2)
	Yb-O_2	2.082(8)	Yb-Fe	4.756(2)
	Yb-S_1	2.931(2)	Yb-Yb^i	4.000(2)
Angles	Cl_1-Yb-O_1	89.9(2)	O_2-Yb-S_1	157.2(2)
	Cl_1-Yb-O_2	96.6(2)	O_2-Yb-S_2	71.5(2)
	Cl_1-Yb-S_1	104.79(7)	S_1-Yb-S_2	86.17(6)
	Cl_1-Yb-S_2	166.08(7)	S_1-Yb-Cl_1	75.35(6)
	Cl_1-Yb-Cl_1^i	81.22(7)	S_2-Yb-Cl_1	93.57(7)
	O_1-Yb-O_2	111.8(2)	C_6-S_2-C_{26}	99.6(4)
	O_1-Yb-S_1	76.4(2)	Yb-O_1-C_{13}	151.9(6)
	O_1-Yb-S_2	101.1(2)	Yb-O_2-C_{28}	154.4(6)

Figure 2.7 Crystal Structure of $[(thiolfan)YbCl]_2$.

Thermal ellipsoid (50% probability) representation of $[(thiolfan)YbCl]_2$, without (top) and with (bottom) *t*-butyl groups. Two crystallographically independent molecules are in the unit cell, only one shown here. Hydrogen atoms and solvent molecules (toluene and diethyl ether) are omitted for clarity. Atoms labeled with ^{i} represent the inverted asymmetric unit of the neighboring unit cell.

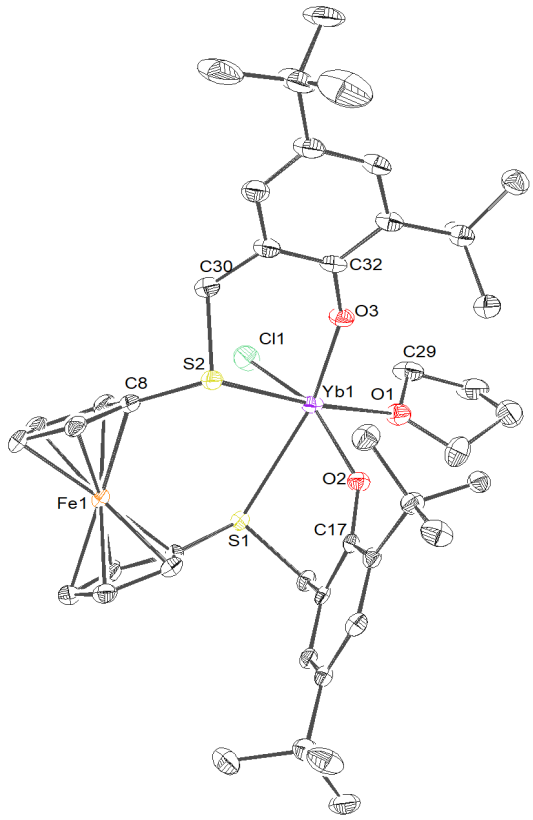

Selected distances (Å) and angles (°) of (thiolfan)YbCl(THF)				
Distances	$Yb\text{-}O_1$	2.316(2)	$Yb\text{-}S_1$	2.9073(7)
	$Yb\text{-}O_2$	2.087(2)	$Yb\text{-}S_2$	2.8830(9)
	$Yb\text{-}O_3$	2.053(2)	Yb-Fe	4.719(7)
	$Yb\text{-}Cl_1$	2.5534(7)		
Angles	$O_1\text{-}Yb\text{-}O_2$	85.83(8)	$S_1\text{-}Yb\text{-}S_2$	88.57(2)
	$O_1\text{-}Yb\text{-}O_3$	98.47(8)	$S_2\text{-}Yb\text{-}O_1$	172.61(6)
	$O_2\text{-}Yb\text{-}O_3$	105.00(8)	$S_2\text{-}Yb\text{-}O_2$	93.70(6)
	$Cl_1\text{-}Yb\text{-}S_1$	80.30(2)	$S_2\text{-}Yb\text{-}O_3$	74.51(6)
	$Cl_1\text{-}Yb\text{-}S_2$	95.67(2)	$C_8\text{-}S_2\text{-}C_{30}$	99.7(1)
	$Cl_1\text{-}Yb\text{-}O_1$	87.79(6)	$Yb\text{-}O_1\text{-}C_{29}$	124.3(1)
	$Cl_1\text{-}Yb\text{-}O_2$	154.50(6)	$Yb\text{-}O_2\text{-}C_{17}$	146.4(2)
	$Cl_1\text{-}Yb\text{-}O_3$	100.35(6)	$Yb\text{-}O_3\text{-}C_{32}$	153.7(2)

Figure 2.8 Crystal Structure of (thiolfan)YbCl(THF).

Thermal ellipsoid (50% probability) representation of (thiolfan)YbCl(THF). Hydrogen and disordered atoms are omitted for clarity.

Table 2.1 Selected Crystal Data for [(thiolfan)YbCl]$_2$ and (thiolfan)YbCl(THF)

	[(thiolfan)YbCl]$_2$	(thiolfan)YbCl(THF)
Identification code	pld1905	pld2306b
CCDC number		2279910
Empirical formula	$C_{91}H_{122}Cl_2Fe_2O_5S_4Yb_2$	$C_{44}H_{60}ClFeO_3S_2Yb$
Formula weight [g/mol]	1952.80	965.38
Temperature [K]	100 (2)	100 (2)
Crystal system	monoclinic	triclinic
Space group	$P2/c$	$P\overline{1}$
a [Å]	18.2162(18)	10.0390(2)
b [Å]	15.0982(15)	15.3323(3)
c [Å]	32.972(3)	15.4616(4)
α [°]	90	85.0770(10)
β [°]	102.091(2)	75.2870(10)
γ [°]	90	87.8680(10)
Volume [Å^3]	8867.2(15)	2293.04(9)
Z	4	2
ρ_{calc} [g/cm^3]	1.463	1.398
μ [mm^{-1}]	2.614	7.857
F(000)	3992	986
Crystal size [mm^3]	0.090×0.080×0.070	0.1 × 0.1 × 0.05
Crystal color	Clear yellow and green (dichroic)	clear light yellow
Crystal shape	block	plate
Radiation	MoK_α (λ=0.71073 Å)	CuK_α (λ=1.54178 Å)
2Θ range for data collection [°]	2.29 to 56.76 (0.75 Å)	5.93 to 136.85 (0.83 Å)
Index ranges	$-24 \le h \le 24$ $-20 \le k \le 20$ $-43 \le l \le 44$	$-11 \le h \le 12$ $-18 \le k \le 18$ $-18 \le l \le 18$
Reflections collected	130664	37470
Independent reflections	22122 R_{int} = 0.0830 R_{sigma} = 0.0675	8103 R_{int} = 0.0421 R_{sigma} = 0.0340
Data/restraints /parameters	22122/0/724	8103/134/488
Goodness-of-fit on F^2	1.134	1.068
Final R indexes [I>=2σ (I)]	R_1 = 0.0724 wR_2 = 0.1454	R_1 = 0.0285 wR_2 = 0.0703
Final R indexes [all data]	R_1 = 0.1176 wR_2 = 0.1611	R_1 = 0.0330 wR_2 = 0.0720
Largest diff. peak/hole e Å^3	4.14/-4.24	1.15/-1.05

NMR Spectra

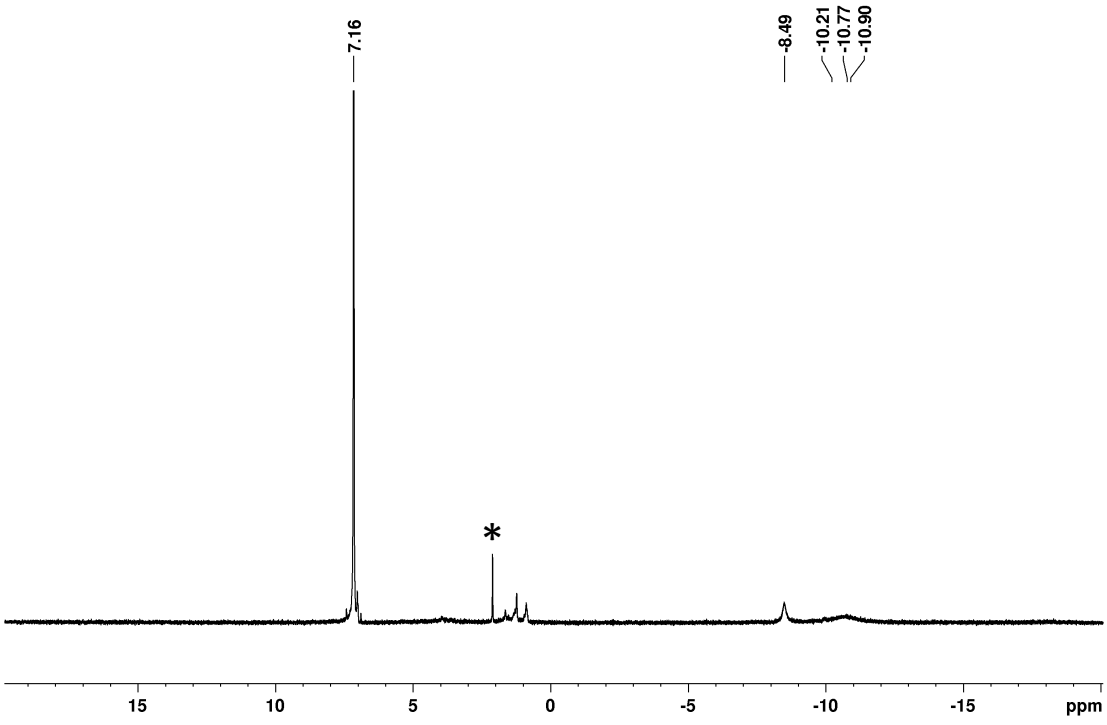

Figure 2.9 ^{1}H NMR Spectrum of (thiolfan)YbCl(THF)

^{1}H NMR spectrum (298 K, 500 MHz, C_6D_6) of (thiolfan)YbCl(THF) (*residual toluene).

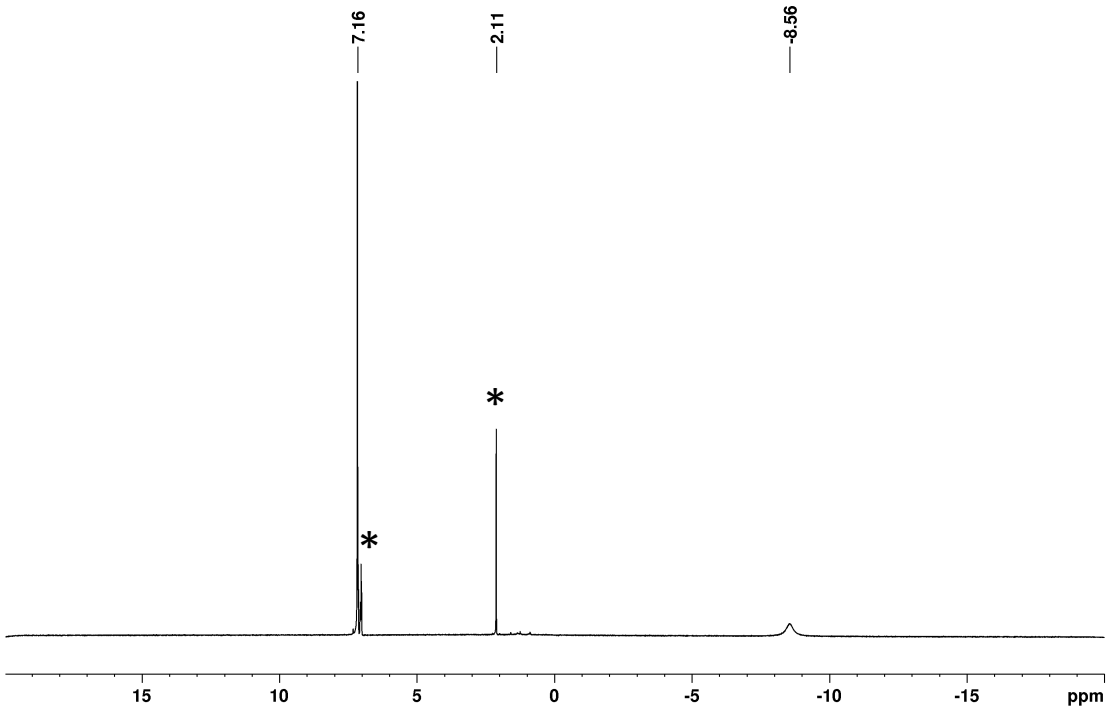

Figure 2.10 ^{1}H NMR Spectrum of (thiolfan*)YbCl(THF)

^{1}H NMR spectrum (98 K, 500 MHz, C_6D_6) of (thiolfan*)YbCl(THF)$_n$ (n = 0 or 1) (*residual toluene)

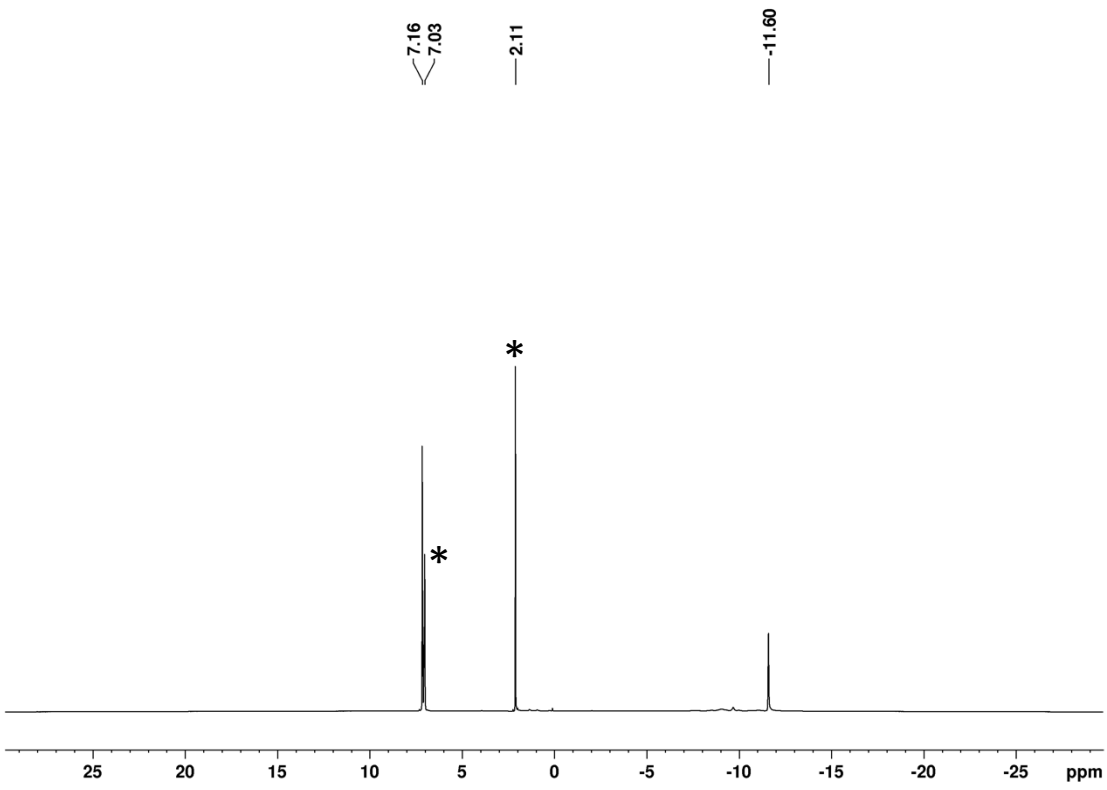

Figure 2.11 ^{1}H NMR Spectrum of (thiolfan)Yb[N(SiMe$_3$)$_2$]

^{1}H NMR spectrum (298 K, 500 MHz, C_6D_6) of (thiolfan)Yb[N(SiMe$_3$)$_2$] (*residual toluene).

Discussion on the Monomer vs. Dimer Equilibrium

As shown in SI Sec. I-C, the solid state molecular structure of $[(thiolfan)YbCl]_2$ shows a dimer bridged by two chlorides (Figure 2.7), while that of (thiolfan)YbCl(THF) shows a monomer with a single THF ligand coordinated (Figure 2.8). For the dimer, the compound was crystallized from toluene in order to perform NMR and single crystal X-ray diffraction measurements. Single crystals of (thiolfan)YbCl(THF) were obtained from a saturated THF solution layered with hexanes. THF is a coordinating solvent, leading to a change from the dimeric to the monomeric structure. We lay out our observations that elaborate on the monomer vs. dimer equilibrium below.

First, we performed a titration experiment by introducing stoichiometric amounts of THF to the sample in toluene and observed a shift in absorption features that trend toward the feature observed when THF is used as a solvent. As shown in Figure 2.12, shifting from 1:1, 1:2, 1:4, and 1:10 ratios of (thiolfan)YbCl monomer to THF shifts the absorption spectra from bimodal to unimodal peaks that reflect the spectra of the sample in THF, even in excess toluene. We added the absorption spectra in toluene and in THF at the top and bottom of the figure to make this trend clear.

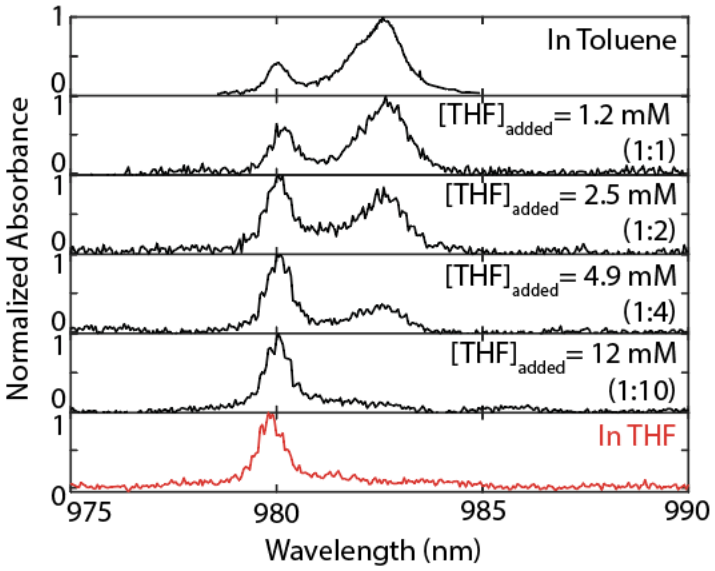

Figure 2.12 Absorption Spectra of [(thiolfan)YbCl]$_2$ in Toluene during THF Dilution
Dilution of [(thiolfan)YbCl]$_2$ in toluene with increasing amounts of THF, showing a gradual shift from the bimodal absorbance feature in toluene to the unimodal feature in THF. The concentration of Yb species is 1.3 mM, which accounts for monomers and dimers. The ratios of the Yb to THF concentrations are shown in brackets. The absorption spectra in toluene and in THF are shown on the top (black) and bottom (red) for comparison.

The change in absorption of these two peaks aligns with an equilibrium constant of 1. The monomer vs. dimer equilibrium that is caused by a single THF coordination can be expressed as:

$$A_2 + 2THF \rightleftharpoons 2A(THF)$$

Where A = (thiolfan)YbCl, A_2 = [(thiolfan)YbCl]$_2$, and $A(THF)$ = (thiolfan)YbCl(THF). The equilibrium constant (K_{eq}) can be written out as:

$$K_{eq} = \frac{[A(THF)]^2}{[A_2][THF]^2}$$

The monomer and dimer concentrations can be related by the total amount of sample added (1.3 mM), either in monomer or dimer forms. This equation can be rearranged to express the monomer concentration as a function of the dimer concentration.

$$[Total\ Yb\ centers\ added] = [A] + 2[A_2] = 1.3\ mM$$

With the above two equations, solving for $[A_2]$ gives:

$$[A_2] = \frac{1}{40}\left(5K_{eq}[THF]^2 \pm \sqrt{5K_{eq}[THF]^2\left(5K_{eq}[THF]^2 + 52\right)} + 26\right)$$

And, solving for $[A(THF)]$ gives:

$$[A(THF)] = \frac{1}{20}\left(\pm\sqrt{25{K_{eq}}^2[THF]^4 + 260K_{eq}[THF]^2} + 5K_{eq}[THF]^2\right)$$

The calculated monomer and dimer concentrations, corresponding to $[A(THF)]$ and $[A_2]$ above, are plotted against $[THF]$ for $K_{eq} = \{0.1, 1, 10\}$ in Figure 2.12. The integrated absorption areas of the peak at 980 nm and 983 nm are plotted below, which reflects the concentration of monomer and dimer in the solution, according to Beer's law. The absorption trend corresponds best to $K_{eq} \sim 1$.

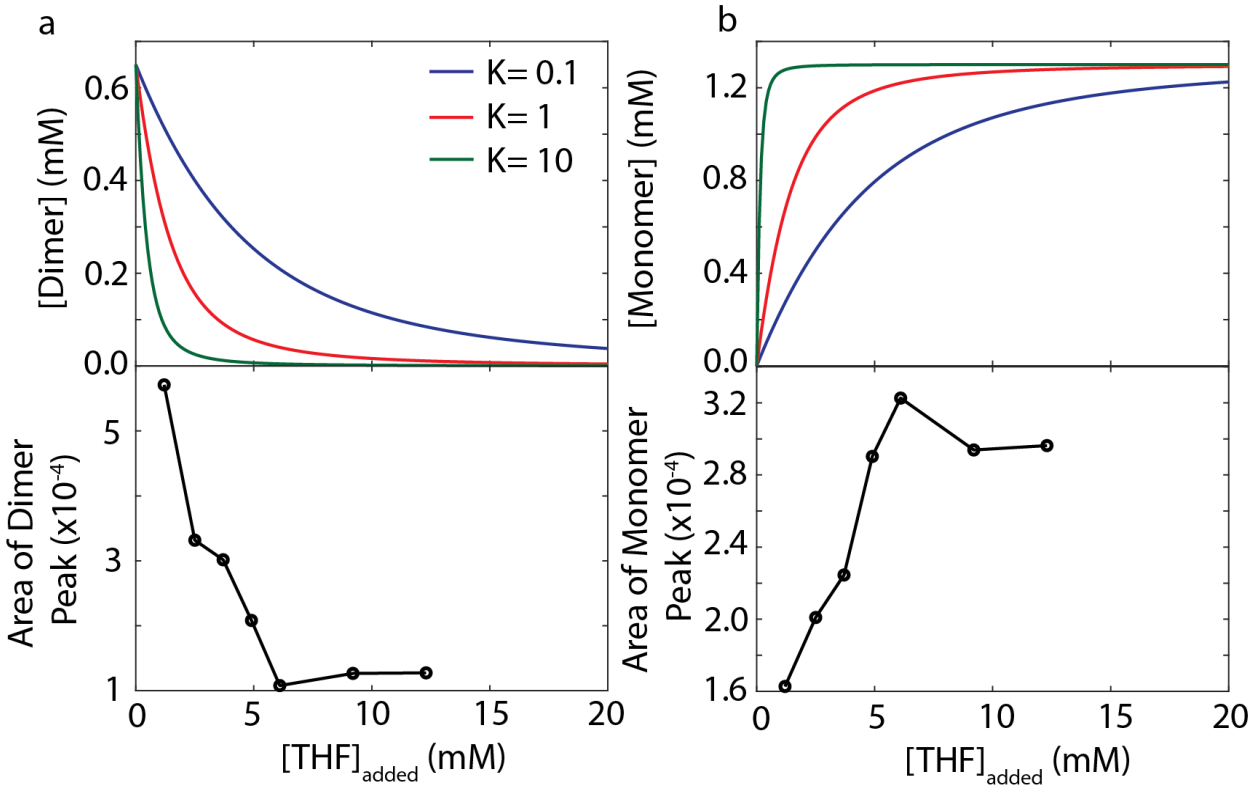

Figure 2.13 Calculated Chemical Equilibria of THF Coordination

a) Top: calculated [Dimer] concentrations, corresponding to $[A_2]$ in the mathematical derivations, for a range of equilibrium constants (K). Bottom: integrated area of the absorption feature at around 983 nm, which shows up in the sample in toluene environment, most likely in a dimer form. b) Top: calculated [Monomer] concentrations, corresponding to $[A(THF)]$ in the mathematical derivations, for a range of equilibrium constants (K). Bottom: integrated area of the absorption feature at around 980nm, which dominates when the sample is in THF environment, most likely in a monomer form.

Second, we performed a DOSY experiment on the yttrium analogue of our sample ([(thiolfan)YbCl]$_2$) in THF-d$_8$, which demonstrates a hydrodynamic radius corresponding to a monomer. Similar to the ytterbium complex, [(thiolfan)YCl]$_2$ also crystalizes as a dimer with chlorides bridging the two yttrium centers.[61] Critically, previous work showed that [(thiolfan)YCl]$_2$ coordinates THF when dissolved in THF.[61] A DOSY experiment was conducted

on [(thiolfan)YCl]$_2$ in THF-d_8 with tetrakis(trimethylsilyl)silane (TMSS) used as an internal standard (Figure 2.14).[62] The hydrodynamic radius (r_H) of (thiolfan)YCl(THF) was derived from the Stokes-Einstein equation: [63]

$$D_t = \frac{kT}{6\pi\eta r_H}$$

where k is the Boltzmann constant, T is the temperature, and η is the solution viscosity (298 K, 0.46 mPa·s, respectively). $r_H = 6.70$ Å was calculated using this equation and compared to the radius of the dimeric structure in the solid state ($r_{X-ray} = 11.20$ Å estimated by measuring the distance from the center of the dimeric molecule to the farthest atom using X-ray crystallographic data), which is 1.67 times of that in solution. The integration of THF to Y proton signals in the ^{1}H NMR spectrum of (thiolfan)YCl(THF) in C_6D_6 was found to be consistent with one coordinated THF to yttrium in prior studies, indicating that the Y analogue of the ytterbium complex also exists as a monomer in THF.[61]

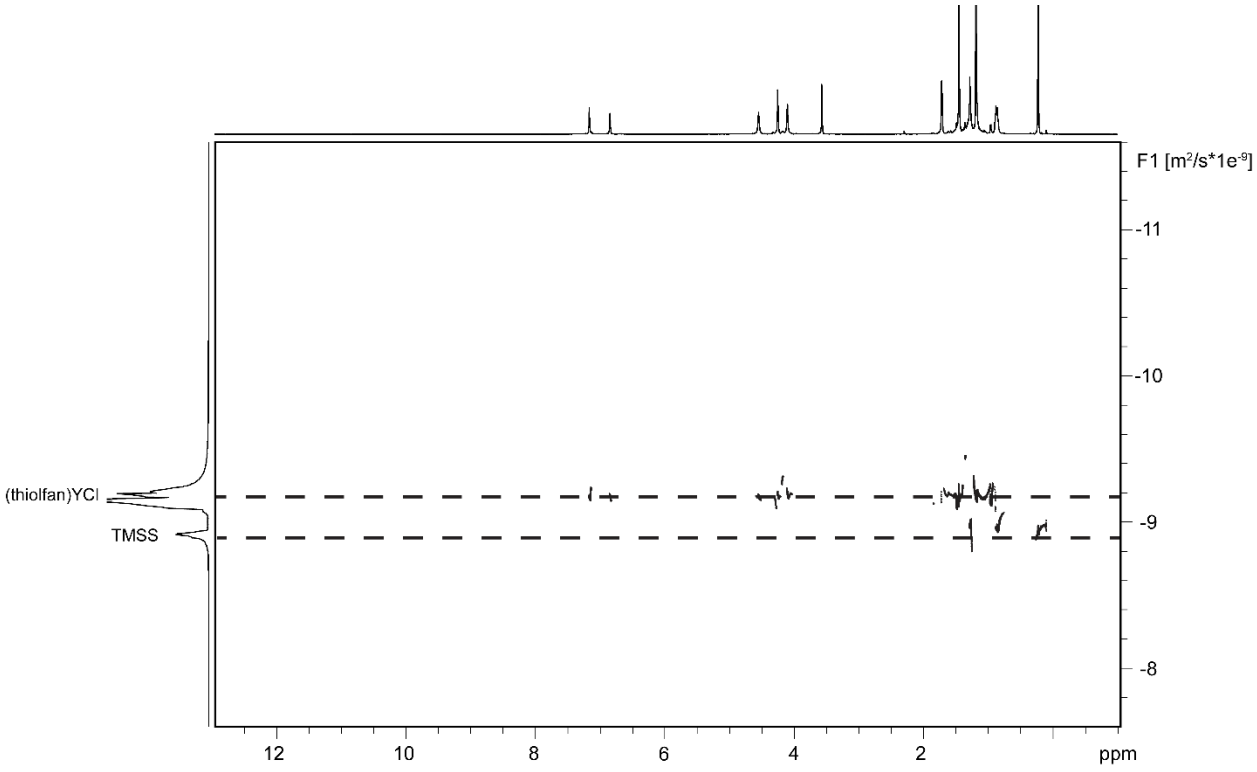

Figure 2.14 DOSY of Yttrium Analogue

DOSY (298 K, 500 MHz, THF-d_8) of (thiolfan)YCl(THF) with TMSS as an internal standard.

Furthermore, a variable temperature ^{1}H NMR experiment was conducted to investigate the equilibrium between the monomeric and dimeric Yb complexes in toluene-d_8 at different temperatures. As the temperature increased, the peak at -8.38 ppm and -10.42 ppm shifted and eventually coalesced into one peak at -7.56 ppm at 354 K (Figure 2.15). In addition, a small peak at -1.34 ppm and a bump at -18.6 ppm appeared and became obvious at elevated temperatures. A similar trend was observed when THF was added to a sample in C_6D_6, where the bump at -10.5 ppm started to disappear and merged with the peak at -8.32 ppm, but the intensity of the peaks at -1.86 ppm and -17.8 ppm both increased (Figure 2.16). In addition, the ^{1}H NMR spectrum of (thiolfan)YbCl(THF) taken in THF-d_8 displayed a sharp peak at -8.92 and a small peak at -17.9 ppm (Figure 2.17). Despite the slight difference in the chemical shifts due to different deuterated

solvents being employed, we hypothesize that increasing temperature and having THF present, either as the NMR solvent or added intentionally to an NMR sample, cause the shift in equilibrium from the dimeric to the monomeric form of the ytterbium complex.[64]

Lastly, theoretical calculations reported in the manuscript are for the monomeric (thiolfan)YbCl(THF) show remarkable alignment with the experimental spectra using THF as a solvent. Unfortunately, performing calculations on the ytterbium dimer is too expensive given the presence of two ytterbium and two iron atoms. In conclusion, our data indicates that (thiolfan)YbCl(THF) is a monomer in THF solution, based on the analyses of single crystal X-ray diffraction, absorption spectra, DOSY of the yttrium analogue, NMR spectra, and theoretical calculations.

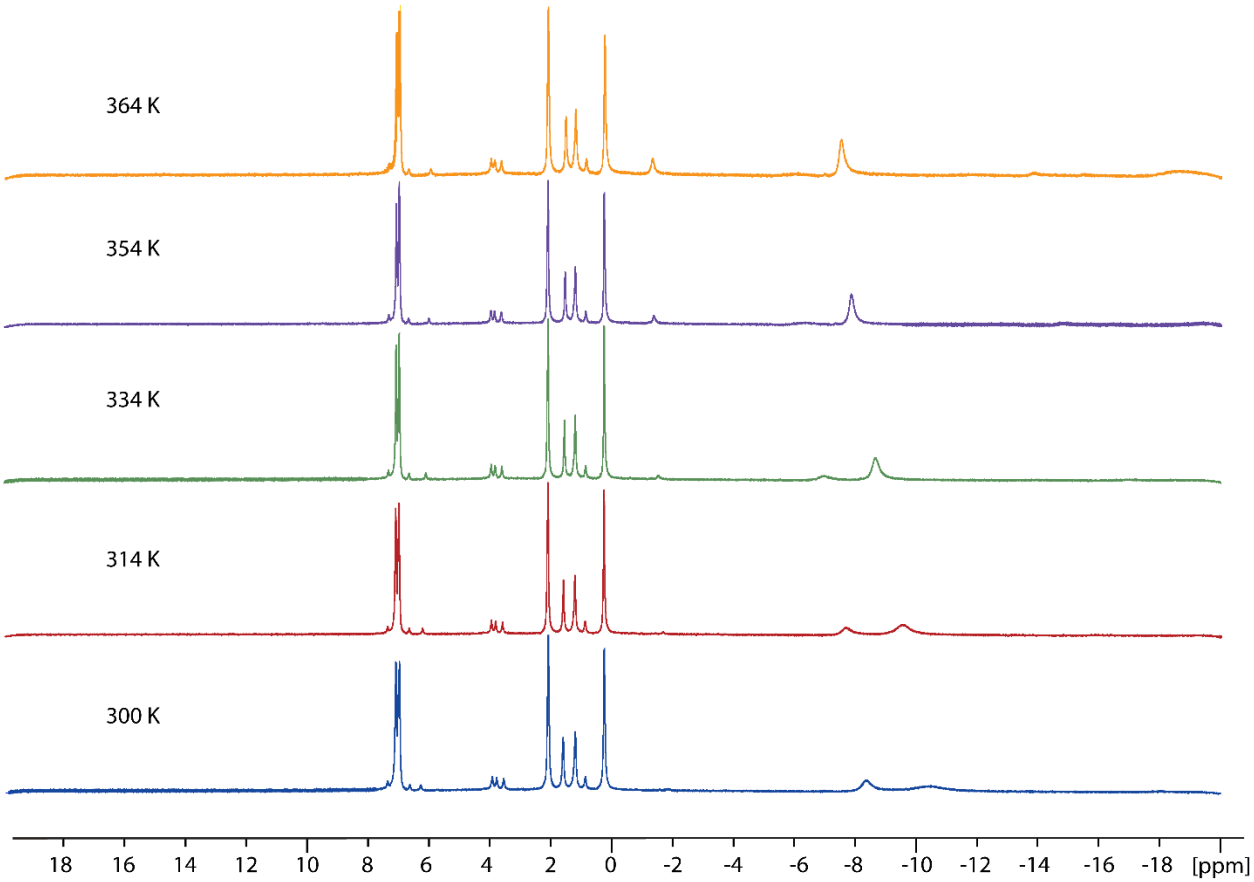

Figure 2.15 Variable temperature ^{1}H NMR study of [(thiolfan)YbCl]$_2$

(500 MHz, toluene-d$_8$)

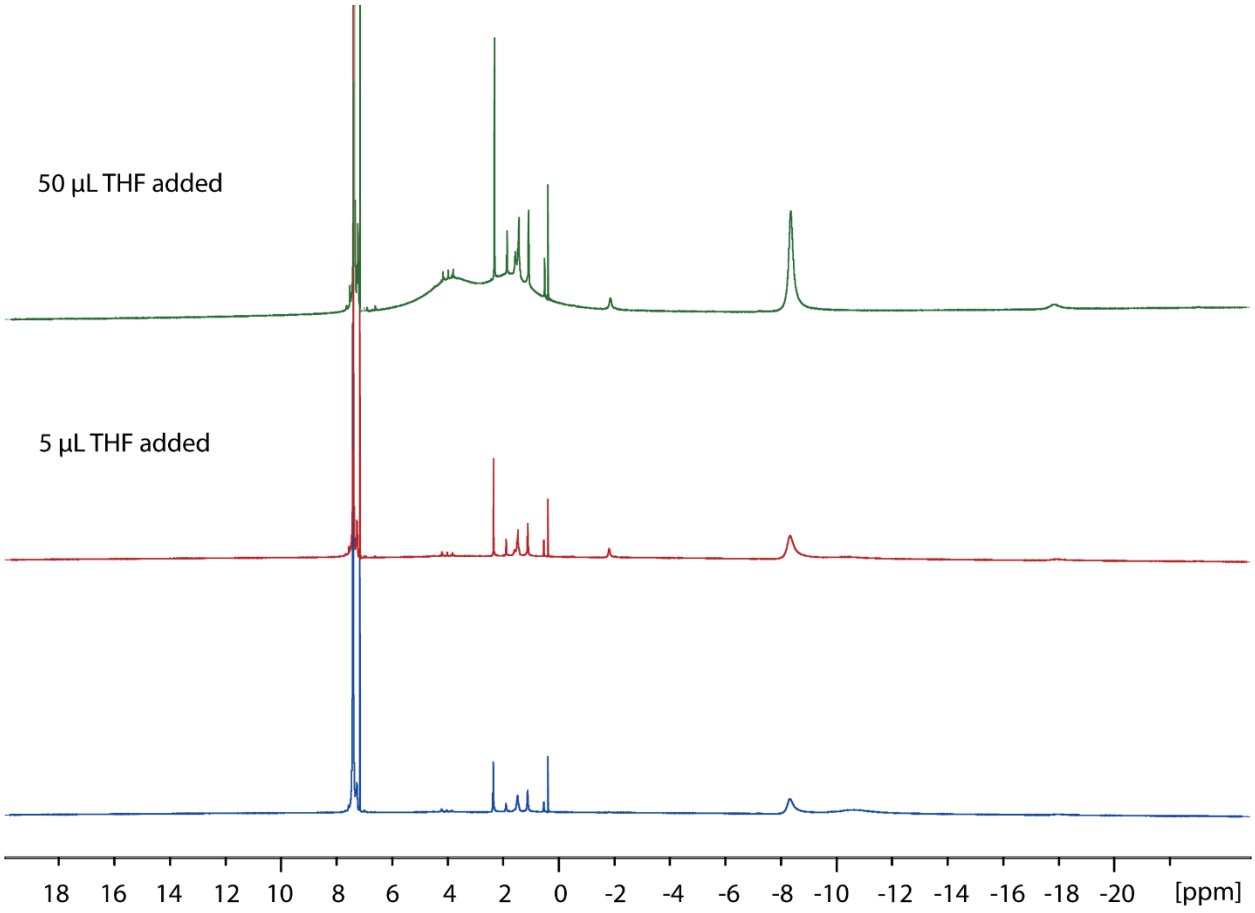

Figure 2.16 ^{1}H NMR spectra of [(thiolfan)YbCl]$_2$ before and after the addition of THF

(298 K, 500 MHz, C_6D_6)

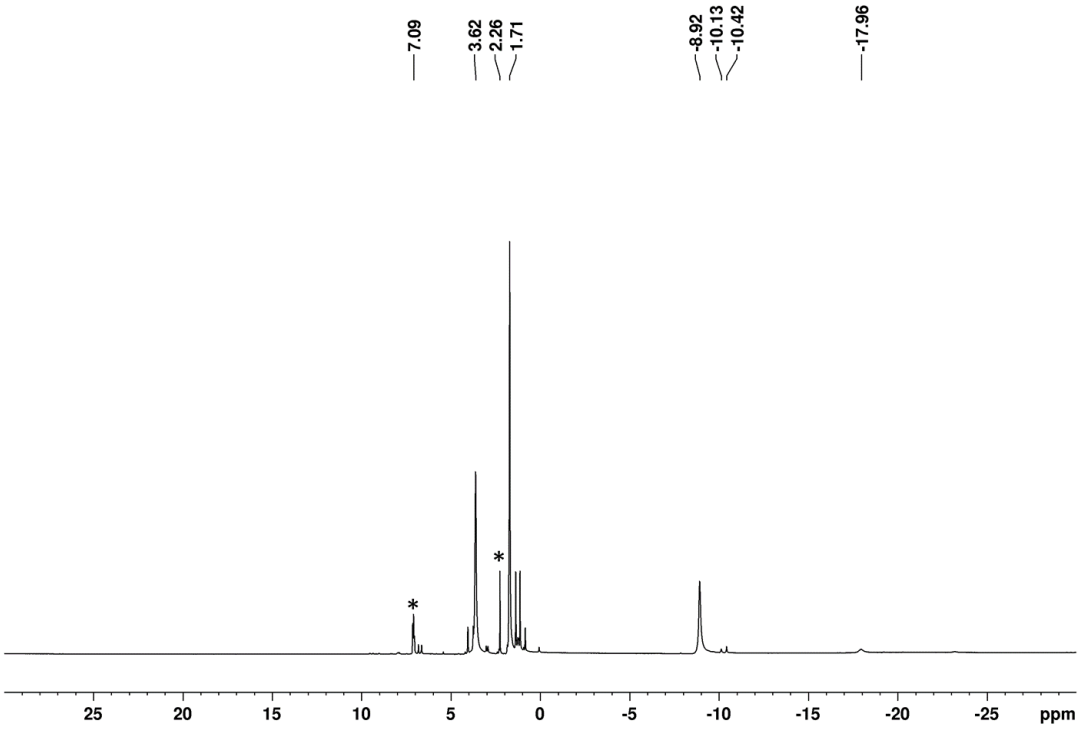

Figure 2.17 ^{1}H NMR spectra of (thiolfan)YbCl(THF) (*residual toluene)
(298 K, 500 MHz, THF-d_8)

Magnetic Properties

The magnetic properties of all three ytterbium compounds in the solid state were investigated using a superconducting quantum interference device (SQUID). Analyses were performed on crushed polycrystalline samples obtained from a solution of toluene/hexanes and sealed in a polyethylene membrane under an inert atmosphere. Direct current (dc) susceptibility measurements were performed in a magnetic field, B, of 1000 Oe and at a temperature range of 2 K to 290 K. Solid-state molecular structure of [(thiolfan)YbCl]$_2$ revealed a dinuclear complex, therefore, at 290 K, $\chi_m T = 4.77\ emu \cdot K/mol$ after diamagnetic correction is comparable with the reported two ytterbium centers ($5.14\ emu \cdot K/mol$, $^{2}F_{7/2}$, $g_J = 8/7$) at room temperature.[65–73] Upon cooling, $\chi_m T$ decreased gradually to $3.67\ emu \cdot K/mol$ at 2 K as a result of depopulation

of the excited crystal field sublevels of Yb^{3+} and/or antiferromagnetic interactions between the two Yb^{3+} centers (Figure 2.18). At low temperature, the magnetization value rose rapidly at low fields, and increases slowly at high fields, then reaches a maximum of 3.76 μ_B at 7 T (Figure 2.19a). Such field dependence of the magnetization of $[thiolfanYbCl]_2$ is typically observed for weakly interacting Yb^{3+} ions.[66,68–71,74] Attempts to fit the field dependent magnetization data using a Brillouin function of two non-interacting Yb^{3+} ions gave incongruent results. The saturation limit at 7 T and 2 K for $[thiolfanYbCl]_2$ was lower than expected for two uncoupled Yb^{3+} centers. This discrepancy may be due to exchange interactions or the presence of low-lying excited states.[73,75,76] The discrepancy between Brillouin function of two uncoupled J = ±2/7 states versus the experimental data of $[thiolfanYbCl]_2$ may also be attributed to magnetic anisotropy. The lack of perfect superimposition of the *M* versus *H/T* curves at 2, 4, 6, 8, and 10 K (Figure 2.19b) suggests the presence of magnetic anisotropy and/or low-lying excited states for the ytterbium complex. However, the measurement was performed on a polycrystalline sample which is insufficient to probe the orientation sensitivity of the anisotropic exchange contribution.[69]

A linear curve was observed in $1/\chi$ vs *T* and a Curie constant was calculated based on the linear fit ($c = 4.39\ emu\ K/mol$). According to the Curie-Weiss law, a negative Weiss constant ($\theta = -4.46K$) was obtained from the graph, indicating anti-ferromagnetic coupling (Figure 2.20). A linear curve was also observed in the *M* vs *H* measurement passing through the origin, confirming the paramagnetic properties of the compound. No hysteresis in isothermal magnetization measurements was observed (Figure 2.21).

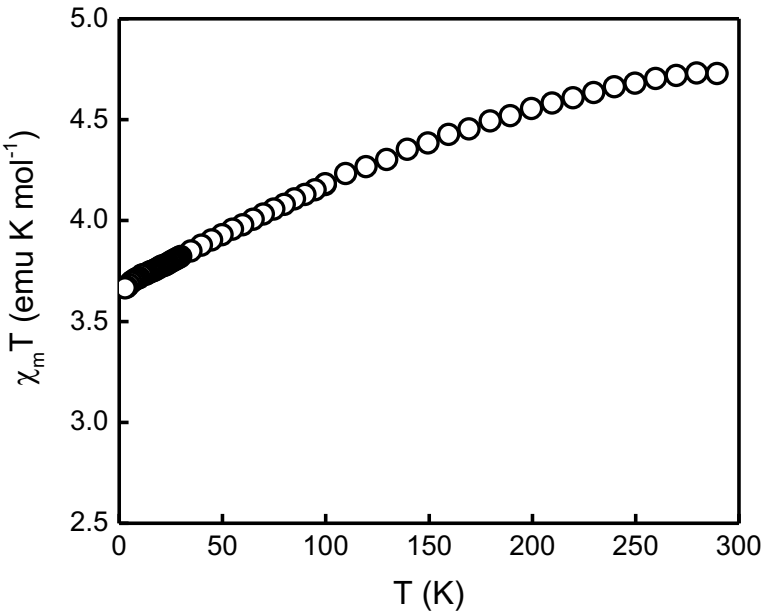

Figure 2.18 Plot of $\chi_m T$ versus T for [(thiolfan)YbCl]$_2$

Taken under a 1000 Oe dc field in the temperature range 2-290 K.

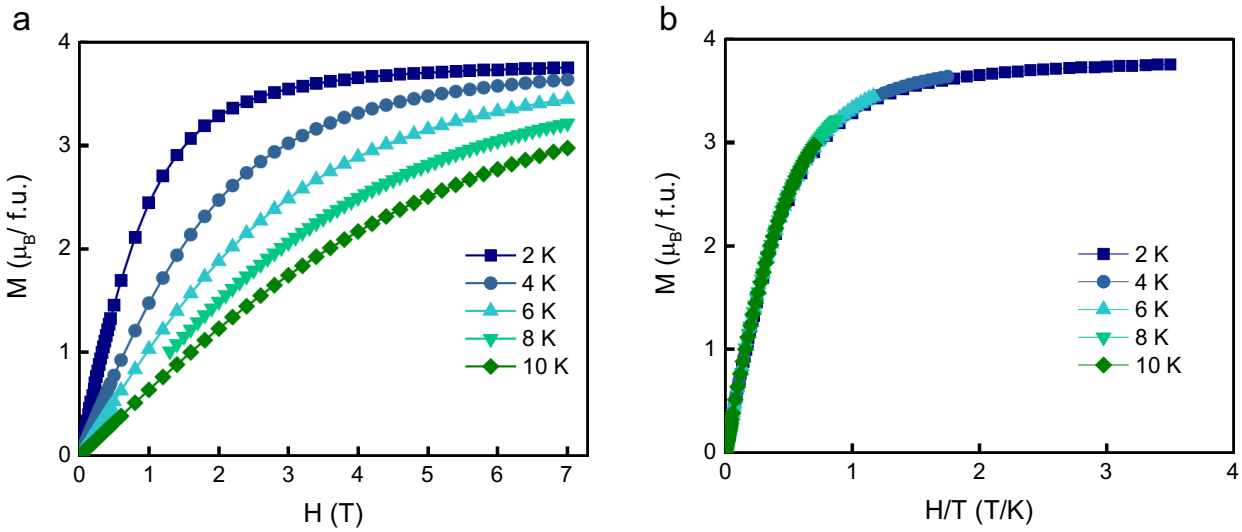

Figure 2.19 Isothermal M vs. H and M vs. H/T plots at 2-10 K

Isothermal *M* vs. *H* plots at 2, 4, 6, 8, and 10 K (a). *M* vs. *H/T* plots at 2, 4, 6, 8, and 10 K (b).

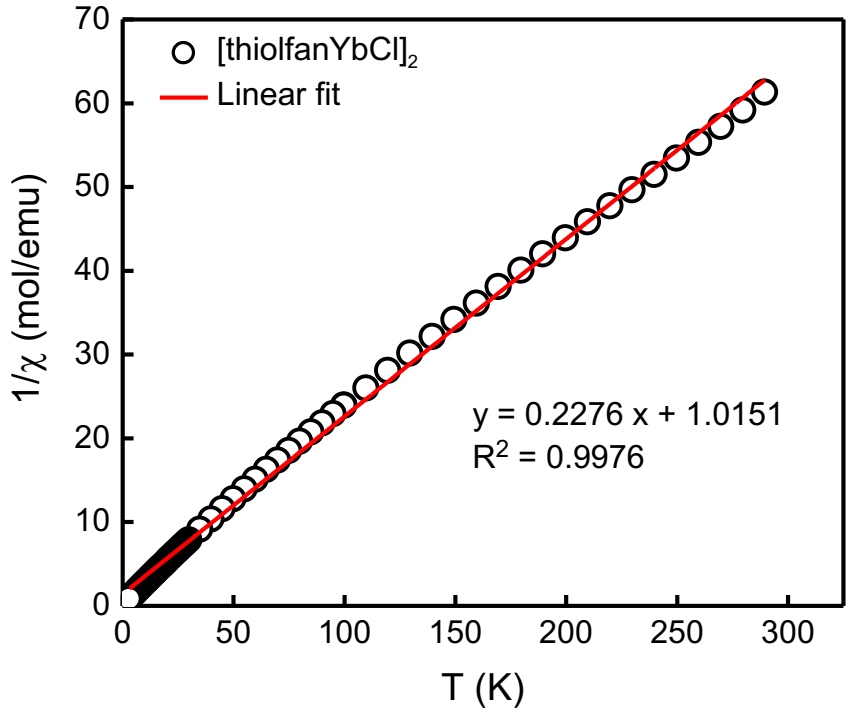

Figure 2.20 Plot of 1/ χ versus *T* for [(thiolfan)YbCl]$_2$.

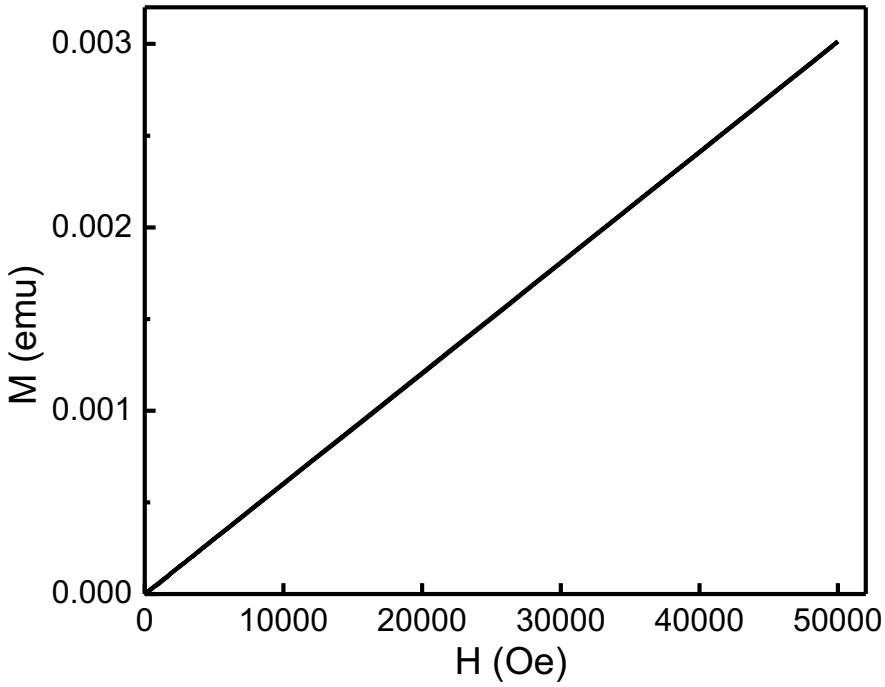

Figure 2.21 Plot of *M* versus *H* at 300 K for [(thiolfan)YbCl]$_2$.

Similarly, direct current (DC) susceptibility measurements in a magnetic field, B, of 1000 Oe and at a temperature range of 2 K to 300 K were also conducted for (thiolfan*)YbCl(THF)$_n$ and (thiolfan)Yb[N(SiMe$_3$)$_2$]. For (thiolfan*)YbCl(THF)$_n$, the room temperature molecular susceptibility and effective magnetic moment $\chi_m T = 2.11\ emu \cdot K/mol$ and $\mu_{eff} = 4.11$ per ytterbium center were calculated based on experimental results (Figure 2.22). For (thiolfan)Yb[N(SiMe$_3$)$_2$], the room temperature molecular susceptibility and effective magnetic moment $\chi_m T = 2.12\ emu \cdot K/mol$ and $\mu_{eff} = 4.12$ per ytterbium center were found (Figure 2.25). Both are comparable with the expected values for one ytterbium center ($2.57\ emu \cdot K/mol$ and $\mu_{eff} = 4.54$) assuming a J = 7/2 (S = ½, L = 3, g_J = 8/7) ground state.[33,77]

Interestingly, upon cooling, $\chi_m T$ of (thiolfan*)YbCl(THF) first decreases gradually as temperature decreases to 1.73 $emu \cdot K/mol$ at 17 K, then slowly increased to 1.75 $emu \cdot K/mol$ at 6 K, followed by a sharp decrease to 1.69 $emu \cdot K/mol$ at 2 K (Figure 2.22). A linear curve was observed in $1/\chi$ vs *T*. The Curie constant was calculated based on the linear fit ($c = 2.13\ emu\ K/mol$), which is comparable to the value of $\chi_m T = 2.11\ emu \cdot K/mol$ previously calculated for one ytterbium center. According to the Curie-Weiss law, a negative Weiss constant ($\theta = -5.89\ K$) was obtained from the graph, indicating a net anti-ferromagnetic coupling in the bulk sample (Figure 2.23). A linear curve was also observed in the *M* vs *H* measurement passing through the origin, confirming the paramagnetic properties of this compound (Figure 2.24).

On the contrary, $\chi_m T$ of (thiolfan)Yb[N(SiMe$_3$)$_2$] only decreased as the temperature decreased until reached the minimum 1.55 $emu \cdot K/mol$ at 2 K (Figure 2.25). Similarly, a linear curve was also observed in the *M* vs *H* measurement passing through the origin, confirming the paramagnetic properties of the amide derivative (Figure 2.27), with a negative Weiss constant ($\theta =$

$-4.08\ K$) obtained based on the linear fitting in $^1/_\chi$ vs T (Figure 2.26). The Curie constant was calculated based on the linear fit ($c = 2.14\ emu\ K/mol$), which is comparable to the value of $\chi_m T = 2.12\ emu \cdot K/mol$ previously calculated for one ytterbium center.

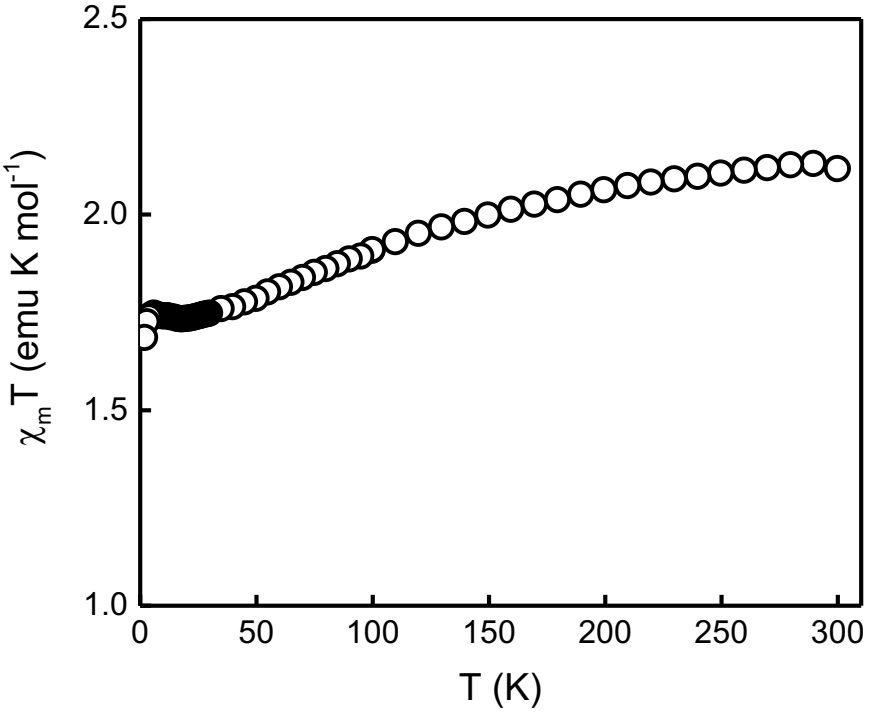

Figure 2.22 Plot of $\chi_m T$ versus T for (thiolfan*)YbCl(THF)$_n$
Taken under a 1000 Oe dc field in the temperature range 2-300 K.

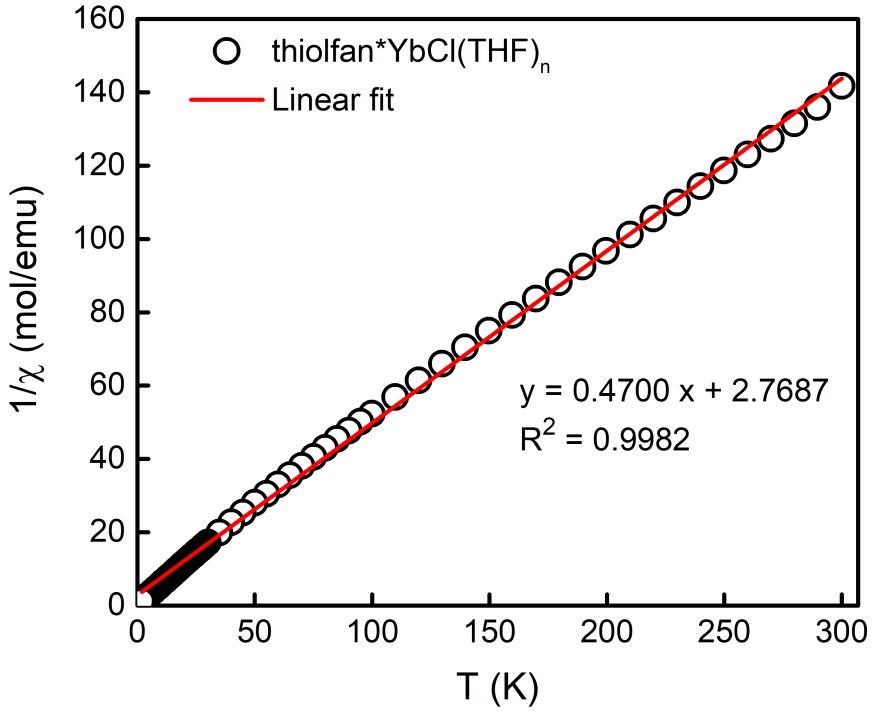

Figure 2.23 Plot of 1/ χ versus *T* for (thiolfan*)YbCl(THF)$_n$.

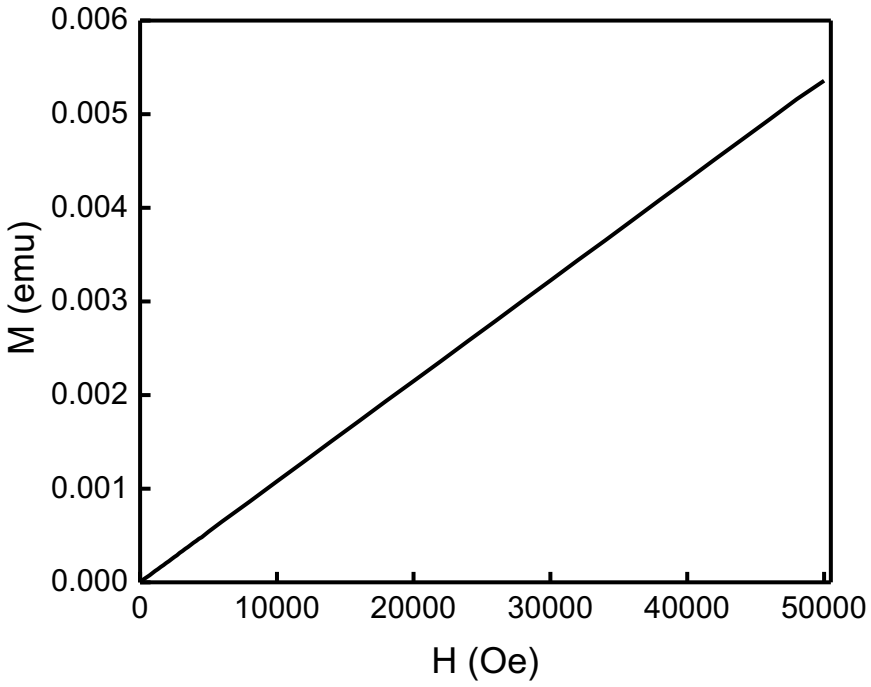

Figure 2.24 Plot of *M* versus *H* at 300 K for (thiolfan*)YbCl(THF)$_n$.

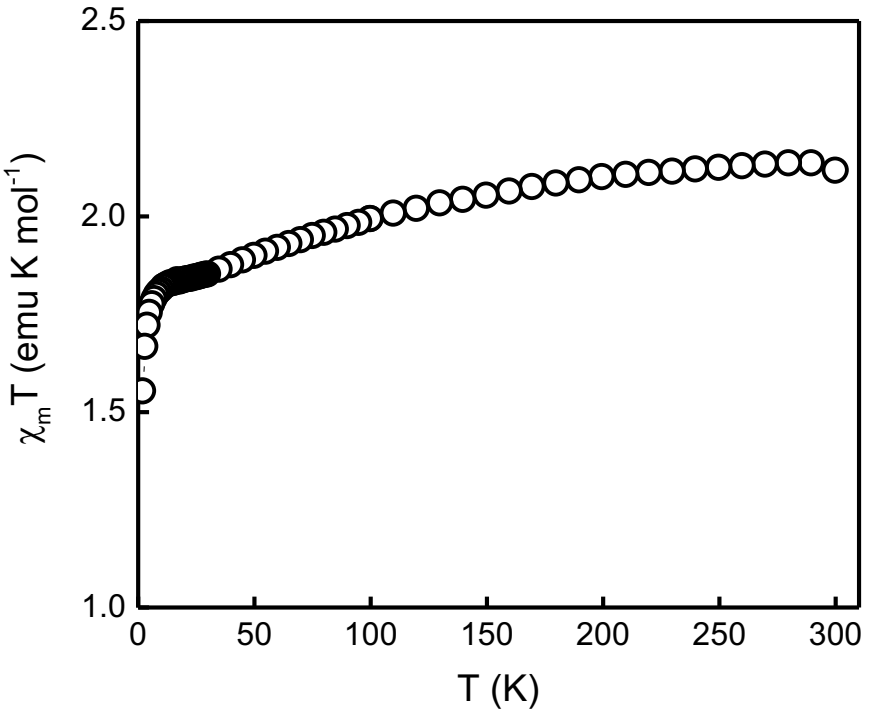

Figure 2.25 Plot of $\chi_m T$ versus T for (thiolfan)Yb[N(SiMe$_3$)$_2$]

Taken under a 1000 Oe dc field in the temperature range 2-300 K.

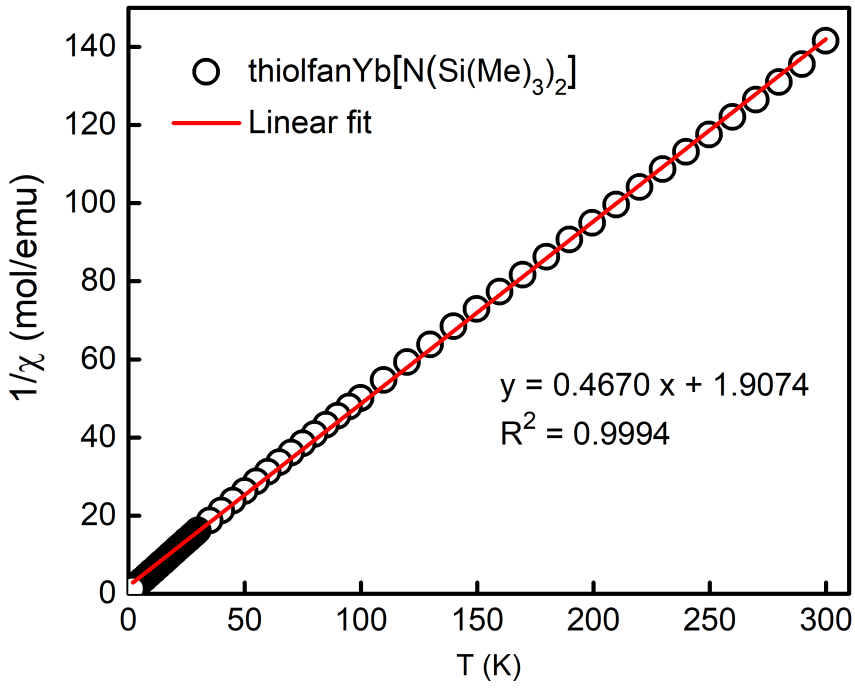

Figure 2.26 Plot of 1/ χ versus T for (thiolfan)Yb[N(SiMe$_3$)$_2$].

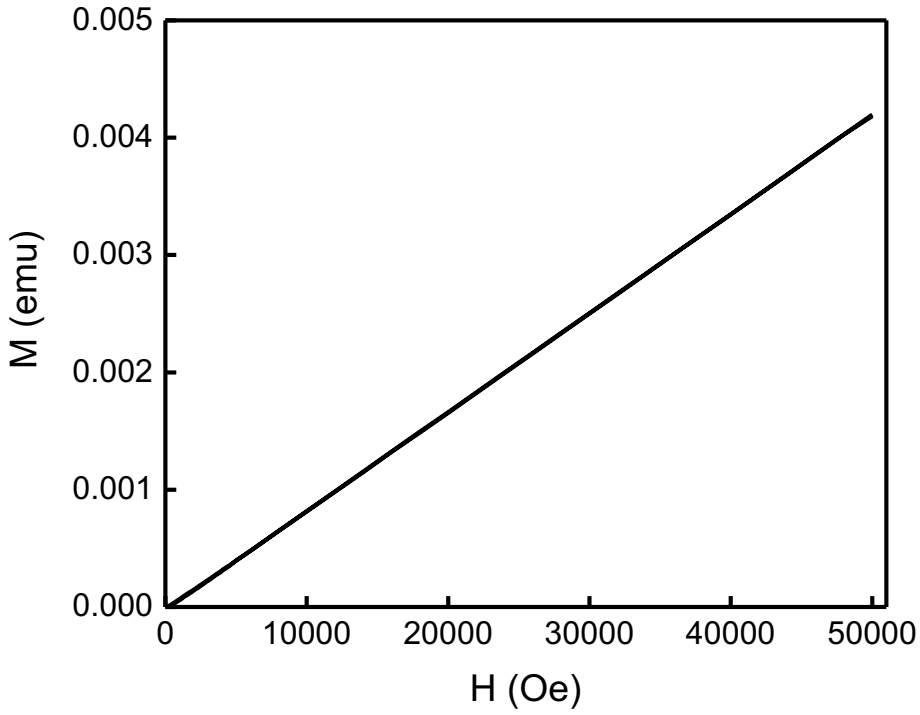

Figure 2.27 Plot of *M* versus *H* at 300 K for (thiolfan)Yb[N(SiMe$_3$)$_2$].

The magnetic susceptibility of each ytterbium compound in solution was measured by NMR spectroscopy using the Evans method in designated deuterated solvents.[24] The molar susceptibility and effective magnetic moment (μ_{eff}) of each compound was calculated based on the following formulae:[78]

$$\chi_m T = \frac{3 \times 10^3 \Delta f}{4\pi f_m c} - \chi_D$$

$$\mu_{eff} = 2.827\sqrt{\chi_m T}$$

where χ_m is the corrected paramagnetic molar susceptibility, T (in K) is the absolute temperature at which the NMR spectrum was taken. Δf (in Hz) is the chemical shift difference of the NMR reference in the presence and absence of the paramagnetic compound (shift of the deuterated solvent referencing peak); f_m (in Hz) is the external magnetic field, C (in mol/L) is the

concentration of the sample and χ_D is the diamagnetic susceptibility. For simplicity, χ_D of (thiolfan*)YbCl(THF)$_n$ (n = 0 or 1) and (thiolfan)Yb[N(SiMe$_3$)$_2$] is estimated based on:

$$\chi_D \approx -\frac{M}{2} \times 10^{-6}$$

where M (in g/mol) is the molecular mass.

The paramagnetic properties of (thiolfan)YbCl(THF)$_n$ were investigated in THF-d$_8$, C$_6$D$_6$, and Tol-d$_8$ (Figures 2.28-2.30). A $\chi_m T = 2.68\ emu \cdot K/mol$ was calculated along with a $\mu_{eff} = 4.63$ based on the difference in δ observed in the ^{1}H NMR spectrum after diamagnetic correction in THF-d$_8$, as expected for one ytterbium center (2.57 $emu \cdot K/mol$ and $\mu_{eff} = 4.54$) assuming a J = 7/2 (S = ½, L = 3, g$_J$ = 8/7) ground state.[33,77] Similar results were obtained using other two solvents, $\chi_m T = 2.08\ emu \cdot K/mol$ was calculated for C$_6$D$_6$, and $2.68\ emu \cdot K/mol$ was calculated for Tol-d$_8$ per ytterbium center. The effective magnetic moment of (thiolfan)YbCl(THF) was calculated based on the formulae above suggesting $\mu_{eff} = 4.63$ in THF-d$_8$, 4.08 in C$_6$D$_6$, and 4.63 in Tol-d$_8$.

Similarly, the molar susceptibility and effective magnetic moment were calculated for (thiolfan*)YbCl(THF)$_n$ (n = 0 or 1) and (thiolfan)Yb[N(SiMe$_3$)$_2$] in C$_6$D$_6$. A $\chi_m T = 2.05\ emu \cdot K/mol$ and $\mu_{eff} = 4.05$ per ytterbium center was found for (thiolfan*)YbCl(THF)$_n$ (calculated based on n = 0, Figure 2.31). $\chi_m T = 2.33\ emu \cdot K/mol$ and $\mu_{eff} = 4.32$ per ytterbium center were found for (thiolfan)Yb[N(SiMe$_3$)$_2$] (Figure 2.32). These results are consistent with the findings for (thiolfan)YbCl(THF)$_n$, and previously reported values per ytterbium center.[33,77]

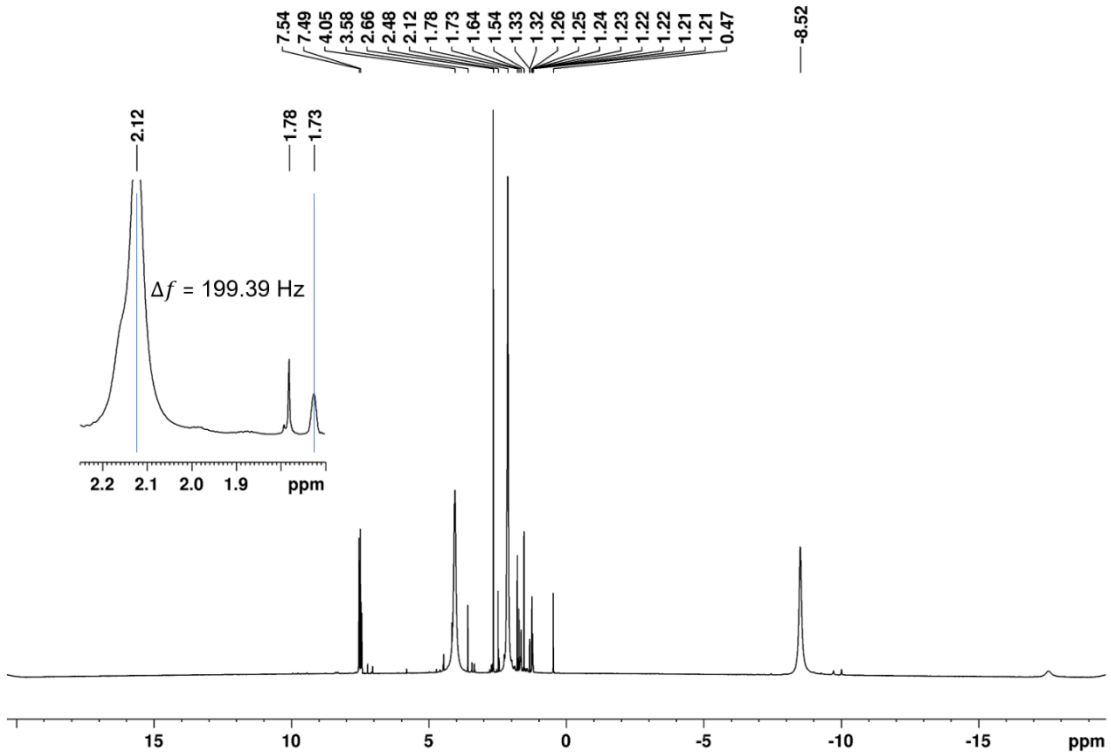

Figure 2.28 ^{1}H NMR spectrum of (thiolfan)YbCl(THF)$_n$

(298 K, 500 MHz, THF-d_8. Chemical shifts of THF-d_8 = 1.72, 3.58 ppm).

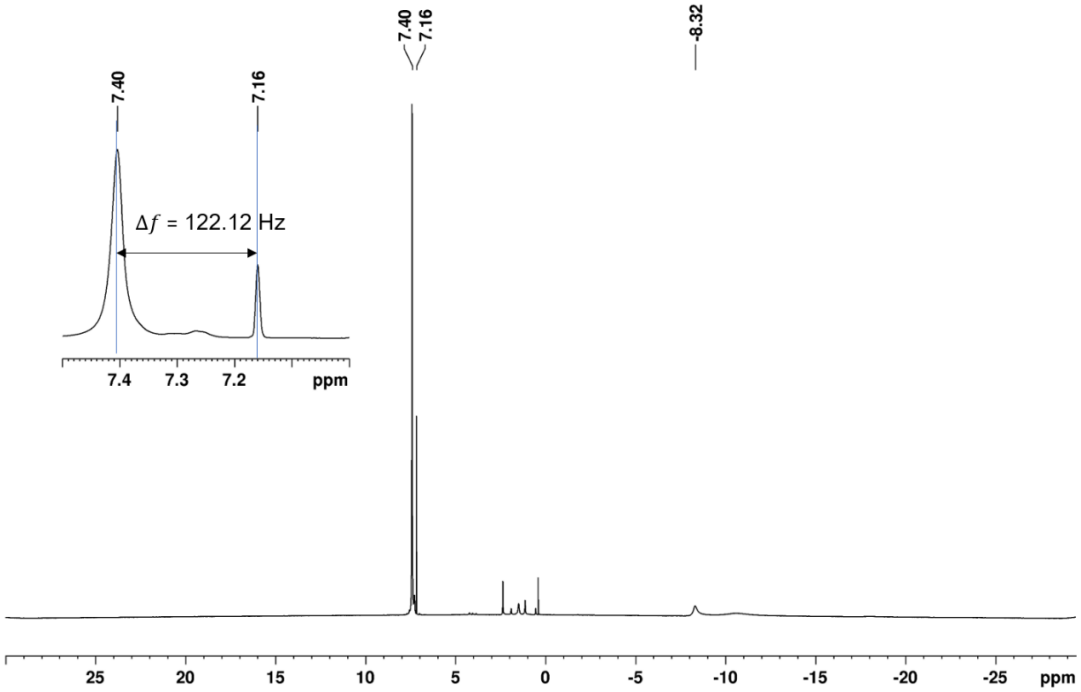

Figure 2.29 ^{1}H NMR spectrum of (thiolfan)YbCl(THF)$_n$

(298 K, 500 MHz, C_6D_6. Chemical shift of C_6D_6 = 7.16 ppm).

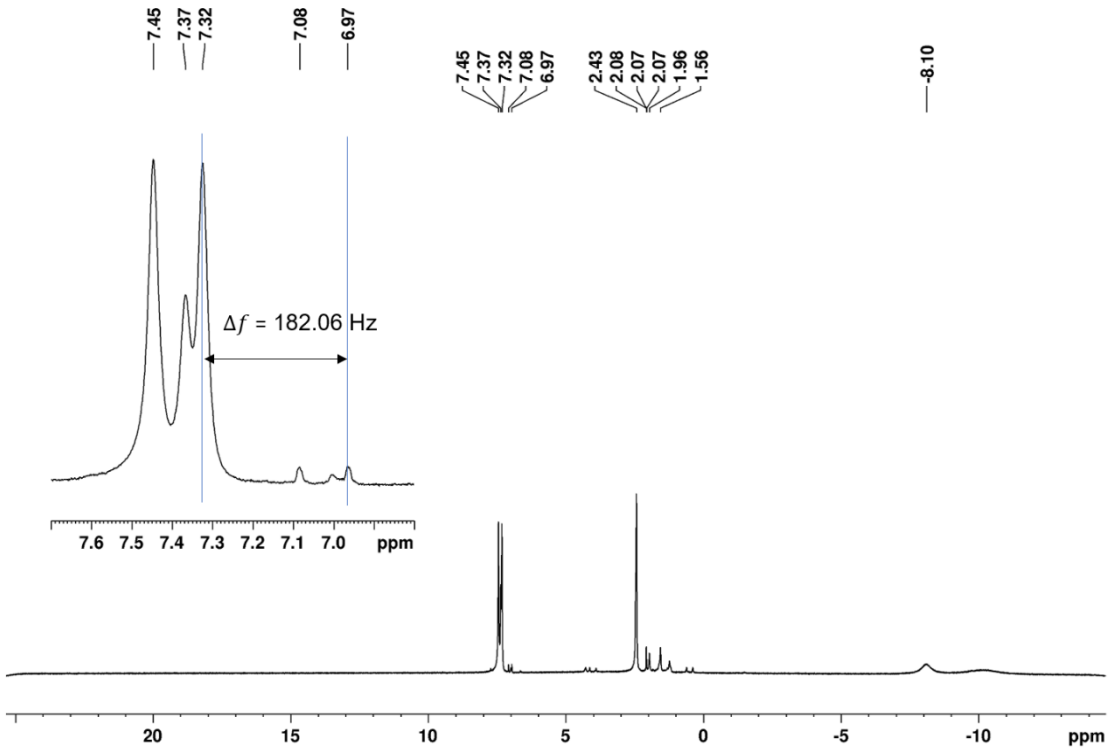

Figure 2.30 ^{1}**H NMR spectrum of (thiolfan)YbCl(THF)$_n$**

(296 K, 500 MHz, Tol-d_8. Chemical shifts of Tol-d_8 = 2.08, 6.97, 7.01, 7.09 ppm).

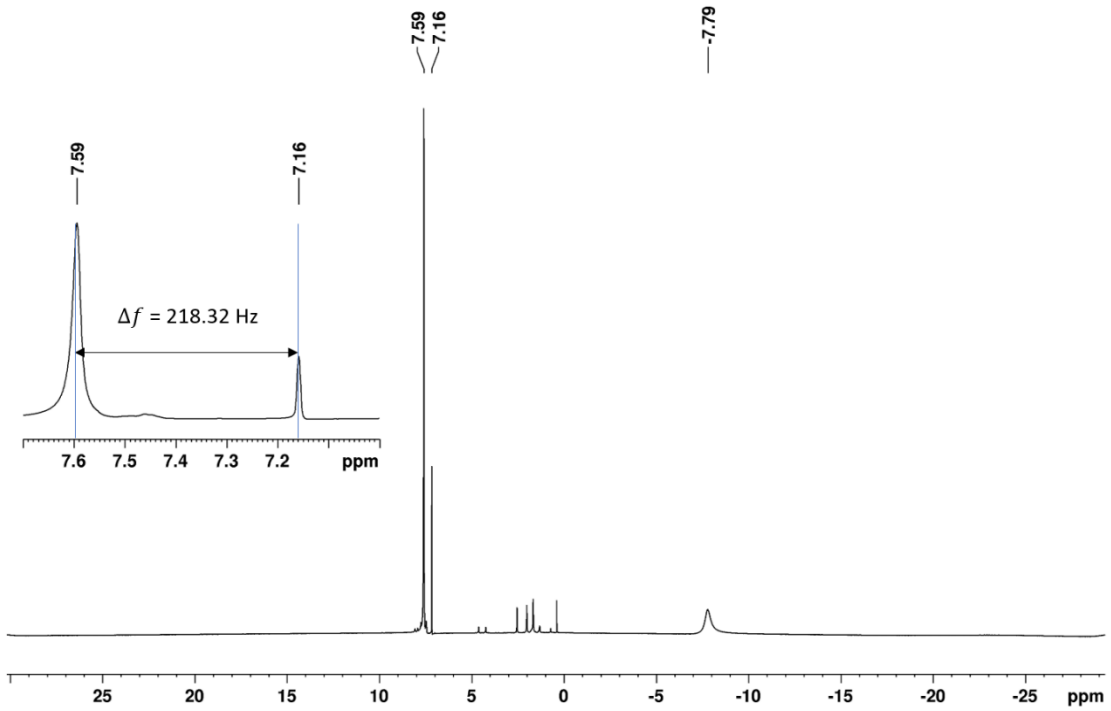

Figure 2.31 ^{1}H NMR spectrum of (thiolfan*)YbCl(THF)$_n$

(298 K, 500 MHz, C_6D_6. Chemical shift of C_6D_6 = 7.16 ppm).

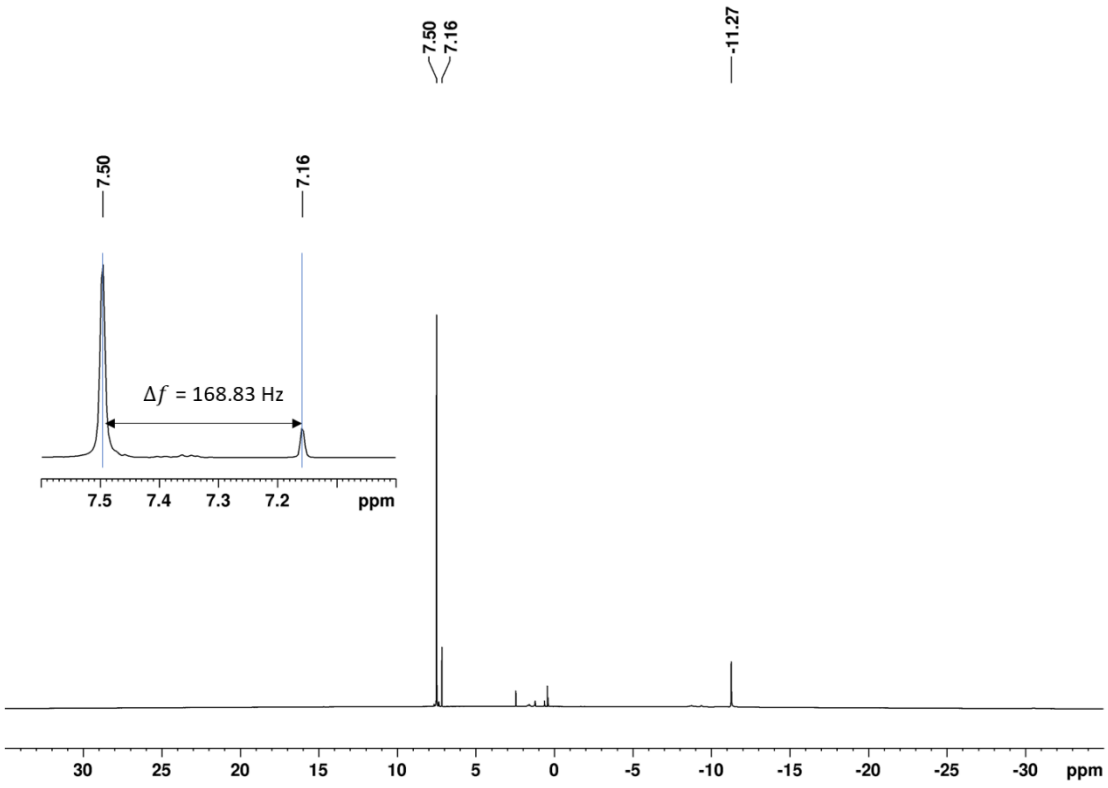

Figure 2.32 ^{1}H NMR spectrum of (thiolfan)Yb[N(SiMe$_3$)$_2$]

(298 K, 500 MHz, C_6D_6. Chemical shift of C_6D_6 = 7.16 ppm).

IR Spectra

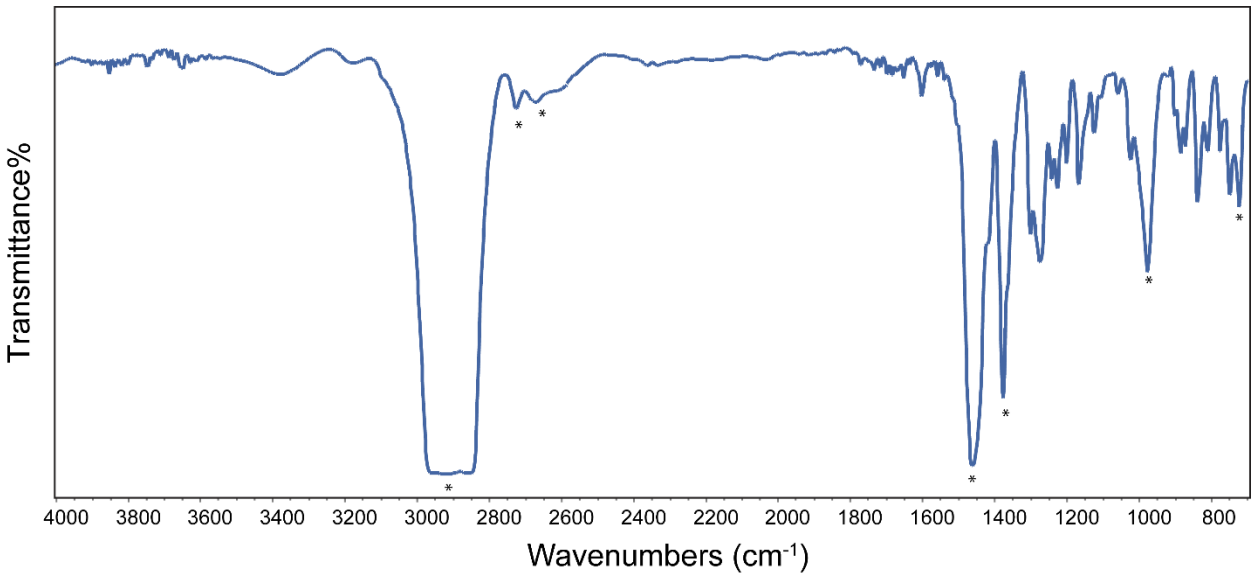

Figure 2.33 IR (Nujol) spectrum of $[(thiolfan)YbCl]_2$

(*: Nujol).

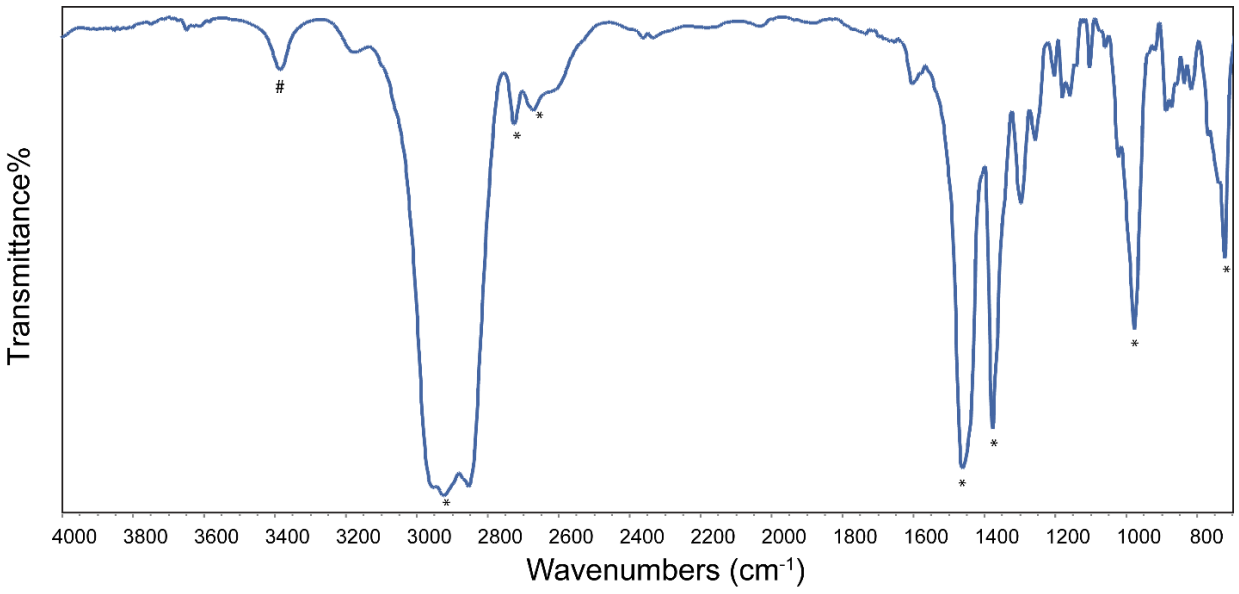

Figure 2.34 IR (Nujol) spectrum of $(thiolfan^*)YbCl(THF)_n$

(*: Nujol; #: trace OH due to minor decomposition of the compound during the measurement).

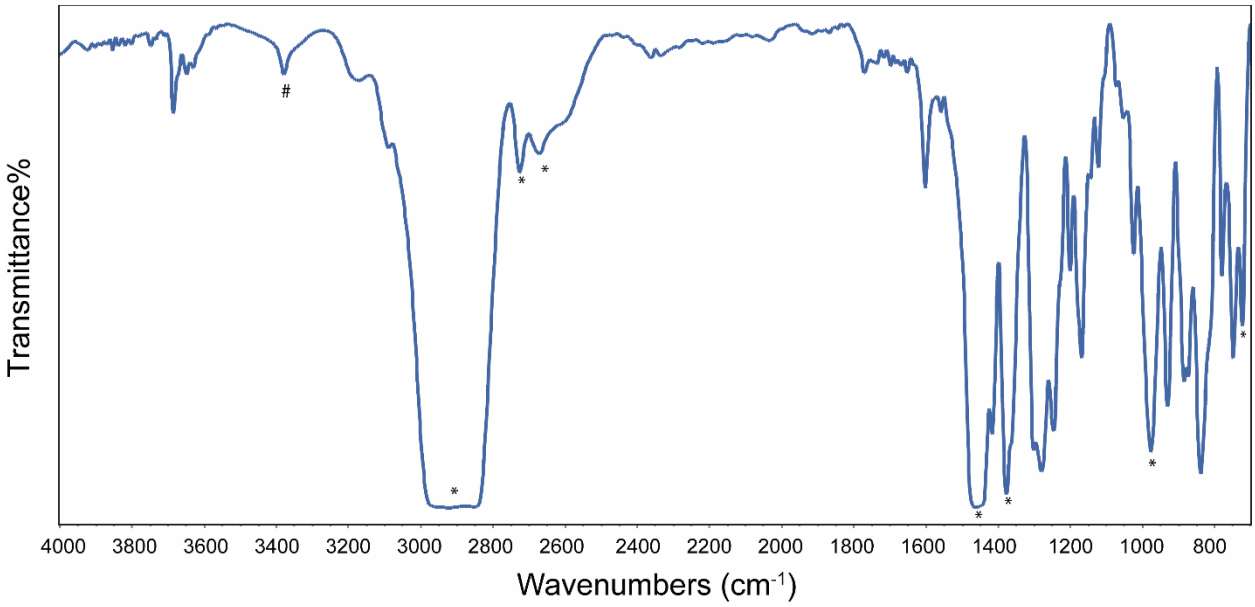

Figure 2.35 IR (Nujol) spectrum of (thiolfan)Yb[N(SiMe$_3$)$_2$]

(*: Nujol; #: trace OH/NH due to minor decomposition of the compound during the measurement).

Details of Electronic Spectroscopy

The absorption band around 400-600 nm is assigned to the supporting ligand, as evident by the comparison between the absorbance of the sample vs. that of H_2(thiolfan).

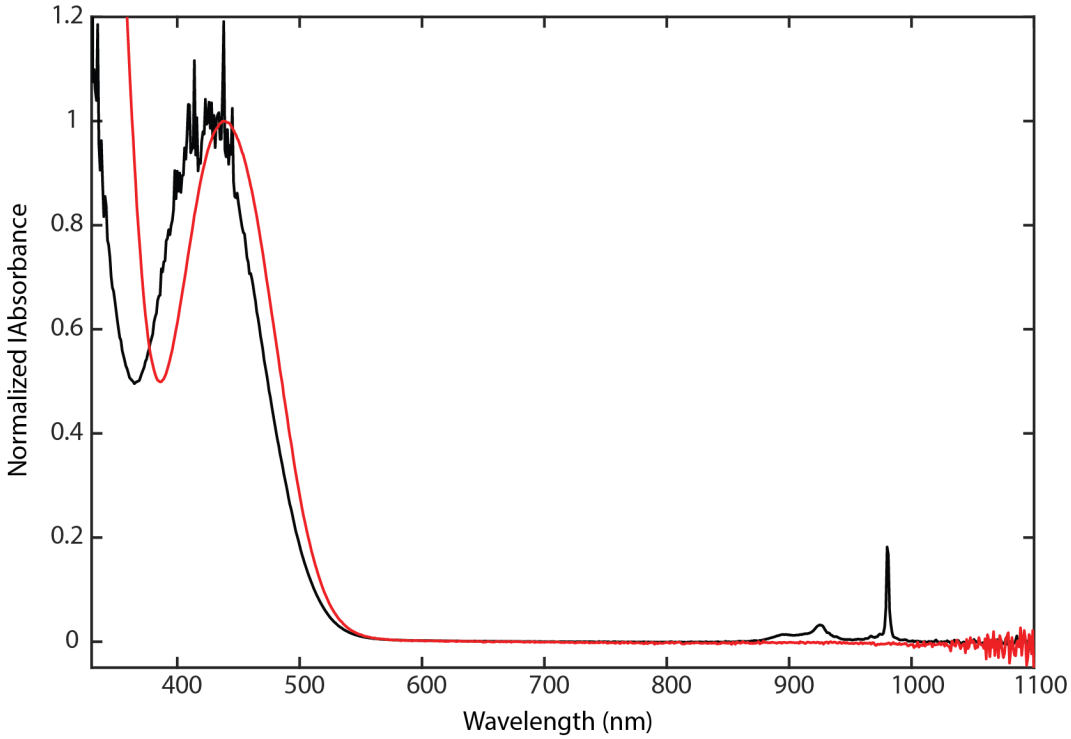

Figure 2.36 Comparison of Ligand vs. Sample Absorption

Absorbance of (thiolfan)YbCl(THF) in black and H_2(thiolfan) in red.

High Resolution Transmission/Absorption Setup

A high-resolution transmission/absorption spectrum of the sample was measured with a tunable narrow band CW laser (M Squared SolsTis Ti:Sapph laser). The laser beam is split into two paths by a polarizing beam splitter (PBS). One beam measures the absorption of the solvent and the other measures the absorption of the sample. The quarter waveplate is used to change the polarization of the laser beam so that we can measure the absorption of σ^- and σ^+light. The two permanent magnets create a strong static magnetic field to induce Zeeman splitting. The translational stage allows us to control the distance between the magnet and the sample and to vary the strength of the magnetic field at the sample's location. The setup is shown in Figure 2.37.

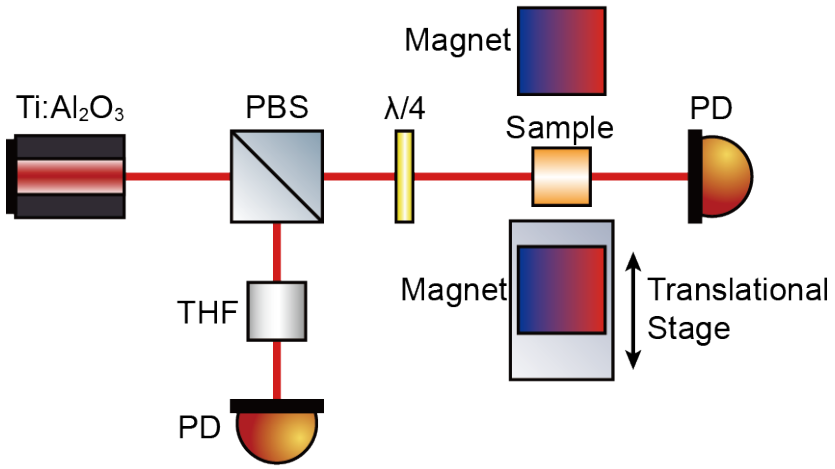

Figure 2.37 Optical setup of the high-resolution transmission/absorption measurement

Investigating Sources of Linewidth Broadening

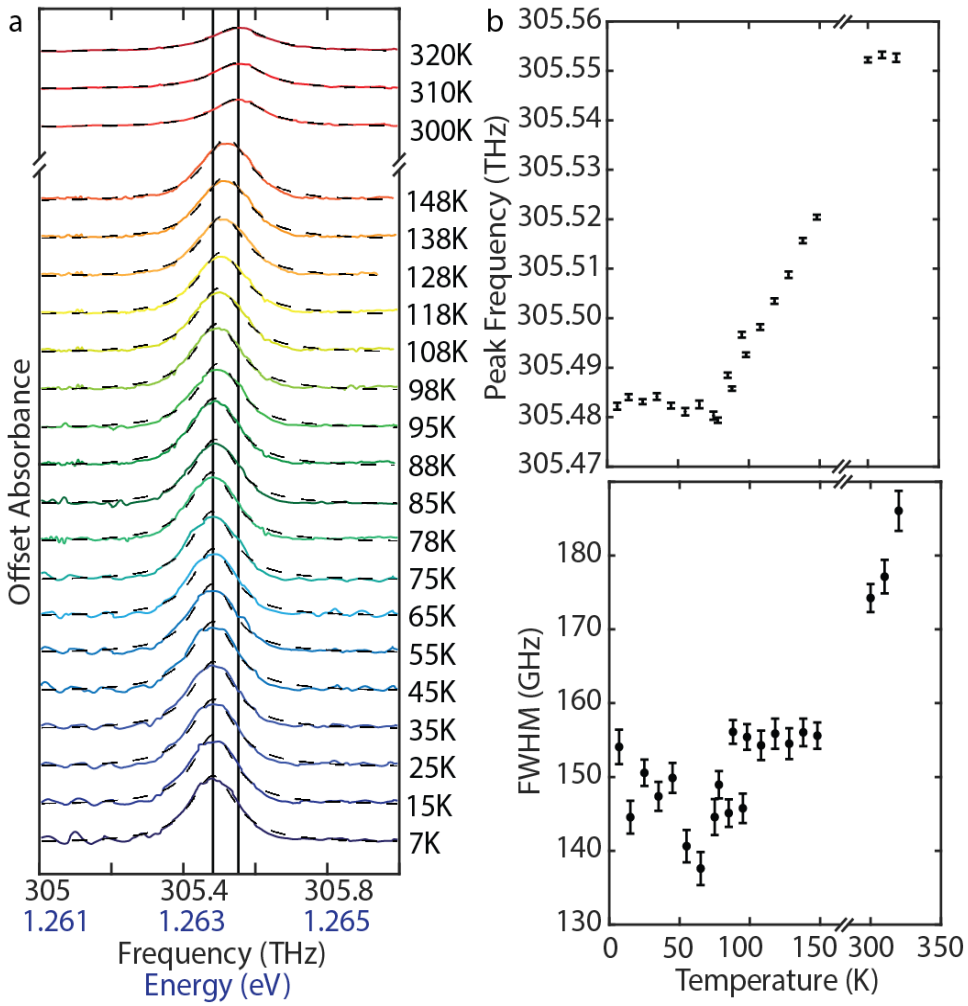

Figure 2.38 Temperature-dependent Absorption Spectra of Sample in 2-MeTHF

a) Temperature-dependent absorbance of (thiolfan)YbCl(THF) and the corresponding Lorentzian fits. b) Fitted peak frequencies and linewidths.

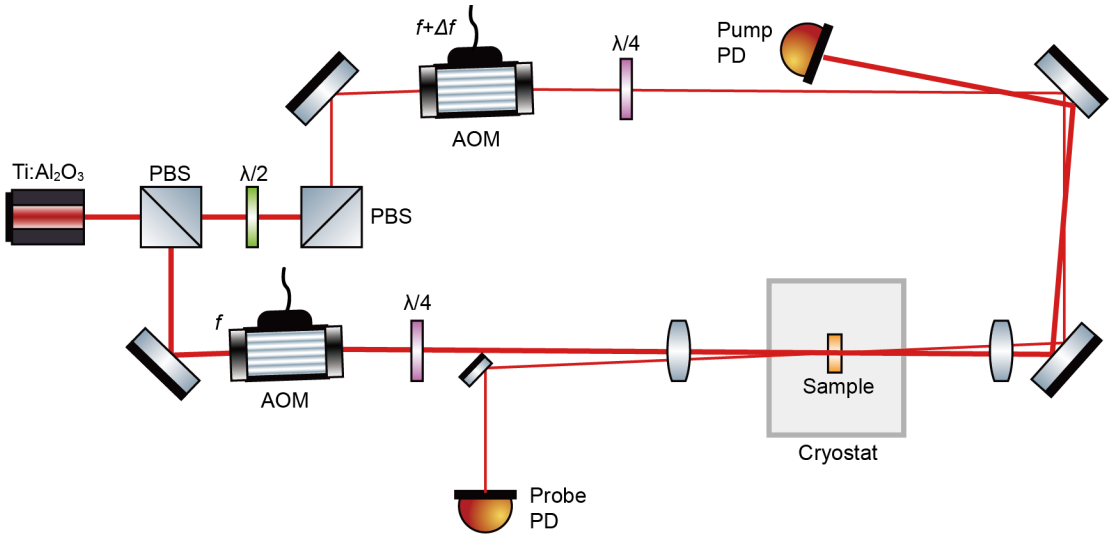

Figure 2.39 Optical setup for spectral hole burning measurement.

Discussion on the Sources of Linewidth Broadening

As shown above in Figure 2.38, over a range of 300 K, the absorption linewidth narrows by 0.1 meV as a function of temperature, but once the sample is frozen, it appears to have no change in linewidth. This suggests that the room temperature linewidth has some component of homogeneous broadening, while the 77 K linewidth consists of many narrower transitions. If the 0.6 meV linewidth is limited by the excited state lifetime, it would correspond to a lifetime of 1.1 ps (where lifetime $\tau = \hbar/\Gamma$, linewidth $\Gamma = 0.6$ meV and $\hbar = 6.6 \times 10^{-16} eV \cdot s$). However, the Einstein A_{21} coefficient can be extracted from the experimental oscillator strength of 9.36×10^{-6}.[79] The corresponding expected excited state decay rate is 912 Hz, which translates to a lifetime of 1.1 ms. Therefore, the 0.6 meV linewidth is not limited by the excited state lifetime.

We also measured the fluorescence lifetime of the room-temperature sample in solution (Figure 2.40). Because there is minimal Stokes shift from the 980 nm absorption and emission peaks, as shown in Figure 2.2 in the chapter, we excited into the ligand absorption band at 420 nm to be able to spectrally filter the excitation from the emission. The resulting lifetime then would include not only the excited state decay rate of the 980 nm transition, but also the time it takes for the excited electron to decay from the ligand-dominated states to the Yb^{3+}-dominated electronic states, from which the emission originates. The measured lifetime was 3.2 μs, which rules out lifetime broadening as the major source of the room-temperature linewidth. The 3.2 μs lifetime would correspond to a 0.2 neV linewidth, which is far narrower than the observed 0.6 meV and close to the 0.41 neV SHB linewidth. Therefore, we conclude that the 0.6 meV linewidth of the room-temperature solution consists of many transitions and some amount of ligand fluctuations, which cause a broader linewidth than the transform-limit.

We also investigated the hyperfine contribution to the spectral linewidth. We also investigate the hyperfine contribution to the spectral linewidth. The isotopic distribution of Yb can be divided into 7 stable isotopes with 3 nuclear spin values {S = 0, 1/2, 5/2}. We obtained ground state g-values and hyperfine (*A*) parameters by fitting the X-band (9.638 GHz) CW-EPR spectrum as shown in Figure 2.41a. For the excited state, we employ the calculated g-values based on CASSCF/RASSI level of theory (SI Sec. III-B). With these parameters, we are able to plot a calculated hyperfine splitting as a function of the external magnetic field strength, as shown in the Figure 2.41b. At zero field, the hyperfine splitting for {S = 0, 1/2, 5/2} is [0, 20.7, 27.2] GHz for the ground state and [0, 14.8, 19.4] GHz for the excited state. Considering all the spin-allowed zero-field transitions, the energy spread shows a minuscule effect compared with the 150 GHz optical peak, this reveals that zero-field hyperfine broadening may not be a major line-broadening contributor. Besides hyperfine splitting, the isotope shift caused by reduced mass is calculated to be around 23 MHz, and the volume effect is around 4 MHz. Overall, the isotopic contributions are found to be orders of magnitude smaller compared to the 150 GHz absorption linewidth of the (thiolfan)YbCl(THF), and are not expected to be the major broadening sources.

Furthermore, we investigated the superhyperfine contributions to the spectral linewidth. A superhyperfine interaction occurs when an unpaired electron couples to multiple nuclei. As it applies to our sample, a deuterated THF coordinating to the Yb^{3+} may cause a change in superhyperfine splitting. In addition, spin-spin dipolar interaction may occur if some other magnetic moment near the Yb^{3+} nucleus interacts with the magnetic dipole that couples to the electronic states involved in transition **IV**. In general, the magnitude of these effects can be gauged by taking the absorption of the sample in THF and deuterated THF. The linewidth of our sample saw an increase in linewidth from 0.6 meV to 0.7 meV and a decrease in molar absorptivity when

using the deuterated solvent (Figure 2.42). The sample concentrations were 3.1 mM in THF and 3.7 mM in THF-d_8. The linewidth stays similar with solvent deuteration, which indicates that superhyperfine interactions do not make up the dominant contributions to the inhomogeneous broadening observed in THF.

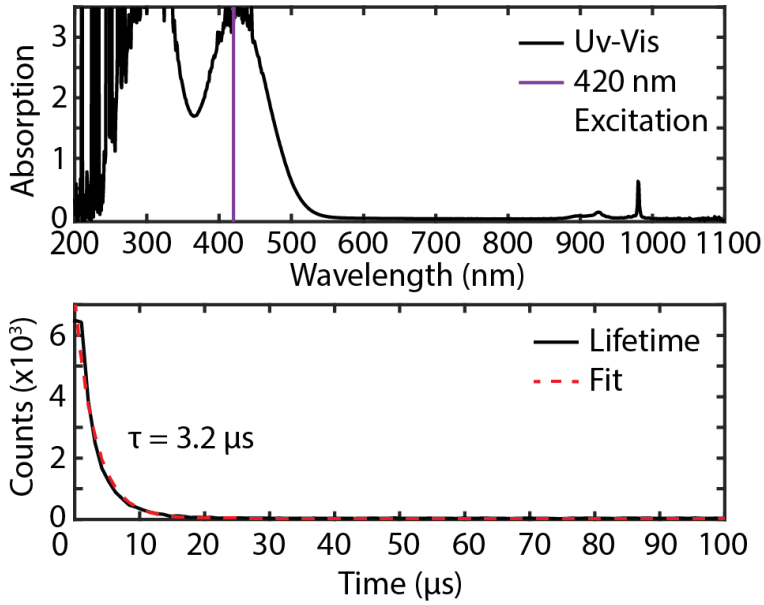

Figure 2.40 Fluorescence Lifetime Measurement of (thiolfan)YbCl(THF)

Top: broad absorption spectra of (thiolfan)YbCl(THF) in THF solution at room temperature. The excitation wavelength is indicated against the sample absorption. Bottom: lifetime measurement of the 980 nm emission and the corresponding fit.

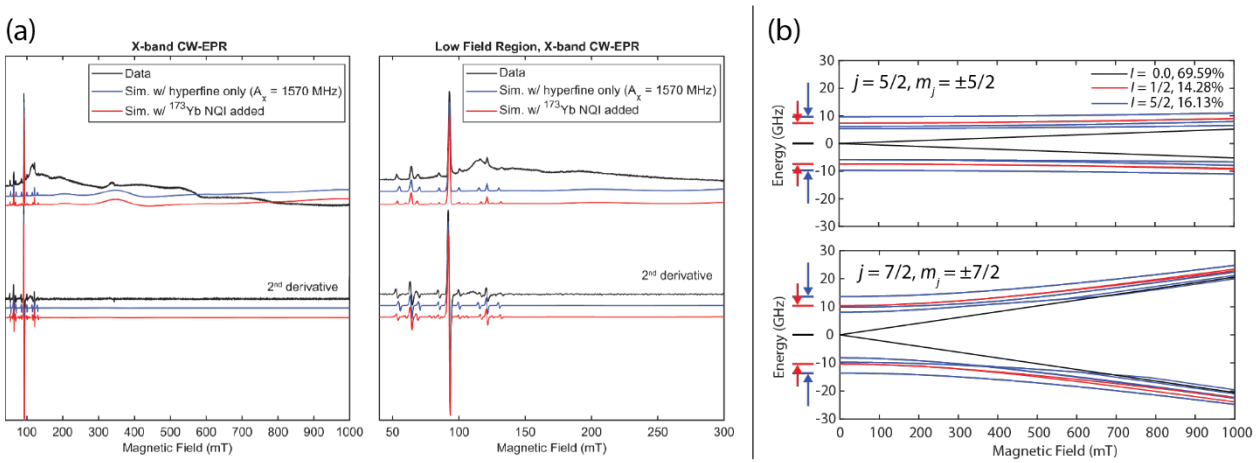

Figure 2.41 X-band CW-EPR Spectrum and Calculate Hyperfine Splitting

(a) X-band CW-EPR spectrum and 2nd derivative of (thiolfan)YbCl(THF) in frozen 2-MeTHF glass in the region from 0-1000 mT (left panel), and 0-300 mT (right panel) with spectral simulations offset underneath using the following parameters: g = [7.41, 0.62, 0.42], $A(^{173}\text{Yb})$ = [1553, 160, 160] MHz, $A(^{171}\text{Yb})$ = [5915, 609, 609] MHz (magnitudes of A scale with respective ^{173}Yb, ^{171}Yb gyromagnetic ratios). Red traces are simulated using only g and A parameters, while the blue traces include an additional nuclear quadrupole interaction with the I = 5/2 nucleus, $Q(^{173}\text{Yb})$ = [-105, -60, 165] MHz. Acquisition parameters: temperature = 5 K; microwave frequency = 9.638 GHz; MW power = 8.8 mW; modulation amplitude = 0.8 mT; conversion time = 10 ms. (b) Calculated hyperfine splitting as a function of the external magnetic field strength of the ground (bottom) and excited state (top) with g and A parameters from fitting and calculations.

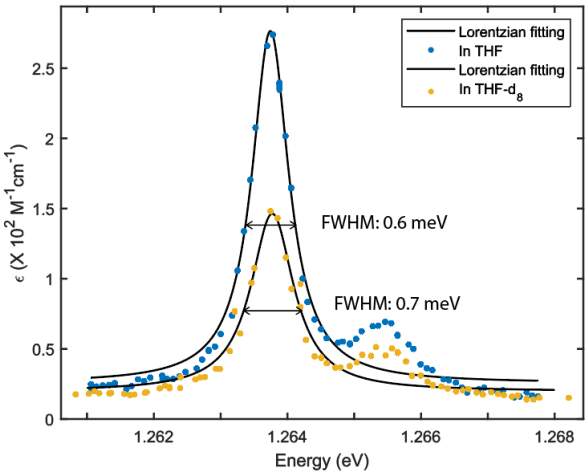

Figure 2.42 Absorption of (thiolfan)YbCl(THF) in THF vs. THF-d_8

Absorption spectra of (thiolfan)YbCl(THF) in THF in blue and in THF-d_8 in yellow, showing an increase in inhomogeneous linewidth from 0.6 to 0.7 meV with solvent deuteration.

FHWM Comparisons and their Corresponding References

Table 2.2 Expanded linewidth comparison.

This table includes ones shown in Figure 2.4a.[33–36,80–90]

Name	Ion Transition	FWHM (meV)	Phase	Temp.	Ref.	# in fig. 2.4a
(thiolfan)YbCl(THF)	Yb^{3+} $^2F_{7/2} - {}^2F_{5/2}$	0.6	Solution	RT		1
Yb^{3+} Helicene	Yb^{3+} $^2F_{7/2} - {}^2F_{5/2}$	3.6	Single Crystal	4 K	30	4
Yb Trensal	Yb^{3+} $^2F_{7/2} - {}^2F_{5/2}$	4.6	Single Crystal	RT	31	5
Yb^{3+} Methide Complex	Yb^{3+} $^2F_{7/2} - {}^2F_{5/2}$	5.1	Solution		32	6
[Yb**L**$_2$(OTf)$_2$](OTf)	Yb^{3+} $^2F_{7/2} - {}^2F_{5/2}$	25.3	Solution	4 K	33	7
$YbPO_4$:5% Er^{3+} Nanocrystals	Yb^{3+} $^2F_{7/2} - {}^2F_{5/2}$	32.8	Colloidal Nanocrystal	RT	77	
Yb^{3+} doped phosphate photonic crystal fiber	Yb^{3+} $^2F_{7/2} - {}^2F_{5/2}$	8	Crystal	RT	78	
Yb^{3+} doped silica glass	Yb^{3+} $^2F_{7/2} - {}^2F_{5/2}$	10	Glass	RT	79	
Yb^{3+}:YAG Crystal	Yb^{3+} $^2F_{7/2} - {}^2F_{5/2}$	3.4	Crystal	RT	80	
Yb(III) N,O-chelated Complex	Yb^{3+} $^2F_{7/2} - {}^2F_{5/2}$	8.4	Crystal	RT	81	
Yb^{3+}:Y_2SiO_5	Yb^{3+} $^2F_{7/2} - {}^2F_{5/2}$	0.4	Crystal	12 K	82	
Yb^{3+}:YVO	Yb^{3+} $^2F_{7/2} - {}^2F_{5/2}$	1e-5	Crystal	40 mK	83	
$Eu(BA)_4(pip)$	Eu^{3+} $^7F_0 - {}^5D_0$	0.027	Crystal	10 K	84	
Eu(trensal)	Eu^{3+} $^7F_0 - {}^5D_0$	0.372	Crystal	4.2 K	85	
Pr^{3+} in $HClO_4$	Pr^{3+} $^3H_4 - {}^3P_0$	26	Solution	RT	86	
Nd^{3+} in $HClO_4$	Nd^{3+} $^4I_{9/2} - {}^3G_{1/2}$	10	Solution	RT	86	
Pm^{3+} in $HClO_4$	Pm^{3+} $^5I_4 - {}^5I_8$	22	Solution	RT	86	
Eu^{3+} in $HClO_4$	Eu^{3+} $^7F_0 - {}^5D_1$	11	Solution	RT	86	
Er^{3+} in $HClO_4$	Er^{3+} $^4I_{15/2} - {}^2K_{15/2}$	17	Solution	RT	86	
Er^{3+}:YVO_4	Er^{3+} $^4I_{15/2}$-$^4I_{14/2}$	6.7e-4	Crystal	1 K	87	
Er^{3+}:Y_2SiO_5	Er^{3+} $^4I_{15/2}$-$^4I_{14/2}$	3.02e-10	Crystal	2 K	88	

Magnetic Dipole Calculations

The transitions between states with the same orbital-angular momentum quantum number are electric dipole (E1) disallowed. Therefore, operators with even symmetry (e.g. magnetic dipole (M1)) might assist in mediating the transitions. However, the theoretical limit for an Yb3+ ion M1 transition ($f \sim 10^{-8}$) is considerably smaller than that measured in (thiolfan)YbCl(THF) ($f \sim 10^{-6}$).[91,92] With the assumption that the f-f transition occurs between two pure 4f atomic orbitals, the transition is expected to be only magnetic-dipole-allowed.[38] The magnetic dipole moment operator, $\widehat{M}$ can be written as:[92]

$$\widehat{\boldsymbol{M}} = -\frac{\mu_B}{\hbar}\sum_i \left(\hat{\boldsymbol{l}}_i + 2\hat{\boldsymbol{s}}_i\right),$$

The magnetic dipole oscillator strength $M1$ is therefore

$$M1_{f\leftarrow i} = \frac{2m_e\left(E_f - E_i\right)}{3\hbar^2 e^2 c^2}\frac{n_r}{2J+1}\left|\langle f\left|\widehat{\boldsymbol{M}}\right|i\rangle\right|^2,$$

or

$$M1_{f\leftarrow i} = \frac{2m_e\left(E_f - E_i\right)}{3\hbar^2 e^2 c^2}\frac{n_r}{2J+1}\left|\langle f\left|\widehat{M}_x\boldsymbol{i} + \widehat{M}_y\boldsymbol{j} + \widehat{M}_z\boldsymbol{k}\right|i\rangle\right|^2,$$

Where

$$\widehat{M}_z = -\frac{\mu_B}{\hbar}\sum_i \left(\hat{l}_{zi} + 2\hat{s}_{zi}\right),$$

$$\widehat{M}_x = -\frac{\mu_B}{2\hbar}\sum_i \left(\hat{l}_+ + \hat{l}_- + 2\hat{S}_+ + 2\hat{S}_-\right)_i,$$

$$\widehat{M}_y = -\frac{\mu_B}{2i\hbar}\sum_i \left(\hat{l}_+ - \hat{l}_- + 2\hat{S}_+ - 2\hat{S}_-\right)_i.$$

From this model, considering only the $M1$ transition is not enough to reproduce the experimental oscillator strength, therefore, a mixing of orbitals with different angular momenta is needed to allow $E1$ (the electric dipole) transition, and $E1$ should be the principal contributor to the transition strength. The Judd-Ofelt perturbation theory has been used previously to explain the enhancement of $E1$ oscillator strengths in lanthanide systems by invoking mixing with the virtual $5d$ orbitals via artificially lowering the $5d$ energy to enhance the electronic $4f/5d$ interaction.[16,39] However, this approach does not fully account for how the transition energies and oscillator strengths are altered by the ligand field, and the single electron-hole picture does not provide enough fitting parameters to use the Judd-Ofelt theory for the Yb^{3+} ion.

Table 2.3 Calculated Transition Energies and Oscillator Strengths

Optical absorption transition energies with corresponding M1 oscillator strengths calculated from an atomic model.

Initial State	Final State	Transition Energy (eV)	Oscillator Strength
1	9	1.2647	1.4E-10
	10		2.7E-08
	11	1.3455	1.5E-10
	12		3.6E-09
	13	1.3834	2.3E-10
	14		2.3E-10
2	9	1.2647	2.5E-08
	10		6.0E-11
	11	1.3455	3.6E-09
	12		1.4E-10
	13	1.3834	6.0E-11
	14		3.2E-10

Electronic Structure Calculations

The ground state of (thiolfan)YbCl(THF) (Figure 2.5a) was optimized in Turbomole,[93] using the TPSSh functional,[94,95] the ANO-RCC basis set[96,97] (ANO-RCC-VTZP for Yb, ANO-RCC-VDZP for Fe, ANO-RCC-VTZ for Cl, O, S, and ANO-RCC-VDZ for C and H), and the D3 dispersion correction.[98] The effect of solvation on geometry optimizations was included by employing the conductor-like screening model (COSMO)[99] with a dielectric constant of $\varepsilon = 7.58$ to model THF. From this optimized geometry, a reduced model was used for multireference calculations below. In the truncated model, the ferrocene unit was removed, and the sulfur atoms were capped with hydrogens, after which the reduced structure was reoptimized.

As implemented in the Openmolcas,[100] the multireference CASSCF/MS-CASPT2 methods [101–105] were used in combination with the same ANO-RCC basis set. The second-order Douglas−Kroll−Hess (DKH2) one-electron spin-less Hamiltonian was applied for all wave function theory calculations to allow for spin-free relativistic effects.[106–108] A complete active space used in the CASSCF calculations comprised 13 electrons in 12 orbitals (7 x Yb 4f-like orbitals and 5 x Yb 5d-like orbitals, Tables 2.4 and 2.5). All orbitals were generated with Visual Molecular Dynamics with an isosurface 0.01.[109] The state-averaged (SA-)CASSCF formalism was used, including 20 lowest-lying states. The dynamic MS-CASPT2 correlation was then included via the CASPT2 module. Spin-orbit coupling was added through the RASSI-SOC module,[110,111] where oscillator strengths and transition energies were calculated for electric and magnetic dipole transitions.

Finally, g tensors and spin-orbit coupling matrix elements were computed with the EPRG (RASSI module for EPR g-factor calculations) and SOC functions in the RASSI-SOC module after applying spin-orbit effects on the basis of the Kramers doublet.[112] Length dipole oscillator

strengths were reported in the main text, the length and velocity dipole results are listed in Table 2.6. Most dominant orbitals involved in the electronic transition from CASSCF and RASSI-SOC calculations are shown in Table 2.7. SOC matrix elements between RASSI-SOC states are listed in Tables 2.8 and 2.9. We see the CAS(12,13) active space produces different spin-orbit couplings between RASSI-SOC states than CAS(7,13). In Table 2.8, we probed how orbital composition affected these SOC matrix elements. SA-7-CASCI takes the orbitals from the CAS(12,13) active space, and does not reoptimize them, computing SOC matrix elements for the first 7 RASSI-SOC states, corresponding to the f-f transitions. SA-7-CASSCF takes the orbitals from the CAS(12,13) active space and reoptimizes them based on the first seven transitions. Since these transitions are dominated by f-f transitions, the orbitals become more f-like in character, i.e., less mixing with 5d. We see the SA-7-CASSCF SOC matrix elements look more like the CAS(7,13) matrix elements in Table 2.8, while SA-7-CASCI look like the CAS(12,13) matrix elements. This underscores the importance of 4f/5d orbital mixing's effect on spin orbit coupling, which in turn mediates oscillator strength. Recent findings suggest that f-orbitals are quite sensitive to SOC and these orbitals should be optimized with SOC-included.[113] One way to include this effect is through an exact two-component transformation (X2C) but the quantitative importance of including SOC via X2C vs. other methods requires further study.[114]

Several limitations of our theoretical calculations should be mentioned. Due to the large system size and number of electrons, the active space used in the CASSCF calculations is still fairly limited, prohibiting us from including all the ligand-metal bonding orbitals. We thus cannot accurately capture the covalency of metal-ligand bonds and how much the pure 4*f* states are influenced by the ligand. Additionally, spin-orbit coupling is added for calculating transitions and oscillator strengths, but (thiolfan)YbCl(THF) orbitals are not optimized to include spin-orbit

coupling. This could allow for an increased 4*f*/5*d* mixing in our complete active space orbitals that we currently do not observe (Figure 2.4b), and could also alter the symmetry of the 4*f* orbitals involved in transitions **II-V**. Furthermore, the multireference calculations are performed in the gas phase and as a static approximation. Dynamic calculations of the molecular vibrational structure and solvent contributions and fluctuations will help aid additional understanding of the nature of the target transition **IV**, such as its linewidth.

Table 2.4 CAS 7 4f Orbitals Involved in the CASSCF Calculation

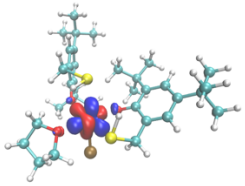

Orbital 1

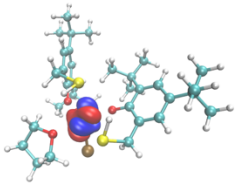

Orbital 2

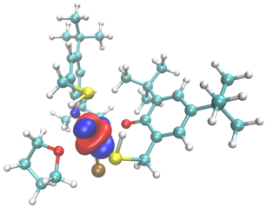

Orbital 3

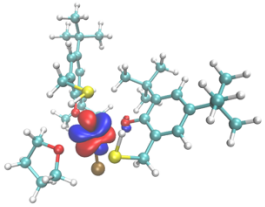

Orbital 4

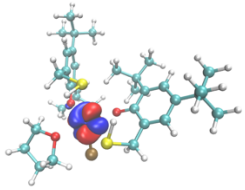

Orbital 5

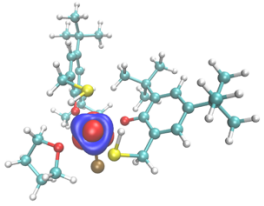

Orbital 6

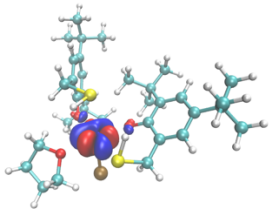

Orbital 7

Table 2.5 CAS 12 Orbitals Involved in the CASSCF Calculations

These orbitals are made up of the 7 4f orbitals and a mixture of virtual 5d/6d orbitals.

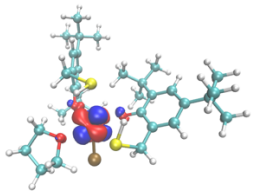

Orbital 1

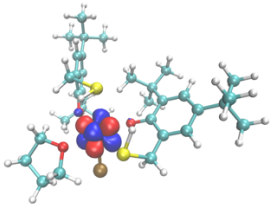

Orbital 2

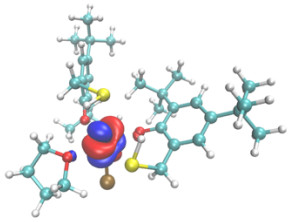

Orbital 3

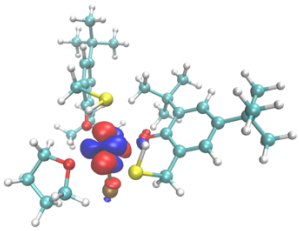

Orbital 4

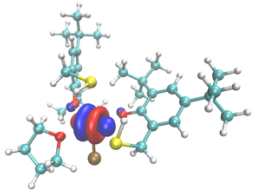

Orbital 5

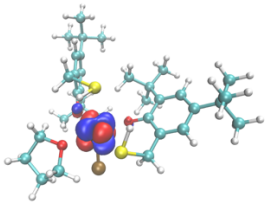

Orbital 6

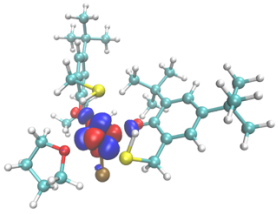

Orbital 7

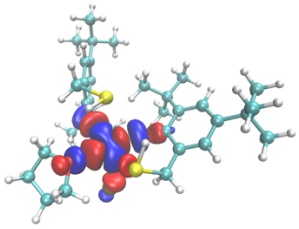

Orbital 8

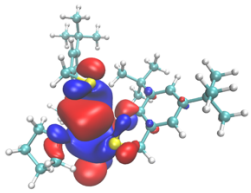

Orbital 9

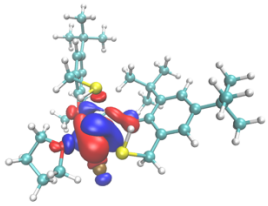

Orbital 10

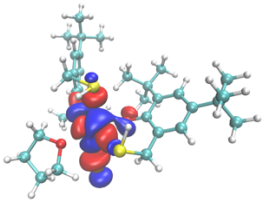

Orbital 11

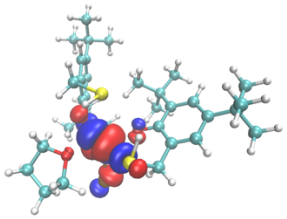

Orbital 12

Table 2.6 Transition Energies and Electric Velocity Dipole Oscillator *S*trengths

Values computed with the RASSI-SOC module between CAS(13,7) and CAS(13,12) active spaces. Length dipole and velocity dipole oscillator strengths are tabulated.

Initial State	Final State	Transition Number	Transition Energy (eV)	Length Dipole Oscillator Strength	Velocity Dipole Oscillator Strength
only 4f orbitals in active space					
1	9	IV	1.288	2.05E-07	2.33E-07
	10	IV		3.5E-08	2.36E-06
	11	III	1.338	1.31E-07	3.60E-06
	12	III		1.37E-07	1.95E-06
	13	II	1.373	1.81E-07	1.15E-06
	14	II		2.60E-07	3.99E-06
2	9	IV	1.288	3.5E-08	2.36E-06
	10	IV		2.05E-07	2.33E-07
	11	III	1.338	1.37E-07	1.95E-06
	12	III		1.31E-07	3.6E-06
	13	II	1.373	2.60E-07	3.99E-06
	14	II		1.81E-07	1.15E-06
3	9	V	1.238	1.95E-08	2.30E-06
	10	V		1.10E-07	2.49E-06
4	9	V	1.238	1.10E-07	2.49E-06
	10	V		1.95E-08	2.30E-06
4f + 5d orbitals in active space					
1	9	IV	1.286	5.17E-07	3.29E-05
	10	IV		7.35E-07	1.76E-05
	11	III	1.364	6.13E-07	1.445E-04
	12	III		3.25E-07	5.84E-05
	13	II	1.413	4.76E-07	9.07E-05
	14	II		4.07E-07	1.20E-04
2	9	IV	1.286	7.35E-07	1.76E-05
	10	IV		5.17E-07	3.29E-05
	11	III	1.364	3.25E-07	5.84E-05
	12	III		6.13E-07	1.45E-04
	13	II	1.413	4.07E-07	1.20E-04
	14	II		4.76E-07	9.07E-05
3	9	V	1.218	4.81E-07	8.26E-05
	10	V		6.79E-08	1.25E-05
4	9	V	1.218	6.79E-08	1.25E-05
	10	V		4.81E-07	8.26E-05

Table 2.7 Atomic Orbital Contributions for Most Dominant Orbitals

Most dominant orbitals involved in the electronic transition from CASSCF and RASSI-SOC calculations. Orbital numbers are from orbitals listed in Tables 4.3, 4.4, respectively.

State	Orbital # (Weight)	AO %
	only 4f orbitals in active space, Table 4.3	
1,2	7 (0.291)	7: 99.9% 4f
	1 (0.592)	1: 99.85% 4f
9,10	2 (0.263)	2: 99.3% 4f
	5 (0.600)	5: 99.6% 4f
	4f + 5d orbitals in active space, Table 4.4	
1,2	2 (0.432)	2: 99.4% 4f
	5 (0.323)	5: 99.6% 4f
9,10	6 (0.434)	6: 99.9% 4f

Table 2.8 Spin-orbit Coupling Matrix Elements

These elements correspond to the transitions between different RASSI-SOC states for CAS(13,7) and CAS(13,12) active spaces.

Bra State	Ket State	Transition Number	SOC Matrix Element
only 4f orbitals in active space			
9	1	IV	455.20
	2	IV	375.17
	3	V	740.96
	4	V	121.04
10	1	IV	375.17
	2	IV	455.20
	3	V	121.04
	4	V	740.96
11	1	III	102.91
	2	III	161.75
12	1	III	161.75
	2	III	102.91
13	1	II	205.49
	2	II	462.18
14	1	II	462.18
	2	II	205.49
4f + 5d orbitals in active space			
9	1	IV	82.37
	2	IV	439.82
	3	V	715.64
	4	V	128.45
10	1	IV	439.82
	2	IV	82.37
	3	V	128.45
	4	V	715.64
11	1	III	404.37
	2	III	451.46
12	1	III	451.46
	2	III	404.37
13	1	II	121.41
	2	II	520.11
14	1	II	520.11
	2	II	121.41

Table 2.9 Spin-orbit coupling matrix elements

These values correspond to transitions between different RASSI-SOC states for SA-7-CASCI vs. SA-7-CASSCF using CAS(13,12) active spaces.

Bra State	Ket State	Transition Number	SOC Matrix Element
		SA-7-CASSCF	
9	1	IV	477.31
	2	IV	294.13
	3	V	627.16
	4	V	168.35
10	1	IV	294.13
	2	IV	477.31
	3	V	168.35
	4	V	627.16
11	1	III	218.96
	2	III	192.36
12	1	III	192.36
	2	III	218.96
13	1	II	5.67
	2	II	515.29
14	1	II	515.29
	2	II	5.67
		SA-7-CASCI	
9	1	IV	82.37
	2	IV	439.82
	3	V	715.64
	4	V	128.45
10	1	IV	439.82
	2	IV	82.37
	3	V	128.45
	4	V	715.64
11	1	III	404.37
	2	III	451.46
12	1	III	451.46
	2	III	404.37
13	1	II	121.41
	2	II	520.11
14	1	II	520.11
	2	II	121.41

Theoretical and Experimental Spectra of All Compounds

According to the methods detailed above, the ground state geometries, transition energies, and oscillator strengths were computed for **1-3**. The theoretical results are plotted against absorption (for all compounds) and emission (for **1**) measurements at room temperature for sample concentrations around 3 mM. For all compounds, the theoretical transition energies and oscillator strengths align to the relative intensities observed experimentally.

The Einstein A_{21} coefficients can be extracted from the calculated oscillator strengths of **1-3** ($2.5 \times 10^{-6}, 3.0 \times 10^{-6}, 1.3 \times 10^{-6}$, respectively), which correspond to 244, 295, and 125 Hz.[79] The corresponding expected excited state decay rates translate to lifetimes of 4.1, 3.4, and 5 ms. Therefore, the observed absorption linewidths for all three compounds are not limited by the excited state lifetime.

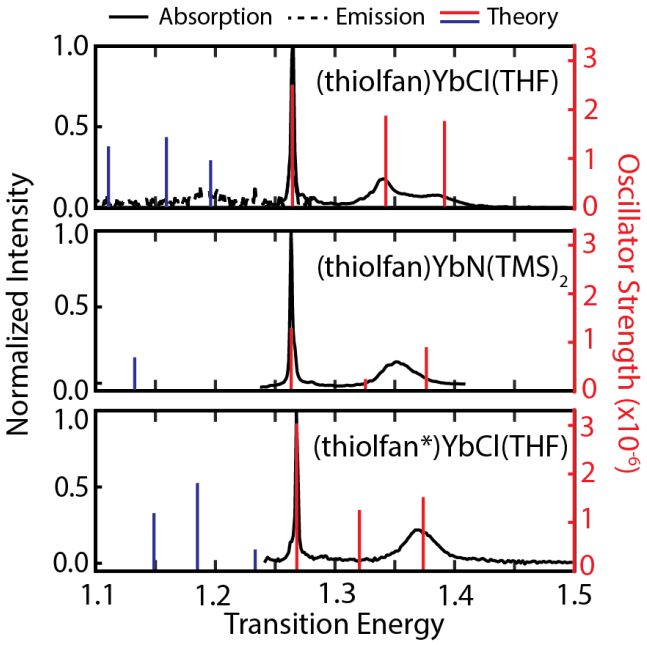

Figure 2.43 Theoretical and experimental spectra comparison.

The absorption and emission spectra were normalized to the intensity of transition **IV**. The theoretical transition energies were shifted by 21.5 meV, 22.3 meV, and 17.0 meV for (thiolfan)YbCl(THF), (thiolfan)YbN(TMS)$_2$, and (thiolfan*)YbCl(THF) to maximize overlap with experimental spectra, which are all within theoretical uncertainty.

Measured vs. Calculated g Factors

Continuous-Wave (CW) EPR spectra of (thiolfan)YbCl were first measured in 2-MeTHF as a frozen glass, which exhibit very prominent, narrow positive features centered around a peak at $g_x = 7.486 \pm 0.008$ (Figures 4.19-4.20). It should be noted that CW-EPR uses modulation of the static magnetic field (B_1) by a small oscillating magnetic field (B_{mod}, typically ±0.1 to 2 mT in magnitude) to detect the first derivative of the EPR absorption spectrum. As such, if all molecular orientations exhibit resonance within the magnetic fields accessible by the instrumentation (1-1000 mT, in this case) the entire EPR spectrum should have approximately equal intensity above and below the baseline. The fact that the most prominent features have purely positive intensity, and that there are no resolved negative features or features which cross

the baseline with similar linewidths implies that such resonances are outside of the accessible magnetic field range of our instrumentation or are inhomogenously broadened beyond detection due to the limitations of field modulation.

In order to further evaluate these questions, we turned to pulse EPR spectroscopy – specifically, field swept electron spin echo (ESE) EPR spectroscopy. In contrast to CW-EPR spectroscopy, pulse EPR spectroscopy enables more direct measurement of the EPR absorption spectrum without the use of field modulation, enabling the measurement of features with extremely broad linewidths in comparison to CW-EPR. Indeed, the X-Band ESE-EPR spectrum of (thiolfan)YbCl (Figure 4.21) exhibits extremely broad linewidths (lw_{pp} ~ 120-400 mT), with intensity starting near 140 mT ($g = 4.78$) and continuing up to the high-field limit of our electromagnet at 1478.5 mT ($g = 0.45$). This indicates that the majority of molecular orientations exhibit significant inhomogenous broadening in the field ranges accessible, and that there is significant spectral intensity above the field ranges accessible by our instrumentation. The latter point is in line with calculations of the full ground state g-matrix, which indicates two principal components may fall below $g = 0.45$ (Table 4.9), or at least a significant portion of molecular orientations exhibit resonant fields below this g-value. Spin relaxation measurements via pulse EPR were performed (inversion recovery for T_1 and Hahn Echo decay for T_m) at 320 and 1200 mT (Figure 4.22) in order to evaluate whether spin relaxation could be responsible for the aforementioned extremely broad linewidths of the CW- and pulse EPR spectra. In general, at temperatures where the spin-lattice relaxation time (T_1) is much longer than the phase memory time (T_m), EPR spectra typically exhibit Lorentzian lineshapes with approximate homogenous peak-peak linewidths proportional to $\frac{2}{\sqrt{3}T_m}$. The shortest T_m value we measure is 0.82 μs at 320 mT, which would correspond to a linewidth of approximately 2 mT – this is in reasonable

agreement with the peak-peak linewidth of the sharp transitions resolved at g = 7.486 in the CW-EPR spectrum (lw_{pp} = 1.6 mT), which correspond to a very small subset of molecular orientations around g_x, but it is two orders of magnitude smaller than the observed linewidths at higher fields in the field-swept pulse EPR spectrum. Therefore, the extremely broad linewidths must be due to inhomogeneous broadening, which most likely arises from heterogeneity in g-values of the spin system due to slight variations in spin orbit coupling contributions.

Attempts were also made to better resolve other possible features in the spectrum by preparing solid samples of paramagnetically diluted Yb(III) complexes by reacting the deprotonated thiolfan ligand with $YbCl_3THF_3$ and YCl_3THF_3 in 10:90, 5:95 and 1:99 percentage ratios following the procedure shown in Section 2.8. The exact concentrations of Yb and Y in the diluted samples were confirmed by inductively coupled plasma (ICP) measurements. EPR measurements on the diluted powder samples were obtained in solid form by packing the solid samples into a quartz capillary tube and inserting into a regular EPR tube. The 10%Yb sample was diluted to 1%Yb by mixing the 10%Yb sample with boron nitride, which appeared to have introduced some organic radical impurity at $g = 2.003$. This serial dilution provides magnetic dilution to investigate whether the features observed in the solution spectra are reproducible, as confirmed by the constant feature that remains at $g_x = 7.486 \pm 0.008$. It should be noted that the g factors derived from EPR spectroscopy and MCD are determined by using $E = g\mu_B B$, where ΔE is the Zeeman energy extracted from the absorption spectra. Using the measured ground state g factor of 7.486, we were then able to estimate the excited state g factor as 3.2 ± 0.2, as shown in Table 4.9.

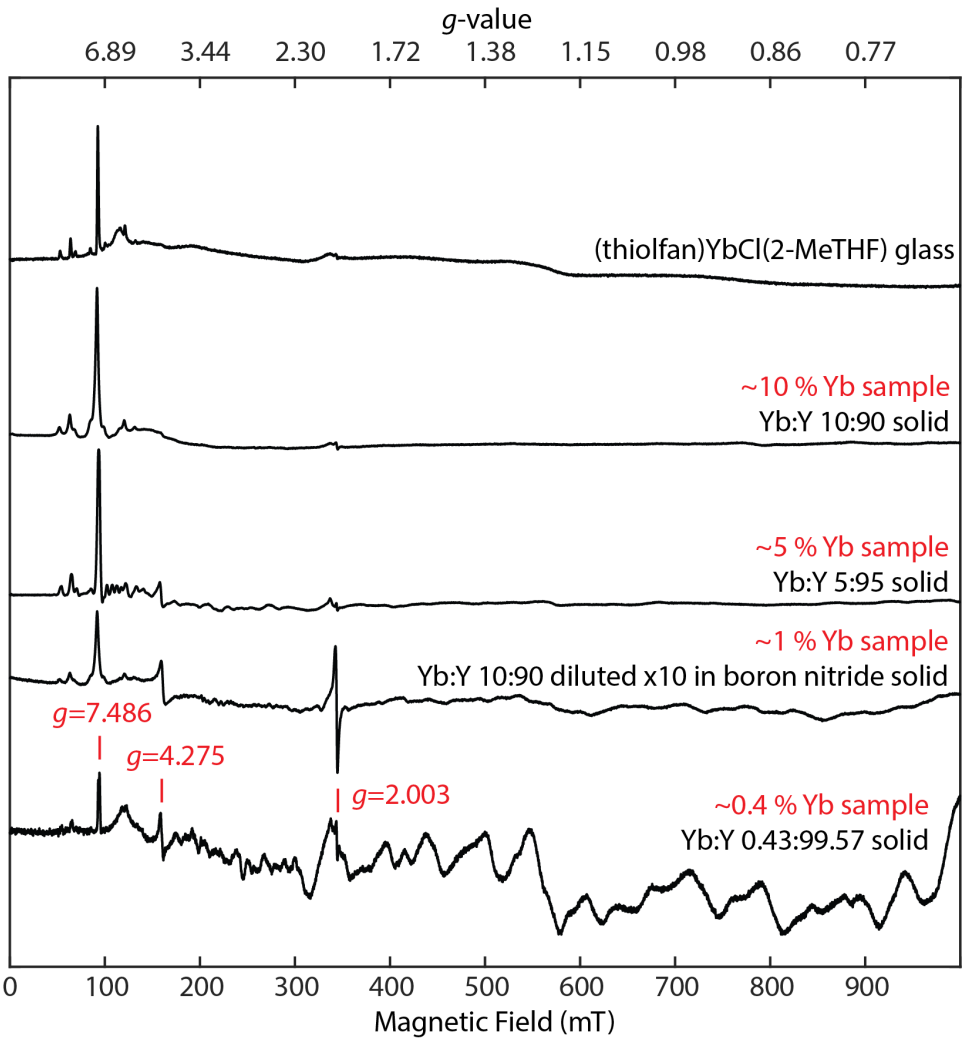

Figure 2.44 X-band CW-EPR spectra of (thiolfan)YbCl(THF)

These spectra were taken in frozen 2-MeTHF glass, Yb:Y 10:90 solid sample, Yb:Y 5:95 solid sample, Yb:Y 10:90 solid sample diluted in boron nitride to obtain 1%Yb sample, and Yb:Y 0.43:99.57 solid sample to resolve EPR peaks. Acquisition parameters: temperature = 5 K; microwave frequency = 9.638 GHz; MW power = 8.8 mW; modulation amplitude = 0.8 mT; conversion time = 10 ms.

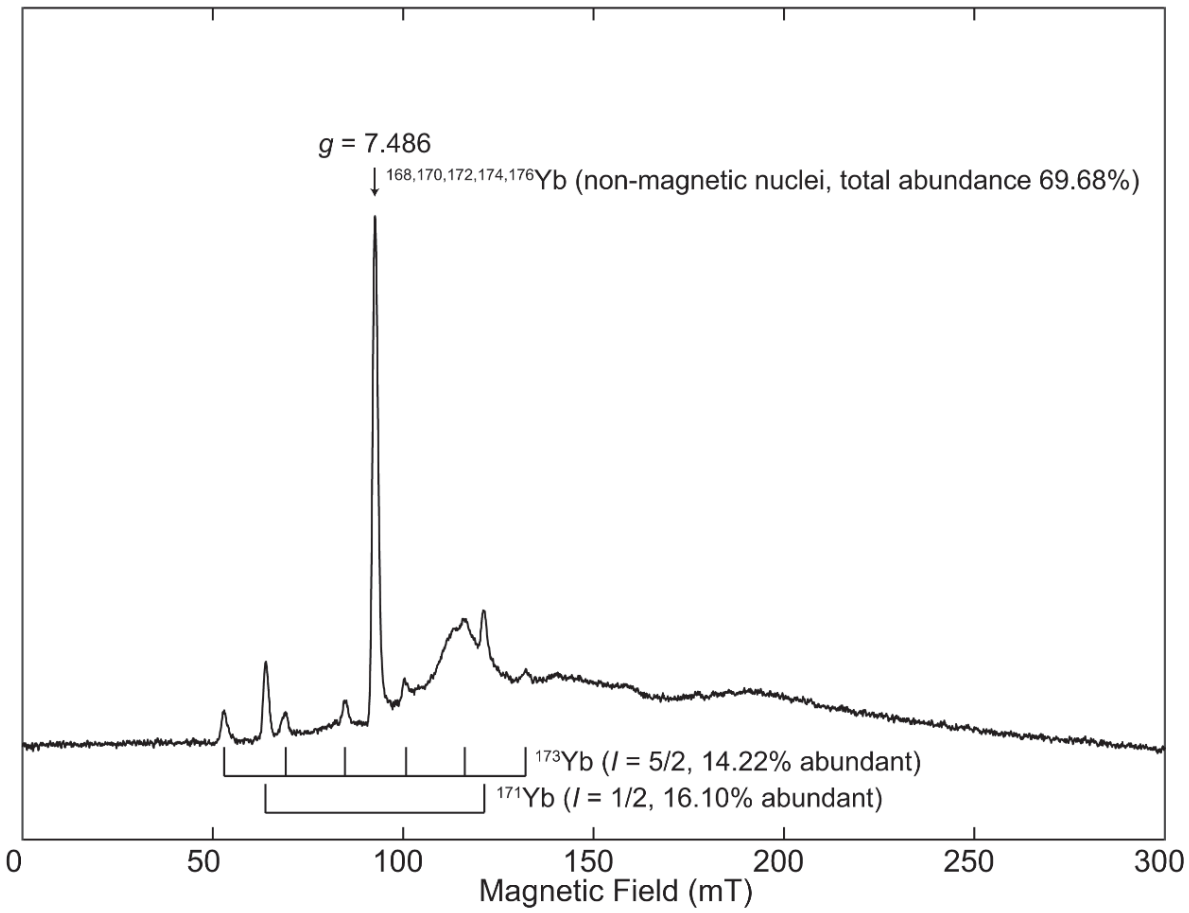

Figure 2.45 X-band CW-EPR spectrum of (thiolfan)YbCl(THF)

This spectrum was taken in frozen 2-MeTHF glass in the region from 0-300 mT, with resolved features arising from hyperfine couplings to magnetic ^{171}Yb and ^{173}Yb nuclei indicated below. Acquisition parameters: temperature = 5 K; microwave frequency = 9.638 GHz; MW power = 8.8 mW; modulation amplitude = 0.8 mT; conversion time = 10 ms.

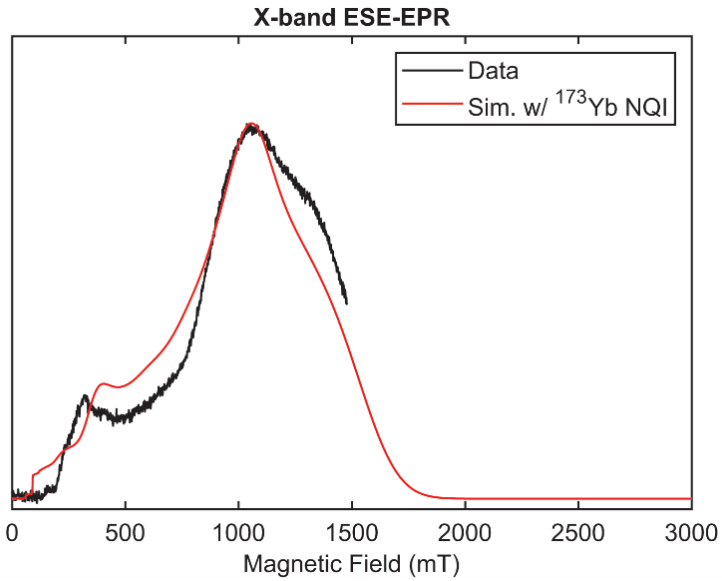

Figure 2.46 X-band ESE-EPR absorption spectrum of (thiolfan)YbCl(THF)

This spectrum was taken frozen 2-MeTHF glass (black trace) with spectral simulation using the following parameters: g = [7.41, 0.62, 0.42], $A(^{173}\text{Yb})$ = [1553, 160, 160] MHz, $A(^{171}\text{Yb})$ = [5915, 609, 609] MHz (A magnitudes scale with respective ^{173}Yb, ^{171}Yb gyromagnetic ratios) Q = [-105, -60, 165]. Acquisition parameters: temperature = 5.6 K; microwave frequency = 9.373 GHz; τ = 300 ns; $\pi/2$, π pulse lengths = 40, 80 ns; shot repetition time (srt) = 500 μs.

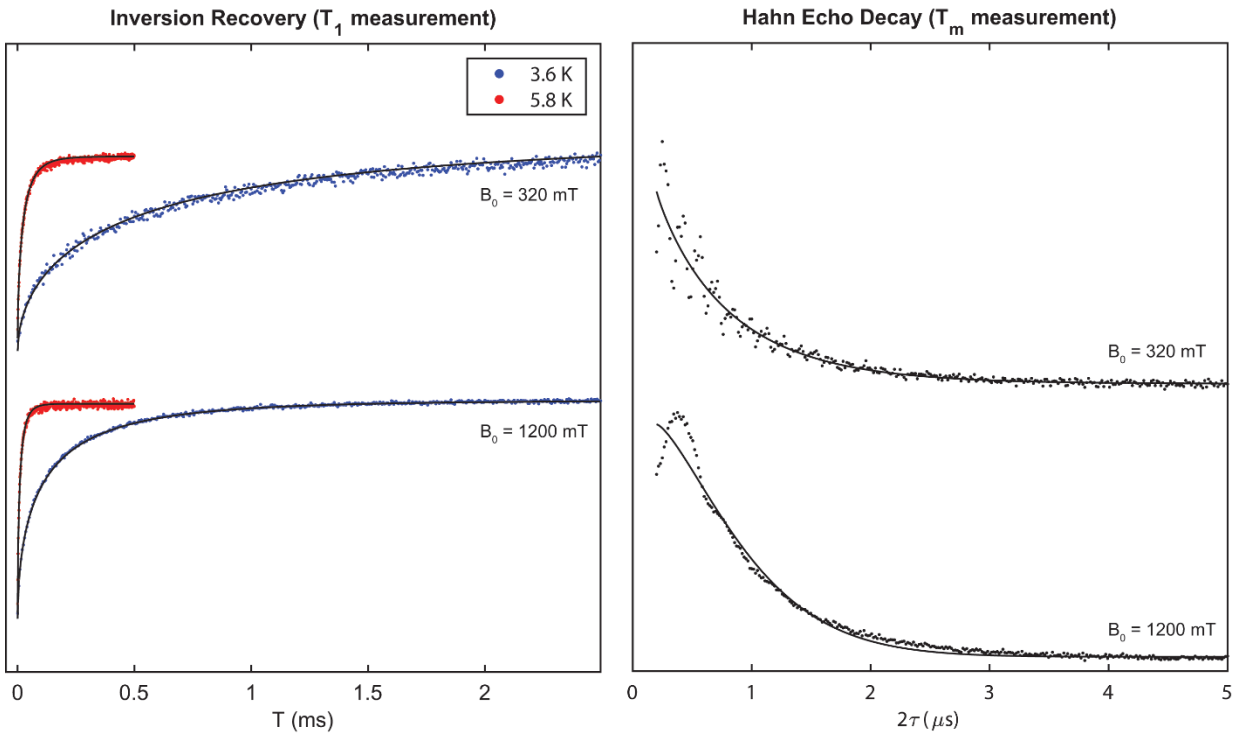

Figure 2.47 T_1 and T_2 Measurements of (thiolfan)YbCl(THF)

Left panel: X-band inversion recovery traces of (thiolfan)YbCl(2-MeTHF) in frozen 2-MeTHF glass at 3.6 (blue) and 5.8 K (red), at fields of 320 mT and 1200 mT. At 3.6 K, T_1 is 518 µs (320 mT, δ = 0.55) and 116 µs (1200 mT, δ = 0.56), and at 5.8 K, T_1 is 23.5 µs (320 mT, δ = 0.69) and 10.4 µs (1200 mT, δ = 0.69). Right panel: X-band Hahn Echo decay traces of (thiolfan)YbCl(2-MeTHF) in frozen 2-MeTHF glass at 3.6 K, at fields of 320 mT and 1200 mT. T_m is 0.82 µs (320 mT, δ = 0.92) and 1.09 µs (1200 mT, δ = 1.4). T_1 and T_m decay constants were extracted through fits of data with a stretched exponential decay function of the form $I = -A(e^{-\left(\frac{T}{T_1}\right)^{\sigma}} - I_0 - 1)$ and $I = -A(e^{-\left(\frac{2\tau}{T_m}\right)^{\sigma}} - I_0)$, respectively, where σ is a stretch function.

Table 2.10 Comparison of Measured and Calculated g Factors

Below are the g factors for the ground and excited states of transition IV in (thiolfan)YbCl(THF), both lower than the theoretical gas phase limits. The g factor calculations were done using the EPRG (RASSI module for EPR g-factor calculations).

	$\lvert m_j \rvert = 7/2$	$\lvert m_j \rvert = 5/2$
Measured from EPR	7.486 ± 0.008	-
Derived from EPR and MCD	-	3.2 ± 0.2
Calculated	$g_x = 7.49$	$g_x = 4.27$
	$g_y = 0.34$	$g_y = 0.17$
	$g_z = 0.38$	$g_z = 0.15$
Landé g factor for Yb^{3+}	8	4.28

Linear Trend Between Static Magnetic Field Strength and Zeeman Splitting

The ground and excited states of (thiolfan)YbCl(THF) are split into two distinct states under an external magnetic field, corresponding to whether the magnetic moment is parallel or antiparallel to the B field. This induced Zeeman splitting is given by $\Delta E = 2g\mu_B B$, where h is the Plank's constant, g is the Landé g-factor and μ_B is the Bohr magneton. The expected linear relationship is confirmed and demonstrated below in Figure 4.25.

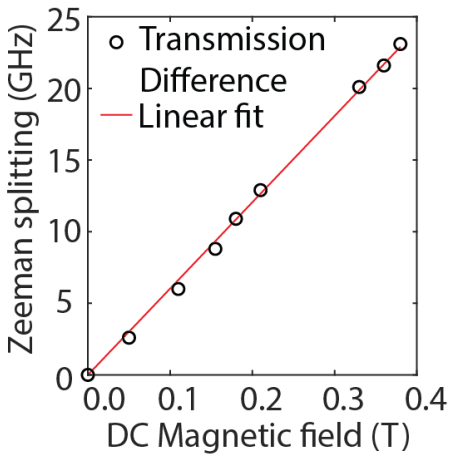

Figure 2.48 Linear Relationship between Zeeman Splitting and External Field
Expected linear relationship between Zeeman splitting and magnetic field strength.

Imaging Setup

We use a home-made external cavity diode laser (ECDL) for imaging (Figure 2.49). The laser is set at the half max of the absorption peak of the sample. We use two lenses to expend the laser beam size to cover the whole cuvette. A permanent magnet is mounted onto a rotating motor beneath the sample. We image the sample with a webcam. Under circularly polarized light, the sample's absorption depends on the strength of the magnetic field, so as we rotate the magnet, the image will blink.

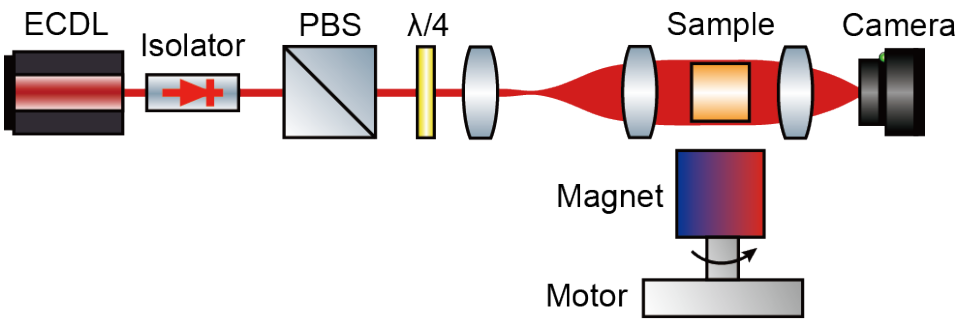

Figure 2.49 Optical setup of the MCD imaging.

The video showing the change in intensity of the transmission image can be found in the extra SI material of the published manuscript.

Direct Measurement of DC Field with Oscillating Polarization

An M Squared SolsTis Ti:Sapph laser with a Lighthouse Sproud pump laser system was used to generate 304 THz to 307 THz light. The laser power needed in this measurement is under 30 mW. The beam is split into two paths, each going through an acousto-optic modulator (AOM; Gooch & Housego 2308-1-1.06 and Isomet SR48607) set at f and f + Δf, and brought together at another polarizing beam splitter (PBS). The resulting beam is oscillating between right- and left-hand circular polarizations at Δf = 100 kHz. The amplitude of the transmitted light was collected with Thorlabs PDA8A. The setup is shown in Figure 2.50.

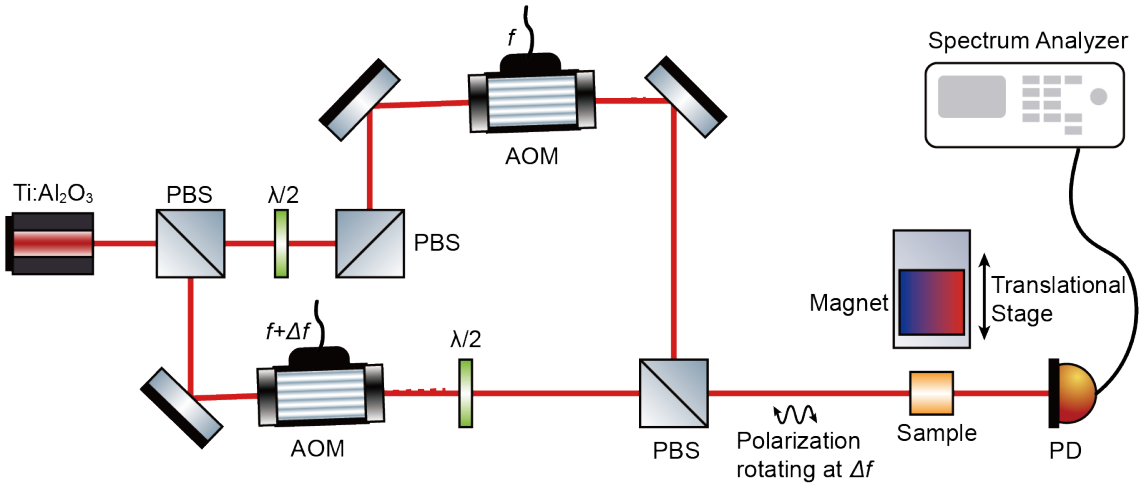

Figure 2.50 Optical Setup for DC Magnetometry

Optical setup for the direct measurement of the magnetic strength of a DC magnet using the MCD shift of the (thiolfan)YbCl(THF) sample.

Direct Measurement of AC Field

The measurement of an AC field was achieved by taking the setup above and adding a Helmholtz coil around the sample holder. This gives rise to two more sidebands at frequency $\Delta f \pm f_{AC}$, and their amplitude is tracked by a spectrum analyzer (Agilent Technologies N9010A). The optical setup is shown in Figure 2.51, and the collected data is shown in Figure 2.52, which shows the change in signal as the magnitude of the AC field is brought down to 0.8 G (the values reported in the manuscript accounted for background noise of the gaussmeter, which is slightly lower than what is shown here). The AC magnetic field was generated by taking the output of an arbitrary waveform generator (Agilent 33220A) to run an oscillating current onto the coil. The field was then measured by a gaussmeter (Lakeshore 410) to confirm its magnitude as well as mathematically confirmed by checking the AC current magnitude.

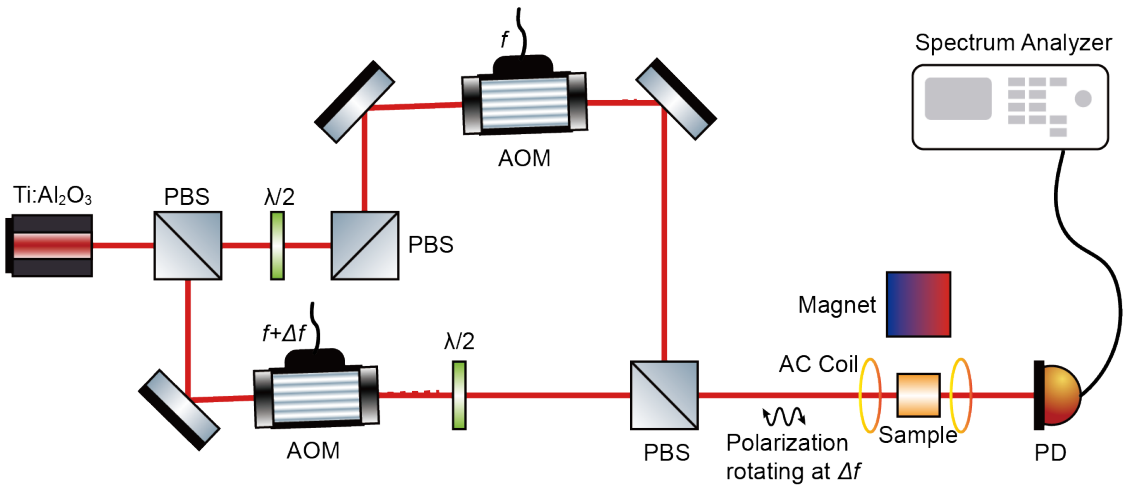

Figure 2.51 Optical Setup for AC Magnetometry

Optical set up of the direct measurement of the magnetic strength of an AC magnet using the MCD shift of the (thiolfan)YbCl(THF) sample.

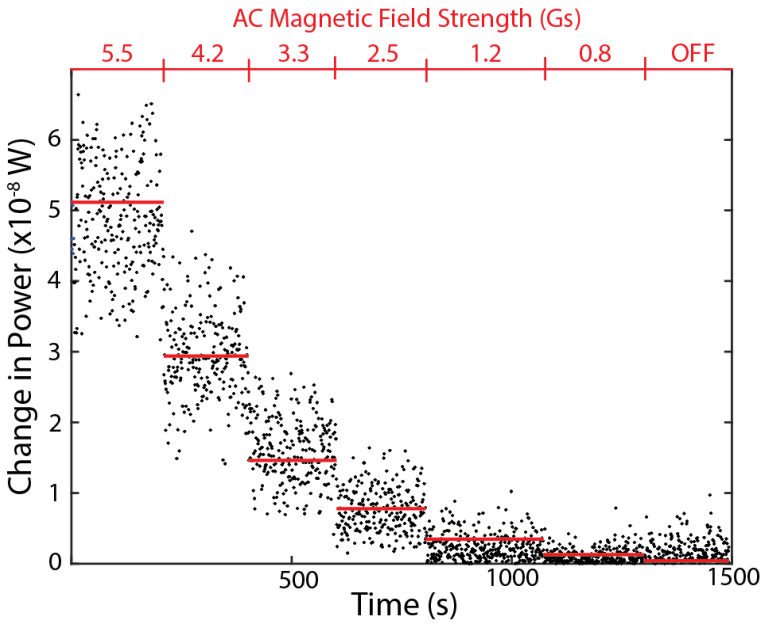

Figure 2.52 Raw Data Collected by Frequency Analyzer with Varying AC Field

Raw data collected by a frequency analyzer as the magnitude of the AC field is changed.

A frequency analyzer was used to track the transmission intensity at the sideband frequency ($\Delta f + f_{AC}$) composed of the frequency at which the polarization of the light is oscillating ($\Delta f = 100\ kHz$) and the frequency of the AC field generated by helmholtz coils ($f_{AC} = 1\ kHz$). The dBm reading was converted to change in power ($dBm = 10 \log P/1\ mW$, where P is the measured power), and the power value was then converted to volts by accounting for the equipment resistance ($P = V^2/R$, where $R = 50\ \Omega$). Voltage noise has units of $V\ Hz^{-1/2}$, which was converted to magnetic noise in units of $T\ Hz^{-1/2}$ by measuring the relationship between our voltage reading and the gaussmeter reading that we conducted separately (Figure 2.53). Using this linear fit, the voltage noise was converted to magnetic noise, which translates to an average sensitivity of 3.3 $\mu T\ Hz^{-1/2}$.

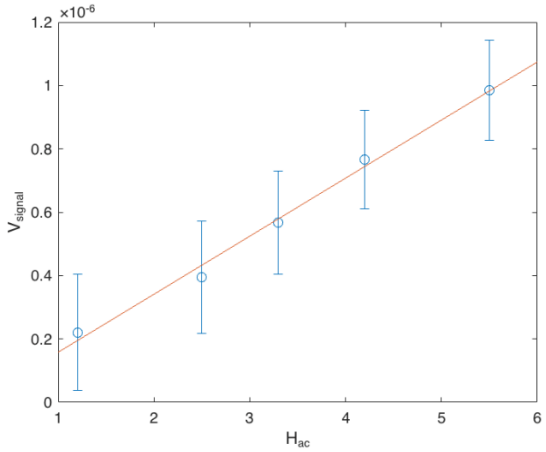

Figure 2.53 Voltage reading corresponding to AC noise.

Voltage reading from the photodetector used for measuring transmission as a function of the AC field strength applied.

Sensor-Sample Distance Estimation

In AVCs, the standoff distance is defined as the distance between the sample and the geometric center of the sensor volume. The spatial resolution is limited by the distance scales set by the diameter of the sensor volume. AVCs face a few practical challenges when it comes to miniaturization. Increasing density (through pressure) requires thicker glass and higher standoff distances, which increases sensor-sample distance. Thus, ALMS is an advantageous alternative to AVCs in that the concentration can be increased drastically without broadening the spectral linewidth as we show in Figure 2.54. Theoretically, ALMS will have a more advantageous tradeoff between density and sensor-sample distance with further device engineering. We demonstrate possible device architectures that will bring ALMS magnetometers to shorter sensor to sample distances than those of AVCs in Figure 2.55.

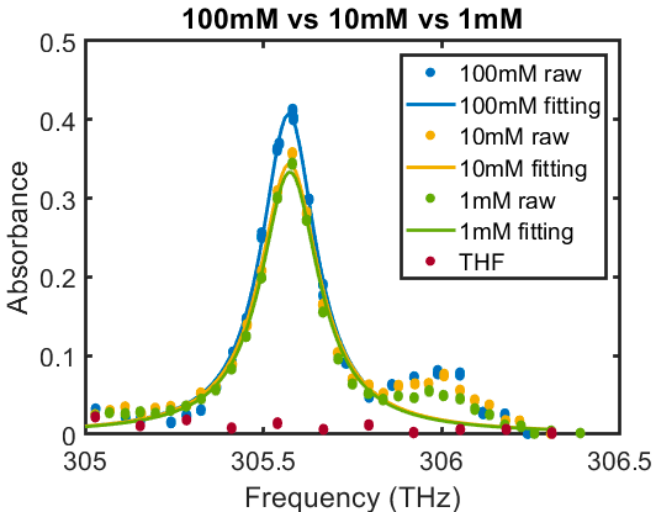

Figure 2.54 Concentration Dependence of Absorption

Absorption spectrum of transition IV of (thiolfan)YbCl(THF) in THF solution with 1 mM, 10 mM, and 100 mM concentrations, demonstrating consistent linewidth.

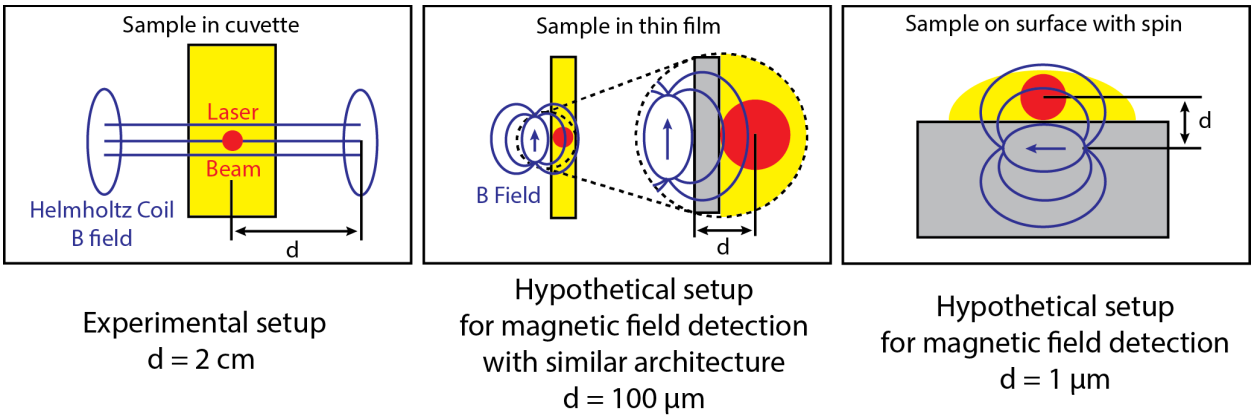

Figure 2.55 Diagrams of realized and proposed device architectures.
Left: actual experimental setup used for AC magnetometry reported in this manuscript. Center: proposed device architecture for a thin film/cuvette format. Right: proposed device architecture for direct casting of ALMS onto surface.

MCD Signal Analysis

The absorption of the ground electronic transition localized at Yb^{3+} for (thiolfan)YbCl(THF) can be expressed as a Lorentzian.

$$\alpha(x, x_0) = \frac{a}{\pi} \frac{\frac{1}{2}\Gamma}{(x - x_0)^2 + \left(\frac{1}{2}\Gamma\right)^2} + c$$

In this equation, a is a scaling factor, Γ is the full-width at half-maximum, x_0 is the center frequency, and c is a constant offset to account for background. For room temperature absorption, the fit values are:

$$a = 8.8498 \times 10^{-4} \text{ eV}$$

$$\Gamma = 0.00064516 \text{ eV} = 0.65\ meV$$

$$x_0 = 1.2637 \text{ eV}$$

The MCD signal is a subtraction between the absorption of the sample with σ^+ and σ^- light, which only differ in their center frequency by $\Delta x = g_{eff}\mu_B B$. Thus, the MCD absorption signal can be expressed as:

$$\mathrm{M}(x, B) = \alpha(x, x_0 + \Delta x) - \alpha(x, x_0 - \Delta x)$$

Where $\alpha(x, x_0 \pm \Delta x)$ indicates the sample absorption with $\sigma^{+/-}$ light.

$$\alpha(x, x_0 \pm \Delta x) = \frac{a}{\pi} \frac{\frac{1}{2}\Gamma}{\left(x - \left(x_0 \pm g_{eff}\mu_B B\right)\right)^2 + \left(\frac{1}{2}\Gamma\right)^2} + c$$

The larger the B-field applied, the further the σ^+ and σ^- absorption peak is split, the larger the MCD signal is. We can backtrack the strength of B field from the measured MCD signal if we know the factor g_{eff}.

For small static magnetic field, we perform a Taylor expansion:

$$\mathrm{M}(x, B) = \alpha(x, x_0 + \Delta x) - \alpha(x, x_0 - \Delta x)$$

$$\approx \alpha(x, x_0) + \frac{\partial \alpha(x, x_0)}{\partial x_0}\Delta x - \alpha(x, x_0) - \frac{\partial \alpha(x, x_0)}{\partial x_0}(-\Delta x)$$

$$= 2\frac{\partial \alpha(x, x_0)}{\partial x_0} g_{eff}\mu_B B$$

The MCD signal $\mathrm{M}(x, B)$ is proportional to the applied static magnetic field B and sensitivity is described by the slope:

$$k(x, x_0, g_{eff}) = 2\frac{\partial \alpha(x, x_0)}{\partial x_0} g_{eff}\mu_B$$

where

$$\frac{\partial\alpha(x,x_0)}{\partial x_0} = \frac{a}{\pi}\frac{\Gamma(x-x_0)}{\left((x-x_0)^2+\left(\frac{1}{2}\Gamma\right)^2\right)^2}$$

With a laser frequency set at $x = x_0 + \Gamma/\sqrt{12}$, this value reaches a maximum

$$\max\left(\frac{\partial\alpha(x,x_0)}{\partial x_0}\right) = \frac{a}{\pi}\frac{\Gamma\frac{\Gamma}{\sqrt{12}}}{\left(\left(\frac{\Gamma}{\sqrt{12}}\right)^2+\left(\frac{1}{2}\Gamma\right)^2\right)^2} = \frac{3\sqrt{3}}{2}\frac{a}{\pi}\frac{1}{\Gamma^2}$$

And the slope is

$$k|_{x=x_0+\Gamma/\sqrt{12}} = \frac{3\sqrt{3}a\mu_B}{\pi}\frac{g_{eff}}{\Gamma^2} \propto \frac{g_{eff}}{\Gamma^2}$$

Thus, the sensitivity is proportional to the effective Landé g-factor g_{eff} and is inversely proportional to the square of linewidth Γ. Therefore, for transitions with the same oscillator strength, if the linewidth is halved, the MCD signal will be boosted by a factor of 4. The narrow absorption linewidth of (thiolfan)YbCl(THF) at room temperature makes it a potential interesting candidate in magnetic field sensing.

Chapter 3

Yb Complex for Quantum Computing and Sensing

In chapter 2, I presented our spectroscopic study of (thiolfan)YbCl(THF) as a prototype molecule for atomic-like molecular sensors (ALMS). The atomic properties of the NIR transition from the Yb^{3+} center are preserved, allowing for the molecule to retain ultra-narrow absorption linewidths in solution at room temperature. This narrow absorption linewidth was used to demonstrate magnetometry measurements based on the magnetic circular dichroism of these narrow transitions. In this chapter, I present further investigation into the potential to achieve electric field sensing and state preparation using (thiolfan)YbCl(THF).

3.1 Electric Field Sensing with (thiolfan)YbCl(THF)

We also explored the potential application of (thiolfan)YbCl(THF) as an electric field sensor, in addition to magnetic field sensing. The external magnetic field can be measured by looking at the differential absorption of right- and left-circularly polarized light of the sample, as shown in chapter 2. This optical method in detecting magnetic field relies on the transition between the Zeeman levels of the ground and excited states. Similarly, an external electric field can be measured by the shift in energy or line shape of the transition between Stark levels, the electric-field analogue of Zeeman levels. Stark spectroscopy or electro-absorption/emission spectroscopy has been used to study a wide range of molecular systems, including inorganic compounds, photosynthetic, catalytical, and biological systems. [115–117]

Stark spectroscopy concerns the changes in absorption due to the change in electric dipole moment ($\Delta\mu$) and polarizability ($\Delta\alpha$) upon excitation. The change in dipole moment

corresponds to the charge separation between the ground and excited states of the transition. The change in polarizability reflects the malleability of the ground and excited state orbitals to an external field. The shift in transition energy under an external electric field is given by:

$$h\Delta\nu = -\Delta\vec{\mu} \cdot \vec{F} - \frac{1}{2}\vec{F} \cdot \Delta\alpha \cdot \vec{F}$$

where $h\Delta\nu$ is the shift in transition energy, $\Delta\vec{\mu}$ is the change in dipole, $\Delta\alpha$ is the change in polarizability, and $\vec{F}$ is the external electric field. These two terms are the linear and quadratic Stark effects, respectively. Because Stark spectroscopy relies on the changes in absorption, similar to MCD spectroscopy demonstrated in chapter 2, molecules with narrow absorption lines are desired. Furthermore, extensive work has been done on studying the Stark effects on narrow absorption lines or spectral hole burning of inhomogeneously broadened features of molecular systems in host matrices.[118–120] Therefore, (thiolfan)YbCl(THF) may be a promising candidate for electric field sensing.

Because the orientation of the individual dipoles matter, usually the sample cell is preferred to be as thin as possible so that the orientation of the molecules is aligned. The sample cell can consist of two glass, quartz, sapphire, or silicon slides that are coated with semi-transparent electrode materials, like ITO or FTO, that are held apart by a spacer of around 25 μm thickness. The compound must form a good optical quality glass, which was confirmed in chapter 2 with 2-MeTHF as a solvent. Ideally, the sample must have a peak absorption of about 0.2-0.6, which is also possible with our sample. After the sample is prepared, an AC electric field is applied of around 1 MV/cm. The magnitude of the applied field depends on sample thickness and applied voltage. Then, the signal is detected with a lock-in amplifier.

Due to the engineering challenge associated with creating a cuvette that is made of ITO/FTO that is compatible with our cryostat, we instead developed a prototype sample holder that could be incorporated into the MCD spectroscopy setup in chapter 2 (figure 3.1). The thin optical cuvette is sandwiched between two copper plates with a 1 mm hole to allow laser transmission. The copper plates are connected to a high-voltage power supply, which we use to apply up to 2.5 kV onto the copper electrodes that are 3 mm apart. We measured the absorption with and without the static external field and were not able to resolve any noticeable difference. However, this measurement was performed at room temperature without a lock-in amplifier. For future measurements, ITO cuvettes to reduce the thickness between electrodes, lock-in amplifier to increase the detection sensitivity, and a lower temperature for measurement may be beneficial. Obtaining a theoretical value for the dipole or polarizability of (thiolfan)YbCl(THF) may also better guide future implementations of this measurement, especially to tailor the strength of the external field. For instance, a dipole change of 0.04 D under 1 MV/cm field will produce an energy shift of 20 GHz, which should be resolvable given the absorption linewidth of 150 GHz at room temperature of (thiolfan)YbCl(THF).

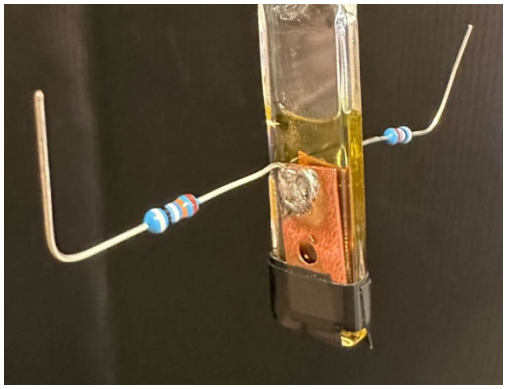

Figure 3.1. Preliminary Electrode Design for Stark Spectroscopy

3.2 State Preparation with (thiolfan)YbCl(THF)

State preparation is a crucial first step to quantum sensing and computing, defined by optically or electrically preparing the population of a physical system to one quantum state. As shown in chapter 2, we can perform spectral hole burning to selectively remove a portion of the ground state of the Zeeman transition. In order to prove that we can achieve state preparation, we must demonstrate the ability to control the change in the depth of the spectral hole. There are two ways we can modulate the ground state, by changing the power of the pump laser or by applying an RF field to the ground state Zeeman levels.

Since we are using a CW pump laser, the pump power will excite a portion of the ground state to the excited state at a constant rate. As long as the power of the pump laser is appreciable and not saturating the transition, it will modulate the spectral hole size. In order to gauge the relevant time scales, we looked at the hole-fill and hole-decay rates. We measured the probe signal and analyzed the rising and decaying rates, as seen in figure 3.2. The probe signal rises corresponding to the effective rate between the excited state decay and pump power, and decays according to the excited state decay rate, as the pump laser is turned on and off at 1 MHz frequency. We observed a decay time of 3.7 μs and rise time of 4.1 μs, corresponding to 43 kHz and 39 kHz linewidths. These decay/rise times deviated from the expected lifetime of 1.6 μs, which corresponds to the 99 kHz linewidth of the spectral hole burning experiment. We also were unable to observe a change in the decay/rise times as we changed the pump power. Therefore, we decided to pursue a different route to modulate the ground state population.

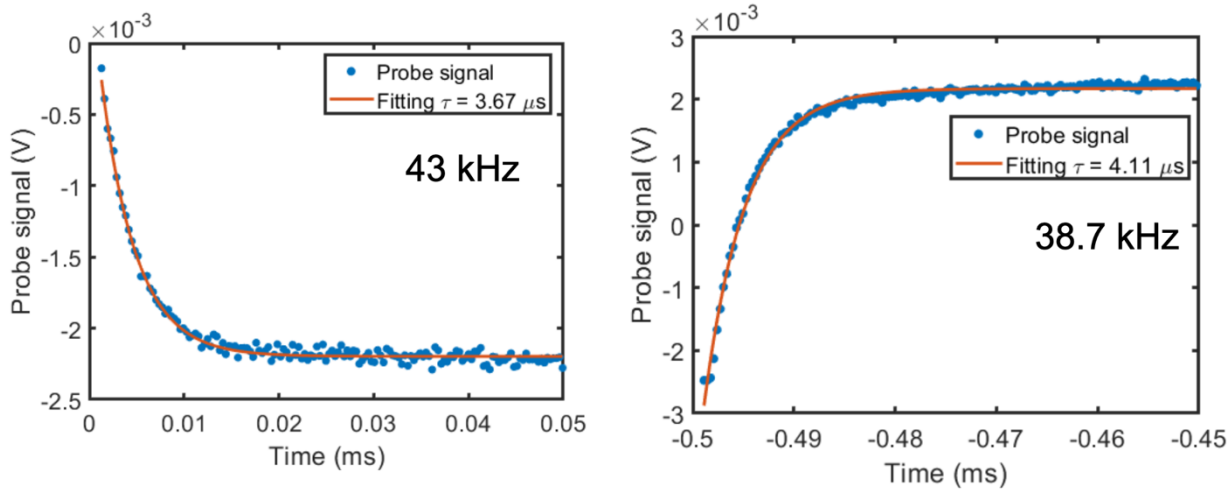

Figure 3.2. Decay and Rising Rates of Spectral Hole Burning

To modulate the transition population, an RF field can be applied to the ground Zeeman states, as shown in Figure 3.3. Since spectral hole burning has to be performed at 77 K, we added an RF coil around the sample holder inside our cryostat, as shown in figure 3.4. The dimensions of the RF coil were determined with the needed strength in mind. Given the X-band EPR spectrum of (thiolfan)YbCl(THF), the ground state resonance for the $m_j = 7/2$ state was measured at 9.6 GHz (Figure 2.45). The magnitude of the emission signal is dictated by the microwave (MW) power and the conversion factor of the resonant cavity, which is 1.3 $GsW^{-1/2}$ (Bruker ER 4116 DM). Given the MW power of 2.2 mW, the strength of the MW amplitude is around 0.06 Gs. This gives a floor to our needed RF field strength. However, considering that the EPR spectrum was taken at 5 K, we probably needed to induce a much higher field than 0.06 Gs to account for further possible broadening at higher temperatures.

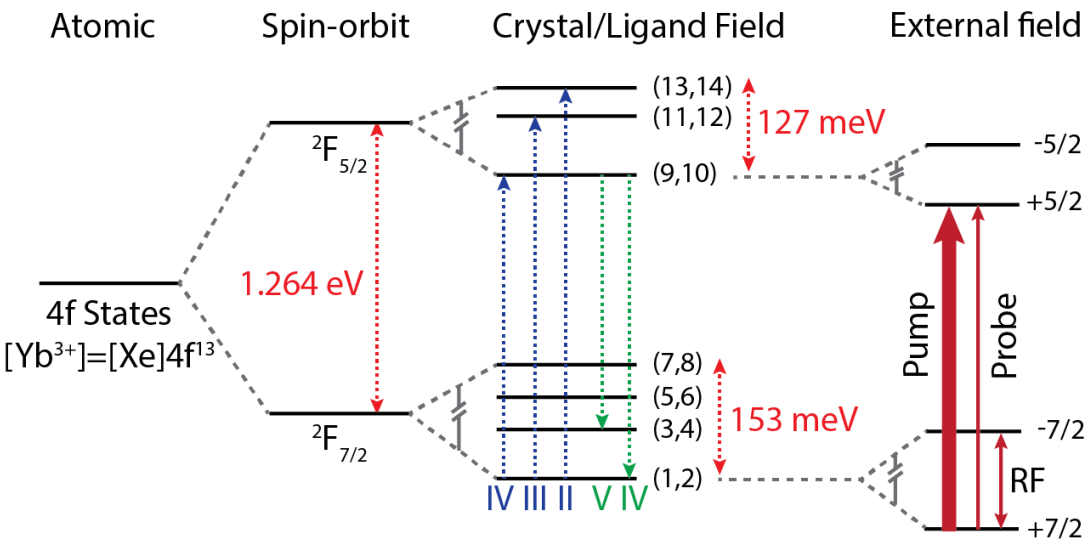

Figure 3.3. State Preparation using Zeeman levels with an RF Field

The strength of the field applied by the RF coils is given by:

$$B_{RF} = \frac{EMF}{2\pi f_{RF} NA}$$

Where EMF is the output voltage, f_{RF} is the AC frequency of the driving current for the RF coils, A is the coil area, and N is the number of turns. We created an RLC circuit to apply AC current onto the RF coils, for which the resonant frequency was around 1.6 MHz. A pick-up coil was inserted between the two sets of RF coils to measure the applied field. We measured 6.3 V for the EMF, which translates to around 1.27 Gs in RF field strength. Then, we applied an external magnetic field with larger coils on the outside that corresponded to ground state splitting of 1.6 MHz. We scanned this magnetic field while monitoring the probe intensity, expecting a rise in spectral hole burning intensity that corresponds to higher probe transition from a deeper spectral hole. However, we were not able to see a noticeable difference in our probe signal.

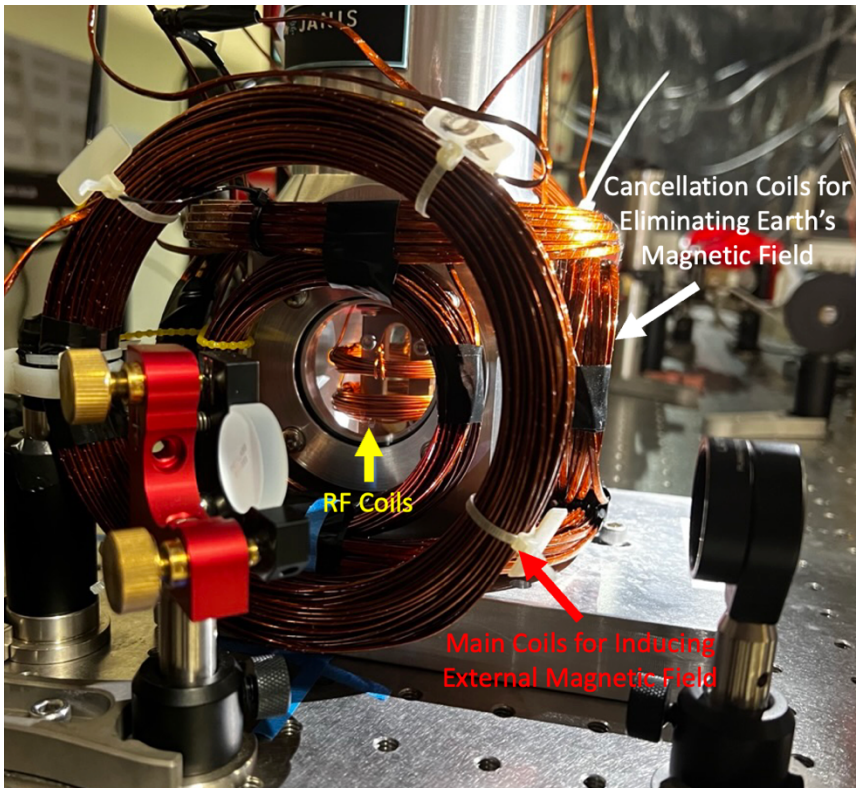

Figure 3.4. Preliminary State Preparation Setup.
Helmholtz Coil Designs for RF Excitation, Cancellation of the Earth's Field, and an External Magnetic Field.

There are several things that may be done to improve this experiment. First, a way to detect the strength of the applied field may better inform whether we are applying enough external field to see an appreciable difference in the ground state population or saturating the transition altogether. This can be achieved by introducing a vacuum compatible magnetometer inside the cryostat. Depending on the needed frequency, three coils may be added to cancel the ambient field. A provisional set was implemented, as shown in Figure 3.4, which needed a dynamic feedback loop to account for the drift in the ambient field. If a stronger field is needed, this optical set up could be modified to be incorporated into an EPR equipment. An optical access can be introduced to the sample holder of an EPR instrument, or an optical fiber can be placed at the top of the EPR tube with an off-axis detection. Second, the sample cuvette and

holder may be improved to accommodate a thinner film, allowing for better alignment of the molecules and thus polarizable spins. Lastly, this experiment should be run at colder temperatures, even with the sample crystallized to optimize spin alignment and linewidth narrowing.

Chapter 4

Molecules Functionalized with Optical Cycling Centers for Quantum Sensing and Computing

4.1 Introduction to Optical Cycling Centers

Quantum computers use quantum states to store and process information and are predicted to be able to tackle questions that are intractable in classical computers. Modern-day computers use bits to represent information while quantum computers use quantum bits (qubits) that can achieve a superposition state by becoming entangled with another qubit. This entangled state has no classical analog and allows more efficient computation of certain operations, such as search algorithms and numerical factorization. These operations may be used in the future to tackle complex problems that current computer architecture is unable to address, such as breaking encryption, identifying macroeconomic trends, and simulating proteins with quantum mechanical treatment.[121] While quantum computers are expected to achieve improved efficiency in certain algorithms, a fully functioning quantum computer has not been realized and further research is necessary, especially in fundamental and materials research.

One of the most reliable qubit systems demonstrated to date uses trapped atomic ions, which are gas phase cations trapped in external electric and magnetic fields.[122] Trapped ions make an effective qubit because they can optically cycle (i.e. be excited by laser radiation and de-excited back to the ground state *multiple times*), allowing for quantum state measurement.[2] Currently, the stability of the gas phase ions relies on cryogenic cooling, electric and magnetic field traps, and vacuum chambers, rendering ionic qubits unscalable. Therefore, the application

of ionic qubits to more stable systems is necessary. The extension of ionic qubits to molecular systems has been hindered by the fact that most molecules do not optically cycle; they have many relaxation pathways, making it less likely to return to the original ground state and excite into the same transition. In this chapter, I will report my research findings into molecular moieties bound to alkaline earth (AE) metals, which are known to optically cycle in gas phase and bind with ligand molecules while retaining their cycling properties. These AE atoms could serve as optical cycling centers (OCCs) within a molecular framework, which will be in solution or solid phase and thus more scalable. However, identifying molecular design principles that dictate the binding of these AE atoms to molecules in such a way that minimizes orbital mixing is crucial.

4.2 Functionalization of Organic Molecules with OCCs

The central challenge in quantum computing is the development of reliable qubits. A functional qubit must be easily prepared in an initial state, manipulated into entangled states, and subsequently read out without losing its state information during processing. My research efforts were aimed at identifying novel platforms for quantum systems that exhibit narrow optical transitions, room-temperature stability, and the potential for scalability, all by applying chemical control over known physical systems.

One of the candidate systems that I researched was a surface-bound AE qubit based on recent gas phase studies, in which alkaline monoalkoxides with long hydrocarbon ligands retained narrow spectroscopic behaviors.[3] AE metal atoms (e.g. Ca, Sr, and Ba) are known to optically cycle in gas phase, and to bond with fluoro, hydroxyl, and even alkoxyl groups while retaining their cycling properties.[123] The retention of cycling properties indicates that the electron

density around the AE atom remains unperturbed by molecular bonds, which allows the AE atomic transition to dominate the molecular transition.

To start, I start with the molecular orbital (MO) theory picture. Tracking the ground and excited states of reported strontium monoalkoxides, the number of carbons in the functional group did not change the excited state energy by a lot, which indicates that the oxygen bridging the Sr and alkanes must be dominating the molecular interaction with Sr (Figure 4.1). In other words, the Sr orbitals must be isolated from the rest of the molecules, and the deviations between the groups may stem from varying amounts of mixing to the orbitals of the bridging oxygen atom. Depending on the energy gap between electronic states of the AE metal and the functional group, the nature of the bond varies from ionic to covalent. For CaOH and SrOH, it has been shown that one of the two ns^2 valence electrons strongly bind to the OH group, creating a M^+-OH^- bond that is strongly ionic in character.[124] This allows for the final valence electron to remain in an open-shell molecular orbital localized around the metal, able to be optically cycled.

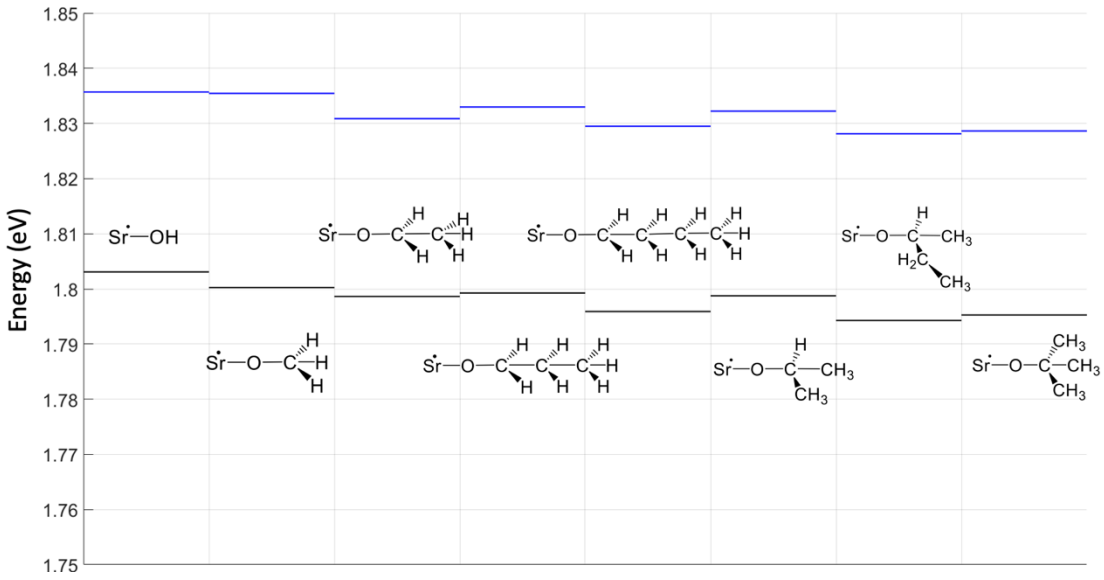

Figure 4.1. HOMO/LUMO Energies of Sr-O-R Molecules with Varying Sizes of R

If the electronic structure remains similar for -OR groups with larger R, then molecular OCCs can scale up in size while retaining its cycling properties. Taking the smallest alkoxide as an example (-OCH_3), you can create the expected molecular orbitals using MO theory, as shown in Figure 4.2. The contributions of Sr, O, and OCH3 orbitals are laid out in Figures 4.10-4.11. Accounting for the ionization energies of Sr (5.69 eV) and of the OCH_3 radical (8 eV), the valence orbitals mix together to create the HOMO and LUMO states that further mix with the nearby 5*p* and 4*d* orbitals of the Sr. Whether the Sr-AE bond remains ionic to retain nearly diagonal ground and excited states can be studied with further theoretical calculations.

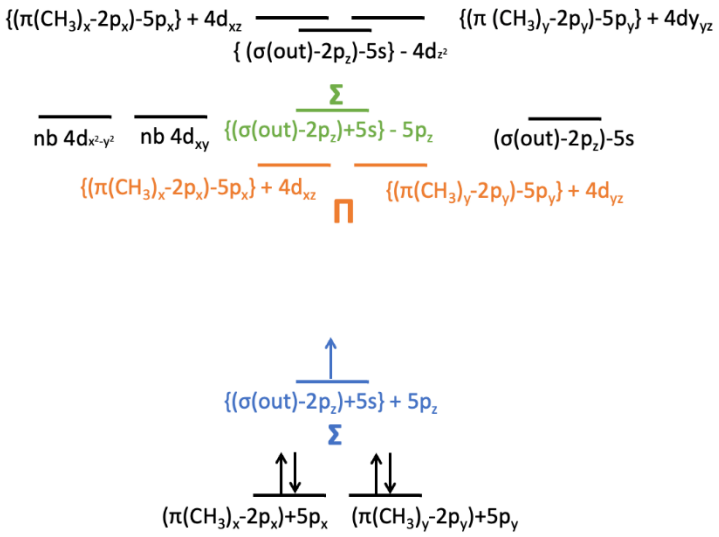

Figure 4.2. Molecular Orbital Picture of the Electronic Structure of $SrOCH_3$

From this discussion, electron density calculation of various linker and substrate molecules was performed by collaborator Dr. Han Guo.[125] The results reveal that the linkers must be rigid to ensure the AE atom remains upright so that it doesn't fall over to react with the surface and is sufficiently electronegative so that the electron density of the AE atom stays isolated from the substrate. Although most rigid linkers provide the upright support that the AE

atoms need, they tend to have π orbital systems that withdraw electron density away from the AE atom.[125] For an aromatic functionalization, the tuning of the electronegativity with aromatic substitution led to significant changes to orbital coupling, leading to direct changes in franck condon factors of the resulting molecular orbitals.[126] While rigidity is desired, an extended conjugated system may be easily mixed into the metal orbital. Therefore, tethering the OCC to a saturated carbon system, such as strained hydrocarbon systems or a diamond surface may be more promising.

In particular, the tetrahedral structure of a diamond crystal allows the functional groups to be orientated vertically and isolates atoms bonded to the surface by a bridging oxygen atom, making it an ideal candidate substrate for this system.[125] Both the HOMO and LUMO states on diamond have localized electron density around the AE atoms, suggesting that it is a promising platform for multiple qubit interactions. Therefore, I investigated surface synthetic techniques to functionalize Sr onto a diamond surface.

4.3 Development of Sr OCCs on Diamond

Employing synthetic techniques, qubit systems can be introduced into environments where they are easier to handle. The successful functionalization of optical centers can enhance its solubility in solvents or even achieve atomic precision in deposition sites. Therefore, I researched how to design and investigate molecular systems that not only have narrow optical features with long coherent lifetimes, but also allow more accessible chemical control over the quantum states of the system. Sr atoms with cycling transitions can be bound to diamond (or other electronically inert) substrates. With sufficient control, these Sr qubits can be placed at a specific density to allow for spatial and photonic interaction, enabling a novel method to transmit quantum information. The behavior of the Sr-diamond system is expected to be like that of AE monoalkoxides, which

has negligible probability to relax into higher-lying vibrational states.[127] Given the localized electron density of the HOMO and LUMO states, the transition between them within the AE-diamond systems should be optically cyclable, without leakage to other energy states.

To develop this system, I first obtained lab-grown CVD diamond wafers and checked their surface smoothness using atomic force microscopy (AFM). The AFM setup includes a cantilever, piezoelectric scanner, a laser positioned at the back of the cantilever, and a position sensitive photodetector. The piezo stage moves the cantilever along the surface of the sample and measures the intensity and phase shift of the reflected laser beam. These measurements provide the height and roughness of the sample surface, allowing nanometer scale analysis of the surface morphology. As shown in Figure 4.4, the surface of the diamond was flat to within nm across microns of raster scanning. There seems to be a preferred grain pattern, where the horizontal lines (blue and orange) saw a greater fluctuation in surface height than the orthogonal lines (yellow and purple), which remained flat to within nm. Considering that carbon bonds are usually 2-3 , the diamond surface most likely fluctuates about 10-20 layers of carbons across microns of the surface. While the aim would be to prepare OCCs on an atomically precise layer, I continued using this diamond substrate for preliminary experiments.

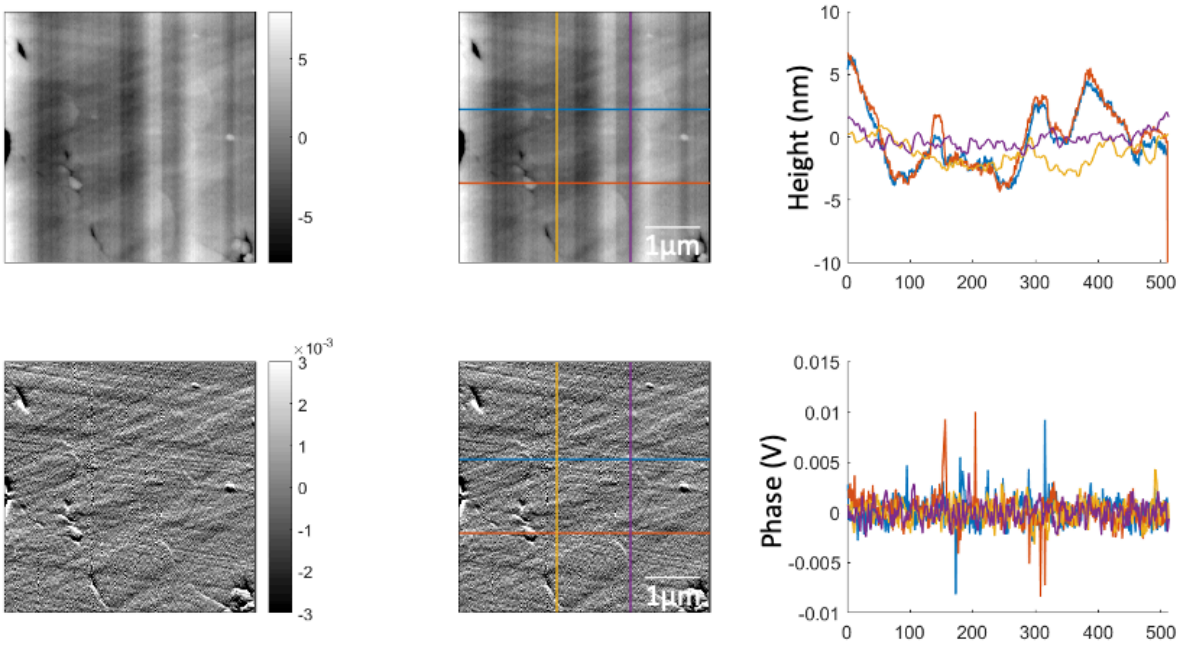

Figure 4.4. AFM Height and Phase Images of Diamond Substrate.
Top panel: height images with scale bar and visual guides, indicating where the slice was taken shown on right. Bottom panel: corresponding phase images.

I confirmed that hydroxylation of the diamond substrate is possible with ozone treatment, via contact angle measurement and x-ray photoelectron spectroscopy (XPS). With ozone treatment, there should be an increase in the amount of hydroxyl groups bound to the surface of the diamond (Figure 4.5a). With about 2-minute exposure to ozone, I was able to observe a decrease in contact angle between water and the diamond substrate before and after ozone treatment, indicating transition to a more hydrophilic, hydroxylated surface (Figure 4.5b). Additionally, the relative increase in sp^3 carbon and COH oxygen signals in the XPS spectra demonstrate an increase in -OH termination of the diamond surface (Figure 4.5c).

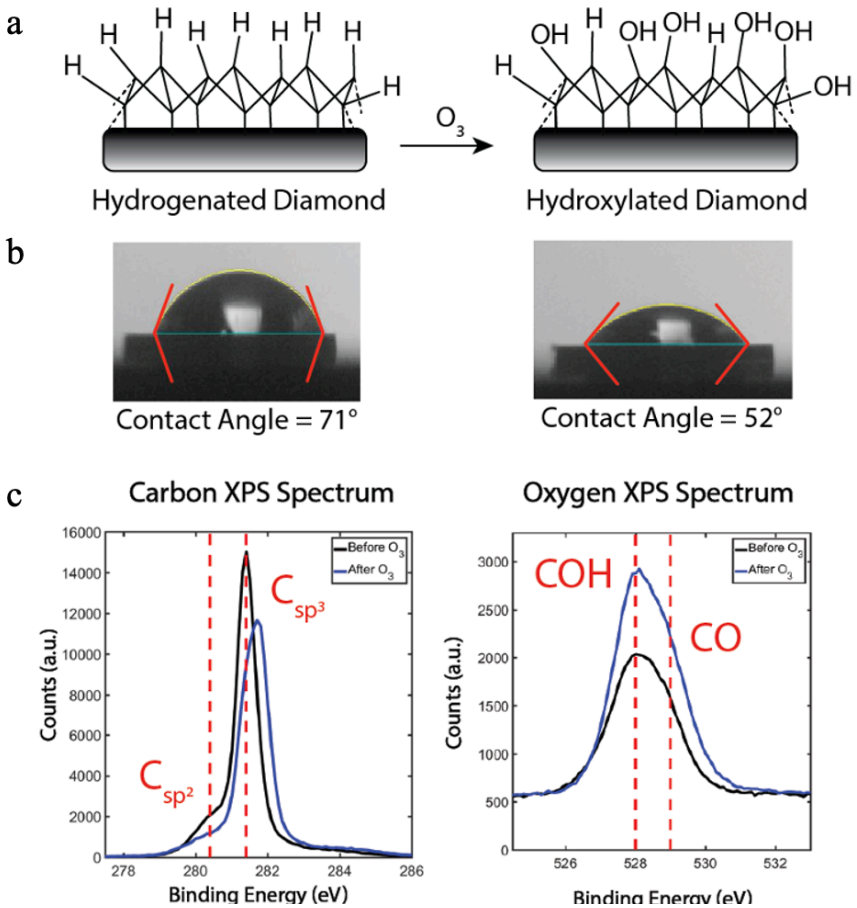

Figure 4.5 Hydroxylation of Diamond Surface Confirmed by Contact Angle and XPS
a) Schematic of hydroxylating diamond by ozone treatment. b) The decrease in contact angle between a water droplet of constant volume and the diamond substrate before and after ozone treatment indicates a cleaner and hydroxylated surface. c) The relative increase in sp^3 carbon and COH oxygen signals demonstrate a clean OH-terminated diamond.

With the substrate hydroxylated, the next step was to introduce metal atoms that will take place of the hydrogens in the OH group. I have deposited Sr atoms on a glass substrate using our custom-built deposition set up (Figure 4.6a) and characterized the surface using x-ray photoelectron spectroscopy (XPS). XPS is a surface characterization technique, which detects the kinetic energy of ejected electrons from the surface that was irradiated with a beam of X-rays. Depending on the energy of the detected electrons, the elements on the surface can be identified,

using the principles of the photoelectric effect. We introduced a glass substrate onto the sample holder, turned on the Sr oven, and checked whether Sr atoms were deposited onto the glass substrate with XPS. A prominent signal from the Sr $3d_{3/2}$ and $3d_{5/3}$ electrons were seen, proving that there were Sr deposited on the glass substrate (Figure 4.6b).

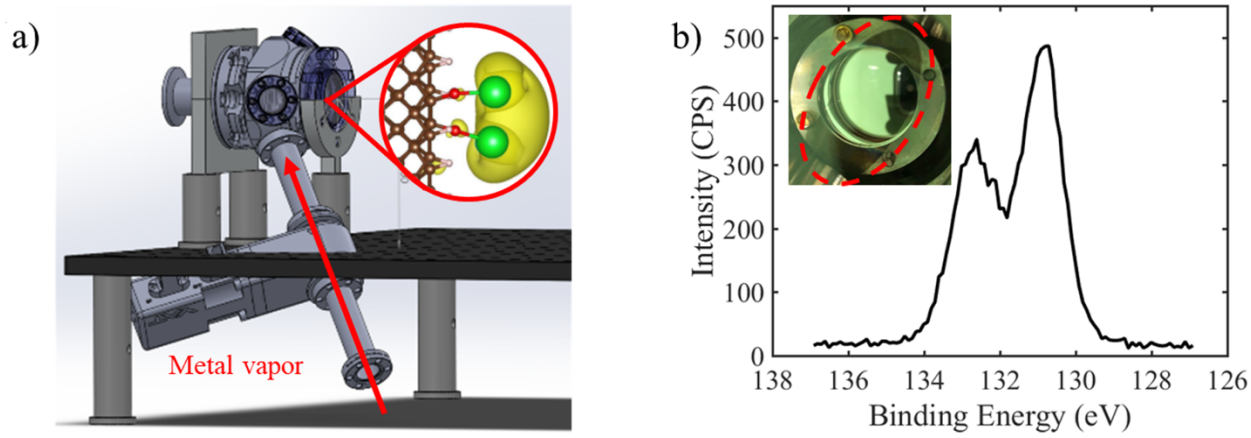

Figure 4.6. Deposition and detection chamber with XPS confirmation.
a) Schematic of the deposition of AE metal atoms. b) A picture of Sr metal deposited on a glass substrate and XPS spectrum showing the Sr $3d_{3/2}$ peak at 133 eV and Sr $3d_{5/2}$ peak at 131 eV.

To further confirm the capabilities of the deposition setup, we deposited Sr, Ca, and Yb onto a variety of substrates, and confirmed the deposition using XPS (Figure 4.7). These 3 metal atoms have been experimentally and/or theoretically observed to optically cycle while bound to a small -OR group. With the optical access designed into the deposition setup, fluorescence can then be collected to study the electronic structure of the metal-substrate system.

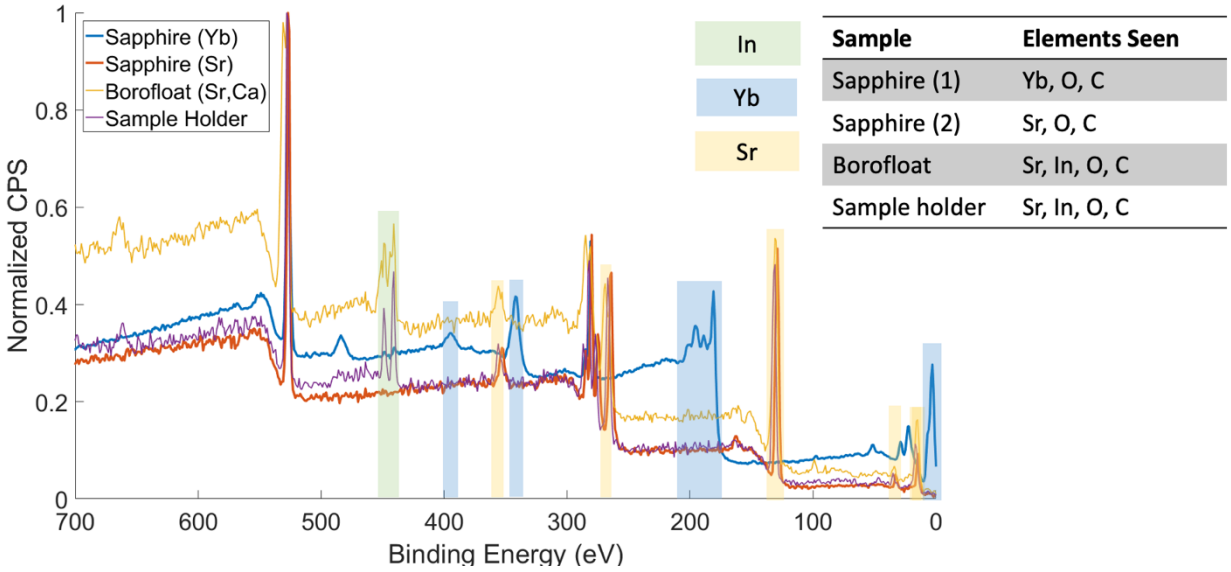

Sample	Elements Seen
Sapphire (1)	Yb, O, C
Sapphire (2)	Sr, O, C
Borofloat	Sr, In, O, C
Sample holder	Sr, In, O, C

Figure 4.7. Diagram of Substrate and Deposited Metal Combinations that were Verified

Although the ground state transition of the AE-substrate system is expected to be near the gas phase atomic transition, the exact transition frequency must be experimentally determined. An excitation spectrum of the gas phase Strontium $^1S_0$ to $^1P_1$ transition at 461nm was measured (Figure 4.8). This was obtained by scanning the excitation wavelength and measuring the emission. The signal-to-noise ratio of the ultrafast setup was difficult to optimize, as a large portion of the laser is scattered off the substrate. We were not able to resolve any other fluorescence near this transition. For future success of this experiment, a more robust deposition technique, where the deposition and verification of the substrate can be performed inside the same chamber, and a more optimized and automated fluorescence set up may be necessary.

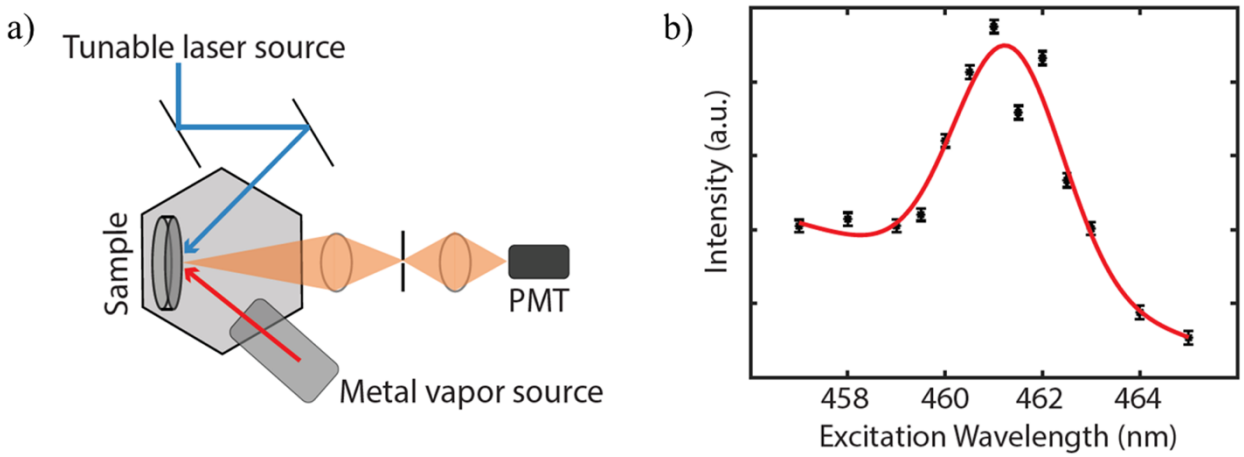

Figure 4.8 Sr Fluorescence after Deposition

a) Diagram of the fluorescence measurement set up, where AE atoms are deposited in situ. b) Excitation spectrum of the gas phase Strontium $^1S_0$ to $^1P_1$ transition at 461nm obtained in the above set up.

Further progress of this study or others similar will develop new methods to functionalize and verify electronically inert surfaces with viable OCCs. Potential designs for surface-OCCs are shown in Figure 4.9, where surface-OCC's are used as quantum sensors (a) and qubits for quantum computing (b).[125] Similar to the design proposed in (a), Atomic protrusion of STM tips to enhance electron microscopy techniques have been observed.[128,129] However, a more robust technique for such deposition must be developed for reliable production of surface-OCCs for quantum sensing. The effective application of chemical control over qubit systems will illuminate a novel path for quantum information science, where chemistry will play a bigger role in determining quantum computer systems.

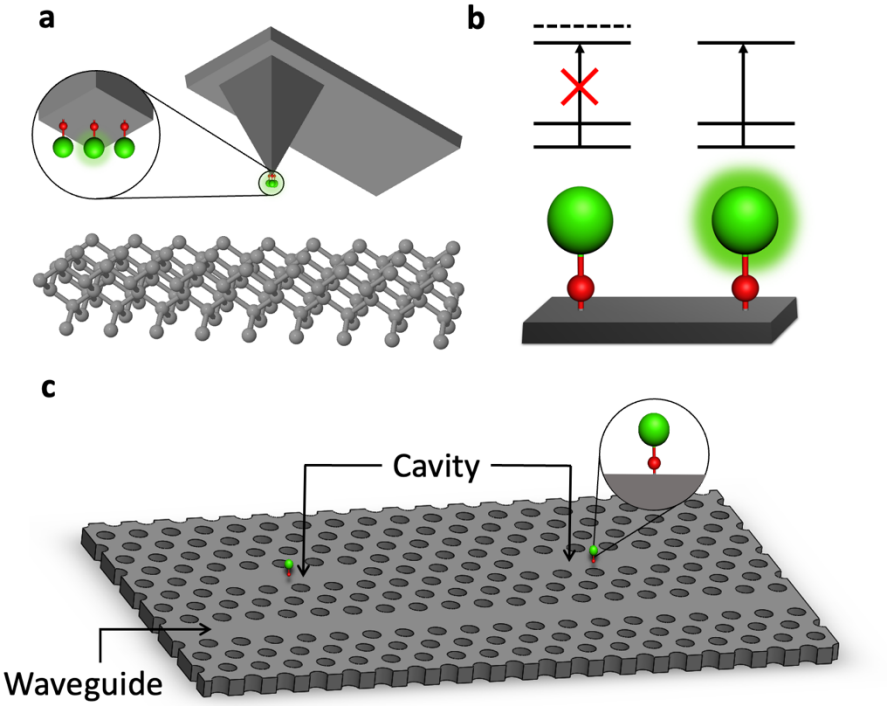

Figure 4.9 Possible Future Implentation of Surface OCCs

a) OCCs on STM tip to enhance fluorescence for surface microscopy techniques. b) Diagram of two OCCs in close proximity to perform a CNOT gate. c) OCCs functionalized onto a photonic waveguide

4.4 Supporting Information

To get to Figure 4.2, I worked out the molecular orbitals of OCH_3, $SrOCH_3$, and then introduced further orbital mixing with nonbonding Sr orbitals. The molecular orbital diagrams for OCH3 and SrOCH3 are shown in Figures 4.10 and 4.11 below.

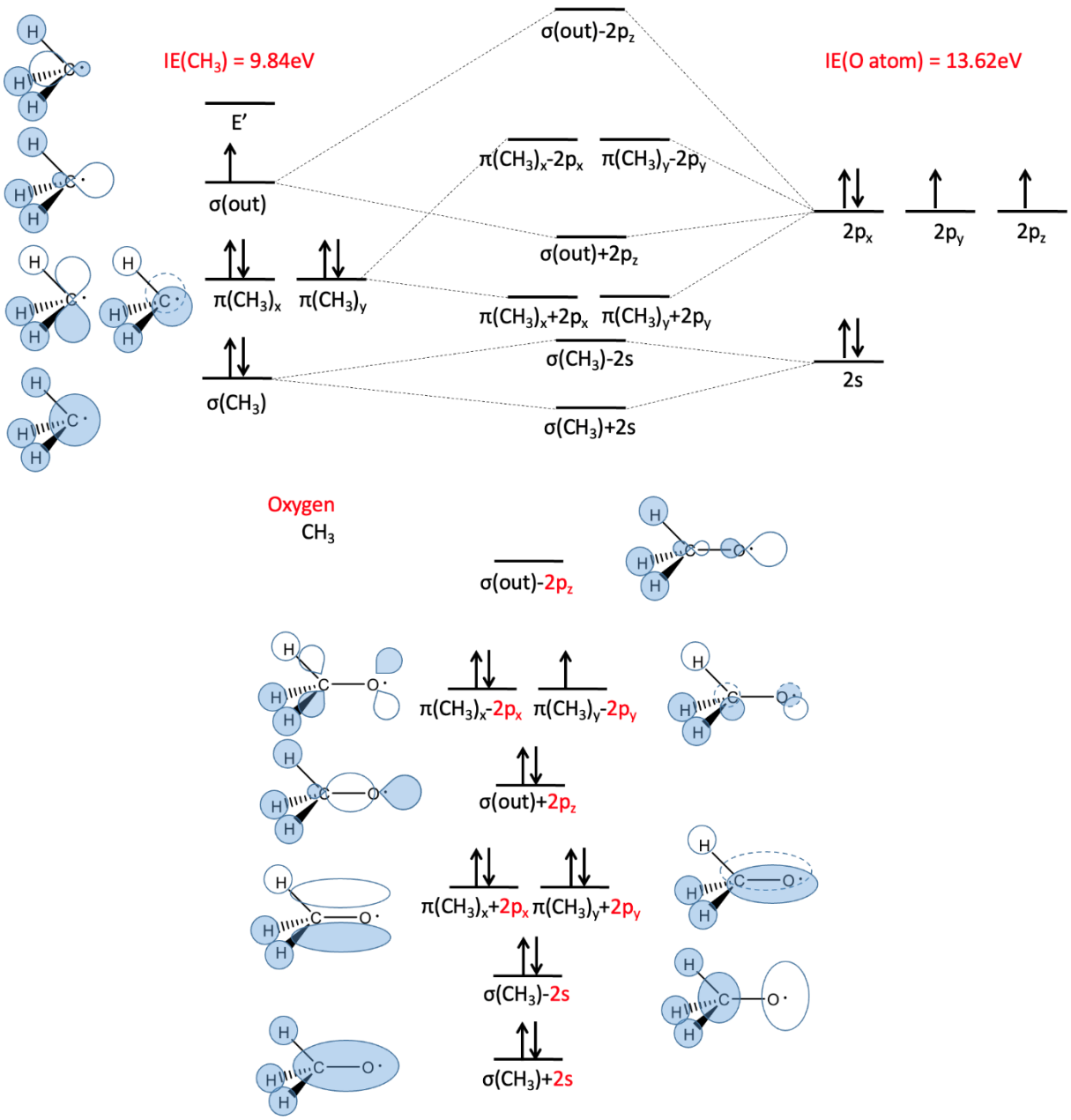

Figure 4.10 Molecular Orbital Diagram of OCH_3

Top: Molecular orbital diagram of combining CH_3 and O. Bottom: The resulting molecular orbitals of OCH_3 and the corresponding visualization of predicted orbitals.

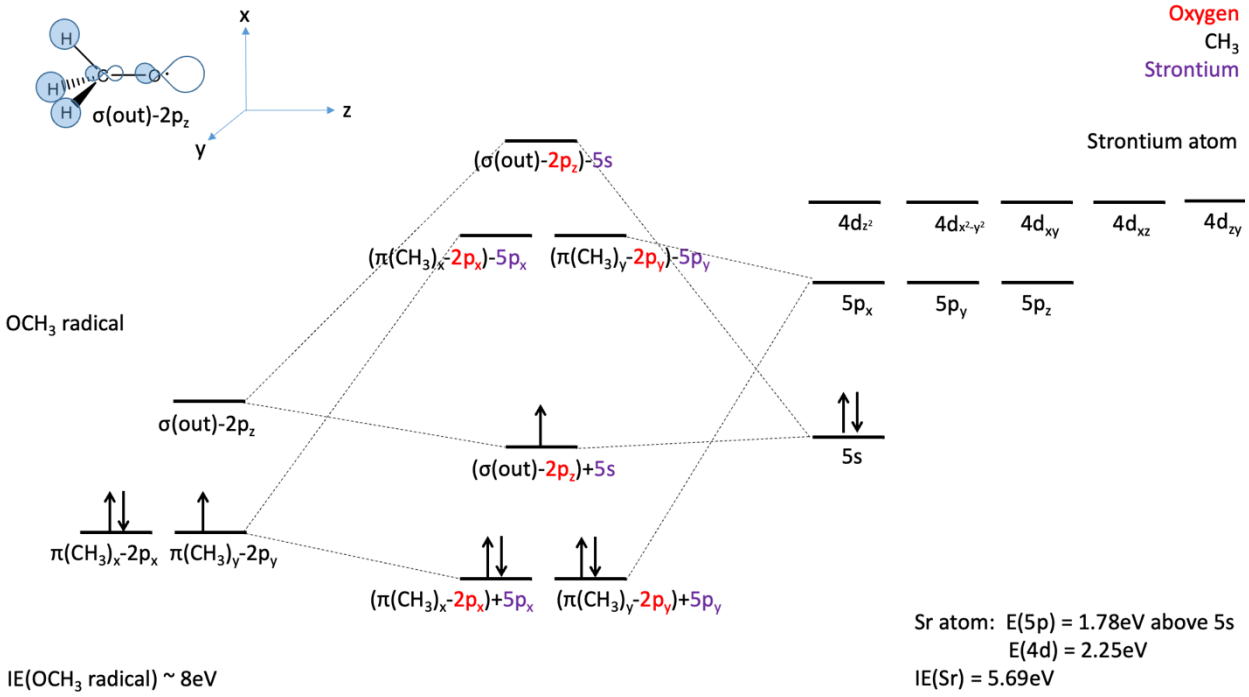

Figure 4.11 Molecular Orbital Diagram of OCH3 radical and Sr atom

Chapter 5

Dielectric Screening Modulates Nanoplatelet Excitons

Adapted with permission from Shin, A. J.; Hossain, A.; Tenney, S. M.; Tan, X.; Tan, L.; Foley, J. J.; Atallah, T. L.; Caram, J. R. Dielectric Screening Modulates Semiconductor Nanoplatelet Excitons. *J. Phys. Chem. Lett.* **2021**, *12*, 4958-4964.

5.1 Semiconductor Nanoplatelets (NPLs)

Colloidal nanoplatelets (NPLs) are an emerging class of optoelectronic substrates, useful due to their high absorptivities, near unity quantum yields, and narrow tunable quantum confined emission.[130–133] Another appealing aspect of these NPLs is the atomic precision over their growth anisotropy: II-VI cadmium chalcogenide NPLs can be synthesized with precisely 2-11 monolayer (ML) thicknesses, and show increasing control over their 2D lateral extent.[134–138] Such structures can also template other II-VI NPLs, including core-shell and core-crown Cd/Zn S/Se/Te heterostructures and mercury chalcogenide infrared emitters, which demonstrate comparable synthetic control.[139–141] With increased tunability of the NPL thickness, colloidal 2D materials warrant further exploration of the extent of synthetic modulation over their photophysical properties and device applicability. In this work, we measure the absorption spectra of zinc-blende II-VI NPLs, which consist of alternating M-X atomic layers (M=Cd, Hg and X=Se, Te), as shown in Figure 5.1a The NPLs have thicknesses of 0.7-1.9 nm and lateral dimensions of 50-200 nm (Figure 5.1b).[142–144] The synthesis procedures for individual NPLs and material characterization can be found in the Supporting Information (Section 5.7; EDS in Table 5.2, FTIR in Figures 5.5-5.6, and TEM in Figures. 5.7-5.8). Motivated by their similarity to other 2D excitonic

semiconductors, such as quantum wells and transition metal dichalcogenides (TMDCs), we use the distinct room temperature features of the absorption spectra (Figure 5.1c) to understand bandgap and excitonic properties. In this work, we apply the Elliott model to fit excitonic absorption features.[145–148] We extract light and heavy hole exciton binding energies (E_B) that are in excellent agreement to the prior limited available experimental results for the heavy hole exciton binding energy in CdSe NPLs.[149,150] In all NPLs, we observe high exciton binding relative to bulk semiconductors.

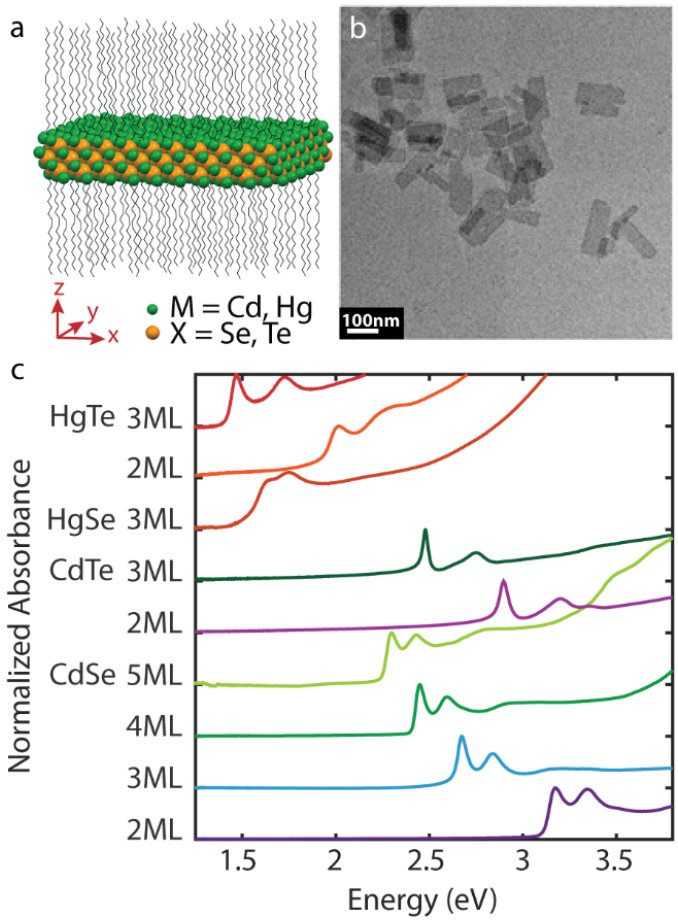

Figure 5.1 MX Nanoplatelet structures and corresponding spectra.
(a) Simplified crystal structure of 3 ML MX (M=Cd, Hg; X= Se, Te) NPL, including organic ligands as an example. (b) TEM image of 3 ML HgSe NPLs, showing nanoscale lateral dimensions. (c) Normalized absorbance spectra of MX NPLs of varying thicknesses, offset for clarity.

In layered Van der Waals semiconductors, high binding energies are attributed to the strong influence of the external dielectric on E_B.[151] To test whether external dielectric plays a similar role in 2D NPLs we study the thickness and solvent dependence on exciton binding energy. We observe that as NPL thickness increases, exciton binding energy decreases, a result that we can recover quantitatively through a minimal electrostatic model of variable thickness dielectric slabs. We further demonstrate dielectric modulation of binding energy by shifting and recovering HgTe E_B through exchange in polarizable solvent. Our results expand upon established colloidal NPLs' excitonic properties and emphasize the importance of the dielectric environment in modulating the photophysical properties.

To establish factors influencing colloidal NPL excitons, we use the absorbance spectra to derive photophysical constants, such as exciton binding energy and band-to-band energy difference (bandgap, E_G), through Elliott model fits. This straightforward method allows for high-throughput measurements to determine E_B values as well as easily monitor solvent dielectric effects on .

5.2 Multiband Elliott Model of Colloidal NPL Systems

The Elliott model describes absorption spectra of 2D and 3D semiconductors, accounting for excitonic resonances and oscillator strengths. The model yields optical transitions, corresponding to excitations from the ground state (valence band electrons) to bound electron-hole excitonic states, followed by a higher energy valence-band to conduction-band continuum of free electron transitions. The absorption features depend on the dimensionality of the semi-conductor as shown in Eq. 1:

$$\alpha_D(E) \propto \sum_{n=1}^{\infty} \left(\frac{E_B \Gamma(n+D-2)}{(n-1)! \left(n+\frac{D-3}{2}\right)^{D+1}} \cdot \delta\left(E - E_G + \frac{E_B}{\left(n+\frac{D-3}{2}\right)^2}\right) \right) + \frac{\left|\Gamma\left(\frac{D-1}{2} + i\beta\right)\right|^2 e^{\pi\beta} \beta^{2-D}}{2^D \pi^{2-\frac{D}{2}} \Gamma\left(\frac{D}{2}\right)} \cdot \Theta(E - E_G) \quad (1)$$

where ω is the excitation frequency, D is the dimensionality of the model system, n is the number of discrete excitonic peaks, E_G is the bandgap energy, $\beta = \sqrt{\frac{E_B}{\hbar\omega - E_G}}$, $\Gamma(n) = (n-1)!$ is the gamma function, $\delta(a-b)$ is the Dirac delta function, and Θ is the Heaviside step function.[148,152] The model reproduces the intensity and absolute positions of absorption features using only E_B and E_G as inputs, for a given dimensionality constant D. The Elliott model has been used to describe inter-band transitions in TMDCs, quantum wells, and 2D layered perovskites—but has not been applied to NPLs.[145,152–157]

In Figure 5.2a, we illustrate the electronic structure of II-VI NPLs and highlight the transitions that are well-described by the Elliott model. The valence band is split into non-degenerate heavy hole (HH) and light hole (LH) bands, which are offset due to spin-orbit coupling.[158,159] In excitonic materials, the exciton binding energy is greater than thermal energy at room temperature ($E_B > kT$). This results in the observed excitonic transition peaks (Figure 5.2a: GS→X_n) within the absorption spectrum, appearing at lower energy than their corresponding band-to-band continuum HH and LH transitions (Figure 5.2a: $E_{G,HH}$ and $E_{G,LH}$).

We extract the E_B and E_G values for the II-VI NPLs with various ML thicknesses by fitting our observed absorption spectra with the Elliott model (a more detailed explanation of the fitting procedure can be found in section 5.7). To account for the linewidth broadening, we convolve Eq. 1 (where $D = 3$) with a tunable hyperbolic secant function resulting in the following expression:

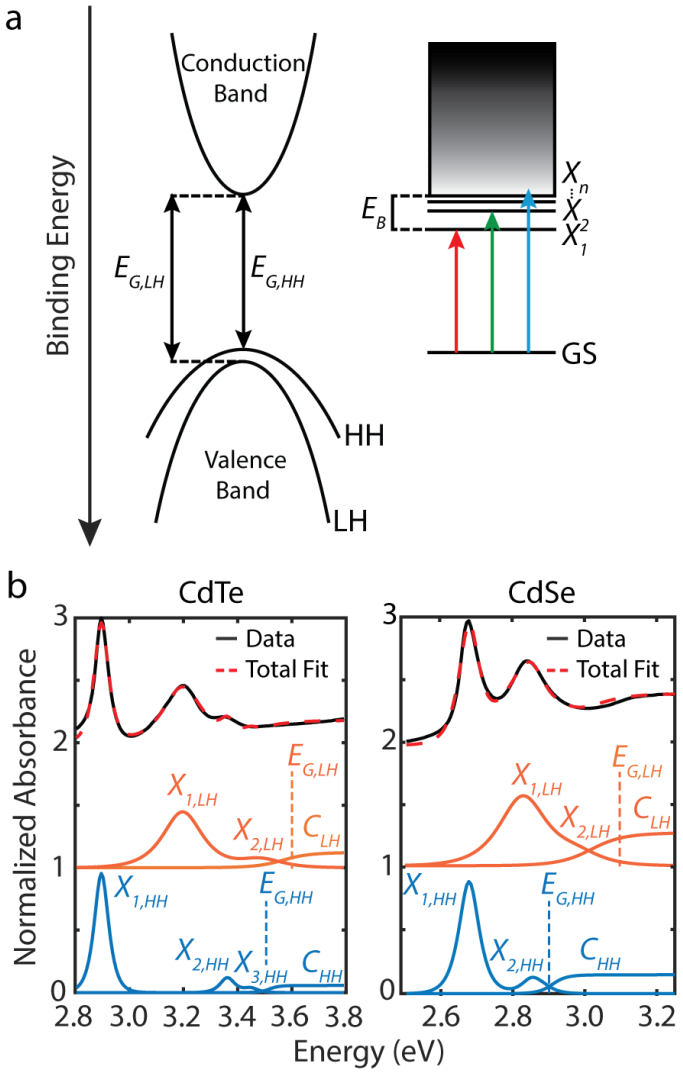

Figure 5.1 Band Diagram and Corresponding Elliott Model Fits of NPL Absorption

(a) Left: Band diagram, showing both light hole (LH) and heavy hole (HH) valence bands. Right: general transition diagram for a HH or LH exciton. (b) Absorption spectra of 2 ML CdTe and 3 ML CdSe NPLs, showing the excitonic features of the modified Elliott model, offset for clarity. The Xn transitions and the onset of the conduction bands (C) are shown.

$$\alpha_x(\omega) \propto \sum_{n=1}^{\infty} \frac{2E_B}{n^3} \operatorname{sech}\left(\frac{\hbar\omega - E_G + \frac{E_B}{n^2}}{\gamma}\right) + \int_{E_G}^{\infty} \operatorname{sech}\left(\frac{\hbar\omega - E'}{\gamma}\right) \frac{1}{1 - \exp\left(-2\pi\sqrt{\frac{E_B}{E' - E_G}}\right)} dE' \quad (2)$$

where α_X is either α_{HH} or α_{LH}, γ is the linewidth broadening factor, and E' is the convolution integration energy variable (step-by-step process of the convolution in SI Sec. IV). We observe that the 3D Elliott model generates a better fit than 2D, which we hypothesize is the result of the finite thickness of NPLs. In SI Sec. V, we provide a mathematical and visual comparison between the two- and three-dimensional Elliott models and fits (Figure 5.9). We account for HH and LH absorption by fitting the sum $\alpha_{Total} = \alpha_{HH} + \alpha_{LH}$.[160,161] In Figure 5.2b, we show examples of typical NPL absorption spectra, the Eq. 2 fit, and fit components corresponding to HH and LH transitions. The spectra are broken down into contributions from continuum and excitonic features with labelled transitions. This straightforward application of the Elliott model determines the absolute positions of HH/LH excitonic transitions from the onset of the continuum. Thus, the modified Elliott model fits the absorption spectra using 8 parameters—line-broadening as well as bandgap and exciton binding energies for light and heavy holes and amplitudes.

5.3 Bandgap and Exciton Binding Energies of CdX and HgX NPLs

The E_G and E_B values for the cadmium and mercury NPLs are shown in Table 5.1. We note reported values of binding energy in 3-5 ML CdSe NPLs, for which our measurement shows excellent agreement. As expected, the bandgap energy increases as the number of MLs decreases due to increasing quantum confinement. Furthermore, the exciton binding energy also increases as the number of MLs decreases. Interestingly, for the same number of MLs, HgX NPLs have higher values (with the exception of 2 ML CdTe and HgTe), which is unexpected as mercury chalcogenides have larger dielectric constants than the cadmium ones.[162,163] This discrepancy may be explained by differences in surface lattice strain between 2 ML CdTe and HgTe, changing valence and conduction band structures and electron-hole interactions.[164,165] Alternatively, our previous work suggests HgTe NPLs have their outer metal atomic layer stripped off during the cation exchange process, resulting in decreased charge density on the surface and a lower dielectric.[139] This would potentially result in a larger exciton binding energy in comparison to the metal terminated CdTe NPLs. In the next section we explore how layer number influences the effective dielectric felt by the bound electron-hole pair.

Table 5.1 Bandgap and Exciton Binding Energies of NPLs.

The values reported in this table are extracted from room-temperature absorption data, using a modified Elliott model. The CdX NPLs are passivatd by oleic acid ligands, whereas HgX NPLs are passivated by oleylamine. Both NPLs are suspended in haxane.

NPL	MLs	$E_{G,HH}$ (eV)	$E_{B,HH}$ (meV)	$E_{G,LH}$ (eV)	$E_{B,LH}$ (meV)	Bulk E_G (eV)/E_B (meV)
CdSe	2	3.5±0.1	430±30 220[b]	3.6±0.1	220±40	1.7[166]/15.7[167]
	3	2.91±0.05	220±20 210[149] 211±5[a]/204[b]	3.1±0.1	190±30	
	4	2.65±0.05	195±20 190[149] 187±2[a]/182[b]	2.7±0.1	170±30	
	5	2.45±0.05	175±20 170[149,150] 167±2[a]/163[b]	2.5±0.1	120±30	
CdTe	2	3.51±0.05	620±30	3.6±0.1	370±35	1.54[168]/10.5[167]
	3	2.67±0.05	210±30	2.9±0.1	200±30	
HgSe	3	1.92±0.05	300±25	1.9±0.1	190±35	0[169]
HgTe	2	2.13±0.05	450±30	2.5±0.1	300±30	0[170]
	3	1.77±0.05	350±25	1.9±0.1	260±30	

[a]Semi-empirical model, [b]Variational approach

5.4 Effects of Dielectric Screening

We observe that exciton binding energies will increase with decreasing NPL thicknesses. To demonstrate this independent of our Elliott fits, we model the excitonic interactions in the NPL with an electron and a hole as point charges within a dielectric slab modelled after the dielectric constant of the NPL's ($\varepsilon_{NPL} \approx 10$). This region is sandwiched by an external dielectric equal to that of organic ligand environment ($\varepsilon_{ext} \approx 2$), illustrated in Figure 5.3a. We utilize the method of images to determine the excitonic electrostatic potential at one of the charges: [171]

$$V = \frac{q}{4\pi\varepsilon_0\varepsilon_{NPL}r} + 2\sum_{N=1}^{\infty}\left[\left(\frac{\varepsilon_{NPL}-\varepsilon_{ext}}{\varepsilon_{NPL}+\varepsilon_{ext}}\right)^n \frac{q}{4\pi\varepsilon_0\varepsilon_{NPL}\sqrt{r^2+n^2t^2}}\right] \quad (3)$$

where q is the magnitude of the point charge, ε_0 is the vacuum permittivity, ε_{NPL} is the dielectric (i.e. relative permittivity) of the NPL, ε_{ext} is the effective dielectric of the external environment, r is the exciton Bohr radius, t is the NPL thickness, and N is the number of image charges (Figure

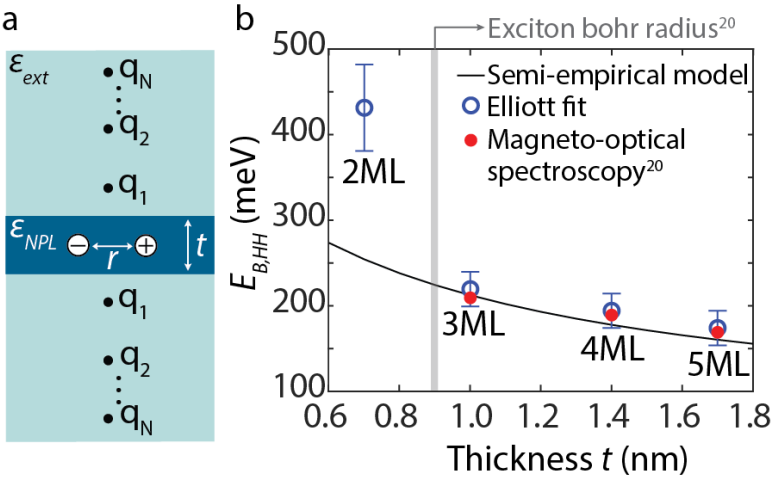

Figure 5.2. Experimental and Simulated Exciton Binding Energies

(a) Visualization of the exciton in the colloidal NPL system as represented in the method of images. (b) The relationship between exciton binding energy and CdSe NPL thickness, indicating the predicted trend of our semi-empirical electrostatic model, extracted values from absorption spectra using the modified Elliott model, and measured values from magneto-optical spectroscopy.

5.3a). The derivation of this potential equation and the effect of n on the extracted binding energy is explored in section 5.7, where we show $N = 20$ image charges reproduce the full potential.

We equate this potential in Eq. 3 to an effective two-point charge Coulombic potential, V_{eff}, with an overall effective relative dielectric constant, ε_{eff}:

$$V_{eff} = \frac{q}{4\pi\varepsilon_0\varepsilon_{eff}r} \tag{4}$$

Solving for ε_{eff} allows us to determine the exciton binding energy through the Rydberg equation:

$$E_B = \frac{e^2}{8\pi{\varepsilon_0}^2{\varepsilon_{eff}}^2 r} \tag{5}$$

The Bohr radii values are derived from the diamagnetic shift coefficient ((σ) obtained by magneto-optical spectroscopy performed by Brumberg et al. for 3-5 ML CdSe NPLs.[149] The E_B values for CdSe NPLs of varying thicknesses are shown in Figure 5.3b, where the data shows good agreement to the trend line produced by taking the average σ and its corresponding E_B's. In section 5.7 Figure 5.10, we describe in detail how each parameter is used to determine the continuous line plotted in Figure 3b. The electrostatic model captures the trend of decreasing E_B with thickness t, consistent with our Elliott fit and literature values of E_B for 3-5 ML CdSe NPLs, as shown in Table 5.1.

It should be noted that we represent electrostatic interactions through mean-field dielectric mediated Coulombic potential. Prior work in TMDCs has shown that the internal polarizability can be heavily dependent on the momentum direction.[172] We hypothesize this may be in part responsible for deviations of experiment to model particularly in thinner nanoplatelets, where the thickness of the NPLs is larger than the exciton Bohr radius (Figure 5.3b: grey line).[149] Our local effective potential computed from the method of images (Eq. 3) thus can be thought of as a first order correction to the 3D binding energy equation. Indeed, in section 5.7, we compute the binding

energy using a basis of hydrogenic orbitals for which we tune the coefficients variationally with the dielectric slab potential, which we find excellent agreement to our electrostatic model, but equivalent deviations for 2ML NPLs. Our results suggest that future simulations of NPL excitons (including high-level GW and Bethe-Saltpeter methods) should consider the more complex termination of organic ligands to fully capture NPL binding energies, especially in quantum confined regimes.[173,174]

5.5 Controlling Exciton Binding Energy by Modulating External Dielectric

To confirm the extent to which external dielectric contrast modulates exciton binding energy, we change the solvent environment, similar to previous work in TMDCs and 2D perovskites. [157,175,176] We measure E_B and E_G using the above Elliott model fit of the absorption spectrum of 3 ML HgTe NPLs (Figure 5.4a-1), initially suspended in hexanes ($\varepsilon_{Hexanes} \approx 1.9$). Then, acetonitrile (also known as MeCN, $\varepsilon_{MeCN} \approx 38$) is added to the hexane layer, and the solutions are vortexed for 1 minute. After letting it settle, the hexane layer is taken out and its absorption spectrum is measured (Figure 5.4a-2; the exact procedure can be found in section 5.7 with FTIR in Figure 5.11, showing no sign of ligand exchange). Finally, the NPLs are returned to their initial hexane environment, after thoroughly washing away the MeCN, and we observe the recovery of the exciton absorption peak, but with increased Rayleigh scatter baseline (Figure 5.4a-3). Altogether, Figure 5.4a shows the resultant shift and recovery of the $X_{1,HH}$ peak of the HgTe spectrum as the NPLs are exposed to a higher dielectric environment and returned to hexanes. Figures 5.4b and 5.4c demonstrate corresponding Elliott fit values that indicate an unchanged E_G in comparison to a 65 meV decrease in $E_{B,HH}$ and a 50 meV decrease in $E_{B,LH}$, supporting the hypothesis that we have increased the effective dielectric and thus lowered the E_B without changing the structure of the NPL. From the decreasing E_B's, we calculate a modest corresponding

increase in ε_{eff} from 13.8 to 15.1, due to the MeCN (Eq. 5). Using Eq. 3, we can infer the increase in ε_{ext} from 2.0 to 3.3; this is notable as the dielectric of MeCN is 38. The small change in ε_{ext} suggests the continued dominance of the aliphatic ligands on the dielectric environment, meaning MeCN only has limited access to the excitonic field lines. Therefore, the shift in HgTe E_B can be attributed to the change in the effective dielectric—suggesting more significant impact of the external dielectric on NPL excitonic behavior, than previously recognized. However, we note that

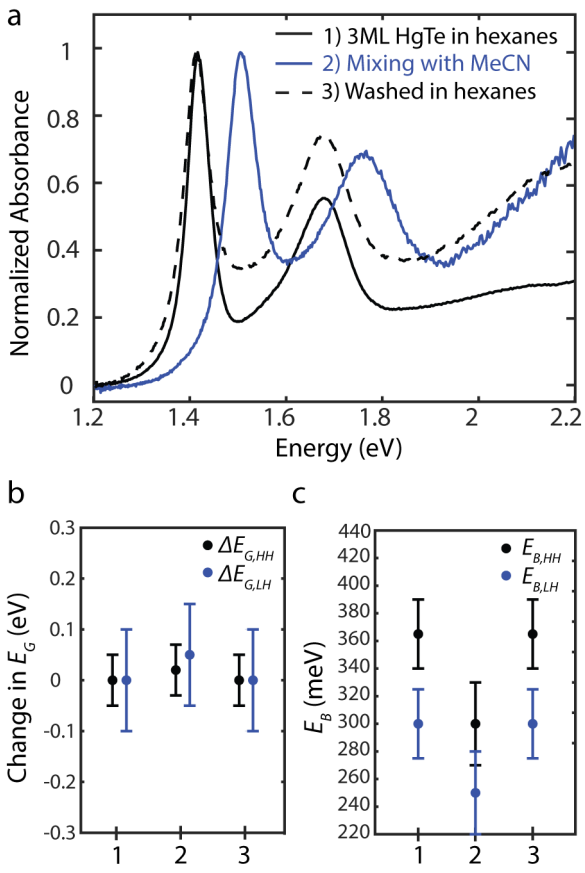

Figure 5.3. Affecting Exciton Binding Energy with Change in Solvent Dielectric

(a) Shift in the $X_{1,HH}$ transition peak as 3 ML HgTe NPLs are vortexed with MeCN mixture and then washed back into hexanes. The baseline increases due to increased Rayleigh scatter. (b) The minimal change in bandgap energy as it corresponds to 1. suspension in hexanes, 2. mixing with MeCN, and 3. washing in hexanes steps, as indicated in (a). (c) The exciton binding energy as it corresponds to steps 1-3, showing a significant decrease in E_B with constant E_G as the NPLs experience a higher solvent dielectric in step 2.

this procedure did not appear to alter the binding energy in cadmium selenide/telluride and mercury selenide nanocrystals (section 5.7; Figures. 5.12-5.15), which we attribute to denser ligand coverage in these metal chalcogenide nanocrystals.[139]

5.6 Conclusions

Our results deviate from the known behaviors of 2D TDMC semiconductors, where the modification of the external dielectric is expected to change not only the exciton binding energy but also the bandgap. In the case of single layer $MoSe_2$, the bandgap and binding energies both differed in comparing vacuum to bilayer graphene.[177,178] Raja et *al.* reported similar effects in monolayer WS_2 which showed micron-sized, spatial fluctuations of the external dielectric screening.[179] Interestingly they observed minimal shifts in the exciton peak, due to compensating shifts in the bandgap and exciton binding energy. However, we believe these complementary shifts in E_B and E_G are monolayer TMDC properties, and not a general feature of 2D semiconductors. In fact, Passarelli et *al.* demonstrated that exciton binding energy in 2D perovskites can be tuned by doping the organic layer.[157] Here, they report an unchanged bandgap energy as they modulate the external dielectric by increasing the dopant concentration, while observing a decrease in the exciton binding energy. In general, we hypothesize that the effect of external dielectric will be more strongly felt in exciton binding energies and less so in bandgaps due to their relatively large Bohr radius.

Another consideration is that external dielectrics do not only modify the strength of the exciton binding energy, but also the spacing of the Rydberg levels. This effect is modeled by Olsen *et al*. with a modified Rytova-Keldysh formalism and observed in monolayer WS_2 by Chernikov *et al.*[174,180–185] In our work, a 3D Wannier exciton model shows good agreement to experimental data, and we lack the resolution to probe deviations from the classical Rydberg series. However,

such deviations may also contribute to the apparent large binding energy observed in 2 ML platelets. We explored both a variational and perturbative treatment of the excitonic Hamiltonian (section 5.7) and found results in good agreement with our effective dielectric model. However, there was no significant improvement in the apparent discrepancy observed for 2 ML platelets, suggesting the insufficiency of effective potential in describing binding energies in this limit.

Exciton binding energies are important experimental parameters which govern absorption, emission, and energy and charge transport. Using a modified Elliott model, we extract binding energies for many NPLs—several of them for the first time—which also show excellent agreement to prior limited measurements. This model represents a simple and accessible tool to probe excitonic and continuum transitions from absorption measurements, complementing sophisticated techniques such as magneto-optical spectroscopy or opto-acoustic methods which were previously used.[149,186]

We also explore the effect of dielectric screening on NPL excitons using a simple semi-empirical electrostatic model, which produced calculated ’s that are in excellent agreement to measured binding energies for 3-5 ML CdSe NPLs. The model confirmed that unlike their bulk and 0D counterparts, nanoplatelet excitonic electrostatic field lines extend beyond the semiconductor itself and are modulated by the external environment. We experimentally confirm the effect of dielectric confinement by modifying NPL external environment and showing a noticeable shift in exciton binding energy, consistent with similar measurements in 2D TMDCs and perovskites.[157,175,186] Uncovering the exciton binding energies of NPLs and understanding how external dielectric screening modulates these resonances further establishes the distinct properties of nanoplatelets that distinguish them from their quantum dot counterparts.

5.7 Supporting Information

This section covers additional details about the results discussed in this chapter, including materials synthesis, characterization, spectral fitting procedures, calculation steps for extracting exciton binding energies from Elliott model fits, variational approach to calculating exciton binding energies, and experimental procedure for dielectric modulation of NPLs.

Materials and Methods

Cadmium acetate dihydrate (Acros, 98%), selenium powder (Acros, 99.5%), tellurium powder (Acros, 99.8%) 1,2-dichlorobenzene (Acros, 99%), cadmium oxide (Alfa Aesar, 99.95%) , oleic acid (Alfa Aesar, 99%), tri-n-octylphosphine (TOP) (Alfa Aesar, 90%), 1-octadecene (ODE) (Alfa Aesar, 90%), mercury (II) acetate (Chem-Impax International, 98.0%), ethanol (Fisher, 95.27%), hexanes (Fisher, 98.5%), toluene (Alpha Aesar, 99.8%), propionic acid (Fisher, 99%), oleylamine (Tokyo Chemical, 50.0%), and triisobutylamine (Sigma Aldrich, 98%) were used.

Synthesis of Precursors

1M TOP-X (X= Se, Te). In a small flask, 5 mmol of X powder and 2 mL of tri-n-octylphosphine were degassed under vacuum at room temperature. Then, under Ar flow, the solution was stirred (at room temperature for TOP-Se, or at 275 °C for TOP-Te) until the dissolution was complete.

Cadmium propionate. 1.036 g cadmium oxide was mixed with 10 mL propionic acid for 1hr under Ar flow. The flask was then opened and heated to 140 °C until the volume was reduced by half. The solution was precipitated with acetone and centrifuged, and the white solid was dried and stored in a vacuum desiccator.

Cadmium myristate. Following Diroll et al,[187] 4.68 g myristic acid was melted at 50 °C followed by the addition of 1.28 g cadmium oxide. Under Ar flow, the reaction was further heated to 250 °C until the solution became clear. Once cooled, the solid white product formed was collected and washed with methanol five times, then dried and stored in a vacuum desiccator.

Synthesis of CdX and HgX NPLs

2 ML CdTe. Following Pedetti *et al*,[188,189] 170 mg cadmium propionate, 104 µL oleic acid, and 10 mL octadecene (ODE) were degassed at 90 °C for 1 hr. Under Ar flow, 130 µL of 1M TOP-Te in 650 µL ODE were injected at 180 °C. After 20 minutes, the reaction was cooled to room temperature and 1 mL of oleic acid was added. The crude mixture was precipitated with ethanol and centrifuged twice, then resuspended in 10 mL hexanes.

2 ML CdSe. Following Dufour *et al*,[190] 170 mg cadmium myristate, 12 mg selenium powder, and 14 mL ODE were degassed at room temperature for 20 min. Under Ar flow, the reaction was heated to 150 °C, and when the temperature reached 110 °C, a mixture of 65 µL propionic acid in 1 mL ODE was injected. After 15 minutes at 150 °C, 1 mL of oleic acid was added and the reaction was cooled to room temperature. The crude mixture was precipitated with 15 mL hexanes and 15 mL ethanol, centrifuged and resuspended in 5 mL hexanes.

3 ML CdTe. Adapted from Izquierdo *et al*,[136,191] 260 mg of cadmium propionate, 0.160 mL of oleic acid, and 20 mL of ODE were degassed under vacuum at 90 °C for 1 hour. Under Ar flow, the reaction was heated to 210 °C and 0.200 mL of 1M TOP-Te mixed with 3.75 mL of octadecene was injected with a syringe pump at a rate of 5 mL/hr. The solution was cooled and 0.500 mL of oleic acid was injected. The NPLs were precipitated with 15 mL hexanes and 15 mL ethanol, centrifuged, and resuspended in 20 mL hexanes.

3 ML CdSe. Adapted from Izquierdo *et al*,[136,191] 240 mg of cadmium acetate dihydrate, 0.150 mL of oleic acid and 15 mL of ODE were degassed under vacuum at 80 °C for 1hr. Under Ar flow, the reaction was heated to 195 °C and 0.4 mL of 1M TOP-Se mixed with 3.75 mL ODE was injected with a syringe pump at a rate of 5 mL/hr. The solution was cooled and the NPLs were precipitated with 15 mL hexanes and 15mL ethanol, centrifuged, and resuspended in 20 mL of hexanes.

4 ML CdSe. Following Pedetti *et al*,[189] 340 mg cadmium myristate, 24 mg Se powder, and 30 mL ODE were degassed at room temperature for 20 minutes. Under Ar flow, the temperature was set to 240 °C. When it reached 205 °C, 80 mg of cadmium acetate were added, and the solution turned red. The solution then reacted at 240 °C for 12 minutes followed by the addition of 2 mL oleic acid and rapid cooling to room temperature. The crude reaction mixture was added to 30 mL hexanes and 40 mL ethanol and centrifuged at 6000 rpm for 10 min, followed by a resuspension in 10 mL hexanes.

5 ML CdSe. Following Pedetti *et al*,[189] 340 mg cadmium myristate and 28 mL ODE were degassed at room temperature for 20 minutes. Under Ar flow, the solution was heated to 250 °C at which point 24 mg of Se powder in 2 mL ODE were swiftly injected. After 30s, 300 mg of cadmium acetate was also added. The reaction was held at 250 °C for an additional 7 minutes, followed by the addition of 1 mL oleic acid and rapid cooling to room temperature. The crude reaction mixture was added to 30 mL hexanes and 40 mL ethanol and centrifuged at 6000 rpm for 10 min, followed by a resuspension in 10 mL hexanes. Further purification was done by adding 1:4 ethanol to hexanes, and centrifuging at 6000 rpm. The supernatant contained mostly 5 ML NPLs.

2 and 3 ML HgX (X=Te, Se). Following a method adapted from Izquierdo *et al*,[139,191] 0.3 mL of 10 mM mercury (II) acetate in oleylamine is added to 0.240 mL of 6mM CdX NPL and 6 mL of hexanes. The solution is stirred at room temperature for 3.5 to 4 hr. The NPLs were then centrifuged at 9000 rpm for 10 minutes and resuspended in 5 mL hexanes.

Material Characterization

Absorption spectra were acquired with an Agilent Cary 60 UV-Vis spectrophotometer. Transmission electron microscopy (TEM) images were acquired with a FEI Tecnai G2 TF20 200 kV TEM. The NPLs were diluted in hexanes and drop casted on Ted Pella, Inc. Formvar 300 mesh copper grids. Infrared (IR) spectroscopy was performed using a Perkin-Elmer Spectrum Two Fourier Transform IR spectrometer equipped with a universal Diamond/ZnSe ATR. NPLs were cleaned using centrifugation and a syringe filter. Energy dispersive X-ray Spectroscopy (EDS) measurements were obtained on a JEOL JSM-6700F FE scanning electron microscope equipped with an EDX detector. The NPLs were purified using a syringe filter and dropcast onto either aluminum or silicon substrate. EDX measurements were collected using an operating bias of 9 kV. The EDS results are shown below.

Table 5.2 Electron Dispersive X-ray Spectroscopy (EDS).

The relative average atomic percent of the different monolayer nanoplatelets. Each value represents the weighted average of 10 scans, with its standard error of the weighted mean calculated from the uncertainty of the individual scans.

Relative Average Atomic Percent (%)				
Element	**2 ML**	**3 ML**	**4 ML**	**5 ML**
Cd	62 ± 7	64 ± 2	61 ± 2	48 ± 1
Se	36 ± 2	36 ± 1	39 ± 1	45 ± 1
Cd	54 ± 4	53 ± 2		
Te	46 ± 4	47 ± 3		
Hg		48 ± 3		
Se		52 ± 3		
Hg	44 ± 2	37 ± 3		
Te	56 ± 4	61 ± 7		
Expected M	60	57	56	55
Expected X	40	43	44	45

Fourier Transform Infrared Spectroscopy (FTIR)

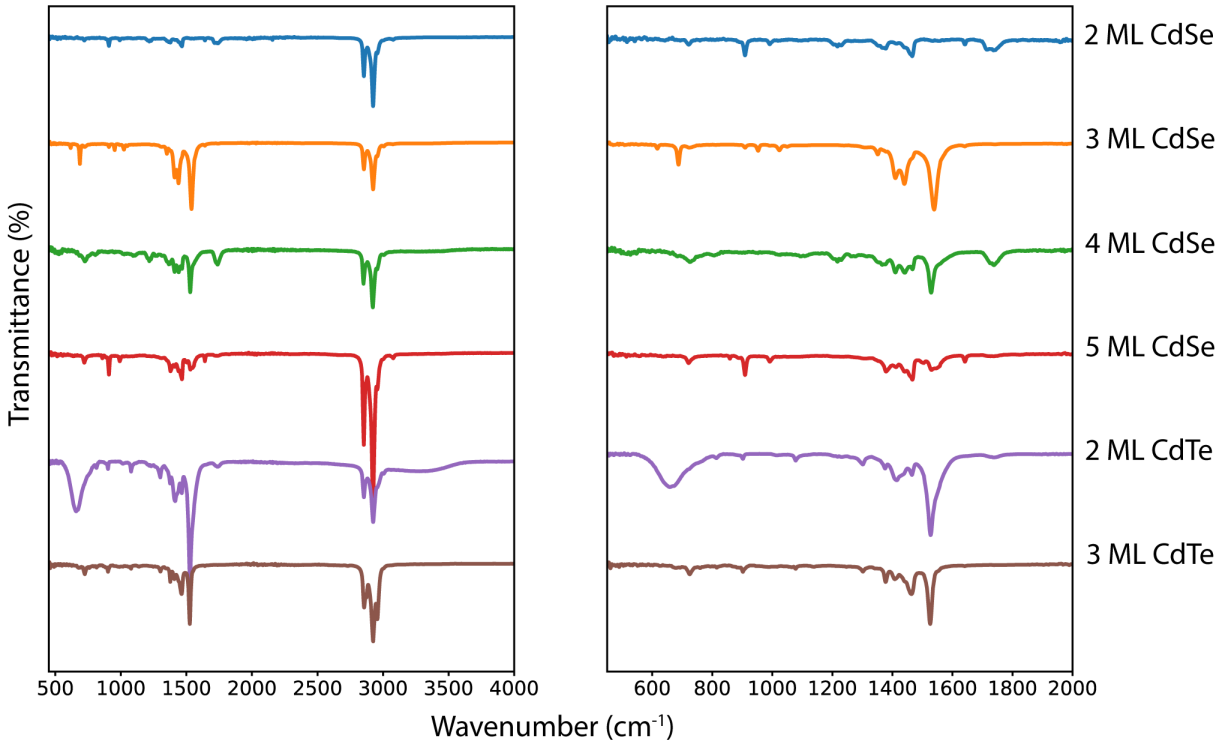

Figure 5.5 FTIR data of different monolayer CdX (X=Se, Te) NPLs.

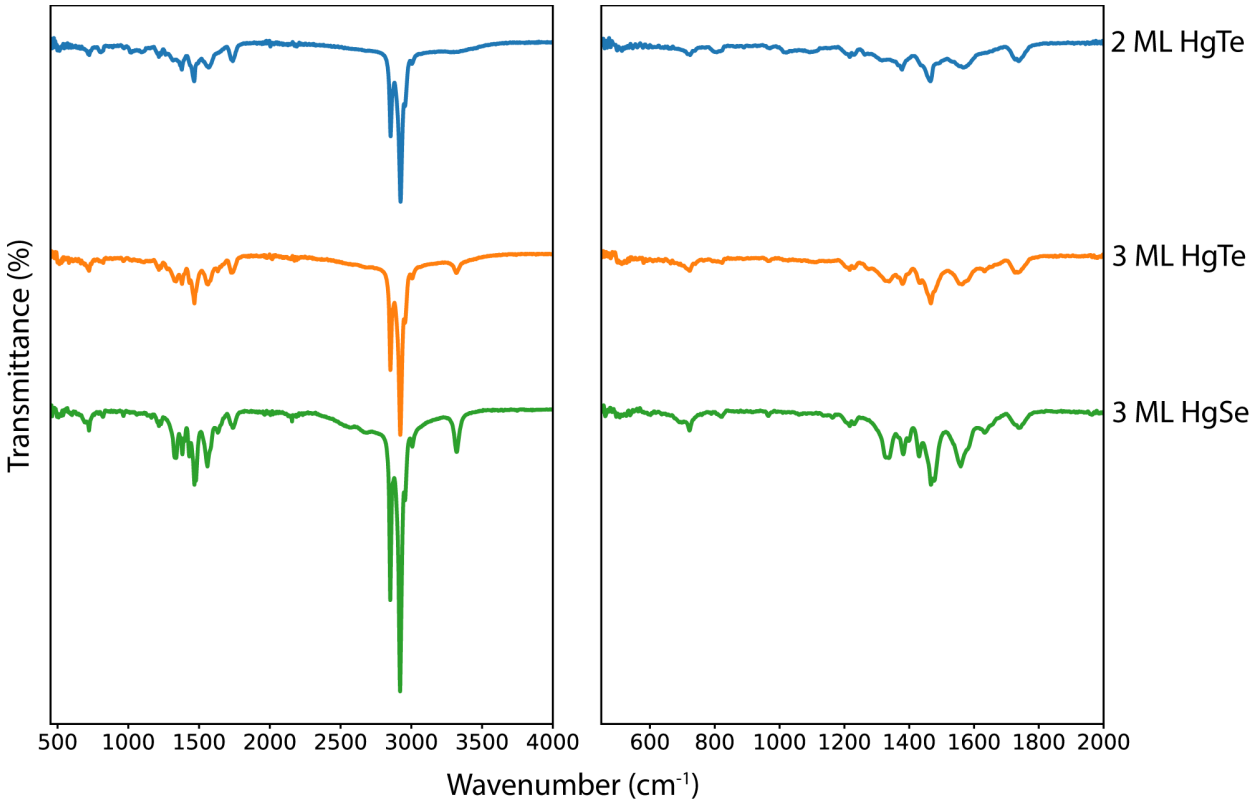

Figure 5.6 FTIR data for different monolayer HgX (X=Se, Te) NPLs.

Transmission Electron Microscopy (TEM)

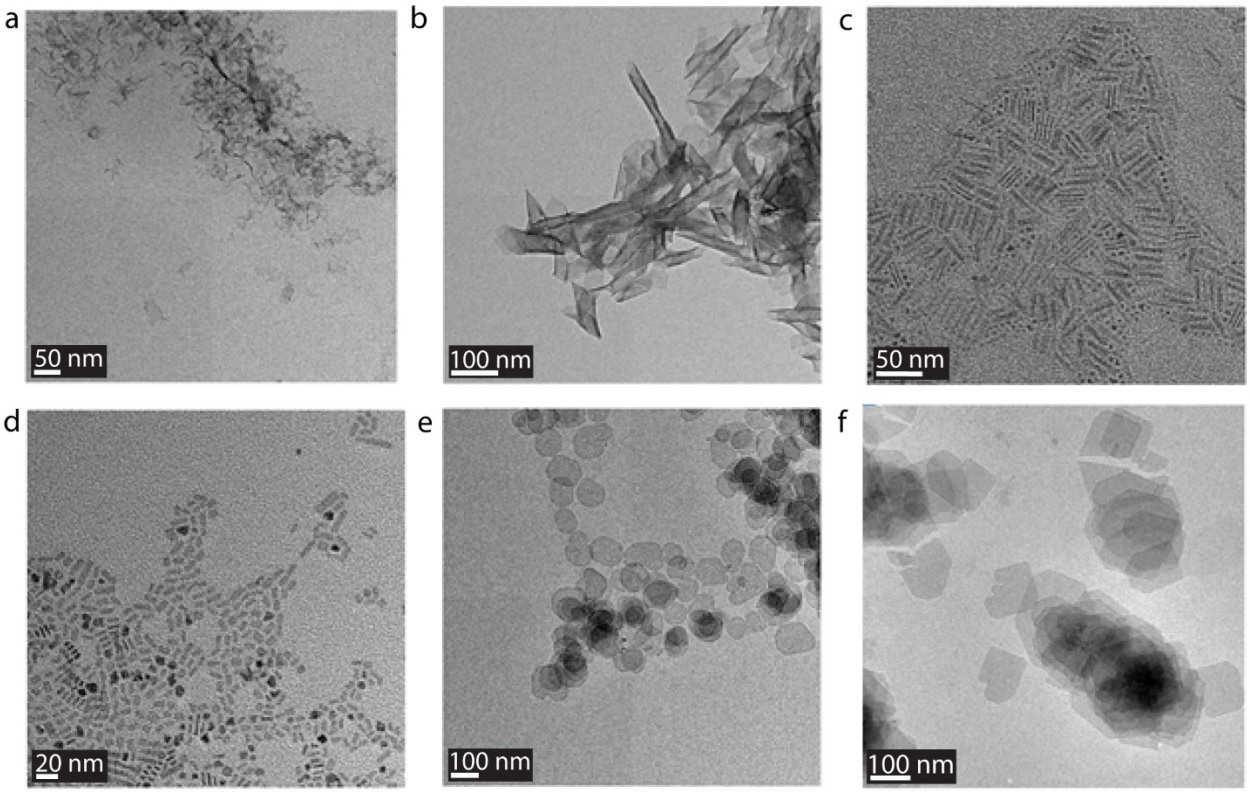

Figure 5.7 TEM images of CdX NPLs.

(a) 2ML CdSe, (b) 3 ML CdSe, (c) 4 ML CdSe, (d) 5 ML CdSe, (e) 2 ML CdTe, and (f) 3 ML CdTe.

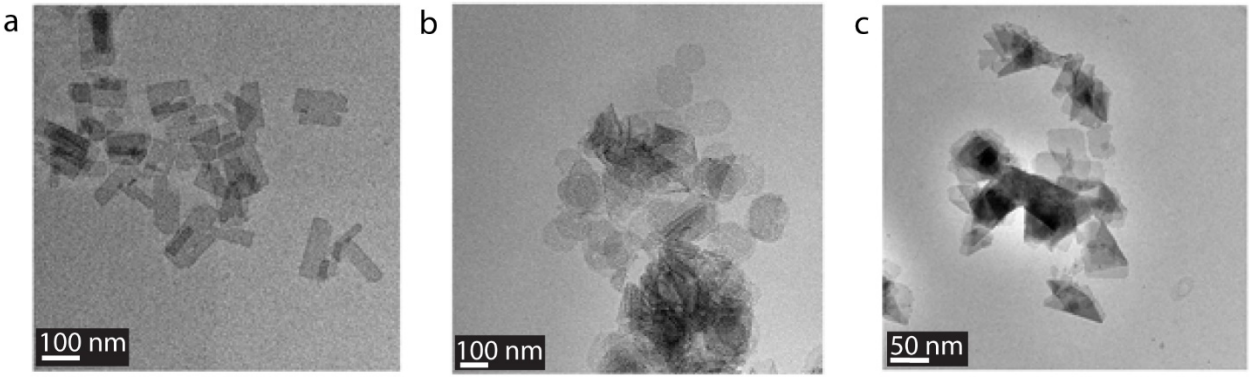

Figure 5.8 TEM images of HgX NPLs.

(a) 3 ML HgSe, (b) 2 ML HgTe, (c) 3 ML HgTe

Fitting of Absorption Spectra

The Elliott function (Eq.1) is used to fit the absorption spectra using a custom two-step optimization program on MATLAB. Given a starting point ($\overrightarrow{\theta_0}$) and upper and lower bounds to describe a region of interest (R_0) for the eight parameters ($E_{B,\,HH}$, $E_{B,\,LH}$, $E_{G,\,HH}$, $E_{G,\,LH}$, K_{HH}, K_{LH}, Γ_{HH}, Γ_{LH}), the program searches the optimal region for the parametric combination that minimizes the sum of squares error. The optimization program first uses Trust-Region Non-Linear Least Squares Regression Algorithm (TR) to obtain a "fit"($\overrightarrow{\theta_1}$) and tighter region of interest R_1. The second part of the program takes $\overrightarrow{\theta_1}$ and R_1 as inputs and uses Hamiltonian Markov Chain Monte Carlo (HMCMC) to create a statistical inference of the best fit ($\overrightarrow{\theta_2}$) by exploring the smaller region, R_1. HMCMC is less likely to fall into local minima and more likely to converge to a global minimum, however it is much more computationally expensive.

Convolution Steps for Linewidth Broadening

In order to account for linewidth broadening in the absorption, the Elliott formulae were convolved with $\left(\frac{E}{\gamma}\right)$, where γ is a broadening factor and τ is the convolution parameter.

D = 3 Convolution

$$\alpha_3^* = \alpha_3(E) * f(E) = \int_{-\infty}^{\infty} d\tau \ \alpha_3(\tau) f(E-\tau)$$

α_3^* will be called the modified Elliot's formula

$$\alpha_3^* \propto \int_{-\infty}^{\infty} d\tau \left[\sum_{n=1}^{\infty} \left(\frac{2E_B}{n^3} \cdot \delta\left(\tau - E_G + \frac{E_B}{n^2}\right)\right) + \frac{1}{1-\mathrm{e}^{-2\pi\sqrt{\frac{E_B}{\tau - E_G}}}} \cdot \Theta(\tau - E_G) \right] \cdot \operatorname{sech}\left(\frac{E-\tau}{\gamma}\right)$$

$$\alpha_3^* \propto \left[\sum_{n=1}^{\infty} \left(\frac{2E_B}{n^3} \int_{-\infty}^{\infty} d\tau \, \delta\left(\tau - E_G + \frac{E_B}{n^2}\right) \operatorname{sech}\left(\frac{E-\tau}{\gamma}\right)\right) + \int_{-\infty}^{\infty} d\tau \frac{\Theta(\tau - E_G)}{1-\mathrm{e}^{-2\pi\sqrt{\frac{E_B}{\tau - E_G}}}} \cdot \operatorname{sech}\left(\frac{E-\tau}{\gamma}\right) \right]$$

Lemmas (1):

Using the properties of the delta function, it follows:

$$\int_{-\infty}^{\infty} d\tau \ \delta(\tau - a) f(b-\tau) = f(b-a)$$

Using the properties of the Heaviside function, it follows:

$$\int_{-\infty}^{\infty} d\tau \ \Theta(\tau - a) f(\tau) = \int_{a}^{\infty} f(\tau)$$

$$\alpha_3^* \propto \left[\sum_{n=1}^{\infty}\left(\frac{2E_B}{n^3}\operatorname{sech}\left(\frac{E-E_G+\frac{E_B}{n^2}}{\gamma}\right)\right)+\int_{E_G}^{\infty} d\tau \frac{\operatorname{sech}\left(\frac{E-\tau}{\gamma}\right)}{1-\mathrm{e}^{-2\pi\sqrt{\frac{E_B}{\tau-E_G}}}}\right]$$

D = 2 Convolution

$$\alpha_2^* = \alpha_2(E) * f(E) = \int_{-\infty}^{\infty} d\tau\, \alpha_2(\tau) f(E-\tau)$$

It follows fairly easily by plugging in $\alpha_2(E)$ and $f(E)$ and substituting τ appropriately and applying Lemmas (1)

$$\alpha_2^* \propto \left[\sum_{n=1}^{\infty}\left(\frac{2E_B}{\left(n-\frac{1}{2}\right)^3}\operatorname{sech}\left(\frac{E-E_G+\frac{E_B}{\left(n-\frac{1}{2}\right)^2}}{\gamma}\right)\right)+\int_{E_G}^{\infty} d\tau \frac{\operatorname{sech}\left(\frac{E-\tau}{\gamma}\right)}{1-\mathrm{e}^{-2\pi\sqrt{\frac{E_B}{\tau-E_G}}}}\right]$$

Derivation of the Elliott's Formula

For the following derivations:

$$E = \hbar\omega$$

$$\beta = \sqrt{\frac{E_B}{E - E_G}},$$

Γ is the Euler-Gamma function

Θ is the Heaviside step function

Below is the Elliot function in general dimension D:

$$\alpha_D(E) \propto \left[\sum_{n=1}^{\infty} \left(\frac{E_B \Gamma(n + D - 2)}{(n-1)! \left(n + \frac{D-3}{2}\right)^{D+1}} \cdot \delta\left(E - E_G + \frac{E_B}{\left(n + \frac{D-3}{2}\right)^2} \right) \right) + \frac{\left| \Gamma(\frac{D-1}{2} + i\beta) \right|^2 e^{\pi\beta} \beta^{2-D}}{2^D \pi^{2-\frac{D}{2}} \Gamma\left(\frac{D}{2}\right)} \cdot \Theta(E - E_G) \right]$$

D = 3 Derivation of Elliott's Formula

$$\alpha_3(E) \propto \left[\sum_{n=1}^{\infty} \left(\frac{E_B \Gamma(n+1)}{(n-1)!\,(n)^4} \cdot \delta\left(E - E_G + \frac{E_B}{n^2} \right) \right) + \frac{|\Gamma(1 + i\beta)|^2 e^{\pi\beta} \beta^{-1}}{2^3 \pi^{\frac{1}{2}} \Gamma\left(\frac{3}{2}\right)} \cdot \Theta(E - E_G) \right]$$

$$\alpha_3(E) \propto \left[\sum_{n=1}^{\infty} \left(\frac{E_B n!}{(n-1)!\,(n)^4} \cdot \delta\left(E - E_G + \frac{E_B}{n^2} \right) \right) + \frac{|\Gamma(1 + i\beta)|^2 e^{\pi\beta} \beta^{-1}}{2^3 \pi^{\frac{1}{2}} \Gamma\left(\frac{3}{2}\right)} \cdot \Theta(E - E_G) \right]$$

Using the Euler's reflection and Legendre's Duplication formulae, it follows:

$$|\Gamma(1+\ i\beta)|^2 = \frac{\pi\beta}{sinh\ (\pi\beta)}$$

Also, important to note: $\Gamma\left(\frac{3}{2}\right) = \frac{\sqrt{\pi}}{2}$ and $sinh\ (x)\ = \frac{1}{2}(e^x - e^{-x})$

$$\alpha_3(E) \propto \left[\sum_{n=1}^{\infty}\left(\frac{E_B}{n^3}\cdot\delta\left(E - E_G + \frac{E_B}{n^2}\right)\right) + \frac{\pi\beta e^{\pi\beta}\beta^{-1}}{8\sqrt{\pi}\frac{\sqrt{\pi}}{2}sinh\ (\pi\beta)}\cdot\Theta(E - E_G)\right]$$

$$\alpha_3(E) \propto \left[\sum_{n=1}^{\infty}\left(\frac{E_B}{n^3}\cdot\delta\left(E - E_G + \frac{E_B}{n^2}\right)\right) + \frac{1}{2(1-e^{-2\pi\beta})}\cdot\Theta(E - E_G)\right]$$

$$\alpha_3(E) \propto \left[\sum_{n=1}^{\infty}\left(\frac{2E_B}{n^3}\cdot\delta\left(E - E_G + \frac{E_B}{n^2}\right)\right) + \frac{1}{1-e^{-2\pi\beta}}\cdot\Theta(E - E_G)\right]$$

D = 2 Derivation of Elliott's Formula

$$\alpha_2(E) \propto \left[\sum_{n=1}^{\infty}\left(\frac{E_B\Gamma(n)}{(n-1)!\left(n-\frac{1}{2}\right)^3}\cdot\delta\left(E - E_G + \frac{E_B}{\left(n-\frac{1}{2}\right)^2}\right)\right) + \frac{\left|\Gamma(\frac{1}{2}+\ i\beta)\right|^2 e^{\pi\beta}}{2^2\,\pi\Gamma(1)}\right.$$

$$\left.\cdot\Theta(E - E_G)\right]$$

$$\alpha_2(E) \propto \left[\sum_{n=1}^{\infty}\left(\frac{E_B(n-1)!}{(n-1)!\left(n-\frac{1}{2}\right)^3}\cdot\delta\left(E - E_G + \frac{E_B}{\left(n-\frac{1}{2}\right)^2}\right)\right) + \frac{\left|\Gamma(\frac{1}{2}+\ i\beta)\right|^2 e^{\pi\beta}}{2^2\,\pi\Gamma(1)}\right.$$

$$\left.\cdot\Theta(E - E_G)\right]$$

Using the Euler's reflection and Legendre's Duplication formulae, one can show:

$$\left|\Gamma(\frac{1}{2}+\ i\beta)\right|^2 = \frac{\pi}{cosh\ (\pi\beta)}$$

Also important to note: $\Gamma(1) = 1$ and $cosh\ (x)\ = \frac{1}{2}(e^x + e^{-x})$

$$\alpha_2(E) \propto \left[\sum_{n=1}^{\infty}\left(\frac{E_B}{\left(n-\frac{1}{2}\right)^3}\cdot\delta\left(E-\ E_G+\frac{E_B}{\left(n-\frac{1}{2}\right)^2}\right)\right)+\frac{\pi e^{\pi\beta}}{2^2\pi\cosh\left(\pi\beta\right)}\cdot\Theta(E-\ E_G)\right]$$

$$\alpha_2(E) \propto \left[\sum_{n=1}^{\infty}\left(\frac{E_B}{\left(n-\frac{1}{2}\right)^3}\cdot\delta\left(E-\ E_G+\frac{E_B}{\left(n-\frac{1}{2}\right)^2}\right)\right)+\frac{1}{2(1+e^{-2\pi\beta})}\cdot\Theta(E-\ E_G)\right]$$

$$\alpha_2(E) \propto \left[\sum_{n=1}^{\infty}\left(\frac{2E_B}{\left(n-\frac{1}{2}\right)^3}\cdot\delta\left(E-\ E_G+\frac{E_B}{\left(n-\frac{1}{2}\right)^2}\right)\right)+\frac{1}{1+e^{-2\pi\beta}}\cdot\Theta(E-\ E_G)\right]$$

The Exciton Binding Energy for 2D vs 3D Elliott's Formulae

Pulling out the n=1 terms for the 3D and 2D Elliot Formulae yields the description of the 1s absorption peak.

$$\text{3D: } 2E_{B,3}\ \delta\left(E-E_G+E_{B,3}\right)$$

$$\text{2D: } 16E_{B,2}\ \delta\left(E-E_G+4E_{B,2}\right)$$

From above, the 3D model predicts the 1s absorption to be 2 times larger than the continuum and the 2D model predicts the 1s absorption to be 16 times larger. For a given absorption spectra, the location of the continuum ($E = E_G$) and 1s peak ($E = E_1$) is fixed by the

data. The difference between these positions $\Delta E = E_G - E_1$ is thereby also fixed, and given by the following expressions:

$$\text{3D: } \Delta E = E_{B,3}$$

$$\text{2D: } \Delta E = 4E_{B,2}$$

$$\Rightarrow \frac{E_{B,3}}{E_{B,2}} = 4$$

This implies that the exciton binding energy predicted by the 2D model will be ~4 times smaller than the binding energy predicted by the 3D model, unless the location of the continuum, i.e.: E_G, is adjusted accordingly by the fitting algorithm. But even so, there is some ambiguity in the literature about what the exciton binding energy actually is, whether it comes from the Elliott model or just ΔE.

Effect of 2D vs. 3D Elliott Model Fitting

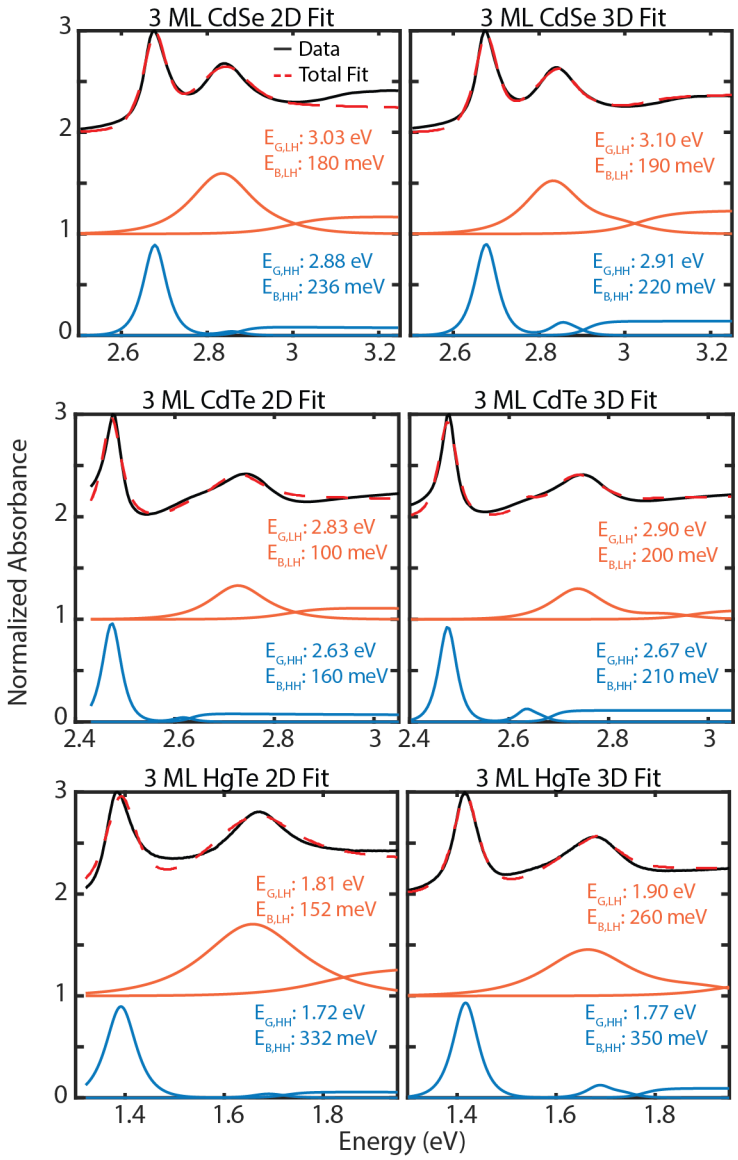

Figure 5.9 2D vs. 3D Elliott Model Fits

Absorption spectra of 3 ML CdSe, CdTe, and HgTe and their 2D (left) vs. 3D (right) Elliott fits.

Useful Approximations

The continuum term $C(E) = \int_{E_G}^{\infty} d\tau \frac{\operatorname{sech}\left(\frac{E-\tau}{\gamma}\right)}{1 \pm e^{-2\pi\sqrt{\frac{E_B}{\tau - E_G}}}}$ can often prolong computation time while fitting as it does not have a closed-form solution and requires the integral to be evaluated for every value of E in the absorption data.

$$\int dx \operatorname{sech}(x) = \arctan\left(\sinh\left(x\right)\right)$$

Which can be used with the u-sub, $= \frac{a-x}{b}$, to show:

$$\int dx \operatorname{sech}\left(\frac{a-x}{b}\right) = -b \arctan\left(\sinh\left(\frac{a-x}{b}\right)\right)$$

Also note:

$$\lim_{x \to -\infty} \sinh(x) = -\infty$$

$$\lim_{x \to -\infty} \arctan(x) = -\frac{\pi}{2}$$

A useful closed-form approximation can be found by taking $e^{-2\pi\sqrt{\frac{E_B}{\tau - E_G}}} = 0$, which simplifies $C(E)$ to:

$$\int_{E_G}^{\infty} d\tau \operatorname{sech}\left(\frac{E-\tau}{\gamma}\right)$$

$$= -\gamma \arctan\left(\sinh\left(\frac{E-\tau}{\gamma}\right)\right), \tau \text{ evaluated from } E_G \to \infty$$

$$= \lim_{\tau \to \infty} -\gamma \arctan\left(\sinh\left(\frac{E-\tau}{\gamma}\right)\right) + \gamma \arctan\left(sinh\left(\frac{E-E_G}{\gamma}\right)\right)$$

$$= \frac{\gamma\pi}{2} + \gamma \arctan\left(sinh\left(\frac{E - E_G}{\gamma}\right)\right)$$

Application of the Method of Images

We detail below the derivation of the potential equation reported. The potentials below are derived from a method of images diagram, as shown in Figure 2.3a of the manuscript.

$$V_{in}(x, y, z) = \frac{e}{4\pi\epsilon_0\epsilon_{in}R(0)} + \sum_{n=1}^{\infty} \frac{q_{i,n}}{4\pi\epsilon_0\epsilon_{in}}\left(\frac{1}{R(nt)} + \frac{1}{R(-nt)}\right)$$

$R(z') = \sqrt{r^2 + (z - z')^2}$,

$r^2 = x^2 + y^2$, exciton Bohr radius

$q_{i,n}$ = nth image charge

t = thickness of NPL

$\epsilon_{in}, \epsilon_{out}$ is the dielectric in and out of the NPL respectively

$$V_{out}(x, y, z) = \frac{q'}{4\pi\epsilon_0\epsilon_{out}R(0)}$$

q' is the shielded charge seen by the outside material.

Applying Boundary Conditions (BCs). By integrating over Maxwell's Equations, the following BCs can be derived:

$$\frac{\partial V_{in}}{\partial x}(x, y, t/2) = \frac{\partial V_{out}}{\partial x}(x, y, t/2)$$

$$\frac{\partial V_{in}}{\partial x}(x, y, -t/2) = \frac{\partial V_{out}}{\partial x}(x, y, -t/2)$$

$$\frac{\partial V_{in}}{\partial y}(x,y,t/2) = \frac{\partial V_{out}}{\partial y}(x,y,t/2)$$

$$\frac{\partial V_{in}}{\partial y}(x,y,-t/2) = \frac{\partial V_{out}}{\partial y}(x,y,-t/2)$$

$$\epsilon_{in}\frac{\partial V_{in}}{\partial z}(x,y,t/2) = \epsilon_{out}\frac{\partial V_{out}}{\partial z}(x,y,t/2)$$

$$\epsilon_{in}\frac{\partial V_{in}}{\partial z}(x,y,-t/2) = \epsilon_{out}\frac{\partial V_{out}}{\partial z}(x,y,-t/2)$$

Applying the BCs results in:

$$q_{i,n} = \left(\frac{\epsilon_{in}-\epsilon_{out}}{\epsilon_{in}+\epsilon_{out}}\right)^n e$$

Final Potential. This yields that the potential inside the NPL caused by an elementary point charge is:

$$V_{in}(x,y,z) = \frac{e}{4\pi\epsilon_0\epsilon_{in}r(0)} + \frac{e}{4\pi\epsilon_0\epsilon_{in}}\sum_{n=1}^{\infty}\left(\frac{\epsilon_{in}-\epsilon_{out}}{\epsilon_{in}+\epsilon_{out}}\right)^n\left(\frac{1}{r(nt)}+\frac{1}{r(-nt)}\right)$$

Limits. To make sense of the formula, look at the formula in some important limits. In order to simplify the calculations, move to the center of the NPL by setting $z = 0$.

$$V(r) = \frac{e}{4\pi\epsilon_0\epsilon_{in}r} + \frac{e}{2\pi\epsilon_0\epsilon_{in}}\sum_{n=1}^{\infty}\left(\frac{\epsilon_{in}-\epsilon_{out}}{\epsilon_{in}+\epsilon_{out}}\right)^n \cdot \frac{1}{\sqrt{r^2+n^2t^2}}$$

Where $r = \sqrt{x^2+y^2}$, in-plane exciton Bohr radius

Limit 1: $t \gg r \rightarrow \frac{r}{t} \ll 1$

$$V(r) = \frac{e}{4\pi\epsilon_0\epsilon_{in}r} + \frac{e}{2\pi\epsilon_0\epsilon_{in}}\sum_{n=1}^{\infty}\left(\frac{\epsilon_{in}-\epsilon_{out}}{\epsilon_{in}+\epsilon_{out}}\right)^n \cdot \frac{1}{t\sqrt{\left(\frac{r}{t}\right)^2 + n^2}}$$

$$V(r) = \frac{e}{4\pi\epsilon_0\epsilon_{in}r} + \frac{e}{2\pi\epsilon_0\epsilon_{in}t}\sum_{n=1}^{\infty}\left(\frac{\epsilon_{in}-\epsilon_{out}}{\epsilon_{in}+\epsilon_{out}}\right)^n \cdot \frac{1}{n}$$

Note that: $\sum_{n=1}^{\infty}\frac{z^n}{n} = -\ln(1-z)\,, \forall|z|<1$

In this case, $z = \frac{\epsilon_{in}-\epsilon_{out}}{\epsilon_{in}+\epsilon_{out}} < 1$, as $\epsilon_{out} > 1$

$$V(r) = \frac{e}{4\pi\epsilon_0\epsilon_{in}r} - \frac{e}{2\pi\epsilon_0\epsilon_{in}t}\ln\left(\frac{2\epsilon_{out}}{\epsilon_{in}+\epsilon_{out}}\right)$$

In the limit, $\frac{1}{t} \to 0$

$$V(r) = \frac{e}{4\pi\epsilon_0\epsilon_{in}r}$$

Only the inside dielectric potential becomes important, which makes sense as the thickness is much larger than the spatial extent. Most of the field lines pass through the material, so the outside dielectric has less of an effect.

Limit 2: $r \gg t \to \frac{t}{r} \ll 1$

$$V(r) = \frac{e}{4\pi\epsilon_0\epsilon_{in}r} + \frac{e}{2\pi\epsilon_0\epsilon_{in}}\sum_{n=1}^{\infty}\left(\frac{\epsilon_{in}-\epsilon_{out}}{\epsilon_{in}+\epsilon_{out}}\right)^n \cdot \frac{1}{r\sqrt{1+n^2\left(\frac{t}{r}\right)^2}}$$

$$V(r) = \frac{e}{4\pi\epsilon_0\epsilon_{in}r} + \frac{e}{2\pi\epsilon_0\epsilon_{in}}\sum_{n=1}^{\infty}\left(\frac{\epsilon_{in}-\epsilon_{out}}{\epsilon_{in}+\epsilon_{out}}\right)^n \cdot \frac{1}{r\sqrt{1+n^2\left(\frac{t}{r}\right)^2}}$$

$$V(r) = \frac{e}{4\pi\epsilon_0\epsilon_{in}r} + \frac{e}{2\pi\epsilon_0\epsilon_{in}r}\sum_{n=1}^{\infty}\left(\frac{\epsilon_{in}-\epsilon_{out}}{\epsilon_{in}+\epsilon_{out}}\right)^n$$

Note that $\sum_{n=1}^{\infty} z^n = \frac{z}{1-z},\ \forall|z|<1$

$$V(r) = \frac{e}{4\pi\epsilon_0\epsilon_{in}r} + \frac{e}{2\pi\epsilon_0\epsilon_{in}r}\cdot\frac{\epsilon_{in}-\epsilon_{out}}{\epsilon_{in}+\epsilon_{out}}\cdot\frac{1}{1-\frac{\epsilon_{in}-\epsilon_{out}}{\epsilon_{in}+\epsilon_{out}}}$$

$$V(r) = \frac{e}{4\pi\epsilon_0\epsilon_{in}r} + \frac{e}{2\pi\epsilon_0\epsilon_{in}r}\cdot\frac{\epsilon_{in}-\epsilon_{out}}{2\epsilon_{out}}$$

$$V(r) = \frac{e}{4\pi\epsilon_0\epsilon_{in}r}\left(1+\frac{\epsilon_{in}-\epsilon_{out}}{\epsilon_{out}}\right)$$

$$V(r) = \frac{e}{4\pi\epsilon_0\epsilon_{out}r}$$

Only the outside dielectric becomes important, which makes sense as thickness is negligible compared to the exciton Bohr radius. Most of the electric field lines pass through outside of the material, so the inside dielectric has less of an effect.

Effect of n from the Method of Images Potential on the Extracted Exciton Binding Energy

Table 5.3 Effect of n Values Used on 3ML CdSe Exciton Binding Energy

Calculated exciton binding energy for 3ML CdSe, using the method of images potential with varying n values. The reported values in the manuscript correspond to n=20

n	E_B (meV)
10	212.5
20	213.001
30	213.008

Elaboration of the Calculation Steps of the Exciton Binding Energy

In this work, we extract the exciton Bohr radius from experimentally determined diamagnetic shift coefficients (σ) as given by this equation:[149]

$$a = \left(\frac{4\pi\varepsilon_0\varepsilon_{\text{eff}}\sigma}{4\pi e^4}\right)^{\frac{1}{3}}$$

We derive the effective dielectric as a function of exciton Bohr radius using the method of images potential. For the pair of (ε_{eff},σ) values that satisfies all the equations we can extract the exciton binding energy as described in the Figure 5.10 below.

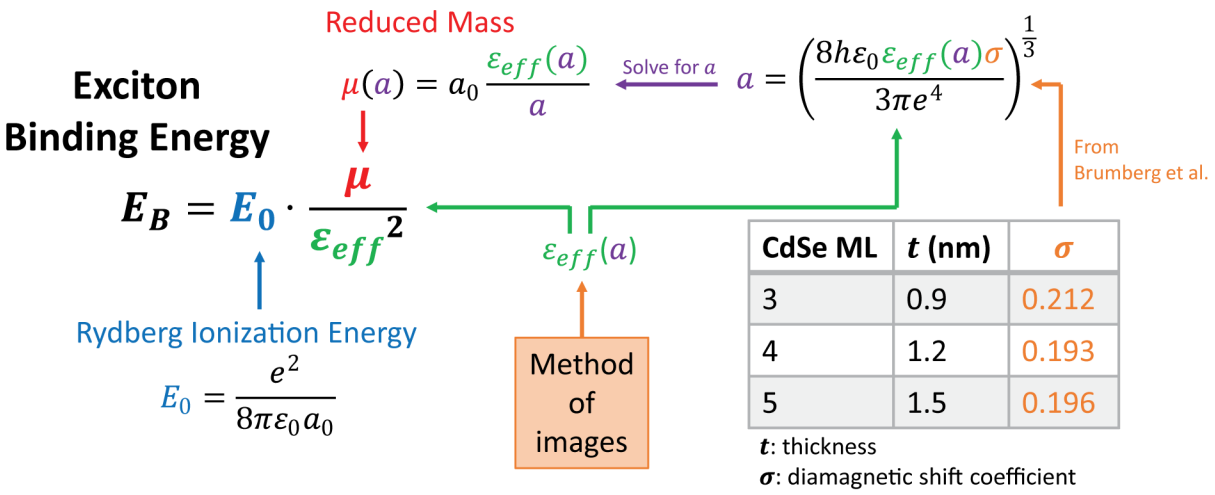

Figure 5.10 Visualization of the Calculation Steps for Exciton Binding Energy. Diagram showing the calculation steps for the exciton binding energy, and the incorporation of experimental diamagnetic shift coefficient to extract the exciton Bohr radius.

Variational Approach to Binding Energies

Here we describe a variational approach to approximate the binding energies of the various nanoplatelets. We model the exciton in the spirit of a hydrogenic system with a central positive charge arising from the hole fixed in the center of the nanoplatelet. This simplified model neglects that excitons may be formed close to the nanoplatelet surface. Furthermore, the similar mass of the electron and the hole invalidates the picture of a central positive charge fixed at the center of the nanoplatelet. Nevertheless, this model captures an essential feature of the excitonic structure that arises from the heterogeneous coulombic attraction between the electron and hole when the exciton Bohr radius is comparable to the nanoplatelet thickness. Within this model, we assume that within the nanoplatelet and in the solvent, the exciton experiences a coulomb potential that is screened by the dielectric constant of the nanoplatelet and solvent, respectively. In the coordinate system of the nanoplatelet that has thickness t along the z axis, the Coulomb potential can be written as:

$$V_{npl}(r) = -\frac{e^2}{4\pi\epsilon_{npl}\,\epsilon_0 r} \text{ when } r\cos(\theta) \leq \frac{t}{2},$$

while in the solvent, the potential has the same coulomb form but is screened by the dielectric of the solvent rather than the nanoplatelet:

$$V_{sol}(r) = -\frac{e^2}{4\pi\epsilon_{sol}\,\epsilon_0 r} \text{ when } r\cos(\theta) > \frac{t}{2}.$$

We can write the Hamiltonian for the exciton as follows:

$$\widehat{H} = -\frac{\hbar^2}{2\mu}\nabla^2 + V_{npl}(r) + \frac{e^2\left(\epsilon_{sol} - \epsilon_{npl}\right)}{4\pi\epsilon_{sol}\epsilon_{npl}\epsilon_0 r} H\left(|r\cos(\theta)| - \frac{t}{2}\right) = \widehat{H}_{npl} + V'(r,\theta),$$

where $H\left(|r\cos(\theta)| - \frac{t}{2}\right)$ is the Heaviside function that goes to 1 for values of $|r\cos(\theta)| > \frac{t}{2}$, i.e. values of the exciton coordinate that experience the dielectric screening associated with the solvent rather than the nanoplatelet. We take $\mu = 0.22\, m_e$ in this work.

We can expand the ground-state wavefunction as linear combinations of hydrogenic energy eigenstates for the bulk nanoplatelet system,

$$\psi_g(r,\theta,\phi\,) = \sum_{n,l} c_{n,l}\,\psi_{n,l,0}(r,\theta,\phi),$$

Where we have limited this expansion by excluding all functions with quantum number $m \neq 0$ since these states cannot couple to the ordinary hydrogenic ground-state through $V'(r,\theta)$. The variational determination of these expansion coefficients for the ground-state is identical to solving the eigenvalue equation

$$\mathbf{Hc} = E\mathbf{c},$$

With elements of **H** given by

$$H_{n,l;n',l'} = \langle \psi_{n,l,0} \mid \widehat{H} \mid \psi_{n',l',m'} \rangle = E'_n \, \delta_{n,n'} \delta_{l,l'} + \langle \psi_{n,l,0} \mid V'(r,\theta) \mid \psi_{n',l',m'} \rangle,$$

where the E'_n contribution is just the ordinary hydrogenic energy scaled by the dielectric constant of the nanoplatelet, and the integral over V' can be taken numerically:

$$\langle V' \rangle = 2\pi \int_{\frac{t}{2}}^{\infty} dr \, r^2 R_{n,l}(r) R_{n',l'}(r)$$

$$\times \left(\int_0^{f(r)} d\theta \sin(\theta) \, (Y_l^{\,0}(\theta,0))^* \, Y_{l'}^0(\theta,0) \right.$$

$$\left. + \int_{\pi - f(r)}^{\pi} d\theta \sin(\theta) \, (Y_l^{\,0}(\theta,0))^* \, Y_{l'}^0(\theta,0) \right)$$

where $f(r) = \cos^{-1}\left(\frac{t}{2r}\right)$, $Y_l^0(\theta,\phi)$ are Spherical Harmonics, and $R_{n,l}(r)$ are radial solutions to the nanoplatelet Hamiltonian $\widehat{H}_{npl}$, which are the ordinary Hydrogenic radial functions with a_0 scaled by the dielectric constant of the nanoplatelet.

We expand $\psi_g(r,\theta,\phi)$ in terms of the hydrogenic functions for all allowed values of n, l from $n = 1, \ldots, 9$ where we find that the binding energy for all relevant thicknesses has converged to less than a 10th of a meV by that basis set size.

Table 5.4 Exciton Binding Energies from Variational Approach

N ML (t, nm)	E_B, $n_{max} = 4$	E_B, $n_{max} = 5$	E_B, $n_{max} = 6$	E_B, $n_{max} = 7$	E_B, $n_{max} = 8$	E_B, $n_{max} = 9$
2 (0.7)	218.87	219.24	219.45	219.59	219.68	219.74
3 (0.9)	203.05	203.36	203.53	203.63	203.71	203.76
4 (1.2)	181.74	181.96	182.08	182.15	182.21	182.24
5 (1.5)	163.05	163.19	163.27	163.32	163.36	163.38

A perturbative approach was also considered, but not pursued due to questions of convergence when the partitioning $\widehat{H}_{npl} = \widehat{H}_0$ and $V'(r,\theta) = \widehat{H}'$ is used. In particular, one expects the perturbative series to converge when:[192,193]

$$\left|\left\langle \psi_p^{(0)} \middle| \widehat{H}' \middle| \psi_q^{(0)} \right\rangle\right| < \frac{1}{2}|(E_p^{(0)} - E_q^{(0)})|.$$

Specifically, we test this criteria for $\psi_p^{(0)} = \psi_{1,0,0}^{(0)}$, $\psi_q^{(0)} = \psi_{2,0,0}^{(0)}$, $E_p^{(0)} = E_1^{(0)}$, and $E_q^{(0)} = E_2^{(0)}$ and find that $\left|\left\langle \psi_{1,0,0}^{(0)} \middle| \widehat{H}' \middle| \psi_{2,0,0}^{(0)} \right\rangle\right| > \frac{1}{2}|(E_1^{(0)} - E_2^{(0)})|$ for the 2 ML and 5 ML cases, thus suggesting the perturbation is too large for convergence of the perturbative series.

Solvent Washing Procedure for External Dielectric Modulation

The procedure for the solvent washing experiment starts with 1 mL of as-prepared HgTe NPLs are added to a vial with $Hg(OAc)_2$/acetonitrile solution. This solution was obtained by dissolving 15 mg $Hg(OAc)_2$ in acetonitrile at room temperature. Two phases can be clearly discerned due to the miscibility of acetonitrile in hexanes. The vial was vigorously agitated for 1 minute (on vortexer), then allowed to settle until the 2 phases were separated again. Colloidal stability of NPLs in hexanes was maintained and no obvious phase transfer happened. The hexanes layer was then taken out and the absorption spectrum were taken. The samples after washing were centrifuged at 14000 rpm for 5 min, with extra oleylamine added to keep the colloidal stability of HgTe NPLs. The supernatant was discarded and the pellet was resuspended in fresh hexanes for another absorption spectrum. It should be noted that this experiment was repeated with just acetonitrile and without any $Hg(OAc)_2$, which led to the same shift in the absorption spectrum.

FTIR of the 3 ML HgTe NPLs during the Washing Process

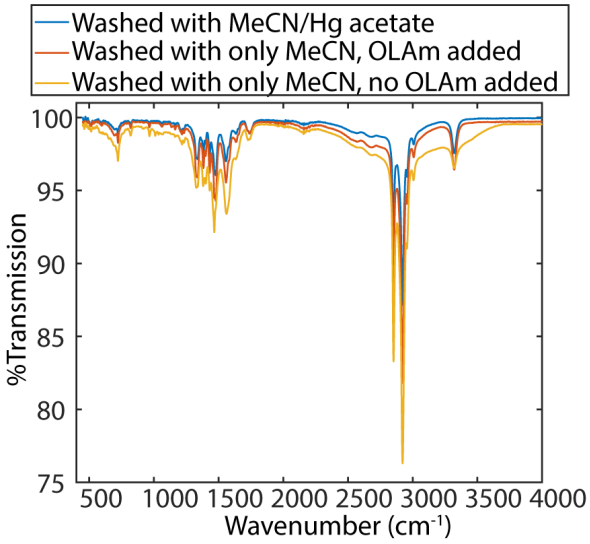

Figure 5.11 FTIR of 3 ML HgTe Nanoplatelets during Washing

FTIR of 3ML HgTe NPLs with varying parameters for the washing procedure, showing that the NPL structure was unchanged.

Solvent Washing Experiment for 3 ML CdTe, CdSe, and HgSe NPLs

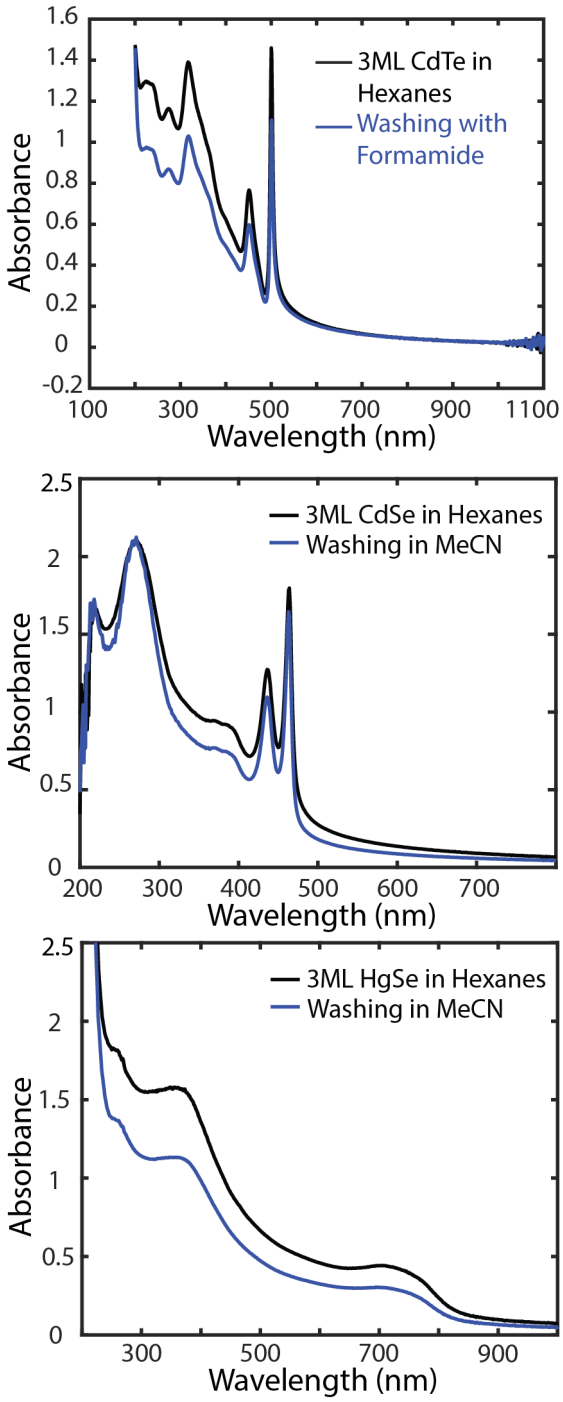

Figure 5.12 Absorption Spectra of Various NPLs after Washing

Absorption spectra of 3 ML CdTe (top), CdSe (middle), and HgSe (bottom) NPLs after the same washing procedure as outlined prior.

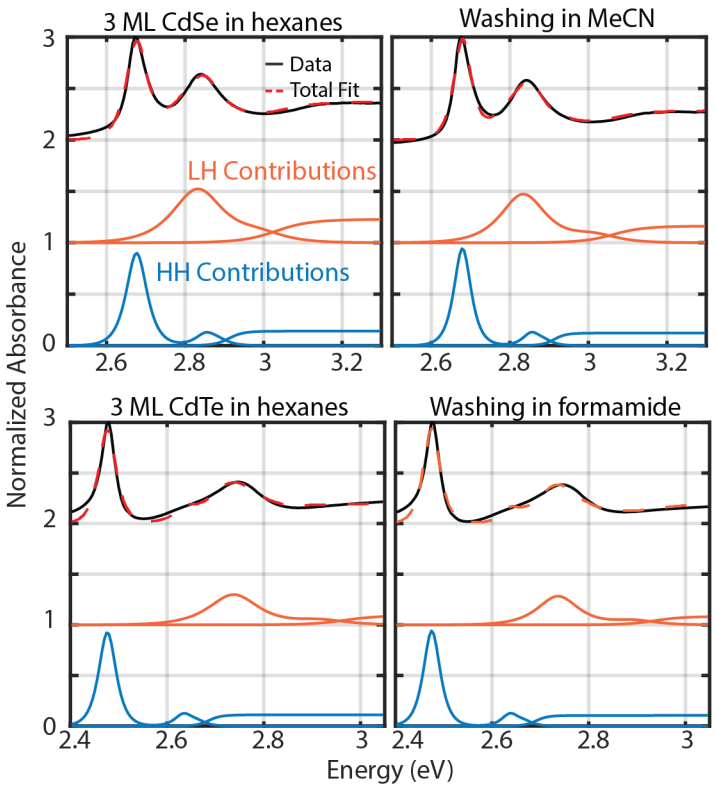

Figure 5.13 Elliott Model Fits of CdSe and CdTe Absorptions

Absorption spectra of 3 ML CdSe (top) and CdTe (bottom), and their corresponding Elliott fit contributions, showing no change.

Further Details for the Solvent Washing Experiment for 3 ML HgTe

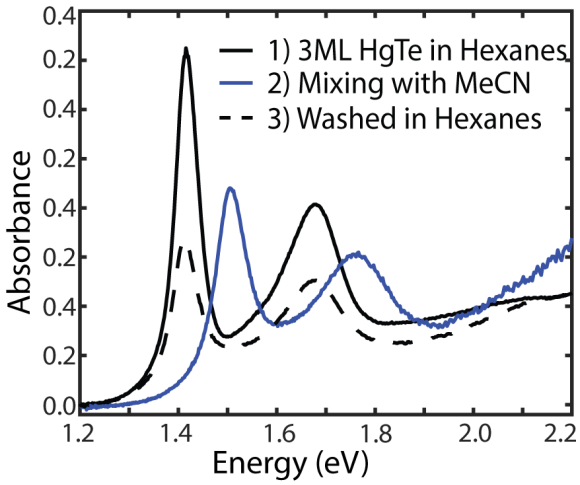

Figure 5.14 3ML Absorption during Washing Procedure

Absorption spectra of 3 ML HgTe for the washing procedure as outlined in Sec. VII-A.

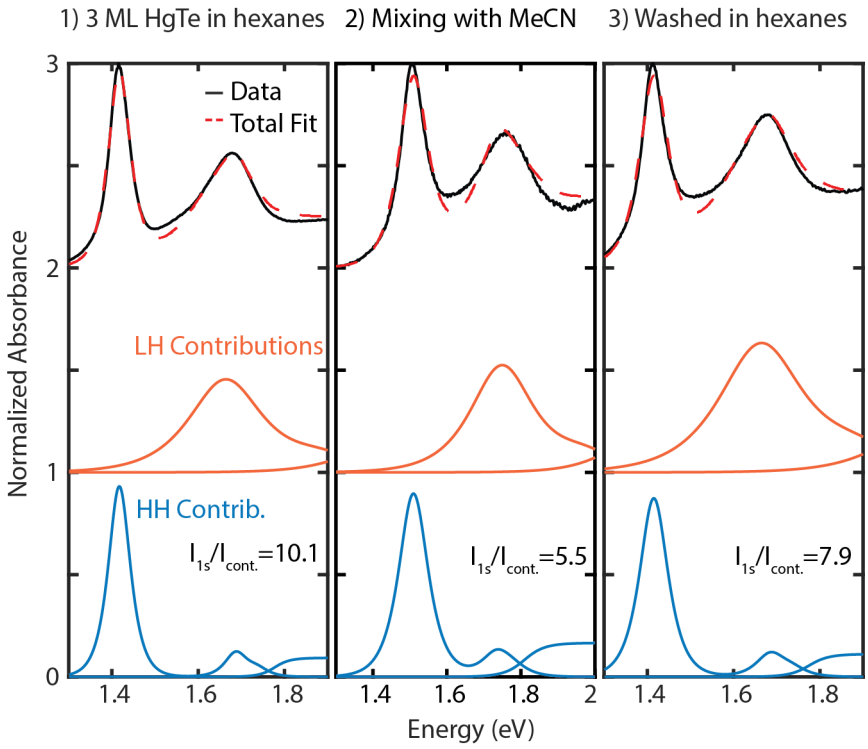

Figure 5.15 Elliott Model Fit Contributions for 3ML HgTe during Washing

The Elliott fit contributions for the 3 ML HgTe absorption data in the washing procedure.

Chapter 6

Software Development for Spectral Analysis

This chapter uses materials with permission from co-authored manuscripts, "Atallah, T. L., Sica, A. V., Shin, A. J., Friedman, H. C., Caram, J. R. Decay Associated Fourier Spectroscopy: Visible to Shortwave Infrared Time-Resolved Photoluminescence Spectra. *J. Phys. Chem. A*. **123**, 6792-6798 (2019)" and "Tenney, S. M., Tan, L. A., Sonnleitner, M. L., Sica, A. V., Shin, A. J. et al. Mesoscale Quantum-Confined Semiconductor Nanoplatelets through Seeded Growth. *Chem. Mater.* ***34***, 6048-6056 (2022)."

6.1 Processing Data Stream from Hydraharp

I helped build the custom Fourier spectrometer that was used to collect the emission and lifetime of (thiolfan)YbCl(THF) in Chapter 2. This optical setup was used to perform decay-associated Fourier spectroscopy (DAFS), which was developed and published by Dr. Timothy Atallah.[194] In DAFS, the emission passes through a variable path length Mach-Zehnder interferometer (MZI) and is detected with simultaneous spectral and temporal resolution. The emission is collected by superconducting nanowire single photon detectors (SNSPDs). The reading from the SNSPDs is sorted by the Hydraharp 400 (Picoquant) module in time-tagged time-resolved (TTTR) mode. I contributed significantly to the development of the custom processing codes to collect and analyze the TTTR data to produce interpretable DAFS spectra.

For a DAFS measurement, the sample is inserted into a stage with off-axis parabolic mirrors for colocalization of excitation and emission (Figure 6.1). The MZI is first aligned to the excitation laser to optimize fringe contract, and then spectral filters are inserted to leave only the

sample emission. The DAFS signal is further optimized to sample emission at each extreme of the translational leg of the MZI before collection. Once collection begins, the SNSPDs detect photons for a given measurement duration, of which information is saved in the data stream from the Hydraharp. This data stream can grow to multiple GBs of information, requiring an efficient processing code.

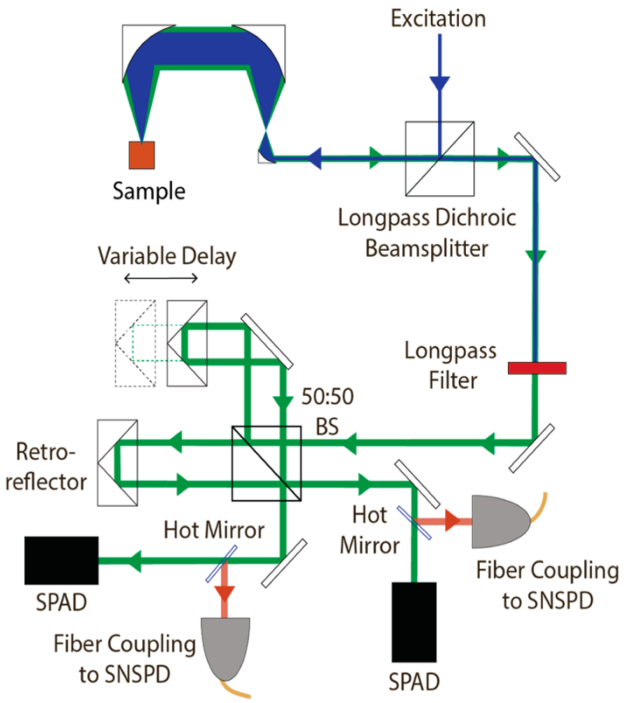

Figure 6.1. DAFS Optical Setup.

The Hydraharp produces a binary file with each photon arrival record stored in units of 32 bits (Figure 6.2). The 32 bit event records are queued in a FIFO (first in first out) buffer that can hold up to 256k events, after which an overflow is marked. In each unit of 32 bits, the first bit is denoted "SPECIAL," and indicates whether there was a photon event (0) or an overflow event (1). An overflow is marked when the FIFO buffer is full, and a new one must be recorded. Therefore, the number of total overflows indicate the number of FIFO buffers (or the number of 256k photon

events) that make up the entire data collection. The next 6 bits make up the channel number of the four channels that are available on the Hydraharp. The next 15 bits make up "DTIME," which represents the arrival time of the photon after the last sync event, or laser pulse. The last 10 bits consist of "NSYNC," which indicates the number of sync events for a photon event and the number of overflows for an overflow event. The relative time of arrival for the photon event, since the laser pulse, can be calculated by multiplying DTIME with the temporal resolution (usually 16 ps or higher). And the real time of arrival of a photon event, since the start of collection, can be calculated by dividing NSYNC by the sync rate and adding it to most recent relative time of arrival.

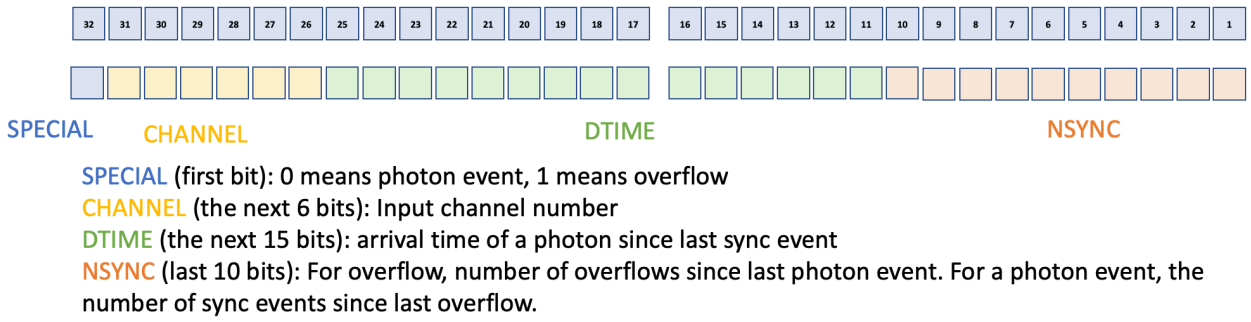

Figure 6.2. Hydraharp photon event binary format.

I developed both the processing code that converts the binary file into decimal numbers, and also the analysis code for interpretating spectral information to produce DAFS spectra. Because the data files can be large, writing a processing code that saves computational memory was necessary. I used two strategies to reduce memory and speed up the code. First, I processed data in smaller sizes (e.g., 25 MBs) so that the code does not have to process the full GBs of data at once. Second, I used an efficient indexing scheme to reduce a double for-loop to a single for-loop code, allowing data to be processed in minutes as opposed to hours. As shown in Figure 6.3, the 32 bit event is pulled from the .ptu file that is generated from the Hydraharp after measurement. Then my MATLAB code takes in a portion of that binary file, converts to decimal

numbers, and stores it in a bivariate histogram. Instead of processing with two for loops to index each x and y axes of the histogram, I used the x and y values as indices themselves to reduce the processing to one for loop. The single for-loop code indexes through the data and stores it in the histogram bin that corresponds to the appropriate photon arrival time and stage position. The entire measurement data is processsed once the procedure in Figure 6.3 is repeated to extend to the full size of the data file.

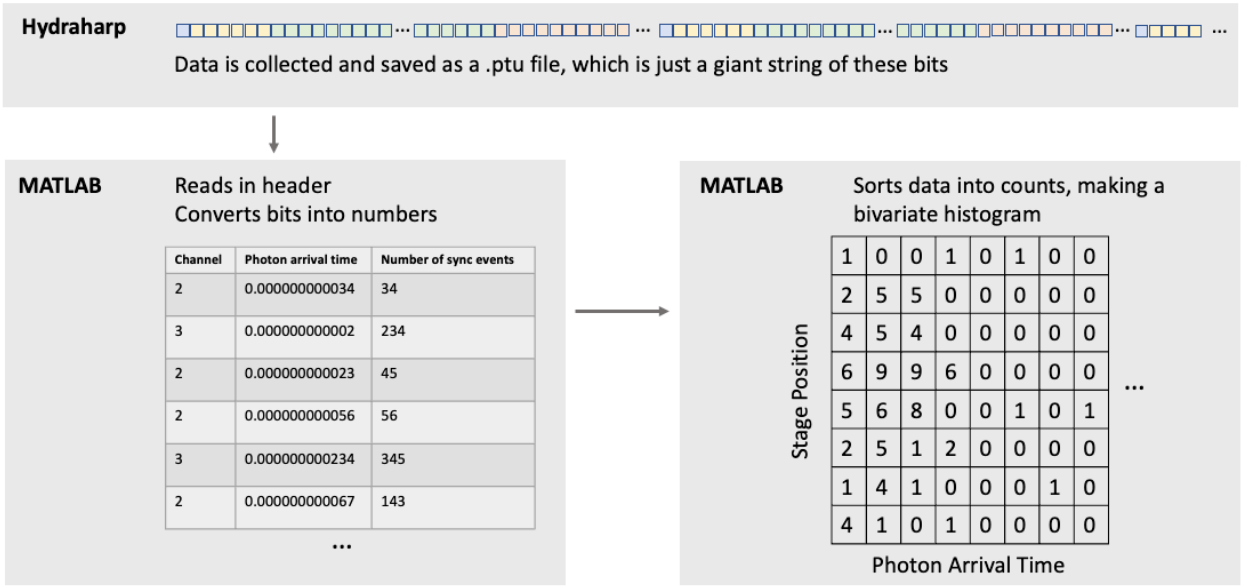

Figure 6.3. Processing Code Design for DAFS Data.

The advantage of our DAFS technique is that it involves time-correlated single photon counting (TCSPC), which allows background free collection of time-resolved photoluminescence. The background-free method is made possible by balanced detection, where two detectors are used to remove constant background. DAFS data is collected for each input channel, which corresponds to individual detectors that were used during the measurement (Figure 6.4a). The detector signals can be plotted against each other to determine correlated signal, which corresponds to constant background. In other words, only scatter will trigger both

detectors simultaneously, because photoluminescence signal will leave the MZI, pass through a beamsplitter, and only trigger one detector. Therefore, the correlated data across both detectors can be extracted out, as shown in Figure 6.4b. Furthermore, the slope of the fitted line can be used to correct for the difference between the two detectors baseline, producing a polished interferometric trace (Figure 6.4c).

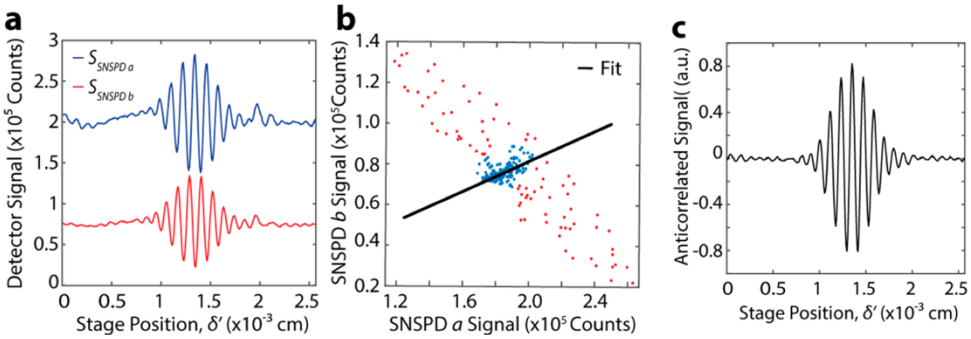

Figure 6.4. Spectral Analysis Code for DAFS

Once the binary file is processed and converted into a bivariate histogram, the number of photons and their arrival time at a particular stage position is indicated in a 2D plot. As shown in Figure 6.5, the DAFS data can be Fourier transformed to produce a time-resolved 2D spectra, which contains both photon energy and lifetime information. The SNSPDs and avalanche photodiode detectors (APDs) expand the wavelength of collection from visible to 2 μm. With this range, we were able to collect photoluminescence from both PbS and CdSe nanocrystals, which emit at 1.1 eV and 2.1 eV, respectively. While there are no energy transfer events between these two species, this method can probe energy transfer dynamics between a variety of species, without the need to separate them before spectroscopic measurements. Therefore, the DAFS technique is unique in that it can capture complex energy transfer dynamics simultaneously.

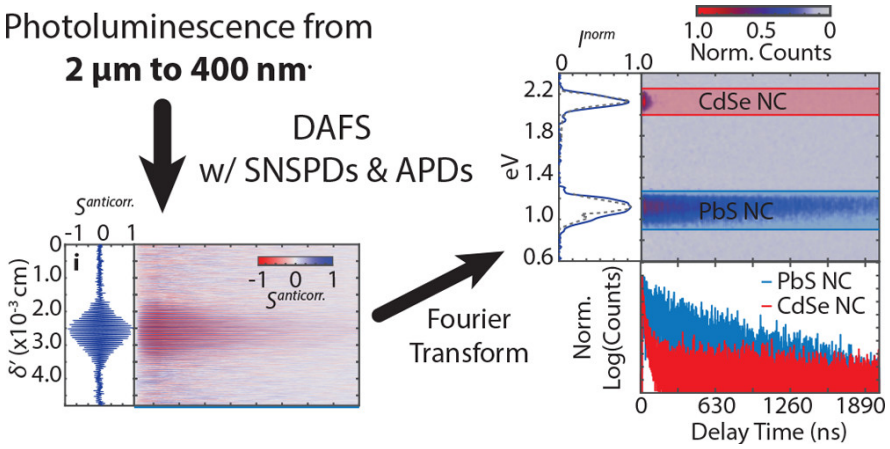

Figure 6.5. DAFS Spectra of PbS and CdSe Nanocrystals

6.2 Analyzing TEM and PL Images of Nanoplatelets

In Chapter 5, I presented published results on the effects of dielectric screening on the binding energy of semiconductor nanoplatelet (NPL) excitons. I continued to collaborate with Dr. Stephanie Tenney, who developed a seeded growth procedure to produce mesoscale CdTe nanoplatelets.[195] With larger NPLs, they were able to be imaged by both optical and electron microscopy to capture inhomogeneities on the surface. The NPLs were imaged with transmission electron microscopy (TEM), and the same NPLs were brought to the microcopy setup to collect photoluminescence (PL) images. I wrote the analysis code to process correlated images from TEM and PL measurements.

Because the TEM and PL images are not aligned at collection, the images had to be processed post-hoc in order to find the correct overlap. The PL images had lower resolution then the TEM images, in which each pixel correlated to a PL intensity across 250 nm (limited by the beam spot). An example PL image of CdTe NPL and its corresponding TEM image are shown in Figure 6.6. The background subtraction for the TEM image was done through a simple intensity filter. The threshold intensity was determined by plotting a histogram of the TEM pixel intensities.

While most of the background was subtracted by indexing out sub-threshold pixel intensities, some background near the edges of the NPL remained and some intensities were removed from the NPL surface. However, a quick intensity filter was sufficient enough for correlation analysis. After the intensity filter, the TEM image was blurred to match the pixelation level of the PL image using gaussian blurring. Then, a single for-loop optimization code was used to find the relative positioning between the blurred TEM and PL images that produced the least difference in intensity.

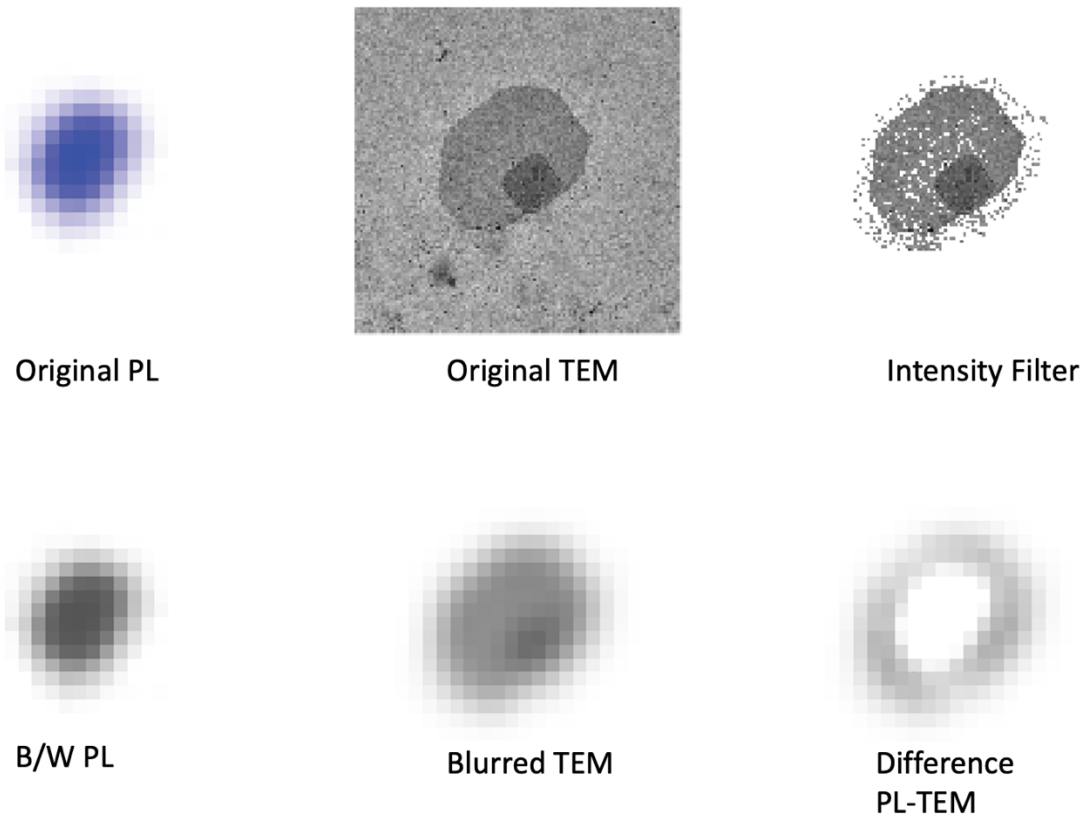

Figure 6.6. Snapshots of Correlated TEM and PL Image Processing Code

6.3 Processing Blinking Emission of Nanoplatelets

With larger nanoplatelets, trace amounts of quantum dots were found in the TEM images, as seen in HgTe and HgSe nanoplatelets NPLs and their infrared emission from quantum dot (QD) defects. We observed a near unity energy transfer from NPL to these QDs, which seem to shift

over time.[139] The QD and NPL energy transfer dynamics are part of an ongoing investigation, in which we observe blinking in the emission traces. In order to analyze the blinking traces, I developed an analysis code that determines the time duration between on and off states. However, determining the on and off intensities can be challenging, especially considering background noise.

The schematic for analyzing blinking traces, assuming just one transition, is shown in Figure 6.7. Assuming just one set of on states, an intensity threshold can be established to generate a corresponding binary trace (orange) to the collected PL intensities (blue). The binary trace can then be further analyzed to identify change points. The time duration between ON and OFF change points are histogrammed to produce the distribution of blinking time intervals. In order to differentiate between ON and OFF change points, I used a for loop and an identifier variable that gets updated after each change point as "0" for OFF and "1" for ON. If the identifier was ON before, then the identifier is changed to the OFF state and the time interval is recorded. At the end of the for loop, these time intervals can be histogrammed to produce the distribution of blinking times.

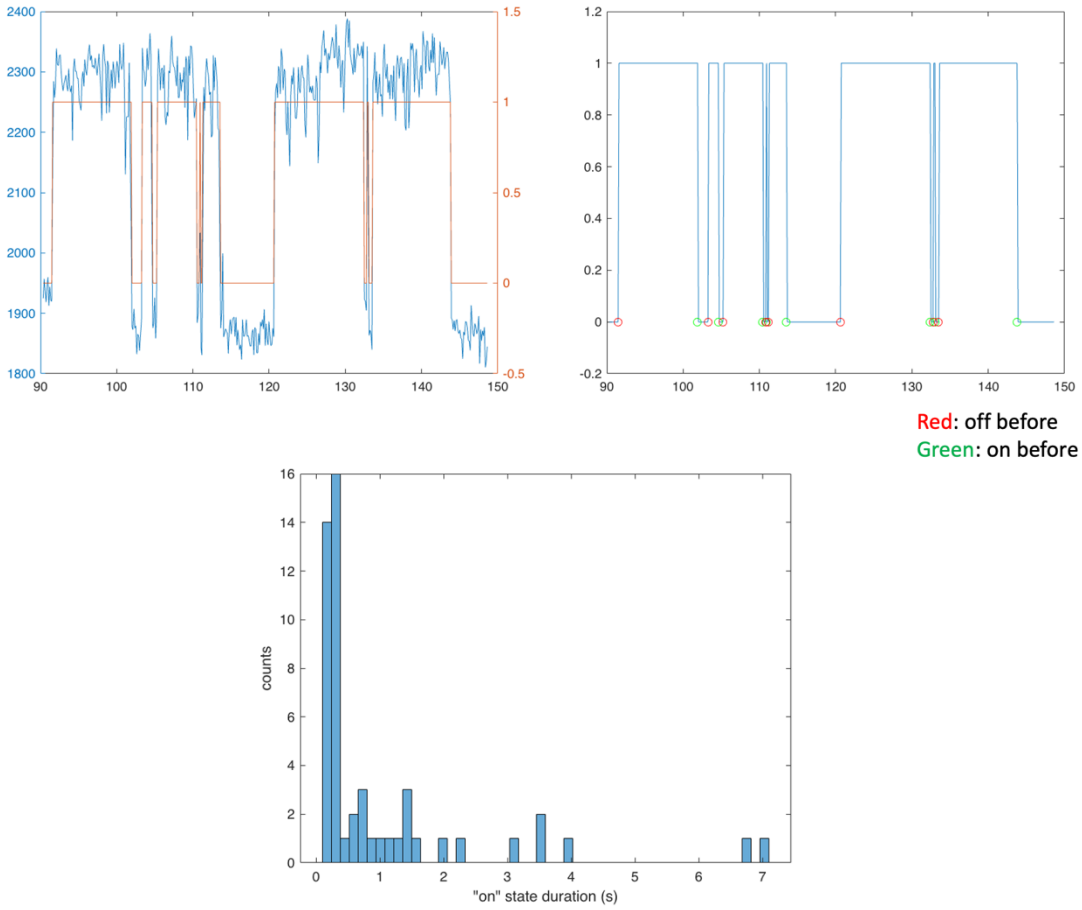

Figure 6.7. Blinking Trace Analysis from One Transition

Chapter 7

Chemical Education Research of Student Virtual Engagement

Adapted with permission from a manuscript in preparation, "Shin, A. J. et al. Observational study of student engagement and its relationship to design elements of remote chemistry discussion sections. *J. Chem. Educ.* (2023) [submitted]."

7.1 Introduction to Distance Learning

Intentional course design that promotes student engagement has been shown to enhance academic satisfaction, motivation, and performance. In this work, we investigate key elements of discussion sections that have been highlighted in prior literature and their effects on student engagement in a remote chemistry setting. We quantify student engagement through direct measurement of camera, mic, and chat usage in order to determine student visual and verbal presence (Figure 7.1). The results of this investigation suggest that the combination of required attendance, TA/LA movement between breakout rooms, small group size, and assigned worksheets are necessary to ensure higher camera usage, while the incorporation of assigned groups and roles lead to further improvements in student use of mic and chat. Additionally, this study suggests that the average level of student engagement remains relatively consistent across the term, which may have implications for establishing classroom norms.

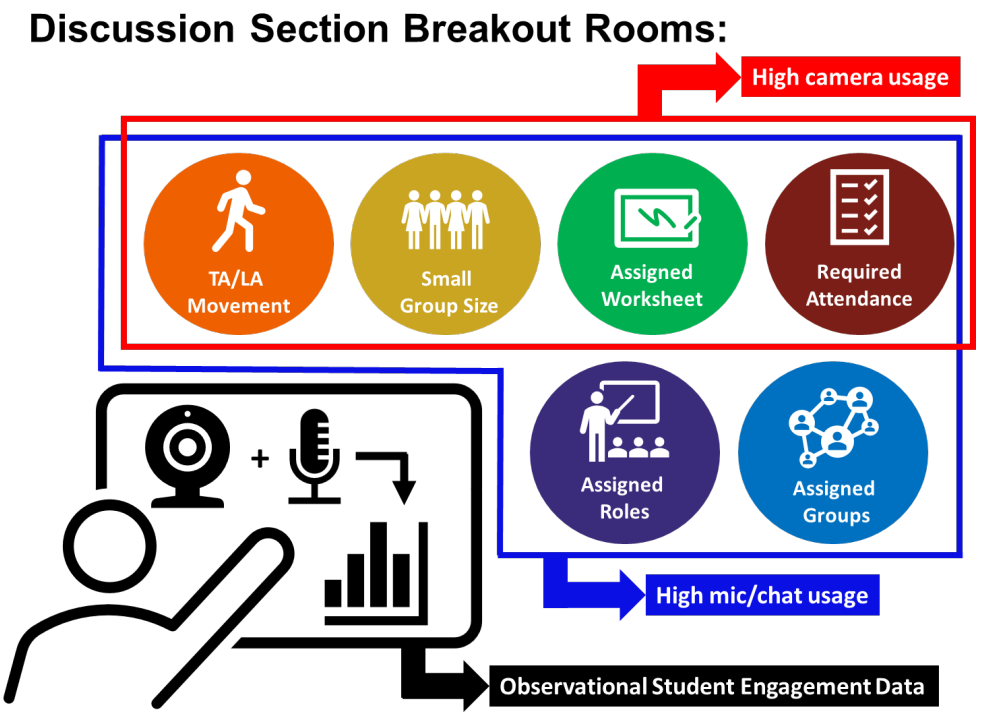

Figure 7.1 Schematic of Observational Study

In response to the COVID-19 pandemic, universities across the globe pivoted from offering in-person to remote instruction within a matter of days. This presented a major challenge for instructors, given the drastic changes that had to be made abruptly to course design. But the concept of remote learning is far from new, and the advent of the internet expanded distance education (DE) long before the pandemic occurred.[196] In 2008, 96% of public two-year colleges and 86% of public four-year colleges offered some form of online courses,[197] and by 2014, it was estimated that 5.8 million students were enrolled in at least one online course in the United States higher education system.[198] Three years after the start of the pandemic, there remains widespread acknowledgement that DE has an important role to play in the future of education.[199,200]

One of the consistent findings of DE literature is that interaction is critical to learning.[201–205] Increasing student-content, student-instructor, and student-student interactions in the online

classroom has been found to positively affect student learning, although the mechanism through which this occurs has not been fully explained.[203] Bernard et al. (2009) hypothesized that incorporating more interaction into the remote classroom may ultimately result in an increase in student cognitive engagement,[203] which has been linked to student motivation, achievement, and persistence, both for F2F and virtual classrooms.[206,207] Therefore, investigating how deliberately structured course interactions influence students' online engagement is an important aspect of effective course design for future DE and perhaps even hybrid implementation.

Despite student engagement suffering during the pandemic,[208] many successful strategies for engaging students in distance learning have been reported.[209–216] Research regarding online learning maintains that an effective online education can be achieved with the development of a learning community.[217–219] Many of these studies investigate approaches that are grounded in the Community of Inquiry (CoI) framework, which highlights the importance of building an online community that allows for students to experience active social, cognitive, and teaching presence.[220] Specific CoI practices include facilitated discussions, structured teams, problem-based learning, and ice-breaker activities.[221–225]

While many of these high-impact practices have also been reported as beneficial in F2F environments,[226–229] it has been suggested that what is ultimately effective in DE may be different from what is effective in F2F education.[211,230,231] This is one reason why comparisons between in-person and distance learning can be misguided. As DE becomes a well-established educational practice, there is ultimately less of a need to compare its methods to F2F education.[203] Rather we should focus on evaluating the effectiveness of remote practices within the context of hybrid and distance education itself.[232,233]

The complete transition to remote instruction during the pandemic provided us with an opportunity to examine the effect specific pedagogical practices have on student engagement in an entirely DE environment. Our research aims to address two questions: (1) how do various design elements of discussion sections affect student video, mic, and chat usage in a DE setting, and (2) to what extent are camera and mic/chat usage correlated to each other?

In addressing these questions, we were able to consider a population of F2F students not typically associated with DE research prior to the pandemic,[234] but who very likely will be the subjects of distance or hybrid learning in the future. Therefore, the insights gained from this research help contribute to the identification of key design elements of future discussion sections in remote and potentially hybrid environments, especially amongst traditional students enrolled in F2F universities. Our results indicate that specific discussion elements have varying impacts on student engagement, suggesting that an informed selection of design elements is critical to ensuring majority student engagement in remote discussion sections in chemistry courses.

7.2 Study Details

This study was conducted in the Department of Chemistry and Biochemistry at a large, public, research-intensive university, and it was determined not to meet the definition of Human Subject Research by the university's Institutional Review Board. By March 2020, the university campus was closed, and most in-person instruction halted due to the COVID-19 pandemic. Between Spring 2020 and Summer 2021 quarters, the vast majority of classes were conducted online, including those observed in this study. Specifically, the study was conducted during the ten-week quarters of Fall 2020 and Winter 2021 (abbreviated F2020 and W2021). The observed chemistry courses consisted of lecture sections with 150-350 students and discussion sections with

25-35 students (Table 1). Further details for these courses are presented in Table S1 and a more comprehensive table of observational details are found in Tables S2 and S3.

The department offers two different chemistry series: one designed for Life Science (LS) majors and one for Physical Science (PS) majors. Within both series, the usual progression includes two general chemistry lecture courses followed by two LS or three PS organic chemistry lecture courses (the laboratory courses are held separately for both series). For the purpose of anonymity and simplicity, the observed courses are labeled with a letter (**A** to **I**), and details of their course descriptions can be found in the Methods section. Notable aspects regarding the number of students and breakout rooms of the observed courses are also shown in Table 1. For F2020, each discussion section was observed once. For W2021, some discussion sections were observed more than once, leading to a larger number of students of observed relative to course enrollment size.

Because the courses observed in this study were held synchronously, enrolled students were required to have stable access to Zoom. Fortunately, resources were readily available to all students; the university library provided laptops, iPads, and other technological devices required for remote learning. Despite this, we must acknowledge that some students in the observed courses may not have turned on their videos due to broadband or privacy issues. This is based on discussions with departmental instructors, as well as reports given in the literature.[235,236]

Table 7.1. Information on Observed Courses.

Course Label	Course Designation (Intended Major, *Course Topic,* Order in Course Series)	Number of Students Observed (NS)	Number of Breakout Rooms Observed (NBR)	Total Number of Learning Assistants	Enrollment Size (Number of Lecture Sections per Course)
		Fall 2020			
A	Physical Sciences *Organic Chemistry* I	37	9	9	121(1)
B	Life Sciences *Organic Chemistry* II	93	9	19	568(2)
C	Life Sciences *Organic Chemistry* I	114	17	27	596(2)
D	Physical Sciences *General Chemistry* I	26	5	20	674(3)
E	Life Sciences *General Chemistry* I	82	21	27	234(1)
		Winter 2021			
F	Life Sciences *Organic Chemistry* II	535	60	32	668(2)
G	Life Sciences *Organic Chemistry* I	212	60	20	394(2)
H	Physical Sciences *General Chemistry* II	259	89	30	575(2)
I	Life Sciences *General Chemistry* II	437	115	14	227(1)

Course abbreviations, corresponding course names, total number of learning assistants, enrollment size, and numbers of students (NS) and breakout rooms (NBR) observed in this study are shown.

Course Setup. For both F2020 and W2021 quarters, the observed courses had 50-minute synchronous lectures online that met 3 times a week. All of the courses held lectures live on Zoom and a few of them provided recordings of the lectures as well (**C**, **E**, **H**, and **I**). The instructors had online office hours that met approximately 3 hours a week. The discussion sections met for 50 minutes each week (except for courses **E** and **I**, which had 110-minute weekly discussion sections) and took place synchronously over Zoom. Generally, the courses had two midterms and one final exam, all taken in a remote format. Any deviation from the above descriptors is presented in Table 7.3.

Discussion Section Setup. This study focused specifically on observed student engagement within discussion sections as discussion sections tend to be more interactive than the lecture component of the course. In general, the purpose of the discussion section is to give students a chance to work on course material as well as to receive additional help. There are no departmental specifications for how discussion sections must be set up and the instructors had full control over the structuring of their discussion sections, including whether attendance was required. For the courses observed in this study, discussion sections met once a week and consisted of 25-35 students, a few Learning Assistants (LAs), and a Teaching Assistant (TA). TAs were graduate students and LAs were undergraduate students who were experienced in the courses and went through an application process to be hired.

While instructors can recruit LAs to assist with discussion, they are not required to do so. This study only included courses that hired LAs in their discussion sections because the study was facilitated through author S. S., the director of the LA program. Nonetheless, it should be noted that many courses at the observed institution incorporate LAs into discussion sections, based on known benefits of LA facilitation: increased student satisfaction,[237] decreased failure rates,[238] and

more equitable classrooms.[239] All LAs were trained on pedagogical techniques through a one-hour weekly seminar and met weekly with the course instructor and/or TAs to prepare for the upcoming discussion. However, the number of assigned LAs (see Table 7.1) and how the LAs were instructed to facilitate discussions (see Figure 7.2) varied by course.

7.3 Methods

Measuring Engagement. In this study, student engagement is quantified by the measurement of camera, mic, and chat usage. There are many ways to define student engagement, with current literature focusing on three main forms. *Behavioral engagement* is situated around participation and can include involvement in activities as well as persistence.[240–244] *Cognitive engagement* is based on student investment, and it includes students' willingness to exert necessary effort as well as the learning strategies students use.[245,246] Lastly, *emotional engagement* focuses on the positive and negative reactions students have towards instructors, peers, and learning the content.[247,248] For this study, we focused specifically on methods to measure behavioral engagement as it is considered a critical aspect of achieving positive academic outcomes and is easily quantifiable through observations.[249,250]

There are numerous established methods for measuring behavioral engagement in technology-mediated learning, from self-report measures such as the NSSE or OSE surveys,[251,252] to descriptive statistics that detail how class time is spent.[253] Given that there has been interest expressed in more direct observations of student engagement,[203] we have developed a straightforward method to quantify student engagement in remote discussion sections. One limitation of collecting observational data is the need to adequately train observers, especially when engagement is measured by more abstract criteria such as a student engaging in explaining or reflecting, or conversely, being distracted or frustrated.[254–256] In this study, easily quantifiable

measures of engagement were used, thus allowing for the observers to readily collect data across multiple classes. One such marker of behavioral engagement is the number of cameras turned ON in a breakout room, which will be referred to as *visual presence*. Prior literature indicates that students who are more engaged will be more likely to turn their cameras ON.[236,257]

With that said, lack of camera usage does not necessarily hinder engagement entirely, given mic and chat options are available in Zoom. For this reason, a second definition of behavioral engagement is included, which quantifies the student-student (F2020) and student-student/TA/LA (W2021) conversations occurring within a breakout room. This will be referred to as *verbal presence*. While verbal presence includes both mic and chat usage, a relatively small portion of observed conversations occurred through chat (e.g., 3% of observed students in W2021 used chat). Therefore, *verbal presence* describes mainly vocal interactions.

The use of camera, mic, and/or chat has been used as an indicator of student engagement previously,[258] and the concepts of visual and verbal presence are grounded in social presence theory, which posits that interaction can be achieved by verbal inflections and nonverbal cues.[259,260] These factors corroborate our choice of camera and mic/chat usage as measures of student engagement. While some nuance will be lost with such broad measures of engagement, the ease for which this data can be collected may prove valuable in situations where the resources to conduct more detailed studies are not readily available.

Data Collection. The authors D. D. B. and A. J. S. were granted access to all Zoom discussion sections for courses **A** - **I** during F2020 and W2021 quarters, respectively (Table 7.1). Discussion sections were selected at random for observation. For F2020, a total of 61 breakout rooms with 352 students were observed in courses **A** - **E,** and for W2021 a total of 342 breakout rooms with 1,434 students were observed in courses **F** - **I**. It should be noted that the total count

for W2021 contains students that were observed more than once. The specifics relating to data collection are detailed below.

Data Collection for Fall 2020: Preliminary observations for F2020 looked at one discussion section each week between weeks 6-9. The observer logged onto the discussion section through Zoom anytime during the middle of class once all the students were placed in breakout rooms. For any given discussion section, all breakout rooms within that discussion section were observed. Discussion section observations occurred for approximately 2 minutes per breakout room, essentially collecting snapshots of each breakout room in order to create an ensemble average of student engagement. This time window was limited to 2 minutes so that the observer could attend all breakout rooms for a given discussion section and still attend other discussion sections that were running simultaneously.

During these discussion observations, several data points were collected (see Table 7.4 for raw data): the total number of breakout rooms visited (NBR), the total number of students observed (NS), the number of breakout rooms where students conversed with other students through mic or chat (BR[SS]), and the number of students with their cameras ON in each breakout room (CAM). Initial measurements in F2020 defined *verbal presence* as the percentage of breakout rooms where a student was observed directly talking to another student (red bar in Figure 7.2, left; BR[SS] (%) in Table 7.4) and *visual presence* as the percentage of cameras turned ON (gray bar in Figure 7.2, left; CAM (%) in Table 7.4).

Data Collection for Winter 2021: In W2021, from weeks 2-10, approximately 4-10 discussion sections from different courses were observed weekly. These sections were sometimes observed more than once across different weeks. Data from weeks 2-10 were analyzed for *visual presence* and reported in this manuscript. Updated definitions for *verbal presence* were still being

finalized during weeks 2-4 of W2021, therefore data collected during weeks 5-10 were used for this measurement. Table 7.6 shows the timeline of the NS and NBR observed for each week during weeks 2-10 during the W2021 quarter in an effort to portray the scale of this study.

Due to the limited student-student interaction observed for some discussion sections in F2020, it was decided to expand the definition of *verbal presence* in W2021 to include students speaking to TAs and LAs as well. Ultimately, we used two new definitions of *verbal presence* for the W2021 study: % of observed breakout rooms with student-student/TA/LA mic/chat usage and % of student-student/TA/LA mic/chat usage. There is a distinction between these two measures that should be noted. For example, having 100% of breakout rooms with observed verbal presence does not mean that all students are participating; it only guarantees that at least one student is communicating via mic/chat in each breakout room. Comparing the % mic/chat usage per breakout room versus per student can provide a better understanding of whether one student is dominating the conversation in a breakout room.

The observation window for this quarter lasted 2-5 minutes on average per breakout room. For W2021, *verbal presence* is defined as the percentage of breakout rooms with any student conversations (light blue bar in Figure 7.2, right; BR[AS] (%) in Table 7.5) and the percentage of students participating in any conversation via mic/chat (dark blue bar in Figure 7.2, right; NS[AS] (%) in Table 7.5), where *any* indicates the expansion of conversation partners to anyone, including other students, TAs, and LAs. The definition for *visual presence* remained the same for W2021 (gray bar in Figure 7.2, right; CAM (%) in Table 7.5). Although all courses were not observed weekly, a majority of them were observed each week (specific details in Table 7.6).

Identifying Discussion Design Elements. This study investigates a combination of six design elements: required attendance, TA/LA movement, assigned worksheets, small group work,

assigned groups, and assigned roles. The choice of these discussion elements was a result of observing how F2020 discussion sections were run. These were some of the recurring design elements frequently observed, and therefore became the primary comparison measurement for discussion structure. These elements are detailed in Table 7.2. While there are other elements that can be considered, these six elements have been previously highlighted in the literature, thereby providing support for their further investigation.

Table 7.2: Description of Various Design Elements Used in Observed Discussion Sections. Discussion sections that contained any of the below elements are marked with a colored box in Figure 7.2.

Design Element	Description
Required attendance	All discussion sections were held synchronously, but not all courses required students to attend discussion. For courses marked for required discussion attendance, students were awarded course credit (not extra credit) for attending that counted towards their final grade.
TA/LA movement	All observed discussion sections used breakout rooms, and TA/LA movement refers to specifically when the TAs and LAs were instructed to move between different breakout rooms rather than stay in one location (e.g., TA stays in the main room and LAs stay in their respective breakout rooms).
Use of small groups	When noting the presence of small group size, we chose to categorize groups as small (having five or fewer students) or large (having six or more students). While the literature surrounding optimal group size lacks consensus, there are recommendations for using groups consisting of 3-5 students.[261]
Assigned worksheets	All courses had a worksheet or problem set for students to work on during discussion, but this element refers to whether the activity was submitted for grading and specifically intended for discussion section only. The structure of the worksheets ranged from low- to high- structured, and both accuracy and completeness grading were counted.
Assigned groups	Observed discussion sections either allowed students to select their own group by joining the breakout room of their choosing, or the TA assigned students to a particular group or breakout room. In this case, a discussion section with assigned groups is one in which the instructor specified that students work in designated teams, and these teams generally remained consistent throughout the quarter.
Assigned roles	Assigned roles indicate whether students were given specific instructions on how to facilitate group discussion. The discussion sections that used team roles did so based on the POGIL (Process Oriented Guided Inquiry Learning) model.[262,263] Students were assigned a new role each week, and the roles rotated weekly.

7.4 Results

The general and organic chemistry courses observed in this study employed varying combinations of design elements, enabling comparisons of the impact these discussion elements have on multiple definitions of student engagement within a DE environment. We present the insights gained from observing camera usage and mic/chat usage in sequential order, elaborating on trends seen individually in F2020, W2021, and across both quarters. Additionally, we investigate the relationship between visual and verbal engagement, specifically determining how correlated these variables are, as well as how consistent both forms of engagement remain during the quarter.

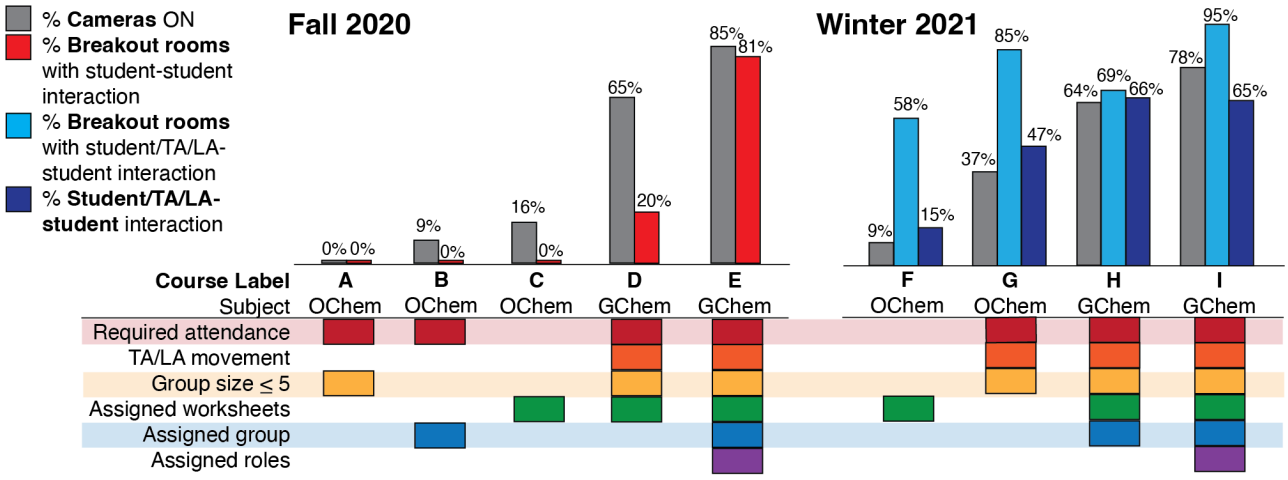

Figure 7.2 Observed Engagement with Varying Discussion Elements

Engagement measures for snapshots of four (F2020) and six (W2021) weeks of discussion sections. For F2020 on the left, the percentage of total students with cameras ON (% Cameras ON) and the percentage of breakout rooms with students engaging another student through mic/chat (% Breakout rooms with student-student interaction) are shown. For W2021, the percentage of total students with cameras ON (% Cameras ON), percentage of breakout rooms with students engaging anyone else through mic/chat (% Breakout rooms with student/TA/LA-student interaction), and the percentage of total students engaging anyone else through mic/chat (% Student/TA/LA-student interaction) are shown.

Impact of Discussion Elements on Student Engagement. *Factors Affecting Visual Presence (i.e., camera usage).* Focusing first on data collected in Fall 2020 (Figure 7.2, left), the course with the most structural elements had the highest indication of visual presence (course **E**) as compared to the less-structured courses (courses **A** - **D**). Examining the data for courses **A** and **B** suggests that required attendance with small or assigned groups only were inadequate for ensuring high visual presence in a remote environment. The large increase in visual presence between courses **A**, **B**, and **C** and courses **D** and **E** suggests that discussions need to be more highly structured to get students to turn their cameras ON. Specifically, it seems that requiring attendance, asking TAs/LAs to move between breakout rooms, and assigning groups and worksheets may be beneficial design elements in terms of promoting visual presence.

Similar trends are also observed in Winter 2021 (Figure 7.2, right), during which the course with the most structure had the highest indications of visual presence (course **I**) compared to less structured courses (courses **F** - **H**). The relatively large increase in camera usage from course **F** to **G** suggests that requiring attendance, using small groups, and encouraging TA/LA movement together may better support camera usage compared to only having an assigned discussion activity. Nonetheless, course **G** did not see particularly high camera usage either compared to courses **H** and **I**; this is in accordance with the Fall 2020 observations that the inclusion of the first four discussion elements was important in ensuring higher camera usage in breakout rooms.

Comparing data collected in F2020 and W2021, course **H** included the same design elements as course **D** with the addition of assigned groups, yet the visual presence observed for both courses **D** and **H** were quite similar. This seems to imply that good camera usage can be achieved without assigning groups, so long as students are held accountable through other means (such as required attendance, working in small groups, and completing assigned activities) and are

adequately supported through TA/LA movement between groups. The progression from courses **D** and **H** to courses **E** and **I** suggests that assigned roles may further encourage visual presence.

Factors Affecting Verbal Presence (i.e., mic/chat usage). In Fall 2020, verbal presence was defined as students directly speaking to other students through mic or chat. Using this definition, no verbal presence was observed in courses **A**, **B**, and **C**. These breakout rooms, however, were not always silent. Instead, most of the dialogue occurred between students and TAs or LAs, rather than with other students. In these breakout rooms, TAs and LAs have been observed to lecture or demonstrate problem solving, and to only occasionally prompt students to speak. Therefore, it appears that additional design elements beyond what was used in courses **A**, **B**, and **C** may be necessary to ensure verbal presence, particularly between students.

Some verbal presence in course **D** is observed, which suggests that TA/LA movement is an important factor for promoting conversations amongst students. This could be because without a TA or LA constantly present in the breakout room, students are made to engage with each other. A very large increase in verbal presence was observed once both assigned groups and assigned roles were included as part of the discussion structure (course **E**). In course **E**, students not only worked with the same group of students each week, but students also were assigned specific group responsibilities that rotated weekly. It should also be pointed out that course **E** had a much higher LA-to-student ratio compared to the other observed courses. The high structure of the course ensured that groups could work independently, yet all groups also had ready access to TA/LA assistance.

As noted in the Methods section, a more general definition of verbal presence was explored in W2021, not only including student-student interactions but also student-TA/LA interactions as well. The change in definition occurred as an effort to investigate the forms of student engagement

that were occurring in less structured courses, such as courses **A**, **B**, and **C**, which had little to no observed verbal presence using the original definition. By altering the definition of engagement to include student interactions with TAs and/or LAs, relatively high verbal presence was seen for all W2021 observed breakout rooms, regardless of discussion structure. Nonetheless, the number of students involved in these conversations varies depending on the design features of the discussion section. For instance, course **F** had much fewer student-student/LA/TA conversations compared to the percent of breakout rooms with observed interactions, indicating that only a few students likely contributed to the overall discussion within a given breakout room.

A similar effect is observed for course **G**. While verbal presence increases from course **F** to course **G**, there is a large difference between the interaction per student and interaction per breakout room. Based on course **G**, it appears that having smaller groups, TA/LA movement, and required attendance may increase verbal presence along with visual presence, although the discussion seems to be occurring primarily between the TA/LA and students. With course **H**, the verbal presence per breakout room and per student are similar, suggesting that multiple students were participating within a breakout room; this indicates that assigning groups and activities can promote student conversations in particular. If groups and activities are not assigned, perhaps TAs and LAs are more likely to lecture, leading to less opportunities for students to interact with other students. Lastly, course **I** shows high verbal presence for both definitions, indicating that assigning roles in addition to the first five elements may not necessarily result in more discussion between students but perhaps can lead to more overall interaction in the percentage of breakout rooms.

Correlative and Temporal Analysis of Camera and Mic/Chat Usage. Given the importance placed on camera usage during remote instruction, we investigated the connection between the number of cameras turned ON and the amount of verbal engagement occurring in a breakout room.

To investigate this relationship, we calculated the percentage of camera usage and mic/chat usage by counting the number of students who had their cameras ON (visual presence) or conversed with another student, TA, or LA through mic/chat (verbal presence) and dividing it by the total number of students observed for that week. In this measurement, students were only observed once per week. This essentially considers the average weekly visual and verbal presence for each course. Because we did not observe each course every week during F2020, only the Winter 2021 data is analyzed in this manner.

The data shows a strong correlation between visual and verbal presence ($R^2 = 0.67$), where higher visual presence is associated with higher verbal presence, as shown by the slope of 0.7 for the fitted line (Figure 7.3a). Interestingly, the courses are generally clustered, with the lowest structured course (course **F**) in the bottom left quadrant and the highest structured courses (courses **H** and **I**) in the top right quadrant of Figure 7.3a. This indicates that the level of visual and verbal presence remains relatively consistent throughout the quarter for each course. Additionally, the ratio of camera usage to mic/chat usage appears to stay consistent across most of the courses, indicating that those two parameters are strongly correlated for the various discussion styles observed.

Visual presence and verbal presence closely track each other over time, where the camera and mic/chat usage percentages remain relatively stable across the observed 9- and 6-week timeframes, respectively (Figure 7.3b). Courses **G** and **H** show less correlation between camera and mic/chat usage during weeks 5-6 and weeks 9-10, respectively. This may be due to smaller sample sizes for courses **G** and **H** (25 and 30 students observed per week on average) relative to the sample sizes of courses **F** and **I** (62 and 56 students observed per week on average). Therefore, the correlation between camera and mic/chat usage seems to stay relatively the same as the quarter

progresses. Unfortunately, our definition of verbal presence was not finalized until week 5 of the W2021 quarter, so it is unclear if the trend differs during the first half of the term for mic/chat usage. Given the trend observed in camera usage and its strong correlation to mic/chat usage, however, it seems the average level of both verbal and visual presence remains relatively stable throughout the quarter.

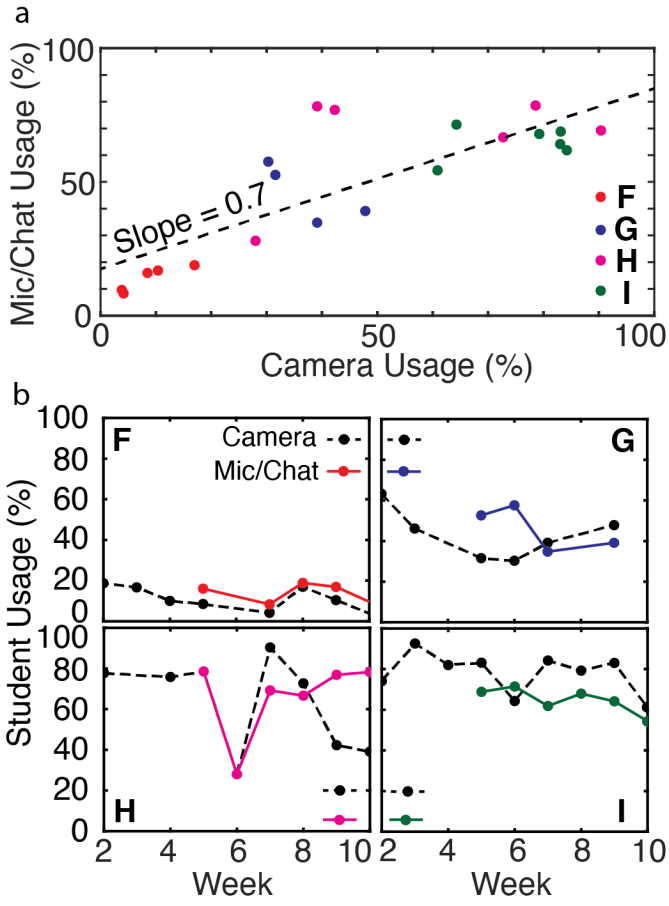

Figure 7.3 Correlative and Temporal Analysis of Observational Data in W2021.

a) Linear trend observed between the percentages of camera usage and mic/chat usage for courses **F** – **I** ($R^2 = 0.67$). b) Week-by-week trend of the same percentages in (a)

7.5 Discussion

While incorporating all of the design elements investigated in this study seems to increase student engagement, it appears that some strategies are more impactful than others in terms of stimulating visual or verbal presence. The data suggests that increased visual and verbal presence is associated with high TA/LA movement, smaller group sizes, and assigned groups and worksheets. This holds true for both F2020 and W2021, where courses **D**, **E**, **G**, **H**, and **I** all had higher levels of visual and verbal presence. With that said, verbal presence did not increase as dramatically as visual presence with the addition of these elements, indicating that camera usage and mic/chat usage are impacted differently by various discussion elements.

These results are aligned with previous DE literature findings, which advocate adding structured elements to a course in order to increase student engagement.[203,207] In particular, smaller class sizes have been connected to higher camera usage,[264] and it has been suggested that groups larger than five make it difficult for students to share out with the rest of the group.[265] However, in this study, small group size and mandatory attendance alone were insufficient at encouraging visual presence, but they did seem to be important factors when used in combination with other design elements.

The TA/LA movement element seems to be another important factor to consider when designing remote classrooms. The isolation experienced in a breakout room is vastly different than that in a F2F classroom, and Woodbury et *al*. suggests that the rotation of instructors between breakout rooms can help with pacing as it may be difficult for students to assess their progress relative to other groups.[266] Thus, the movement of instructors between breakout rooms contributes to students' overall social presence, perhaps because frequent visits helps students stay on track and engaged with the content. Interestingly, this study indicates that having a TA or LA remain in

the same breakout room for the entire session can be a deterrent to student camara usage and dialogue, even if there is an assigned activity for students to work on.

Our results also highlight the importance of assigned activities, teams, and roles. These are critical elements of POGIL (Process Oriented Guided Inquiry Learning), which has been shown to increase engagement in the F2F environment.[267,268] While remote learning requires a different level of structure than in-person learning,[232] these practices have been found to be beneficial in the virtual classroom, both through this work and the work of others. It has been shown that pre-assigned groups increase student interaction,[210] and structured activities lead to more collaboration in breakout rooms.[212,213,223,269] Furthermore, students with assigned roles tend to have a stronger online presence,[270] interact more with other students,[271] and are better at acquiring collaborative knowledge.[272,273]

While this study alludes to general benefits gained by implementing high-impact practices in the remote environment, it also provides insight into how specific forms of student engagement are differentially impacted. We observed highest amounts of dialogue not only when students were grouped in small teams and assigned an activity to work on, but when students also had specific responsibilities within those groups through assigned roles. This suggests that verbal presence is promoted by creating an atmosphere of familiarity and accountability amongst students.

Another interesting finding is that W2021 courses saw much higher verbal presence in breakout rooms, even for less-structured discussion sections. This is most likely a result of the broader definition used for verbal presence and not because of any substantial differences due to the courses observed or course timing. It seems students are more willing to engage with the TA or LA rather than their peers. Furthermore, the differences seen in verbal presence *per breakout room* as opposed to *per student* indicates that oftentimes only a few students were engaged in

conversation, highlighting the importance of combining TA/LA movement with assigned groups and activities to stimulate dialogue between students. This has been seen in other studies, where easy access to a tutor is seen as a key strength of distance education.[230] But if the goal is to encourage students to converse specifically with other students, the availability of TA/LA assistance needs to be well planned to ensure that TAs and LAs do not dominate the conversation.

In terms of camera usage as a measure of engagement, visual presence may be a reasonable indicator of verbal presence. Many benefits have been attributed to using cameras in distance education, including providing nonverbal cues and establishing interpersonal relationships.[274–277] Many instructors therefore felt frustrated at the lack of camera usage during the pandemic, and studies during that time indicated that turning cameras OFF led to feelings of disconnect amongst students.[257,278] The absence of visual presence was also linked to a more "divide-and-conquer" mindset,[216] and having cameras ON was found to increase equal participation amongst group members.[279] While this study is unable to determine any causal relationship between visual and verbal presence, it does suggest that the two are related. This outcome may be worthy of further investigation, as it can potentially provide a means to measure student engagement quickly and easily in virtual classrooms. While it can be time consuming to count the number of verbal interactions occurring in a breakout room, it is feasible for a TA or LA to drop into a breakout room and count the number of cameras turned ON.

Of course there are many reasons why a student turns their camera OFF, including concern over privacy and weak internet connection.[235,258] Zoom fatigue poses difficulties as well, and a concern is that the fatigue brought on by maintaining a constant visual presence may lead to less verbal engagement, although this study did not show that effect.[280] There are certainly good reasons not to mandate camera usage for equity purposes. With that said, this study points to the

relatively consistent nature of student preferences towards visual and verbal presence. Little change occurred across the quarter, despite increased familiarity with peers, TAs, and LAs. As other studies have noted, it is advisable to establish expectations around participation and engagement early as it may be less likely to change once the term is underway.[218,281–283]

Finally, there are noticeable differences between general chemistry and organic chemistry in terms of student visual and verbal engagement. Students enrolled in organic chemistry (**A**, **B**, **C**, **F**, and **G**) generally had less overall engagement relative to students enrolled in general chemistry, regardless of whether the course was designed for Life Science (course **B**, **C**, **F**, and **G**) or Physical Science (course **A**) majors. Perhaps because the students who take organic chemistry are further along in their academic career, organic chemistry discussion sections tend to have less structure than general chemistry discussion sections. This seems to be a factor in the lower observed engagement given that organic chemistry student engagement was higher when more structured elements were included (course **G**). This points to the fact that students beyond their first year may still benefit from courses with higher structure.

7.6 Conclusions

We present the results of an observational study, in which student engagement is measured and quantified through camera and mic/chat usage. We observe a correlation between higher visual and verbal presence with incremental addition of discussion elements explored in this work. In addition to this finding, different course elements had varying impacts on student engagement, with particular combinations leading to better or worse results. Therefore, it is advisable for instructors to target specific outcomes on visual or verbal presence amongst students using intentional course design. We detail our recommendations based on these findings below.

In order to increase visual presence, it seems a combination of required attendance, small group size, assigned worksheets, and TA/LA movement are necessary. Simply assigning students to groups or providing an assigned worksheet alone does not seem to produce high camera usage. This indicates that the discussion elements explored have varying impacts on visual presence, while the above selection of four elements in particular seem to be key in ensuring majority camera usage. While adding additional structural features such as assigned groups or assigned roles may further increase visual presence, student camera usage was seen to be sufficiently high without those additional features.

To promote student-student conversations specifically, establishing a team-based structure seemed pivotal. There was an increase in conversations between students in the course that added assigned worksheets and assigned groups to the first three elements (required attendance, TA/LA movement, and small group size), highlighting the importance of social accountability for verbal presence amongst students. While TA/LA movement was important in stimulating dialogue overall, it was found that students may be more inclined to engage with TAs and LAs, as opposed to their peers. This highlights the importance of combining TA/LA movement with small or assigned groups to promote direct student interactions, with assigned worksheets and roles leading to further improvement. In general, different structural elements seem to be more impactful at eliciting specific types of social presence. Depending on the overall goal an instructor is hoping to achieve, they may need to focus on varying aspects of supportive group work.

In terms of evaluating visual and verbal presence, we found that the average level of camera usage remained relatively consistent throughout the quarter. Similarly, mic/chat usage remained consistent in the second half of the quarter. Thus, establishing expectations and laying out participation requirements early seems crucial in ensuring a base-level of engagement as increased

familiarity with peers, LAs, TAs, and course structure over time did not seem to have a dramatic impact in increasing visual and verbal presence amongst students.

Additionally, there was a strong correlation between visual and verbal presence. This suggests that observing camera usage can be sufficient to reflect student-to-student/TA/LA interactions, indicating that a quick count of students with cameras ON may be an efficient and quantitative method for instructors or TAs to evaluate student engagement in remote discussion sections. With that said, it should be noted that *per breakout room* and *per student* definitions of verbal presence led to distinct differences in the observed impact on mic/chat usage. This can be an interesting avenue for future education research, in which expanding the definition of student social presence may deepen our understanding of how pedagogical practices affect specific student behavior.

The insights gained from this work point to a base-level of design elements that be may necessary to ensure majority student engagement in remote discussion sections, both in general and organic chemistry. Our findings suggest that instructors should select elements that are intended to target specific student behavior, as demonstrated by the varying effects on visual and verbal presence noted in this study. Further research into student engagement in a variety of DE environments will contribute to a developing library of key strategies designed to increase specific forms of student interactions in remote and hybrid chemistry courses.

Limitations. We acknowledge that this investigation is an observational study and therefore only tentative conclusions can be drawn from the comparisons made between courses. With that said, we believe that the insights drawn are valuable and highlight avenues that warrant further investigation. Ultimately there are many limitations on the conclusions we can draw from this work due to the challenges in measuring engagement with statistical accuracy and the

difficulties in having proper controls. Longer and larger data collection, especially for mic/chat usage, may lead to more robust results. The time interval chosen for observation in F2020 was particularly short and therefore verbal presence may be underestimated for that quarter. While camera usage does appear to be linked to verbal engagement, neither visual nor verbal presence alone is a comprehensive measure of a student's engagement. Furthermore, there are other factors besides lack of engagement that may lead to a student turning off their camera.[235,236] While the discussion elements we investigated are supported by prior literature, there are other structural elements not discussed in this study that could have impacted student visual and verbal engagement. We also recognize that many differences could arise due to overall course structure that are unrelated to discussion setup, including approach to high-stakes assessments and instructor mindset.[284,285]

7.7 Supporting Information

Table 7.3 Unique Course Descriptions in Fall 2020 and Winter 2021 Quarters.

Fall 2020					
Course Label	A	B	C	D	E
Intended Major	Physical Sciences	Life Sciences	Life Sciences	Physical Sciences	Life Sciences
Assessment	Quizzes graded on completion. Open book/note.	One midterm.	Open book/note.	Open book/note.	Open book/note. 2-stage midterms. Final exam in groups.
Discuss-ion	Discussion participation is 5.2% of total grade.	Discussion participation is 15% of total grade. Graded on participation via worksheet submission. Can skip 2 sections without penalty.	Discussion worksheet submission 12 % of total grade. Can skip 2 submissions without penalty.	Discussion participation 5% of total grade.	Discussion worksheet 13% of total grade. 110-min weekly sections. Students completed a google doc in addition to worksheet.
Total Grading	High stakes 84.1% Low stakes 10.5% Participation 5.2%	High stakes 55% Low stakes 45% Participation 0%	High stakes 45% Low stakes 42% Participation 12%	High stakes 75% Low stakes 20% Participation 5%	High stakes 45% Low stakes 48% Participation 7 %
Winter 2021					
Course Label	F	G	H	I	
Intended Major	Life Sciences	Life Sciences	Physical Sciences	Life Sciences	
Assessment	All exams open book/note. Lowest exam dropped and highest doubled.	All exams open book/note.	2-stage midterm. Final exam on zoom.	2-stage midterms.	
Discussion	Optional discussion participation for 2.7% extra credit. Upload to google drive and receive full credit based on weekly worksheet completion.	Discussion Participation 10% of total grade.	Discussion participation 5% of total grade. Allowed 2 absences without penalty	Discussion worksheet 10% of total grade. 110-min weekly sections	
Total Grading	High stakes 100% Low stakes 0% Participation 0%	High stakes 60% Low stakes 30% Participation 10%	High stakes 62% Low stakes 28% Participation 10%	High stakes 43% Low stakes 52% Participation 5%	

Two-stage exam consists of both individual and group work. High stakes assignments include both midterm and final exams, low stakes include quizzes and homework, and participation includes clickers and surveys.

Table 7.4 Total Observational Data for F2020 Presented in this Study

Class	NS	NBR	NS/BR	CAM	CAM (%)	BR[SS]	BR[SS] (%)
A	37	9	4	0	0%	0	0%
B	93	9	10	8	9%	0	0%
C	114	17	7	18	16%	0	0%
D	26	5	5	17	65%	1	20%
E	82	21	4	70	85%	17	81%

NS = Total Number of Students Observed, NBR = Total Number of Breakout Rooms Observed, NS/BR = Average Student Per Breakout Room, CAM = Total Number of Cameras Observed "On", BR[SS] = Total Number of Breakout Rooms with Observed Student-Student Interaction.

Table 7.5 Total Observational Data for W2021 Presented in this Study

Class	NS	NBR	NS/BR	CAM	CAM (%)	BR[AS]	NS[AS]	BR[AS] (%)	NS[AS] (%)
F	312	36	9	29	9%	21	47	58%	15%
G	98	27	4	36	37%	23	46	85%	47%
H	176	62	3	112	64%	43	117	69%	66%
I	333	88	4	26	78%	84	215	95%	65%

NS = Total Number of Students Observed, NBR = Total Number of Breakout Rooms Observed, NS/BR = Average Student Per Breakout Room, CAM = Total Number of Cameras Observed "On", BR[AS] = Total Number of Breakout Rooms with ANY Observed Student-Student/TA/LA Interaction, NS[AS] = Total Number of Students Observed with ANY Observed Student-Student/TA/LA Interaction. It should be noted that this table concerns numbers specifically in weeks 5-10 to only count data that was presented in the main text. Therefore, the total number of students and breakout rooms observed throughout the quarter are higher, as shown in Table 1 in the manuscript.

Table 7.6 Week-by-week Layout of Observation Quantities for W2021.

Week/Course	**2**	**3**	**4**	**5**	**6**	**7**	**8**	**9**	**10**
F (LS *Organic Chemistry* II)	59	54	110	106	N/A	24	53	77	52
	6	6	12	12	N/A	3	6	9	6
G (LS *Organic Chemistry* I)	49	65	N/A	19	33	23	N/A	23	N/A
	14	19	N/A	5	10	6	N/A	6	N/A
H (PS *General Chemistry* II)	54	N/A	29	28	25	52	22	26	23
	18	N/A	9	9	9	18	7	10	9
I (LS *General Chemistry* II)	27	27	50	77	28	76	53	53	46
	7	7	13	21	7	21	13	14	12

Letter label and generic course descriptions for the classes observed in W2021 for this study and their corresponding number of students (NS, white rows) and breakout rooms (NBR, gray rows) that were observed. For the course descriptors, LS indicates Life Sciences and PS indicates Physical Sciences majors in the format of {Intended Major Course Topic Order in Course Series}. The corresponding values for F2020 were not available but should be similar to the data shown here for W2021. "N/A" indicates that the course was not observed that week.

References

1. Newton, I. & Patent Office Deposit Collection. *Opticks: or, A treatise of the reflexions, refractions, inflexions and colours of light. Also two treatises of the species and magnitude of curvilinear figures.* (1704).
2. Kirchoff, G. Ueber die Fraunhofer'schen Linien. *Ann. Phys.* **185**, 148–150 (1860).
3. Walsh, A. Atomic absorption spectroscopy and its applications - old and new. *Pure & Appl. Chem.* **49**, 1621–1628 (1977).
4. Budker, D. & Romalis, M. Optical magnetometry. *Nature Physics.* **3**, 227–234 (2007).
5. Shah, V., Knappe, S., Schwindt, P. D. D. & Kitching, J. Subpicotesla atomic magnetometry with a microfabricated vapour cell. *Nat. Photonics.* **1**, 649–652 (2007).
6. Degen, C. L., Reinhard, F. & Cappellaro, P. Quantum sensing. *Rev. Mod. Phys.* **89**, 035002 (2017).
7. Kominis, I. K., Kornack, T. W., Allred, J. C. & Romalis, M. v. A subfemtotesla multichannel atomic magnetometer. *Nature.* **422**, 596–599 (2003).
8. Kitching, J., Knappe, S. & Donley, E. A. Atomic Sensors-A Review. *IEEE Sens. J.* **11**, (2011).
9. Savukov, I. M. & Romalis, M. v. NMR Detection with an Atomic Magnetometer. *Phys. Rev. Lett.* **94**, 123001 (2005).
10. Allred, J. C., Lyman, R. N., Kornack, T. W. & Romalis, M. v. High-sensitivity atomic magnetometer unaffected by spin-exchange relaxation. *Phys. Rev. Lett.* **89**, 1308011–1308014 (2002).
11. Budker, D., Kimball, D. F., Rochester, S. M., Yashchuk, V. v. & Zolotorev, M. Sensitive magnetometry based on nonlinear magneto-optical rotation. *Phys. Rev. A.* **62**, 043403 (2000).
12. Seltzer, S. J. & Romalis, M. v. Unshielded three-axis vector operation of a spin-exchange-relaxation-free atomic magnetometer. *Appl. Phys. Lett.* **85**, 4804 (2004).
13. Kitching, J. Chip-scale atomic devices. *Appl. Phys. Rev.* **5**, 31302 (2018).
14. Parker, D., Suturina, E. A., Kuprov, I. & Chilton, N. F. How the Ligand Field in Lanthanide Coordination Complexes Determines Magnetic Susceptibility Anisotropy, Paramagnetic NMR Shift, and Relaxation Behavior. *Acc. Chem. Res.* **53**, 1520–1534 (2020).
15. Buono-core, G. E., Li, H. & Marciniak, B. Quenching of excited states by lanthanide ions and chelates in solution. *Coord. Chem. Rev.* **99**, 55–87 (1990).

16. Walsh, B. M. Judd-Ofelt theory: principles and practices. *Advances in Spectroscopy for Lasers and Sensing.* 403–433 (2006).

17. An, J., Shade, C. M., Chengelis-Czegan, D. A., ephane Petoud, S. & Rosi, N. L. Zinc-Adeninate Metal-Organic Framework for Aqueous Encapsulation and Sensitization of Near-infrared and Visible Emitting Lanthanide Cations. *J. Am. Chem. So.c* **133**, 1220–1223 (2011).

18. di Bari, L., Pintacuda, G. & Salvadori, P. Stereochemistry and Near-Infrared Circular Dichroism of a Chiral Yb Complex. *J. Am. Chem. Soc.* **122**, 5557–5562 (2000).

19. Wang, H., Gould, P. L. & Stwalley, W. C. Photoassociative spectroscopy of ultracold 39K atoms in a high-density vapor-cell magneto-optical trap. *Phys. Rev. A.* **53**, R1216 (1996).

20. Sushkov, A. O. & Budker, D. Production of long-lived atomic vapor inside high-density buffer gas. *Phys. Rev. A.* **77**, 042707 (2008).

21. Schempp, H. *et al.* Full counting statistics of laser excited Rydberg aggregates in a one-dimensional geometry. *Phys. Rev. Lett.* **112**, 013002 (2014).

22. Malossi, N. *et al.* Full counting statistics and phase diagram of a dissipative rydberg gas. *Phys. Rev. Lett.* **113**, 023006 (2014).

23. Geomagnetism Magnetic Field Calculators. https://www.ngdc.noaa.gov/geomag/calculators/magcalc.shtml#igrfwmm.

24. Evans, D. F. *The Determination of the Pararnagnetic Susceptibility of Substances in Xolution by Nuclear Magnetic Resonance. J. Chem. Phys.* 81 (1958).

25. Dey, A., Kalita, P. & Chandrasekhar, V. Lanthanide(III)-Based Single-Ion Magnets. *ACS Omega.* **3**, 9462–9475 (2018).

26. Flanagan, B. M., Bernhardt, P. v., Krausz, E. R., Lüthi, S. R. & Riley, M. J. A ligand-field analysis of the trensal (h3trensal = 2,2′,2″-tris(salicylideneimino)triethylamine) ligand. An application of the angular overlap model to lanthanides. *Inorg. Chem.* **41**, 5024–5033 (2002).

27. Martin, W. C., Zalubas, R. & Hagan, L. *Atomic Energy Levels - The Rare-Earth Elements*. vol. 60 (1978).

28. Atallah, T. L. *et al.* Decay-Associated Fourier Spectroscopy: Visible to Shortwave Infrared Time-Resolved Photoluminescence Spectra. *Journal of Physical Chemistry A* **123**, 6792–6798 (2019).

29. Deetz, J. D. *et al.* Liquid-to-glass transition of tetrahydrofuran and 2-methyltetrahydrofuran. *Chinese Physics B.* **21**, 086402 (2012).

30. Ning, Y. *et al.* Highly luminescent, biocompatible ytterbium(iii) complexes as near-infrared fluorophores for living cell imaging. *Chem. Sci.* **9**, 3742–3753 (2018).

31. Shavaleev, N. M., Scopelliti, R., Gumy, F. & Bünzli, J.-C. G. Surprisingly Bright Near-Infrared Luminescence and Short Radiative Lifetimes of Ytterbium in Hetero-Binuclear Yb−Na Chelates. *Inorg. Chem*. **48**, 7937–7946 (2009).

32. Mor, O. E. *et al.* Tapered Optical Fibers Coated with Rare-Earth Complexes for Quantum Applications. *ACS Photonics.* **9**, 2676–2682 (2022).

33. Atzori, M. *et al.* Helicene-Based Ligands Enable Strong Magneto-Chiral Dichroism in a Chiral Ytterbium Complex. *J. Am. Chem. Soc.* **143**, 2671–2675 (2021).

34. Pedersen, K. S. *et al.* Design of Single-Molecule Magnets: Insufficiency of the Anisotropy Barrier as the Sole Criterion. *Inorg. Chem.* **54**, 7600–7606 (2015).

35. Kirmiz, A., Saiki, D. J. & Augustine, M. P. Cavity ring-down observation of Yb3+ optical absorption in room temperature solution. *Spectrochim. Acta. A. Mol. Biomol. Spectrosc.* **75**, 1211–1217 (2010).

36. Gorczyński, A. *et al.* New field-induced single ion magnets based on prolate Er(iii) and Yb(iii) ions: tuning the energy barrier Ueff by the choice of counterions within an N3-tridentate Schiff-base scaffold. *Inorg. Chem. Front.* **5**, 605–618 (2018).

37. Petit, P. O., Petit, J., Goldner, P. & Viana, B. Inhomogeneous broadening of optical transitions in Yb:$CaYAlO_4$. *Opt. Mater.* 30, 1093–1097 (2008).

38. Wen, J. *et al.* Ab-initio calculations of Judd–Ofelt intensity parameters for transitions between crystal-field levels. *J. Lumin.* **152**, 54–57 (2014).

39. Wen, J. *et al.* Crystal field interactions between Ce^{3+} ion and fluoride ligands: a theoretical investigation. *Mater. Res. Express.* **2**, 086202 (2015).

40. Barandiarán, Z. & Seijo, L. On the Bond Length Change upon $4f^1 \rightarrow 5d^1$ Excitations in Eightfold Coordination: $CaF_2:Ce^{3+}$ Cubic Defects. *Theor. Chem. Acc.* 116, 505–508 (2006).

41. Stephens, P. J. Theory of Magnetic Circular Dichroism. *J. Chem. Phys.* **52**, 3489 (2003).

42. Dunbar, T. D., Warren, W. L., Tuttle, B. A., Randall, C. A. & Tsur, Y. Electron Paramagnetic Resonance Investigations of Lanthanide-Doped Barium Titanate: Dopant Site Occupancy. *J. Phys. Chem. B.* **108**, 908–917 (2004).

43. Schwindt, P. D. D. *et al.* Chip-scale atomic magnetometer. *Appl. Phys. Lett.* **85**, 6409 (2004).

44. Casola, F., van der Sar, T. & Yacoby, A. Probing condensed matter physics with magnetometry based on nitrogen-vacancy centres in diamond. *Nat. Rev. Mat.* **3**, 1–13 (2018).

45. Degen, C. Microscopy with single spins. *Nat. Nanotechnol.* **3**, 643–644 (2008).

46. Appel, P. Scanning Nanomagnetometry: Probing Magnetism with Single Spins in Diamond. University of Basel (2017).

47. Seltzer, S. J., Meares, P. J. & Romalis, M. V. Synchronous optical pumping of quantum revival beats for atomic magnetometry. *Phys. Rev. A.* **75**, 051407 (2007).

48. Li, S., Dai, P., Liu, J., Xu, Z. & Chida, K. Spin relaxation of rubidium atoms in an octadecyltrichlorosilane anti-relaxation and anti-reflection coated vacuum multipass cell. *Opt. Mater. Express.* **12**, 4384 (2022).

49. Kominis, I. K., Kornack, T. W., Allred, J. C. & Romalis, M. V. A subfemtotesla multichannel atomic magnetometer. *Nature.* **422**, 596–599 (2003).

50. Aslam, N. *et al.* Quantum sensors for biomedical applications. *Nat. Rev. Phys.* **5**, 157–169 (2023).

51. B. Pangborn, A., A. Giardello, M., H. Grubbs, R., K. Rosen, R. & J. Timmers, F. Safe and Convenient Procedure for Solvent Purification. *Organometallics.* **15**, 1518–1520 (1996).

52. Whitelaw, M. T., Kennedy, A. R. & Mulvey, R. E. Structural Similarity in a Series of Alkali Metal Aluminates with Heteroleptic tert-Butoxide–Isobutyl Ligand Sets. *Eur. J. Inorg. Chem.* **2020**, 2912–2918 (2020).

53. Wang, X. *et al.* Redox Control of Group 4 Metal Ring-Opening Polymerization Activity toward l-Lactide and ε-Caprolactone. *J. Am. Chem. Soc.* **136**, 11264–11267 (2014).

54. Wei, J., N. Riffel, M. & L. Diaconescu, P. Redox Control of Aluminum Ring-Opening Polymerization: A Combined Experimental and DFT Investigation. *Macromolecules.* **50**, 1847–1861 (2017).

55. Bain, G. A. & Berry, J. F. Diamagnetic Corrections and Pascal's Constants. *J. Chem. Educ.* **85**, 532 (2008).

56. Bruker. SAINT, V8.34A; Bruker AXS. Inc.: Madison, Wisconsin, USA.

57. Krause, L., Herbst-Irmer, R., Sheldrick, G. M. & Stalke, D. Comparison of silver and molybdenum microfocus X-ray sources for single-crystal structure determination. *J. Appl. Crystallogr.* **48**, 3–10 (2015).

58. Sheldrick, G. M. *SHELXT* – Integrated space-group and crystal-structure determination. *Acta. Crystallogr. A. Found. Adv.* **71**, 3–8 (2015).

59. Sheldrick, G. M. Crystal structure refinement with *SHELXL*. *Acta. Crystallogr. C. Struct. Chem.* **71**, 3–8 (2015).

60. Dolomanov, O. V., Bourhis, L. J., Gildea, R. J., Howard, J. A. K. & Puschmann, H. *OLEX2* : a complete structure solution, refinement and analysis program. *J. Appl. Crystallogr.* **42**, 339–341 (2009).

61. Wang, X., L. Brosmer, J., Thevenon, A. & L. Diaconescu, P. Highly Active Yttrium Catalysts for the Ring-Opening Polymerization of ε-Caprolactone and δ-Valerolactone. *Organometallics.* **34**, 4700–4706 (2015).

62. Yu, I., Acosta-Ramírez, A. & Mehrkhodavandi, P. Mechanism of Living Lactide Polymerization by Dinuclear Indium Catalysts and Its Impact on Isoselectivity. *J. Am. Chem. Soc.* **134**, 12758–12773 (2012).

63. Zuccaccia, D. & Macchioni, A. An Accurate Methodology to Identify the Level of Aggregation in Solution by PGSE NMR Measurements: The Case of Half-Sandwich Diamino Ruthenium(II) Salts. *Organometallics.* **24**, 3476–3486 (2005).

64. Platel, R. H., White, A. J. P. & Williams, C. K. Bis(phosphinic)diamido Yttrium Amide, Alkoxide, and Aryloxide Complexes: An Evaluation of Lactide Ring-Opening Polymerization Initiator Efficiency. *Inorg. Chem.* **50**, 7718–7728 (2011).

65. Lefeuvre, B. *et al.* Redox-modulations of photophysical and single-molecule magnet properties in ytterbium complexes involving extended-TTF triads. *Molecules.* **25**, (2020).

66. Mandal, L., Biswas, S., Cosquer, G., Shen, Y. & Yamashita, M. Anion-driven structures and SMM behavior of dinuclear terbium and ytterbium complexes. *Dalton Trans.* **47**, 17493–17499 (2018).

67. Sun, O. *et al.* A series of dinuclear lanthanide(III) complexes constructed from Schiff base and β-diketonate ligands: Synthesis, structure, luminescence and SMM behavior. *Cryst. Eng. Comm.* **18**, 4627–4635 (2016).

68. Brunet, G. *et al.* Exploring the dual functionality of an ytterbium complex for luminescence thermometry and slow magnetic relaxation. *Chem. Sci.* **10**, 6799–6808 (2019).

69. Buch, C. D. *et al.* Design of pure heterodinuclear lanthanoid cryptate complexes. *Chem. Sci.* **12**, 6983–6991 (2021).

70. Chen, W. Bin *et al.* Understanding the near-infrared fluorescence and field-induced single-molecule-magnetic properties of dinuclear and one-dimensional-chain ytterbium complexes based on 2-hydroxy-3-methoxybenzoic acid. *Inorg. Chem. Front.* **7**, 3136–3145 (2020).

71. Lin, P. H. *et al.* Ytterbium can relax slowly too: A field-induced Yb 2 single-molecule magnet. *Dalton Trans.* **41**, 12349–12352 (2012).

72. Liu, T.-Q. *et al.* Near-IR Luminescence and Field-Induced Single Molecule Magnet of Four Salen-type Ytterbium Complexes. *Inorg. Chem.* **54**, 221–228 (2014).

73. Pointillart, F. *et al.* A redox-active luminescent ytterbium based single molecule magnet. *Chem. Commun.* **49**, 615–617 (2013).

74. Chiang, L., Herasymchuk, K., Thomas, F. & Storr, T. Influence of Electron-Withdrawing Substituents on the Electronic Structure of Oxidized Ni and Cu Salen Complexes. *Inorg. Chem.* **54**, 5970–5980 (2015).

75. Dogaheh, S. G., Khanmohammadi, H. & Sañudo, E. C. Double-decker luminescent ytterbium and erbium SMMs with symmetric and asymmetric Schiff base ligands. *New. J. Chem.* 41, 10101–10111 (2017).

76. Kimachi, Y., Hidaka, Y., Ohno, T. R., Kroll, G. H. & Weaver, J. H. Reactive metal overlayer formation on high-temperature superconductors at 20 K. *J. Appl. Phys.* **69**, 3176–3181 (1991).

77. Layfield, R. & Murugesu, M. *Lanthanides and Actinides in Molecular Magnetism.* (Wiley-VCH, 2015).

78. Miao, Q. *Design, synthesis and application of paramagnetic NMR probes for protein strucutre studies.* (Leiden University, 2019).

79. Hilborn, R. C. Einstein coefficients, cross sections, *f* values, dipole moments, and all that. *Am. J. Phys.* **50**, 982–986 (1982).

80. Suyver, J. F. *et al.* Novel materials doped with trivalent lanthanides and transition metal ions showing near-infrared to visible photon upconversion. *Opt. Mater.* **27**, 1111–1130 (2005).

81. Wang, L. *et al.* Ytterbium-doped phosphate glass single mode photonic crystal fiber with all solid structure. *Opt. Mater. Express.* **5**, 742 (2015).

82. Zhang, W. *et al.* Yb-doped silica glass and photonic crystal fiber based on laser sintering technology. *Laser Phys.* **26**, 035801 (2016).

83. Yb:YAG. *Crytur* https://www.crytur.com/materials/ybyag/ (2022).

84. Katkova, M. A. *et al.* Near-infrared electroluminescent lanthanide [Pr(iii), Nd(iii), Ho(iii), Er(iii), Tm(iii), and Yb(iii)] N,O-chelated complexes for organic light-emitting devices. *J. Mater. Chem.* **21**, 16611 (2011).

85. Welinski, S., Ferrier, A., Afzelius, M. & Goldner, P. High-resolution optical spectroscopy and magnetic properties of Yb^{3+} in Y_2SiO_5. *Phys. Rev. B.* 94, 155116 (2016).

86. Kindem, J. M. *et al.* Control and single-shot readout of an ion embedded in a nanophotonic cavity. *Nature.* **580**, 201–204 (2020).

87. Serrano, D. *et al.* Ultra-narrow optical linewidths in rare-earth molecular crystals. *Nature.* **603**, 241–246 (2022).

88. Kinkead, S. A. & Abney, K. D., "f-Element speciation in strongly acidic media: Lanthanides and mid-actinide metals, oxides, fluorides, and oxide fluorides in superacids" in *Handbook on the Physics and Chemistry of Rare Earths,* Gschneidner, Jr., K. A.,

Eyring, L., Choppin, G. R. & Lander, G. H, Eds. (Elsevier Science B. V., 1994), pp 507–527

89. Xie, T. *et al.* Characterization of Er^{3+}:YVO_4 for microwave to optical transduction. *Phys. Rev. B.* 104, 054111 (2021).

90. Boettger, T., Sun, Y., Thiel, C. W. & Cone, R. L. "Material optimization of Er^{3+}:Y_2SiO_5 at 1.5 μm for optical processing, memory, and laser frequency stabilization applications", Proc. SPIE 4988, Advanced Optical Data Storage, 51 (June 30, 2003).

91. Carnall, W. T., Fields, P. R. & Rajnak, K. Spectral Intensities of the Trivalent Lanthanides and Actinides in Solution. II. Pm^{3+}, Sm^{3+}, Eu^{3+}, Gd^{3+}, Tb^{3+}, Dy^{3+}, and Ho^{3+}. *J. Chem. Phys.* 49, 4412 (2003).

92. Dodson, C. M. & Zia, R. Magnetic dipole and electric quadrupole transitions in the trivalent lanthanide series: Calculated emission rates and oscillator strengths. *Phys. Rev. B.* **86**, 125102 (2012).

93. TURBOMOLE V7.2 2017, a development of University of Karlsruhe and Forschungszentrum Karlsruhe GmbH, 1989-2007, TURBOMOLE GmbH, since 2007; available from http://www.turbomole.com.

94. Staroverov, V. N., Scuseria, G. E., Tao, J. & Perdew, J. P. Comparative assessment of a new nonempirical density functional: Molecules and hydrogen-bonded complexes. *J. Chem. Phys.* **119**, 12129–12137 (2003).

95. Tao, J., Perdew, J. P., Staroverov, V. N. & Scuseria, G. E. Climbing the density functional ladder: Nonempirical meta–generalized gradient approximation designed for molecules and solids. *Phys. Rev. Lett.* **91**, (2003).

96. Widmark, P.-O., Malmqvist, P. Å., & Roos, B. O. Density matrix averaged atomic natural orbital (ANO) basis sets for correlated molecular wave functions. *Theor. Chim. Acta.* 77 (1990).

97. Roos, B. O. et al. New Relativistic Atomic Natural Orbital Basis Sets for Lanthanide Atoms with Applications to the Ce Diatom and LuF_3. *J. Phys. Chem. A.* 112, 11431–11435 (2008).

98. Grimme, S., Antony, J., Ehrlich, S. & Krieg, H. A consistent and accurate *ab initio* parametrization of density functional dispersion correction (DFT-D) for the 94 elements H-Pu. *J. Chem. Phys.* **132**, 154104 (2010).

99. Schäfer, A., Klamt, A., Sattel, D., Lohrenz, J. C. W. & Eckert, F. COSMO implementation in TURBOMOLE: Extension of an efficient quantum chemical code towards liquid systems. *Phy. Chem. Chem. Phys.* **2**, 2187–2193 (2000).

100. Fdez. Galván, I. et al. OpenMolcas: From Source Code to Insight. *J. Chem. Theory Comp.* 15, 5925–5964 (2019).

101. Roos, B. O., Taylor, P. R. & Sigbahn, P. E. M. A complete active space SCF method (CASSCF) using a density matrix formulated super-CI approach. *Chem. Phys.* **48**, 157–173 (1980).

102. Siegbahn, P. E. M., Almlöf, J., Heiberg, A. & Roos, B. O. The complete active space SCF (CASSCF) method in a Newton–Raphson formulation with application to the HNO molecule. *J. Chem. Phys.* **74**, 2384–2396 (1981).

103. Andersson, K. Different forms of the zeroth-order Hamiltonian in second-order perturbation theory with a complete active space self-consistent field reference function. *Theor. Chim. Acta.* **91**, 31–46 (1995).

104. Andersson, Kerstin., Malmqvist, P. Aake., Roos, B. O., Sadlej, A. J. & Wolinski, Krzysztof. Second-order perturbation theory with a CASSCF reference function. *J. Phys. Chem.* **94**, 5483–5488 (1990).

105. Finley, J., Malmqvist, P.-Å., Roos, B. O. & Serrano-Andrés, L. The multi-state CASPT2 method. *Chem. Phys. Lett.* **288**, 299–306 (1998).

106. Douglas, M. & Kroll, N. M. Quantum electrodynamical corrections to the fine structure of helium. *Ann. Phys.* **82**, 89–155 (1974).

107. Hess, B. A. Relativistic electronic-structure calculations employing a two-component no-pair formalism with external-field projection operators. *Phys. Rev. A.* **33**, 3742–3748 (1986).

108. Jansen, G. & Hess, B. A. Revision of the Douglas-Kroll transformation. *Phys. Rev. A.* **39**, 6016–6017 (1989).

109. Humphrey, W., Dalke, A. & Schulten, K. VMD - Visual Molecular Dynamics'. *J. Molec. Graphics.* **14**, 33–38 (1996).

110. Malmqvist, P. Å., Roos, B. O. & Schimmelpfennig, B. The restricted active space (RAS) state interaction approach with spin–orbit coupling. *Chem. Phys. Lett.* **357**, 230–240 (2002).

111. Malmqvist, P.-Å. & Roos, B. O. The CASSCF state interaction method. *Chem. Phys. Lett.* **155**, 189–194 (1989).

112. Vancoillie, S., Malmqvist, P. Å. & Pierloot, K. Calculation of EPR g tensors for transition-metal complexes based on multiconfigurational perturbation theory (CASPT2). *Chem. Phys. Chem.* **8**, 1803–1815 (2007).

113. Chmaisani, W., El-Kork, N., Elmoussaoui, S. & Korek, M. Electronic Structure Calculations with the Spin Orbit Effect of the Low-Lying Electronic States of the YbBr Molecule. *ACS Omega.* **4**, 14987–14995 (2019).

114. Hu, H. *et al.* Relativistic Two-Component Multireference Configuration Interaction Method with Tunable Correlation Space. *J. Chem. Theory Comput.* **16**, 2975–2984 (2020).

115. Boxer, S. G. Stark Spectroscopy of Photosynthetic Systems. *Biophysical Techniques in Photosynthesis.* 177–189 (Kluwer Academic Publishers).

116. Bhattacharyya, D. *et al.* Vibrational Stark shift spectroscopy of catalysts under the influence of electric fields at electrode–solution interfaces. *Chem. Sci.* **12**, 10131–10149 (2021).

117. Bublitz, G. U. & Boxer, S. G. STARK SPECTROSCOPY: Applications in Chemistry, Biology, and Materials Science. *Annu. Rev. Phys. Chem.* **48**, 213–242 (1997).

118. Hochstrasser, R. M. Electric field effects on oriented molecules and molecular crystals. *Acc. Chem. Res.* **6**, 263–269 (1973).

119. Gafert, J., Ober, C., Orth, K. & Friedrich, J. Thermal Broadening of an Optical Transition in a Chromoprotein between 50 mK and 15 K. *J. Phys. Chem.* **99**, 14561–14565 (1995).

120. Kohler, B. E. & Woehl, J. C. Effects of Electrostatic Fields and Potentials on the Electronic Energies of Conjugated Organic Molecules. *J. Phys. Chem. A.* **103**, 2435–2445 (1999).

121. Figliola, P. *Quantum Information Science: Applications, Global Research and Development, and Policy Considerations*. (2019).

122. Bruzewicz, C. D., Chiaverini, J., McConnell, R. & Sage, J. M. Trapped-ion quantum computing: Progress and challenges. *Appl. Phys. Rev.* **6**, 021314 (2019).

123. Brazier, C. R., Ellingboe, L. C., Kinsey-Nielsen, S. & Bernath, P. F. Laser spectroscopy of alkaline earth monoalkoxide free radicals. *J. Am. Chem. Soc.* **108**, 2126–2132 (1986).

124. Li, M., Kłos, J., Petrov, A. & Kotochigova, S. Emulating optical cycling centers in polyatomic molecules. *Commun. Phys.* **2**, 148 (2019).

125. Guo, H. *et al.* Surface chemical trapping of optical cycling centers. *Phys. Chem. Chem. Phys.* **23**, 211–218 (2021).

126. Dickerson, C. E. *et al.* Franck-Condon Tuning of Optical Cycling Centers by Organic Functionalization. *Phys. Rev. Lett.* **126**, 123002 (2021).

127. Kozyryev, I., Steimle, T. C., Yu, P., Nguyen, D.-T. & Doyle, J. M. Determination of CaOH and $CaOCH_3$ vibrational branching ratios for direct laser cooling and trapping. *New. J. Phys.* **21**, 052002 (2019).

128. Liu, H.-W. *et al.* Robust Tipless Positioning Device for Near-Field Investigations: Press and Roll Scan (PROscan). *ACS Nano.* **16**, 12831–12839 (2022).

129. Ohzono, T. & Fujihira, M. Effect of an Atomic Scale Protrusion on a Tip Surface on Molecular Stick-Slip Motion and Friction Anisotropy in Friction Force Microscopy. *Jpn. J. Appl. Phys.* **39**, 6029 (2000).

130. Tessier, M. D. *et al.* Spectroscopy of colloidal semiconductor core/shell nanoplatelets with high quantum yield. *Nano Lett.* **13**, 3321–3328 (2013).

131. Nasilowski, M., Mahler, B., Lhuillier, E., Ithurria, S. & Dubertret, B. Two-Dimensional Colloidal Nanocrystals. *Chem. Rev.* **116**, 10934–10982 (2016).

132. Guzelturk, B., Kelestemur, Y., Olutas, M., Delikanli, S. & Demir, H. V. Amplified spontaneous emission and lasing in colloidal nanoplatelets. *ACS Nano.* **8**, 6599–6605 (2014).

133. Grim, J. Q. *et al.* Continuous-wave biexciton lasing at room temperature using solution-processed quantum wells. *Nat. Nanotechnol.* **9**, 891–895 (2014).

134. Ithurria, S. & Dubertret, B. Quasi 2D colloidal CdSe platelets with thicknesses controlled at the atomic level. *J. Am. Chem. Soc.* **130**, 16504–16505 (2008).

135. Bouet, C. *et al.* Two-dimensional growth of CdSe nanocrystals, from nanoplatelets to nanosheets. *Chem. Mater.* **25**, 639–645 (2013).

136. Izquierdo, E. *et al.* Coupled HgSe colloidal quantum wells through a tunable barrier: A strategy to uncouple optical and transport band gap. *Chem. Mater.* **30**, 4065–4072 (2018).

137. Meerbach, C. *et al.* Halide-Assisted Synthesis of Cadmium Chalcogenide Nanoplatelets. *Chem. Mater.* **32**, 566–574 (2020).

138. Moghaddam, N. *et al.* Surface Modification of CdE (E: S, Se, and Te) Nanoplatelets to Reach Thicker Nanoplatelets and Homostructures with Confinement-Induced Intraparticle Type I Energy Level Alignment. *J. Am. Chem. Soc.* **143**, 1863–1872 (2021).

139. Tenney, S. M. *et al.* Mercury Chalcogenide Nanoplatelet-Quantum Dot Heterostructures as a New Class of Continuously Tunable Bright Shortwave Infrared Emitters. *J. Phys. Chem. Lett.* **11**, 3473–3480 (2020).

140. Hines, M. A. & Guyot-Sionnest, P. Synthesis and characterization of strongly luminescing ZnS-capped CdSe nanocrystals. *J. Phys. Chem.* **100**, 468–471 (1996).

141. Mahler, B., Nadal, B., Bouet, C., Patriarche, G. & Dubertret, B. Core/shell colloidal semiconductor nanoplatelets. *J. Am. Chem. Soc.* **134**, 18591–18598 (2012).

142. Christodoulou, S. *et al.* Chloride-Induced Thickness Control in CdSe Nanoplatelets. *Nano Lett.* **18**, 6248–6254 (2018).

143. Ithurria, S., Bousquet, G. & Dubertret, B. Continuous transition from 3D to 1D confinement observed during the formation of CdSe nanoplatelets. *J. Am. Chem. Soc.* **133**, 3070–3077 (2011).

144. Sun, H. & Buhro, W. E. CoreShell Cadmium Telluride Quantum Platelets with Absorptions Spanning the Visible Spectrum. *ACS Nano.* **13**, 6982–6991 (2019).

145. Chaves, A. J., Ribeiro, R. M., Frederico, T. & Peres, N. M. R. Excitonic effects in the optical properties of 2D materials:an equation of motion approach. *2D Mater.* **4**, 025086 (2017).

146. Van Der Donck, M. & Peeters, F. M. Interlayer excitons in transition metal dichalcogenide heterostructures. *Phys. Rev. B.* **98**, 115104 (2018).

147. Wannier, G. H. The structure of electronic excitation levels in insulating crystals. *Phys. Rev.* **52**, 191–197 (1937).

148. Elliott, R. J. Intensity of optical absorption by excitons. *Phys. Rev.***108**, 1384–1389 (1957).

149. Brumberg, A. *et al.* Determination of the In-Plane Exciton Radius in 2D CdSe Nanoplatelets via Magneto-optical Spectroscopy. *ACS Nano.* **13**, 8589–8596 (2019).

150. Scott, R. *et al.* Time-Resolved Stark Spectroscopy in CdSe Nanoplatelets: Exciton Binding Energy, Polarizability, and Field-Dependent Radiative Rates. *Nano Lett.* **16**, 6576–6583 (2016).

151. Chhowalla, M., Jena, D. & Zhang, H. Two-dimensional semiconductors for transistors. *Nat. Rev. Mater*. **1**, 1–15.

152. Christol, P., Lefebvre, P. & Mathieu, H. A single equation describes excitonic absorption spectra in all quantum-sized semiconductors. *IEEE J. Quantum Electron.* **30**, 2287–2292 (1994).

153. Green, M. A., Ho-Baillie, A. & Snaith, H. J. The emergence of perovskite solar cells. *Nat. Photon.* **8**, (2014).

154. Blakemore, J. S. Semiconducting and other major properties of gallium arsenide. *J. Appl. Phys.* **53**, R123–R181 (1982).

155. Feldmann, J. *et al.* Linewidth Dependence of Radiative Exciton Lifetimes in Quantum Wells. *Phys. Rev. Lett.* **59**, 2337–2340 (1987).

156. Manser, J. S., Christians, J. A. & Kamat, P. V. Intriguing Optoelectronic Properties of Metal Halide Perovskites. *Chem. Rev.* **116**, 12956–13008 (2016).

157. Passarelli, J. V. *et al.* Tunable exciton binding energy in 2D hybrid layered perovskites through donor–acceptor interactions within the organic layer. *Nat. Chem.* **12**, 672–682 (2020).

158. Vasiliev, R. B. *et al.* High-energy exciton transitions in quasi-two-dimensional cadmium chalcogenide nanoplatelets. *Phys. Rev. B.* **95**, 165414 (2017).

159. Moghaddam, N. *et al.* The Strong Confinement Regime in HgTe Two-Dimensional Nanoplatelets. *J. Phys. Chem. C.* **124**, 23460–23468 (2020).

160. Fernández, M. *et al.* Optical properties of MOVPE-grown ZnS epilayers on (100) GaAs. *Phys. Rev. B.* **55**, 7660–7666 (1997).

161. Campi, D. & Coriasso, C. Optical nonlinearities in multiple quantum wells: Generalized Elliott formula. *Phys. Rev. B.* **51**, 10719–10728 (1995).

162. Baars, J. & Sorger, F. Reststrahlen spectra of HgTe and CdxHg1-xTe. *Solid State Commun.* **10**, 875–878 (1972).

163. Geick, R., Perry, C. H. & Mitra, S. S. Lattice vibrational properties of hexagonal CdSe. *J. Appl. Phys.* **37**, 1994–1997 (1966).

164. He, K., Poole, C., Mak, K. F. & Shan, J. Experimental Demonstration of Continuous Electronic Structure Tuning via Strain in Atomically Thin MoS2. *Nano Lett.* **13**, 2931–2936 (2013).

165. Peelaers, H. & Van de Walle, C. G. Effects of strain on band structure and effective masses in MoS_2. *Phys. Rev. B.* **86**, 241401 (2012).

166. Soloviev, V. N., Eichhöfer, A., Fenske, D. & Banin, U. Molecular Limit of a Bulk Semiconductor: Size Dependence of the "Band Gap" in CdSe Cluster Molecules. *J. Am. Chem. Soc.* **122**, 2673–2674 (2000).

167. Warlimont, H. & Martienssen, W. *Springer Handbook of Materials Data*. (Springer, 2018).

168. David Kumar, M. M. & Devadason, S. Structural and optical properties of CdTe/CdSe heterostructure multilayer thin films prepared by physical vapor deposition technique. *Appl. Nanosci.* **3**, 453–459 (2013).

169. Akinlami, J. O. Electronic structure and optical properties of HgSe. *Semiconductor Physics, Quantum Electronics and Optoelectronics.* **21**, 288–293 (2018).

170. Livache, C. *et al.* Effect of Pressure on Interband and Intraband Transition of Mercury Chalcogenide Quantum Dots. *J. Phys. Chem. C.* **123**, 13122–13130 (2019).

171. John David Jackson. *Classical Electrodynamics*. (Wiley, 1998).

172. Cudazzo, P., Attaccalite, C., Tokatly, I. V. & Rubio, A. Strong Charge-Transfer Excitonic Effects and the Bose-Einstein Exciton Condensate in Graphane. *Phys. Rev. Lett.* **104**, 226804 (2010).

173. Greenwood, A. R., Mazzotti, S., Norris, D. J. & Galli, G. Determining the Structure–Property Relationships of Quasi-Two-Dimensional Semiconductor Nanoplatelets. *J. Phys. Chem. C.* **125**, 4820–4827 (2021).

174. Olsen, T., Latini, S., Rasmussen, F. & Thygesen, K. S. Simple Screened Hydrogen Model of Excitons in Two-Dimensional Materials. *Phys. Rev. Lett.* **116**, 056401 (2016).

175. Lin, Y. *et al.* Dielectric screening of excitons and trions in single-layer MoS_2. *Nano Lett.* **14**, 5569–5576 (2014).

176. Choi, J., Zhang, H., Du, H. & Choi, J. H. Understanding Solvent Effects on the Properties of Two-Dimensional Transition Metal Dichalcogenides. *ACS Appl Mater Interfaces.* **8**, 8864–8869 (2016).

177. Ugeda, M. M. *et al.* Giant bandgap renormalization and excitonic effects in a monolayer transition metal dichalcogenide semiconductor. *Nat. Mater.* **13**, 1091–1095 (2014).

178. Thygesen, K. S. Calculating excitons, plasmons, and quasiparticles in 2D materials and van der Waals heterostructures. *2D Mater.* **4**, 022004 (2017).

179. Raja, A. *et al.* Dielectric disorder in two-dimensional materials. *Nat. Nanotechnol.* **14**, 832–837 (2019).

180. Chernikov, A. *et al.* Exciton Binding Energy and Nonhydrogenic Rydberg Series in Monolayer WS_2. *Phys. Rev. Lett.* **113**, 076802 (2014).

181. Rytova, N. S. Screened Potential of a Point Charge in a Thin Film. *Mosc. Univ. Phys. Bull.* **22**, 18 (1967).

182. Keldysh, L. Coulomb Interaction in Thin Semiconductor and Semimetal Films. *JETP Lett.* **29**, 658–660 (1979).

183. Cavalcante, L. S. R., Chaves, A., Van Duppen, B., Peeters, F. M. & Reichman, D. R. Electrostatics of electron-hole interactions in van der Waals heterostructures. *Phys. Rev. B.* **97**, 125427 (2018).

184. Latini, S., Olsen, T. & Thygesen, K. S. Excitons in van der Waals heterostructures: The important role of dielectric screening. *Phys. Rev. B.* **92**, 245123 (2015).

185. Cudazzo, P., Tokatly, I. V. & Rubio, A. Dielectric screening in two-dimensional insulators: Implications for excitonic and impurity states in graphane. *Phys. Rev. B.* **84**, 085406 (2011).

186. Zelewski, S. J. *et al.* Exciton Binding Energy of Two-Dimensional Highly Luminescent Colloidal Nanostructures Determined from Combined Optical and Photoacoustic Spectroscopies. *J. Phys. Chem. Lett.* **10**, 3459–3464 (2019).

187. Diroll, B. T., Talapin, D. V. & Schaller, R. D. Violet-to-Blue Gain and Lasing from Colloidal CdS Nanoplatelets: Low-Threshold Stimulated Emission Despite Low Photoluminescence Quantum Yield. *ACS Photonics.* **4**, 576–583 (2017).

188. Pedetti, S. *et al.* Optimized Synthesis of CdTe Nanoplatelets and Photoresponse of CdTe Nanoplatelets Films. *Chem. Mater.* **25**, 2455–2462 (2013).

189. Pedetti, S., Ithurria, S., Heuclin, H., Patriarche, G. & Dubertret, B. Type-II CdSe/CdTe Core/Crown Semiconductor Nanoplatelets. *J. Am. Chem. Soc.* **136**, 16430–16438 (2014).

190. Dufour, M. *et al.* Halide Ligands To Release Strain in Cadmium Chalcogenide Nanoplatelets and Achieve High Brightness. *ACS Nano.* **13**, 5326–5334 (2019).

191. Izquierdo, E. *et al.* Strongly Confined HgTe 2D Nanoplatelets as Narrow Near-Infrared Emitters. *J. Am. Chem. Soc.* **138**, 10496–10501 (2016).

192. Finley, J. P. Maximum radius of convergence perturbation theory. *J. Chem. Phys.* **112**, 6997–7001 (2000).

193. Zwiebach, B. Chapter 1: Non-degenerate and degenerate perturbation theory. in *Quantum Physics III* (MIT OCW 8.06, 2018).

194. Atallah, T. L. *et al.* Decay-Associated Fourier Spectroscopy: Visible to Shortwave Infrared Time-Resolved Photoluminescence Spectra. *J. Phys. Chem. A.* **123**, 6792–6798 (2019).

195. Tenney, S. M. *et al.* Mesoscale Quantum-Confined Semiconductor Nanoplatelets through Seeded Growth. *Chem. Mater.* **34**, 6048–6056 (2022).

196. Barnard, J. The World Wide Web and Higher Education: The Promise of Virtual Universities and Online Libraries. **37**, 30–35 (1997).

197. Parsad, B. & Lewis, L. *Distance Education at Degree-Granting Postsecondary Institutions: 2006-07(NCES 2009-044)*. (2008).

198. Allen, I. E. & Seaman, J. *Online report card: Tracking online education in the United States.* (2016).

199. Schwartz, H. *Remote Learning Is Here to Stay: Results from the First American School District Panel Survey*. (RAND Corporation, 2020).

200. Bhagat, S. & Kim, D. J. Higher Education Amidst COVID-19: Challenges and Silver Lining. *Information Systems Management* **37**, 366–371 (2020).

201. Parker, A. Interaction in Distance Education: The Critical Conversation. **12**, 13–17 (1999).

202. Thurmond, V. A. & Wambach, K. Understanding Interactions in Distance Education: A Review of the Literature. **1**, 9–26 (2004).

203. Bernard, R. M. *et al.* A Meta-Analysis of Three Types of Interaction Treatments in Distance Education. *Rev. Educ. Res.* **79**, 1243–1289 (2009).

204. Moore, M. G. Editorial: Three types of interaction. *American Journal of Distance Education.* **3**, 1–7 (1989).

205. Kumar, P., Saxena, C. & Baber, H. Learner-content interaction in e-learning- the moderating role of perceived harm of COVID-19 in assessing the satisfaction of learners. *Smart Learning Environments* **8**, (2021).

206. Tinto, V. Exploring the Character of Student Persistence in Higher Education: The Impact of Perception, Motivation, and Engagement. in *Handbook of Research on Student Engagement* (eds. Reschly, A. L. & Christenson, S. L.) (Springer International Publishing, 2022).

207. Martin, F. & Bolliger, D. U. Engagement Matters: Student Perceptions on the Importance of Engagement Strategies in the Online Learning Environment. *Online Learning.* **22**, (2018).

208. Wester, E. R., Walsh, L. L., Arango-Caro, S. & Callis-Duehl, K. L. Student Engagement Declines in STEM Undergraduates during COVID-19–Driven Remote Learning. *J. Microbiol. Biol. Educ.* **22**, ev22i1.2385 (2021).

209. Perets, E. A. *et al.* Impact of the Emergency Transition to Remote Teaching on Student Engagement in a Non-STEM Undergraduate Chemistry Course in the Time of COVID-19. *J. Chem. Educ.* **97**, 2439–2447 (2020).

210. Fung, F. M. & Lam, Y. How COVID-19 Disrupted Our "Flipped" Freshman Organic Chemistry Course: Insights Gained from Singapore. *J. Chem. Educ.* **97**, 2573–2580 (2020).

211. Van Heuvelen, K. M., Daub, G. W. & Ryswyk, H. Van. Emergency Remote Instruction during the COVID-19 Pandemic Reshapes Collaborative Learning in General Chemistry. *J. Chem. Educ.* **97**, 2884–2888 (2020).

212. Singhal, M. K. Facilitating Virtual Medicinal Chemistry Active Learning Assignments Using Advanced Zoom Features during COVID-19 Campus Closure. *J. Chem. Educ.* **97**, 2711–2714 (2020).

213. Wenzel, T. Collaborative Group Learning in Remotely Taught Analytical Chemistry Courses. *J. Chem. Educ.* **97**, 2715–2718 (2020).

214. Jamieson, M. V. Keeping a Learning Community and Academic Integrity Intact after a Mid-Term Shift to Online Learning in Chemical Engineering Design During the COVID-19 Pandemic. *J. Chem. Educ.* **97**, 2768–2772 (2020).

215. Fulfer, K. D. *et al.* #StayCentred: Maintaining Personal Education at Centre College During COVID-19. *J. Chem. Educ.* **97**, 2783–2787 (2020).

216. Gemmel, P. M., Goetz, M. K., James, N. M., Jesse, K. A. & Ratliff, B. J. Collaborative Learning in Chemistry: Impact of COVID-19. *J. Chem. Educ.* **97**, 2899–2904 (2020).

217. Shea, P. A study of students' sense of learning community in online environments. *Journal of Online Learning.* **10**, 35–44.

218. Thompson, T. L. & MacDonald, C. J. Community building, emergent design and expecting the unexpected: Creating a quality eLearning experience. *Internet High Educ.* **8**, 233–249.

219. Rovai, A. P. Sense of community, perceived cognitive learning, and persistence in asynchronous learning networks. *Internet High Educ.* **5**, 319–332 (2002).

220. Swan, K. & Ice, P. The community of inquiry framework ten years later: Introduction to the special issue. *Internet High Educ.* **13**, 1–4 (2010).

221. Fiock, H. Designing a Community of Inquiry in Online Courses. *The International Review of Research in Open and Distributed Learning.* **21**, 134–152 (2020).

222. Richardson, J. C. *et al.* Using the Community of Inquiry Framework to Inform Effective Instructional Design. in *The Next Generation of Distance Education* (eds. Moller, L. & Huett, J.) 97–125 (2012).

223. Flener-Lovitt, C., Bailey, K. & Han, R. Using Structured Teams to Develop Social Presence in Asynchronous Chemistry Courses. *J. Chem. Educ.* **97**, 2519–2525 (2020).

224. DeNoyelles, A., Zydney, J. M. & Chen, B. Strategies for creating a community of inquiry through online asynchronous discussions. *MERLOT Journal of Online Learning and Teaching.* **10**, (2014).

225. Garrison, D. R., Anderson, T. & Archer, W. Critical Inquiry in a Text-Based Environment: Computer Conferencing in Higher Education. *Internet High Educ.* **2**, 87–105 (1999).

226. Eberlein, T. *et al.* Pedagogies of engagement in science: A comparison of PBL, POGIL, and PLTL. *Biochemistry and Molecular Biology Education.* **36**, 262–273 (2008).

227. Raker, J. R., Dood, A. J., Srinivasan, S. & Murphy, K. L. Pedagogies of engagement use in postsecondary chemistry education in the United States: results from a national survey. *Chemistry Education Research and Practice.* **22**, 30–42 (2021).

228. Tanner, K. D. Structure Matters: Twenty-One Teaching Strategies to Promote Student Engagement and Cultivate Classroom Equity. *CBE—Life Sciences Education.* **12**, 322–331 (2013).

229. *Handbook of Research on Student Engagement*. (Springer International Publishing, 2022). doi:10.1007/978-3-031-07853-8.

230. Gillies, D. Student perspectives on videoconferencing in teacher education at a distance. *Distance Education.* **29**, 107–118 (2008).

231. Bernard, R. M. *et al.* How Does Distance Education Compare With Classroom Instruction? A Meta-Analysis of the Empirical Literature. *Rev. Educ. Res.* **74**, 379–439 (2004).

232. Clark, R. E. Evaluating Distance Education: Strategies and Cautions. **1**, 3–16 (2000).

233. Smith, P. L. & Dillon, C. L. Comparing distance learning and classroom learning: Conceptual considerations. **13**, 6–23 (2009).

234. Dutton, J., Dutton, M. & Perry, J. How do online students differ from lecture students? *Online Learning.* **6**, (2019).

235. Gherheș, V., Șimon, S. & Para, I. Analysing Students' Reasons for Keeping Their Webcams on or off during Online Classes. *Sustainability.* **13**, 3203 (2021).

236. Castelli, F. R. & Sarvary, M. A. Why students do not turn on their video cameras during online classes and an equitable and inclusive plan to encourage them to do so. *Ecol. Evo.l* **11**, 3565–3576 (2021).

237. Talbot, R. M., Hartley, L. & Wee, B. Transforming Undergraduate Science Education With Learning Assistants: Student Satisfaction in Large Enrollment Courses. *The Journal of College Science Teaching.* **44**, 24 (2015).

238. Alzen, J. L., Langdon, L. S. & Otero, V. K. A logistic regression investigation of the relationship between the Learning Assistant model and failure rates in introductory STEM courses. *Int. J. STEM Educ.* **5**, 56 (2018).

239. Van Dusen, B. & Nissen, J. Associations between learning assistants, passing introductory physics, and equity: A quantitative critical race theory investigation. *Phys. Rev. Phys. Educ. Res.* **16**, 010117 (2020).

240. Karweit, N. Time and Learning: A Review. in *School and Classroom Organization.* 69–95 (L. Erlbaum Associates, 1989).

241. Peterson, P., Swing, S., Stark, K. & Wass, G. Students' cognitions and time on task during mathematics instruction. *Am. Educ. Res. J* **21**, 487–515 (1984).

242. Appleton, J. J., Christenson, S. L. & Furlong, M. J. Student engagement with school: Critical conceptual and methodological issues of the construct. *Psychol. Sch.* **45**, 369–386 (2008).

243. Furlong, M. J. & Christenson, S. L. Engaging students with school and academics: A relevant construct for all students. *Psychol. Sch.* **45**, 365–368 (2008).

244. DeMonbrun, M. *et al.* Creating an Instrument to Measure Student Response to Instructional Practices. *The Journal for Engineering Education.* **106**, 273–298 (2017).

245. Boekarts, M., Pntrich, P. R. & Zeidner, M. *Handbook of self-regulation: Theory, research, and applications*. (Academic Press, 2000).

246. Zimmerman, B. J. Self-regulated learning and academic achievement: An overview. *Educ. Psychol.* **21**, 3–17 (1990).

247. Yamamoto, K., Thomas, E. C. & Karns, E. A. School-related attitudes in middle-school-age students. *Am. Educ. Res. J.* **6**, 191–206 (1969).

248. Epstein, J. L. & McPartland, J. M. The concept and measurement of the quality of school life. *Am. Educ. Res. J.* **13**, 15–30 (1976).

249. Fredricks, J. A., Blumenfeld, P. C. & Paris, A. H. School Engagement: Potential of the Concept, State of the Evidence. *Rev. Educ. Res.* **74**, 59–109 (2004).

250. Nguyen, K. A. *et al.* Instructor strategies to aid implementation of active learning: a systematic literature review. *Int. J. STEM Educ.* **8**, 9 (2021).

251. Kuh, G. D. Assessing What Really Matters to Student Learning *Inside The National Survey of Student Engagement*. *Change: The Magazine of Higher Learning.* **33**, 10–17 (2001).

252. Dixson, M. D. Measuring Student Engagement in the Online Course: The Online Student Engagement Scale (OSE). *Online Learning.* **19**, (2015).

253. Henrie, C. R., Halverson, L. R. & Graham, C. R. Measuring student engagement in technology-mediated learning: A review. *Comput. Educ.* **90**, 36–53 (2015).

254. Hayden, K., Ouyang, Y., Scinski, L., Olszewski, B. & Bielefeldt, T. Increasing Student Interest and Attitudes in STEM: Professional Development and Activities to Engage and Inspire Learners.

255. Baker, R. S. *et al.* Towards Sensor-Free Affect Detection in Cognitive Tutor Algebra. in *International Conference on Educational Data Mining.* (2012).

256. Bluemink, J. & Järvelä, S. Face-to-face encounters as contextual support for Web-based discussions in a teacher education course. *Internet. High. Educ.* **7**, 199–215 (2004).

257. Schwenck, C. M. & Pryor, J. D. Student perspectives on camera usage to engage and connect in foundational education classes: It's time to turn your cameras on. *International Journal of Educational Research Open.* **2**, 100079 (2021).

258. Giesbers, B., Rienties, B., Tempelaar, D. & Gijselaers, W. Investigating the relations between motivation, tool use, participation, and performance in an e-learning course using web-videoconferencing. *Comput. Human Behav.* **29**, 285–292 (2013).

259. Short, J., Williams, E. & Christie, B. *The Social Psychology of Telecommunications*. (John Wiley & Sons, Ltd, 1976).

260. Cui, G., Lockee, B. & Meng, C. Building modern online social presence: A review of social presence theory and its instructional design implications for future trends. *Educ. Inf. Technol. (Dordr)* **18**, 661–685 (2013).

261. Oakley, B., Brent, R., Felder, R. M. & Elhajj, I. Turning Student Groups into Effective Teams. *Journal of Student Centered Learning.* **2**, 26 (2004).

262. *Process Oriented Guided Inquiry Learning (POGIL)*. vol. 994 (American Chemical Society, 2008).

263. Rodriguez, J.-M. G., Hunter, K. H., Scharlott, L. J. & Becker, N. M. A Review of Research on Process Oriented Guided Inquiry Learning: Implications for Research and Practice. *J. Chem. Educ.* **97**, 3506–3520 (2020).

264. Li, N. *et al.* Picturing One's Self: Camera Use in Zoom Classes during the COVID-19 Pandemic. in *L@S '22: Ninth (2022) ACM Conference on Learning @ Scale* .151–162 (ACM, 2022).

265. AbuSeileek, A. F. The effect of computer-assisted cooperative learning methods and group size on the EFL learners' achievement in communication skills. *Comput. Educ.* **58**, 231–239 (2012).

266. Woodbury, J., Arneson, J. B. & Offerdahl, E. G. Adapting Team-Based Learning for an Online Biochemistry Course. *J. Chem. Educ.* **99**, 2964–2971 (2022).

267. Myers, T., Monypenny, R. & Trevathan, J. Overcoming the glassy-eyed nod: An application of process-oriented guided inquiry learning techniques in information technology. *Journal of Learning Design.* **5**, 12–22 (2012).

268. Jin, G. & Bierma, T. J. Guided-Inquiry Learning in Environmental Health. *J. Environ. Health.* **73**, 80–85 (2011).

269. Chandler, K. Using Breakout Rooms in Synchronous Online Tutorials. *Journal of Perspectives in Applied Academic Practice.* **4**, (2016).

270. Vonderwell, S. & Zachariah, S. Factors that Influence Participation In Online Learning. *Journal of Research on Technology in Education.* **38**, 213–230 (2005).

271. Wise, A. F., Saghafian, M. & Padmanabhan, P. Towards more precise design guidance: specifying and testing the functions of assigned student roles in online discussions. *Educational Technology Research and Development.* **60**, 55–82 (2012).

272. Reiserer, M., Ertl, B. & Mandl, H. Fostering Collaborative Knowledge Construction in Desktop Video-conferencing. Effects of Content Schemes and Cooperation Scripts in Peer Teaching Settings. in *Computer Support for Collaborative Learning.* 379–388 (Routledge, 2001).

273. Ertl, B., Fischer, F. & Mandl, H. Conceptual and socio-cognitive support for collaborative learning in videoconferencing environments. *Comput. Educ.* **47**, 298–315 (2006).

274. Mottet, T. P. Interactive television instructors' perceptions of students' nonverbal responsiveness and their influence on distance teaching. *Commun. Educ.* **49**, 146–164 (2000).

275. Olson, J. S., Olson, G. M. & Meader, D. K. What mix of video and audio is useful for small groups doing remote real-time design work? in 362–368 (1995).

276. Mottet, T. P. & Richmond, V. P. Student nonverbal communication and its influence on teachers and teaching. in *Communication for Teachers* (eds. Chesebro, J. L. & McCroskey, J. C.) 47–61 (Allyn & Bacon, 2002).

277. Falloon, G. Making the Connection: Moore's Theory of Transactional Distance and Its Relevance to the Use of a Virtual Classroom in Postgraduate Online Teacher Education. *Journal of Research on Technology in Education.* **43**, 187–209 (2011).

278. Selco, J. I. & Habbak, M. STEM Students' Perceptions on Emergency Online Learning during the COVID-19 Pandemic: Challenges and Successes. *Educ. Sci. (Basel)* **11**, 799 (2021).

279. Jayasundara, J. M. P. V. K., Gilbert, T., Kersten, S. & Meng, L. How UK HE STEM Students Were Motivated to Switch Their Cameras on: A Study of the Development of Compassionate Communications in Task-focused Online Group Meetings. *Educ. Sci. (Basel)* **12**, 317 (2022).

280. Shockley, K. M. *et al.* The fatiguing effects of camera use in virtual meetings: A within-person field experiment. *Journal of Applied Psychology.* **106**, 1137–1155 (2021).

281. Tharayil, S. *et al.* Strategies to mitigate student resistance to active learning. *Int. J. STEM Educ.* **5**, 7 (2018).

282. Song, L., Singleton, E. S., Hill, J. R. & Koh, M. H. Improving online learning: Student perceptions of useful and challenging characteristics. *Internet High Educ.* **7**, 59–70 (2004).

283. Conrad, D. L. Engagement, Excitement, Anxiety, and Fear: Learners' Experiences of Starting an Online Course. *American Journal of Distance Education.* **16**, 205–226 (2002).

284. Bowen, R. S. & Cooper, M. M. Grading on a Curve as a Systemic Issue of Equity in Chemistry Education. *J. Chem. Educ.* **99**, 185–194 (2022).

285. Canning, E. A., Muenks, K., Green, D. J. & Murphy, M. C. STEM faculty who believe ability is fixed have larger racial achievement gaps and inspire less student motivation in their classes. *Sci. Adv.* **5**, eaau4734 (2019).